



Dottorato di Ricerca in Fisica

UNIVERSITÀ DI PISA

GRADUATE COURSE IN PHYSICS

UNIVERSITY OF PISA

---

PhD Thesis:

**Search for an invisible  $Z'$  in  $\mu^+\mu^-$  plus  
missing energy events at Belle II**

---

CANDIDATE  
**Laura Zani**

SUPERVISOR  
**Prof. Francesco Forti**



Dottorato di Ricerca in Fisica  
**UNIVERSITÀ DI PISA**

Dottorato di Ricerca in Fisica XXXII ciclo

# Contents

<b>Contents</b>	<b>i</b>
<b>Introduction</b>	<b>1</b>
<b>1 Physics motivations</b>	<b>5</b>
1.1 Introduction to the Standard Model . . . . .	5
1.2 Dark Matter puzzle . . . . .	12
1.3 Light Thermal Dark Matter and possible SM extensions . . . . .	15
1.4 Dark Matter detection methods . . . . .	18
1.5 Dark sector searches at accelerators . . . . .	23
1.5.1 Search for invisible particles at accelerators . . . . .	24
1.5.2 Dark photon searches at lepton colliders . . . . .	25
1.6 Alternative SM extensions: the $L_\mu - L_\tau$ model . . . . .	28
1.6.1 Invisible $Z'$ produced in dimuon plus missing energy events in $e^+e^-$ collisions at Belle II . . . . .	31
<b>2 SuperKEKB accelerator</b>	<b>33</b>
2.1 Introduction on experiments at the $B$ factories . . . . .	33
2.1.1 The asymmetric $B$ factory concept . . . . .	34
2.1.2 The first generation of $B$ factories: PEP-II and KEKB . . . . .	35
2.2 The second generation: SuperKEKB design upgrades . . . . .	38
2.2.1 Nano beam scheme overview . . . . .	39
2.3 SuperKEKB commissioning and running phases . . . . .	41
2.3.1 Phase 1: first beam background measurements . . . . .	42
2.3.2 Phase 2: first collisions . . . . .	43
2.3.3 Phase 3: first physics with the full vertex detector . . . . .	45
<b>3 Belle II experiment</b>	<b>49</b>
3.1 Belle II upgrade overview . . . . .	49
3.1.1 The Pixel Detector . . . . .	51
3.1.2 The Silicon Vertex Detector . . . . .	52
3.1.3 The Central Drift Chamber . . . . .	54
3.1.4 Particle Identification devices . . . . .	55
3.1.5 The Electromagnetic Calorimeter . . . . .	57
3.1.6 The neutral kaon and muon detector . . . . .	58
3.2 The trigger system at Belle II . . . . .	60

3.3	Overview of the <i>Belle II analysis software framework</i> . . . . .	61
3.3.1	The <i>basf2</i> code . . . . .	61
3.3.2	Input/output: simulation and reconstruction in <i>basf2</i> . . . . .	63
3.3.3	Condition Data . . . . .	64
3.4	Data sets . . . . .	64
3.4.1	Monte Carlo samples . . . . .	64
3.4.2	Experimental data set . . . . .	66
3.4.3	Belle II detector during Phase 2 . . . . .	66
<b>4</b>	<b>Analysis overview and event selection</b>	<b>69</b>
4.1	Analysis Strategy . . . . .	69
4.2	Candidate Reconstruction . . . . .	71
4.3	Event Selection . . . . .	72
4.4	Background Rejection: $\tau$ suppression and analysis optimization . . . . .	75
4.4.1	LFV $Z'$ to invisible . . . . .	83
<b>5</b>	<b>Signal study</b>	<b>87</b>
5.1	Signal yield extraction . . . . .	87
5.1.1	Signal shape study . . . . .	87
5.1.2	Signal width . . . . .	90
5.2	Recoil mass resolution . . . . .	90
<b>6</b>	<b>Data validation studies</b>	<b>97</b>
6.1	Data validation with $ee$ sample . . . . .	98
6.2	Data validation with $\mu^+\mu^-\gamma$ sample . . . . .	99
6.3	Data validation with a reversed $\tau$ suppression procedure . . . . .	103
6.4	Trigger data validation . . . . .	107
6.5	Data validation summary . . . . .	108
<b>7</b>	<b>Detector studies and systematic uncertainty evaluation</b>	<b>111</b>
7.1	Main systematic uncertainty sources . . . . .	111
7.2	Trigger efficiency . . . . .	114
7.3	Particle ID selection . . . . .	115
7.4	Tracking efficiency . . . . .	115
<b>8</b>	<b>Results and conclusions</b>	<b>129</b>
8.1	Expected sensitivities . . . . .	129
8.2	Results on Phase 2 data . . . . .	134
8.3	Phase 3 improvement and prospects . . . . .	138
8.3.1	The luminosity increase . . . . .	138
8.3.2	The muon ID improvement . . . . .	138
8.3.3	The VXD impact on recoil mass resolution . . . . .	139
8.3.4	Projection results . . . . .	140
8.3.5	Next plans . . . . .	142
8.4	Conclusions . . . . .	143
	<b>Appendices</b>	<b>145</b>

---

<b>A</b>	<b>Event selection and signal shape study results</b>	<b>147</b>
A.1	The standard $Z'$ selection results . . . . .	147
A.2	The LFV $Z'$ selection results . . . . .	150
A.3	Signal shape study: toy MC results . . . . .	151
<b>B</b>	<b>Performance studies on Phase 2 data</b>	<b>155</b>
B.1	The trigger efficiency study . . . . .	155
B.1.1	Plateau efficiency . . . . .	156
B.1.2	Systematic uncertainty evaluation . . . . .	157
B.2	The lepton identification study . . . . .	158
B.3	The track reconstruction efficiency study . . . . .	160
B.3.1	Calibration procedure . . . . .	166
B.3.2	Systematic uncertainty evaluation . . . . .	170
<b>C</b>	<b>Upper limit calculation</b>	<b>173</b>
C.1	Bayesian approach procedure and results . . . . .	173
C.1.1	LFV $Z'$ expected sensitivity results . . . . .	175
C.2	Frequentist approach procedure and results . . . . .	177
C.3	Null hypothesis testing . . . . .	184
<b>D</b>	<b>Phase 3 improvement and prospects: supplementary plots</b>	<b>187</b>
	<b>Acknowledgment</b>	<b>189</b>
	<b>Bibliography</b>	<b>191</b>



# Introduction

The Standard Model (SM) of particle physics has been proven by many experimental results to be a predictive theory and currently the best known description of the fundamental constituents of nature and their interactions. However, it cannot account for some known phenomena, such as the existence of dark matter, established by many astrophysical and cosmological observations which provide the measurement for its relic abundance. Dark matter (DM) is among the most compelling issues for new physics beyond the SM, but remains a complicated mystery to solve, since almost nothing is known about its origin and its nature. Therefore it deserves to be searched for with all available experimental tools.

The dark matter puzzle can be addressed by assuming a thermal production in the early universe. In most of the theoretical frameworks, to account for the measured relic abundance and avoid DM overproduction, a new mediator that can couple to DM and SM particles is required to enhance the DM annihilation rate. A simple solution to extend the SM and account for this additional mediator is by considering a dark gauge  $U_D(1)$  invariance which is associated with a new massive boson that can connect the SM particles to the unknown constituents of a new hidden sector.

The work presented in this thesis concerns the search for an invisibly decaying  $Z'$  boson produced radiatively in  $e^+e^-$  annihilations to a final state with a muon pair + missing energy. The analyzed data have been recorded during the pilot run of the Belle II experiment, installed at the SuperKEKB electron-positron collider at the KEK laboratory, in Tsukuba (Japan), which took its first physics data from April to July 2018.

An overview of the dark matter problem is presented in chapter 1, motivating the search for light dark sectors and DM mediators. I introduce the three portals allowed by renormalisable theories, in particular focusing on the vector portal which envisions the existence of a new spin-1 massive boson (*dark photon*) coupling SM and dark sector particles. The kinetic mixing mechanism responsible for the coupling is described, along with the theoretical framework related to the  $L_\mu - L_\tau$  symmetry, one of the possible SM extensions based on a new  $U_{L_\mu - L_\tau}(1)$  gauge symmetry used to interpret the results presented in this thesis. The detection methods currently exploited for DM searches are briefly described, with a particular focus on the search for direct DM production at particle accelerators and on the different signatures that can be used, depending on the type of the DM mediator under study and the experimental facilities.

The second generation of  $B$  factories, the SuperKEKB collider, plays an important role in this search. Chapter 2 describes the  $B$  factory concept and the main upgrades needed to achieve the design SuperKEKB luminosity of  $8 \times 10^{35} \text{ cm}^{-2}\text{s}^{-1}$ , 40 times higher than its predecessor KEKB. It also presents the main phases of the accelerator commissioning and its luminosity run plan, which is crucial for the data taking and physics reach of the Belle II experiment, discussed in detail in chapter 3. In particular, I summarize the improvements

with respect to Belle needed to meet the high luminosity requirements, and briefly describe the sub-detectors, the trigger system, and the software framework relevant for this analysis, as well as the different data sets, both from real collisions and from Monte Carlo simulation, that have been used for this study.

The analysis strategy is detailed in chapter 4, where the signal signature for the detection of the process  $e^+e^- \rightarrow \mu^+\mu^-Z'$ , with the  $Z'$  decaying to an invisible final state, is described and it should be noticed this is the first time the invisible signature has been explored. The main observable for this search is the invariant mass of the recoil system against the combined four-vector of two reconstructed muons in the center-of-mass frame, in events where nothing else is detected. The criteria for selecting the interesting events and the optimal strategy to suppress the main backgrounds, coming mostly from QED processes and four-lepton final-state events that could mimic the two-muon + missing energy signal signature, are also presented. The same analysis chain, except for the particle identification requirements, can be applied to the final state with a muon-electron pair, which allows the measurement of the expected background rate for the process  $e^+e^- \rightarrow \mu^\pm e^\mp + \text{invisible}$ , that could be explained by models involving a Lepton Flavor Violating (LFV)  $Z'$ .

The signal extraction strategy is based on a Poisson counting experiment technique, motivated by the low statistics of the expected yields, and is explained in chapter 5, along with the full simulation study of the signal shape and the extrapolation of the signal width needed for the binning scheme definition. Finally, I present the comparisons of the recoil mass resolution as measured in simulation and in actual data, where differences have found to be negligible.

Since this study is optimized as a blind analysis, we could not look at the recoil mass distribution of the reconstructed signal candidate in data before the approval for unblinding. Therefore, in order to measure the agreement between data and Monte Carlo and to estimate the systematic uncertainty on the expected background yields and signal efficiencies evaluated from simulation, we compared data and simulated distributions for different signal-free control samples. The data validation studies, which are an essential part of the analysis, are described in chapter 6.

All the performance studies on Belle II 2018 data which have been implemented to measure the efficiencies entering the analysis selections and to evaluate the associated systematic uncertainties are reported in chapter 7. In particular, I developed the analysis to measure the discrepancy of track reconstruction efficiency between data and simulation exploiting a specific decay topology of the process  $e^+e^- \rightarrow \tau^+\tau^-$ . A summary of the study and the main findings are reported at the end of chapter 7 and further details are given in Appendix B.

To conclude, in chapter 8 the expected sensitivities from the simulation are computed and compared to the results on Belle II 2018 data, from which upper limits at 90% credibility level (CL) are provided. The statistical analysis of the expected background yields has been developed in a Bayesian approach, which has been compared to the results from frequentist techniques and turned out to provide the most conservative limits. The technical details of the implemented strategy are given in the Appendix C. The application of the statistical analysis to the unblinded data showed no significant excess in neither the standard nor the LFV  $Z'$  channels. The 90% CL upper limit on the cross section for the process  $e^+e^- \rightarrow \mu^+\mu^-Z'$ ,  $Z' \rightarrow \text{invisible}$  is measured and also interpreted as an exclusion limit in the space of the  $Z'$  coupling constant  $g'$  as a function of the reconstructed  $Z'$  mass. The 90% CL upper limit on the quantity cross section times efficiency for the LFV  $Z'$  search is also provided. A paper reporting the results from the analysis on Belle II 2018 data has been submitted to

*Physical Review Letters*. Finally, I discuss the prospects of this analysis on Belle II 2019 data, considering several improvement factors related to the fully installed detector and the increased luminosity.

In summary, this work measures the first upper limit on the cross section for the invisibly decaying  $Z'$  produced in association with a muon pair at  $e^+e^-$  collisions at the Belle II experiment and it provides also the first upper limit on the model independent search for a LFV  $Z'$ . Moreover, this thesis assesses the capability to provide competitive constraints on the  $L_\mu - L_\tau$  model with the upcoming Belle II 2019 data, that could solve both the known tension in the SM regarding the anomalous magnetic moment of the muon and one of the most compelling issue for modern particle physics such as dark matter.



# Chapter 1

## Physics motivations

The Standard Model (SM) of elementary particle physics is a unified gauge theory of electroweak and strong interactions that is currently our best understanding of the fundamental constituents of nature and of three of the four fundamental forces that rule matter interactions. Although its many successes in predicting almost all the experimental results with the highest accuracy, the Standard Model cannot answer to some open questions in physics and moreover it does not include the gravity in its unified treatment of the fundamental interactions. Some of the most striking phenomena that are unexplained by the Standard Model are the existence of a kind of matter that almost does not interact with the SM particles, if not gravitationally, the dark matter (DM); the different abundance of matter and anti-matter in the Universe that seems to imply an over abundance of matter, known as *baryon asymmetry*; the neutrino oscillations and their masses; the fundamental hierarchy problem, concerning the number of lepton and quark families and their mass differences.

Therefore the effort to search for physics beyond the SM is well motivated, and the search for a dark sector, that feebly couples to the SM particles and could both explain some of the measured tensions between theory and experiments and the nature of the dark matter, is of particular interest.

After a brief overview of the SM in Section 1.1, the rest of the chapter introduces the problem of dark matter (Section 1.2) and the main evidences for it, specifically focusing on the possibility of a light dark matter scenario (Section 1.3). The experimental methods to search for dark matter are summarized in Section 1.4, with a special focus on searches for dark sector signatures at accelerators (Section 1.5). Finally, in Section 1.6 among the possible alternative SM extensions foreseen by light dark matter scenarios, the  $L_\mu - L_\tau$  model framework will be addressed and the motivations to search for an invisibly decaying dark boson  $Z'$  at electron-positron colliders in the reaction  $e^+e^- \rightarrow \mu^+\mu^-Z'$ ,  $Z' \rightarrow \text{invisible}$  will be given, being this search the main topic of this thesis work.

### 1.1 Introduction to the Standard Model

The Standard Model is the phenomenological description of electromagnetism, weak and strong interactions. Formally, it is a unified quantum field theory obeying the gauge group symmetry  $SU(3)_c \times SU(2)_L \times U(1)_Y$ <sup>1</sup>. The model includes a unified description of electro-

---

<sup>1</sup>here  $c$  denotes the color charge,  $L$  the chiral component and  $Y$  the hyper-charge.

magnetic and weak interactions within the electroweak theory, which possesses the symmetry group  $SU(2) \otimes U(1)$  and correlates the electromagnetic and weak coupling constants, and the theory of *quantum chromodynamics* (QCD), describing the strong interaction phenomena.

According to the SM description of nature, matter is composed of two kinds of  $\frac{1}{2}$ -spin particles (fermions): leptons and quarks. Leptons denote particles that, if charged, interact both electromagnetically and weakly, if neutral only weakly. Quarks are the fermionic constituents of hadrons — and then nuclei — and they interact strongly, weakly and electromagnetically.

Both leptons and quarks consist of six types of particles gathered into doublets, which give rise to the three mass generations, or families. The same structure is repeated for anti-particles. All stable matter in the universe belongs to the first and lightest generation, while the heavier doublets correspond to unstable particles which decay to the lighter generations. All doublets have two components differing for one unit charge.

Leptons ( $e, \mu, \tau$ ) with a unitary electric charge are coupled in doublets to a neutral lepton, the neutrino, and they are assigned a lepton number, which is a conserved quantum number in SM interactions. Anti-leptons have the same masses and opposite quantum numbers.

Quarks exist in 6 types, known as *flavors*, and have a fractionary electric charge equal to  $+\frac{2}{3}e$  and  $-\frac{1}{3}e$  for *up*- and *down*- type quarks, respectively. Moreover they possess an additional strong charge, the *color*. Three colors exist in the theory of strong interaction, as described in the QCD, which predicts that when quarks combine to form a meson (bound state of quark-antiquark) or a baryon (bound state of three quarks) they must produce a colorless object, due to the *confinement* principle.

The SM framework interprets the interactions between matter particles through the exchange of virtual bosons, the force-carrying particles, which arise as excitations of the associated gauge fields:

- the photons and the weak bosons  $W^{+/-}, Z^0$  for the electroweak interactions;
- the gluons, for strong interaction;
- additionally, the Higgs boson, as unique scalar field of the theory, provide the mechanism for particles to acquire masses.

The mass mechanism in the SM is implemented through the spontaneous symmetry breaking introduced by the Higgs complex scalar field, which has a non-zero vacuum expectation value ( $vev$ ) and generates the masses of the gauge vector bosons ( $W^+, W^-, Z^0$ ) and all the fermions in the model [1]. Figure 1.1 shows all the particles, fermions and bosons, mentioned above and reports also their main properties (mass, charge, spin).

The mathematical description of the SM is summarized by the Lagrangian that in a general renormalisable form can be written as:

$$\mathcal{L}_{SM} = \mathcal{L}_{kin} + \mathcal{L}_{EW} + \mathcal{L}_{QCD} + \mathcal{L}_{Higgs} + \mathcal{L}_{Yuk} \quad (1.1)$$

The term  $\mathcal{L}_{kin}$  is the kinetic part associated to the gauge bosons and describes their self-interactions, expressed through the strength tensors of the gauge boson fields  $B_\mu$ , associated to the  $U(1)_Y$  hypercharge symmetry,  $W_\mu^a$ , for the  $SU(2)_L$  chiral symmetry and the eight gluon generators  $G_\mu^A$  for  $SU(3)_c$ :

$$\mathcal{L}_{kin} = -\frac{1}{4}B_{\mu\nu}B^{\mu\nu} - \frac{1}{4}W_{\mu\nu}^a W_a^{\mu\nu} - \frac{1}{4}G_{\mu\nu}^A G_A^{\mu\nu}.$$

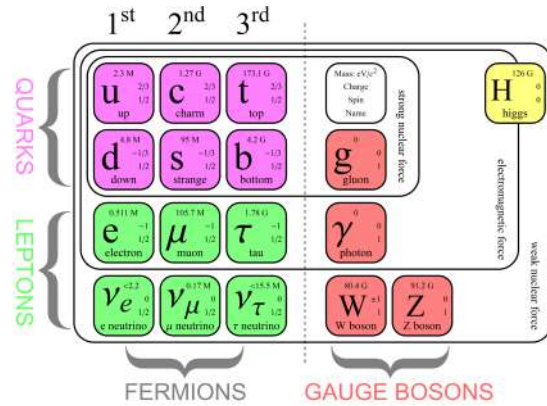


**Figure 1.1:** The Standard Model particles are shown. For each particle, mass, charge, spin and name are given. All the fermions are gathered in the first, second and third column, representing the three mass generations. Quarks are grouped in the first two rows. Their masses varies from a few  $\text{MeV}/c^2$  ( $u, d$ ) to a hundred  $\text{GeV}/c^2$  ( $t$ ). In the third and fourth rows, the leptons doublets are shown, with masses going from fractions of  $eV/c^2$  to almost 2  $\text{GeV}/c^2$  ( $\tau$ ). The fourth column contains the gauge bosons, the force carrying particles of fundamental interactions. The Higgs boson is represented on the top right corner of this chart.

The term  $\mathcal{L}_{EW}$  describes the electroweak theory:

$$\mathcal{L}_{EW} = \bar{\psi}_f \gamma^\mu (i\partial_\mu - \frac{1}{2}g'Y_W B_\mu - \frac{1}{2}g\tau_a W_\mu^a) \psi_f,$$

where the fermions fields  $\psi$  are represented through Dirac spinors, with the index  $f$  running on the flavors. The partial derivatives give the fermion kinetic term. The coupling constants  $g'$  and  $g$  are respectively the electromagnetic and weak couplings correlated by the theory;  $Y_W$  is the hypercharge coupling defined by the identity  $Q = T_3 + Y_W/2$ , being  $Q$  the electric charge and  $T_3$  the third component of the weak isospin. Finally the  $\tau_a$  matrices are the Pauli matrices, whose eigenvalues give the isospin charges of particles interacting with the  $W^\pm$  fields.

The term  $\mathcal{L}_{QCD}$  is instead the description of quark-gluon interactions according to the QCD theory,

$$\mathcal{L}_{QCD} = \bar{\psi}_{f,i} \gamma^\mu (ig_S G_{A,\mu} T_{A,ij}) \psi_{f,j},$$

where  $g_S$  is the strong coupling constant and  $T_{A,ij} = \lambda_{A,ij}/2$ , with  $\lambda_{ij}$  the matrices of  $SU_c(3)$  and  $i, j = 1, \dots, 3$  are the color indices.

The term  $\mathcal{L}_{Higgs}$  includes the Higgs kinetic contribution and its interactions with the gauge bosons of the theory through the covariant derivatives, plus the quartic potential:

$$\mathcal{L}_{Higgs} = \mathcal{L}_{derivatives} + \mu^2 |\phi|^2 - \lambda |\phi|^4 \quad (1.2)$$

where  $\phi = \begin{pmatrix} \phi_+ \\ \phi_0 \end{pmatrix}$  is the Higgs complex scalar field. Choosing  $\mu^2 < 0$  and  $\lambda > 0$  the scalar potential in Equation 1.2 is (up to a constant term):

$$\mathcal{L}_{Higgs,\phi} = -\lambda \left( \phi^\dagger \phi - \frac{v}{2} \right)^2$$

which is minimized by  $\phi^2 = \mu^2/\lambda$ , meaning that the field acquires a non-zero *vacuum expectation value* (*vev*),  $\langle\phi\rangle = v/\sqrt{2}$ , with  $v^2 = -\frac{\mu^2}{\lambda}$ . Only the length of the vector  $\phi$  is fixed, but not its direction, which is arbitrarily chosen to point to the real direction of the down component:

$$\langle\phi\rangle = \begin{pmatrix} 0 \\ v/\sqrt{2} \end{pmatrix}.$$

The interaction of the quarks and leptons with the Higgs field is described by the last part  $\mathcal{L}_{Yuk}$ , where fermions are represented as doublets and singlets of the  $SU(2)_L$  chiral group:

$$\mathcal{L}_{Yuk} = y_{ij}^d \bar{Q}_L^i \phi D_R^j + y_{ij}^u \bar{Q}_L^i \phi^\dagger U_R^j + y_{ij}^e \bar{e}_L^i \phi e_R^j + h.c.,$$

where  $Q_L^i$  is the left-handed quark doublet,  $D^i$  ( $U^i$ ) the right-handed down(up)-type quark singlet and similarly for leptons, the left-handed doublet  $e_L^i$  and the right-handed singlet  $e_R^j$ . The indices  $i, j$  run over the three generations, being  $i(j)$  associated to the left(right)-handed multiplet, while the constants  $y_{ij}^{u,d,e}$  are the elements of the Yukawa mass matrices respectively for up-type, down-type quarks and leptons. After spontaneously symmetry breaking the Higgs doublet in unitary gauge is:

$$\phi(x) = \frac{1}{\sqrt{2}} \begin{pmatrix} 0 \\ v + h(x) \end{pmatrix},$$

and for example writing out the Higgs-lepton interaction term

$$\mathcal{L} = -\frac{y_{ij}^e}{\sqrt{2}} v (\bar{e}_L e_R + \bar{e}_R e_L) - \frac{y_{ij}^e}{\sqrt{2}} h (\bar{e}_L e_R + \bar{e}_R e_L),$$

it can be noticed that, if the the Yukawa coupling is chosen to be consistent with the observed lepton masses  $m_{ij}^e = y_{ij}^e v/\sqrt{2}$ , the fermion masses arise from the coupling of the left-handed and right-handed massless chiral fermions to the Higgs field through its non-zero vacuum expectation value.

In general the  $m_{ij}^q$  matrices for quarks are not diagonal and a basis change represented by a unitary transformation is needed to diagonalize them:

$$\hat{m}_{ij}^q = V_{Lik}^q m_{kl}^q (V_R^{q\dagger})_{lj},$$

where  $\hat{m}_{ij}^q$  indicates the diagonalised matrix. This corresponds to write the left-chiral and right-chiral interaction-basis fields as the mass-basis fields (primed) rotated by  $V_L$  and  $V_R$  respectively:

$$\begin{aligned} q_L^i &= (V_L^q)_{ij} q_L^{\prime j} \\ q_R^i &= (V_R^q)_{ij} q_R^{\prime j}, \end{aligned}$$

where the interaction-basis fields (left side of the formula) are obtained as a linear combination of mass-basis fields (right side of the formula). In the mass basis, the Yukawa interactions are diagonal, but as a consequence of the basis change the matrix expressing the couplings of the W bosons is not:

$$\mathcal{L}_{Wqq} \propto = \frac{g}{\sqrt{2}} \bar{u}_L \gamma_\mu d_L W^\mu \rightarrow \frac{g}{\sqrt{2}} \bar{u}_L^{\prime i} \gamma_\mu (V_{uL} V_{dL}^\dagger) d_L^{\prime j} W^\mu. \quad (1.3)$$

The element  $V_{uL}V_{dL}^\dagger = V_{ud}$  indicates the Cabibbo-Kobayashi-Maskawa (CKM) unitary matrix which represents the basis change:

$$\hat{V}_{CKM} = \begin{pmatrix} V_{ud} & V_{us} & V_{ub} \\ V_{cd} & V_{cs} & V_{cb} \\ V_{td} & V_{ts} & V_{tb} \end{pmatrix}. \quad (1.4)$$

Four free parameters are needed to describe it: three mixing angles which are real parameters and one irreducible complex phase. The CKM matrix describes the flavor transitions between quarks, which are mediated by the weak interaction charged currents. Transitions are allowed between up and down-type quarks, not only within the same doublets, but also between different generations, even though the latter are suppressed. Nicola Cabibbo first explained this suppression through the principle of the quark mixing describing the aforementioned rotation of the mass quark eigenstates ( $d', s'$ ) to the weak interaction eigenstates ( $d, s$ ) [2]:

$$|d\rangle = \cos\theta_C|d'\rangle + \sin\theta_C|s'\rangle, \quad (1.5)$$

$$|s\rangle = -\sin\theta_C|d'\rangle + \cos\theta_C|s'\rangle. \quad (1.6)$$

Experimental observations allowed Cabibbo to estimate  $\sin\theta_C \simeq 0.23$ , which explains the mixing in the scenario of two quark families. The extension to the three quark generations is provided by the Kobayashi-Maskawa mechanism [3] which explains the source of the violation of the combined symmetries of charge-conjugation and parity ( $CP$ ) in the SM. In the standard parameterization the CKM matrix is:

$$V_{CKM} = \begin{pmatrix} c_{12}c_{13} & s_{12}c_{13} & s_{13}e^{-i\delta} \\ -s_{12}c_{23} - c_{12}s_{23}s_{13}e^{i\delta} & c_{12}c_{23} - s_{12}s_{23}s_{13}e^{i\delta} & s_{23}c_{13} \\ s_{12}s_{23} - c_{12}c_{23}s_{13}e^{i\delta} & -c_{12}s_{23} - s_{12}c_{23}s_{13}e^{i\delta} & c_{23}c_{13} \end{pmatrix}. \quad (1.7)$$

It is written as the composition of three rotations and its elements are given in terms of sine ( $s_{ij}$ ) and cosine ( $c_{ij}$ ) of the three mixing angles ( $\theta_{ij}$ ) and the complex phase  $\delta$ . The Cabibbo  $2 \times 2$  matrix is embodied in the CKM extension and  $|V_{us}| = s_{12} = \sin\theta_C$ . Experimental observations establish  $|V_{ub}| = s_{13} \sim 10^{-3}$ , from which it can be derived that  $c_{13}$  is close to one. The hierarchical trend of the mixing angles  $s_{13} \ll s_{23} \ll s_{12} \ll 1$  is highlighted by the Wolfenstein parameterization, which is an expansion in terms of the small parameter  $\lambda = 0.2272 \pm 0.0010 = s_{12}$ . The CKM mixing matrix expressed as function of the independent parameters ( $A, \lambda, \rho, \eta$ ) becomes:

$$V_{CKM} = \begin{pmatrix} 1 - \lambda^2/2 & \lambda & A\lambda^3(\rho - i\eta) \\ -\lambda & 1 - \lambda^2/2 & A\lambda^2 \\ A\lambda^3(1 - \rho - i\eta) & -A\lambda^2 & 1 \end{pmatrix} + \mathcal{O}(\lambda^4). \quad (1.8)$$

In this parameterization the  $CP$  violation arises from the imaginary part  $\eta$  and the connection between the two formalisms is given by the transformation rules:

$$s_{12} = \lambda = \frac{|V_{us}|}{\sqrt{|V_{ud}|^2 + |V_{us}|^2}}, \quad s_{23} = A\lambda^2 = \lambda \frac{|V_{cb}|}{|V_{us}|}, \quad s_{13}e^{i\delta} = A\lambda^3(\rho + i\eta) = V_{ub}^*, \quad (1.9)$$

and finally:

$$\rho = \frac{s_{13}}{s_{23}s_{12}} \cos\delta \quad \eta = \frac{s_{13}}{s_{23}s_{12}} \sin\delta$$

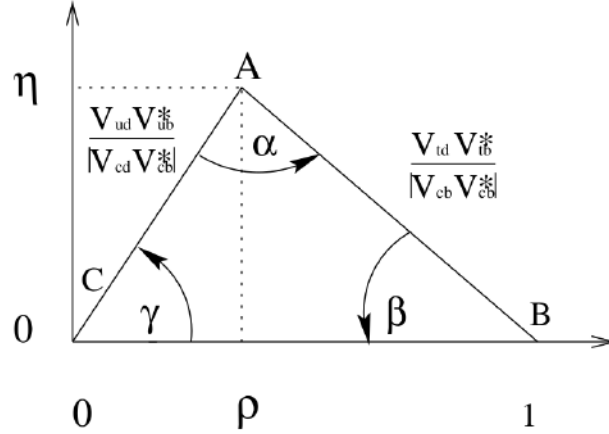


**Figure 1.2:** The normalized unitarity triangle in the  $(\rho, \eta)$  plane. The vertex A has coordinates  $(\bar{\rho}, \bar{\eta})$ .

The Wolfenstein parameterization underlines that the diagonal elements are close to one, while the mixing strength is reduced for off-diagonal elements, resulting in smaller couplings that explain the favored transitions within the same quark doublet. The expansion until  $\mathcal{O}(\lambda^4)$  for the matrix element is meaningful, since the first corrections only occurs at  $\mathcal{O}(\lambda^7) - \mathcal{O}(\lambda^8)$  for  $V_{us}, V_{cb}$ .

The unitarity of CKM matrix is translated into relations between the rows and columns of the matrix itself. In particular, for  $j \neq k$  the relations  $\sum_i V_{ij} V_{ik}^* = 0$  can be regarded as triangles in the complex plane  $(\rho, \eta)$ . They all have the same area corresponding to half of the Jarlskog invariant  $J$  which is a phase-convention independent measure of the occurring  $CP$  violation,  $Im[V_{ij} V_{kl} V_{il}^* V_{kj}^*] = J \sum_{m,n} \epsilon_{ikm} \epsilon_{jln}$ . The most studied triangle is the one given by:

$$V_{ud} V_{ub}^* + V_{cd} V_{cb}^* + V_{td} V_{tb}^* = 0. \quad (1.10)$$

Dividing the above equation by  $V_{cd} V_{cb}^*$  one gets:

$$\frac{V_{ud} V_{ub}^*}{V_{cd} V_{cb}^*} + 1 + \frac{V_{td} V_{tb}^*}{V_{cd} V_{cb}^*} \quad (1.11)$$

known as the normalized *unitarity triangle*. Its representation is given in Figure 1.2. The normalized side of the triangle has vertices  $(0, 0)$  and  $(0, 1)$  in the  $(\rho, \eta)$  plane. The remaining vertex has coordinates  $(\bar{\rho}, \bar{\eta})$ , with  $\bar{\rho} = \rho(1 - \lambda^2/2)$  and  $\bar{\eta} = \eta(1 - \lambda^2/2)$ . The three internal angles can also be defined as function of the CKM matrix elements:

$$\alpha = \arg \left[ \frac{V_{ub}^* V_{ud}}{V_{tb}^* V_{td}} \right], \quad \beta = \arg \left[ \frac{V_{tb}^* V_{td}}{V_{cb}^* V_{cd}} \right], \quad \gamma = \arg \left[ \frac{V_{cb}^* V_{cd}}{V_{ub}^* V_{ud}} \right]. \quad (1.12)$$

The  $CP$ -violating condition corresponds to  $\eta \neq 0$  or equivalently to a non-vanishing area of the unitarity triangle ( $J \neq 0$ ). An overview of the most recent experimental limits for  $\bar{\rho}, \bar{\eta}$  is given in Figure 1.3. Precise measurements of CKM observables are one of the main goals of the  $B$  factories (see also chapter 2), to better constrain the SM tensions and to look for physics Beyond the Standard Model (BSM) by exploiting the luminosity frontier.



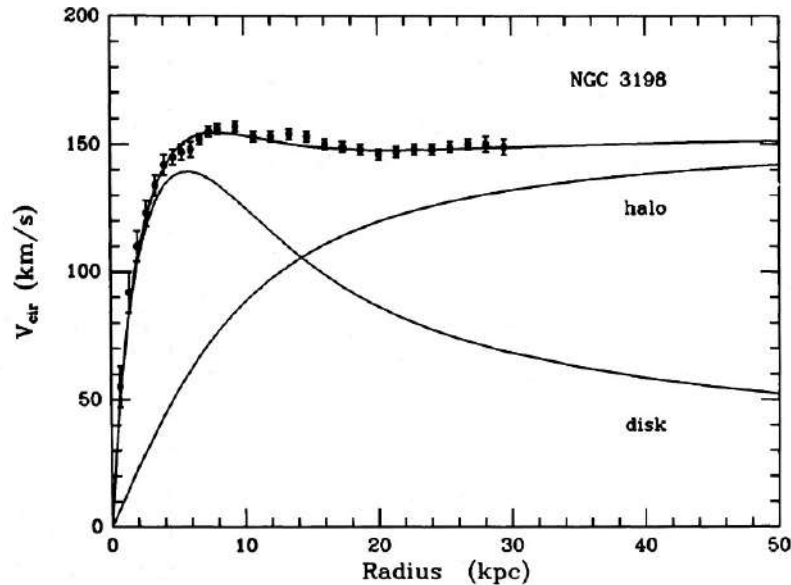


**Figure 1.4:** Measured rotation curve of NCG 3198 galaxy (dots with error bars), compared to theoretical prediction for a velocity due to a massive disk plus a DM halo components (solid lines), as modeled in [4].

## 1.2 Dark Matter puzzle

One of the most compelling motivations to look for BSM physics is the dark matter puzzle, which is yet unsolved. Since the beginning of the 20<sup>th</sup> century, many astrophysical and cosmological observations have proved the existence of a type of matter which seems to interact only gravitationally with the SM particles and it is blind to strong and electroweak forces, hence being *dark*. The first claim for a large dark matter (DM) abundance in our Universe came from the observed discrepancy between the measured rotation curves of spiral galaxies and the virial theorem prediction, based on standard gravity. From the Newtonian potential law, the rotational velocity is expected to fall as  $v = \sqrt{\frac{GM(r)}{r}}$  at a distance  $r \gg R_g$ , being  $R_g$  the galaxy disk radius. Zwicky in 1933 was the first using this theorem while studying the velocity dispersion of galaxies in the Coma cluster to postulate the existence of *dark* matter in the Universe in a much larger amount than the luminous matter. In 1978, Vera Rubin measured the first experimental evidence, followed by many other observations [4], for the presence of dark matter as theorized by Zwicky almost 40 years before with the application of the virial theorem, showing that the rotation curves from experimental data were flat (data reported in Figure 1.4). Therefore, given  $v = const$ , the observations could be explained by assuming a spherical mass halo of not-luminous matter with a density  $\rho = \frac{1}{r^2}$  and consequently an effective mass at distance  $r$  which is linearly growing with the radius itself,  $M(r) \sim r$ .

Other evidences for DM are the lensing effect observed in elliptical galaxies and galaxy-cluster collisions, which again point to a larger mass content with respect to the visible (electromagnetically detectable) amount and the precision measurement of the Cosmic Microwave Background (CMB) small fluctuations [5], provided by the Cosmic Microwave Background Explorer (COBE) and the Wilkinson Microwave Anisotropy Probe (WMAP). These obser-

vations provided a solid experimental basis for the standard model of cosmology, the  $\Lambda$ CDM cosmological model. According to this model, the total energy-matter density  $\Omega$  is consistent with the inflationary paradigm of a flat-geometry space time, which corresponds to  $\Omega = 1$ . Less than 5% can be attributed to the normal baryonic matter,  $\Omega_B = 0.05$ ; almost 23% of the energy-matter content of the Universe is associated to the *cold dark matter* (CDM),  $\Omega_C = 0.23$ , while the largest contribution (more than 70%) is attributed to the dark energy,  $\Omega_\Lambda = 0.72$ , which is related to the non-zero cosmological constant  $\Lambda$  of Einstein's equations of general relativity, responsible for the accelerated expansion rate of the Universe. Though the cosmological model and the dark energy do not directly impact our understanding of particle physics, the experimental confirmation of the cosmological model has reached such a level of accuracy that provides important constraints on the particle content of the Universe. Moreover, the particle content itself determines the way how the large-scale structures evolved in the Universe: lighter particles remaining relativistic during the expansion and cooling of the Universe affect differently its evolution than massive particles, which can be considered non-relativistic just a few years after the Big Bang.

So far the nature of DM is completely unknown and its properties don't match any known SM particle, being very stable with a lifetime comparable to that of the Universe and showing a relic abundance observed from precision CMB measurements which exceeds by almost a factor 5 the ordinary baryonic matter abundance. The study of cosmological history indicates that non-relativistic cold dark matter is required to explain clusters formation in the early Universe and create any structure such as stars and galaxies. However, alternative explanations for dark matter have been also postulated, such as for example a modified Newtonian gravity or furthermore the existence of DM candidates that are not necessarily new particles.

Massive Astrophysical Compact Halo Objects (MACHOs) are possible non-particle DM candidates. The MACHOs are interpreted in the context of a galactic DM Halo as compact objects detected through the lensing effect produced by their transit [6, 7]. Viable candidates can be highly condensed objects, such as black holes, neutron stars, brown dwarfs, planets. Recently, new constraints from astrophysics observations regarding optical microlensing effects and dynamics of stars capture and destruction of white dwarfs draw new attention to the hypothesis of primordial black holes that could potentially account for all the dark matter [8].

Axions are other possible non-baryonic CDM candidates, that however possesses a particle nature. Axions were introduced to solve the  $CP$  violation problem in strong interaction [9], which is an example of *fine-tuning* problem: it happens when a parameter allowed by theory has to take a very precise value to be consistent with experimental results. The famous solution proposed by Peccei and Quinn [10] postulates an additional chiral  $U(1)$  invariance associated to a dynamic field, whose spontaneous symmetry breaking results in a new massive particle, the axion. The strongest constraints come from astrophysical observations, from stellar cooling and processes related to supernovae dynamics, which limit the axions mass to be lower than tens of meV and disfavor their thermal production, given their very low interaction rate [11]. Nonetheless, they remain a viable DM solution and many dedicated experiments look for them [12, 13, 14].

### The thermal DM scenario: *freeze-out* mechanism

For analogy with the successful description of ordinary matter given by the Standard Model and based on the concepts of particles and their interactions, the possibility of rich *dark sectors* seems well motivated. Dark sectors include new particles that do not couple directly to the SM and they are theoretically well-motivated frameworks, supported by string theories and many BSM scenarios. Dark matter could be either secluded in dark sectors or mediate interactions with the SM particles. Within this assumption, several hypotheses have been made for possible DM candidates. Usually, the standard DM production as explained through

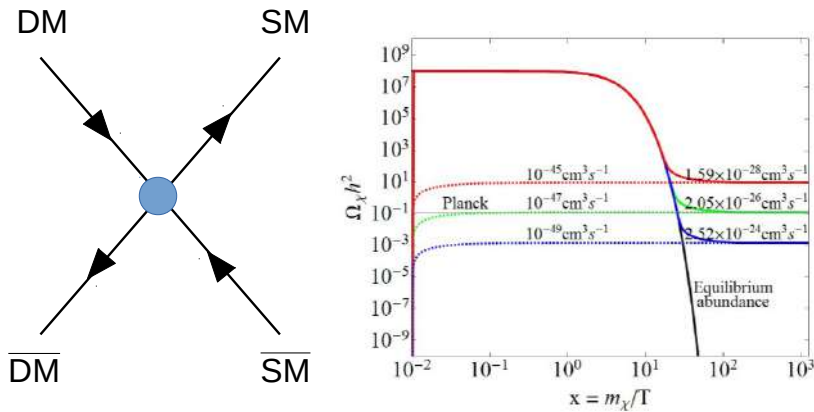


**Figure 1.5:** On the left, the dark matter annihilation process into SM particles is depicted. On the right, the relic abundance is shown as a function of  $x = m_\chi/T$ , for an assumed  $m_\chi = 100 \text{ GeV}/c^2$ , being  $T$  the temperature reached during the expansion, for different annihilation cross sections in the freeze out scenario. The black solid line reports the relic abundance observed from Planck results. Picture taken from [15].

the *freeze-out* mechanism [16] derived from the Boltzmann equations, relies on the thermal equilibrium between dark matter and the plasma in the early Universe through dark matter annihilation processes. A visualization of such process is given in Figure 1.5. While the Universe expands and the plasma temperature decreases, the DM number density is also exponentially suppressed and the annihilation rate becomes too small at the temperature to which the Universe has cooled. Dark matter decouples and the relic density is reached. The temperature of the decoupling also allow to estimate the needed cross section to observe DM-SM interactions, which turns out to be of order of weak-interaction ( $\sigma_{DM-DM} = 3 \times 10^{-36} \text{ cm}^2$ ). Neutrinos were considered as relativistic DM candidate, but being their density constrained also by their fermionic nature and being neutrinos *hot* DM candidates, they could not account for the observed relic abundance and they have been discarded in favor of sterile neutrinos, that could additionally explain the problem of the smallness of neutrino masses. The thermal origin suggesting a non gravitational interaction and a mass scale comparable to the weak scale made the Weakly Interacting Massive Particle (WIMP) paradigm one of the most compelling solution for the DM problem. WIMPs are cold DM candidates, with a mass from below few  $\text{GeV}/c^2$  to several  $\text{TeV}/c^2$ , whose properties correspond to the description of particle candidates predicted by supersymmetric (SUSY) models, as the weakly interacting neutralino. This unexpected matching between SUSY candidates and DM candidates is what

is known as the WIMP miracle [17].

However, despite the strong theoretical motivations for such a candidate, the lack of experimental evidences and the rising of several theories for low mass DM, consistent with the boundaries imposed by the cosmological history of the Universe, have strongly motivated a new *light dark matter* scenario, with candidates in the mass range between  $\text{keV}/c^2$  and few  $\text{GeV}/c^2$ . The simple thermal relic framework, with abundance fixed by *freeze-out* in the early Universe, allows DM in the MeV-GeV mass range if there are light mediators that control the annihilation rate [18]. Further motivation for light mediators comes from DM self-interactions [19], that might explain the discrepancies between  $N$ -body simulations of collisionless cold DM and observations on small scales [20].

The Dark Matter inquiry has therefore not only to answer the question what dark matter is made of, but it has also to explain the cosmological observations and the measured relic abundance in a coherent picture and in this context, the null results from the direct searches for thermal dark matter (WIMP) further motivates the effort to search for light dark sector signatures.

### Alternative non-thermal DM production

Other possibilities for light DM production include the *asymmetric DM* paradigm. It arises from the consideration that the baryon density and the DM density in the Universe are measured to be the same order of magnitude,  $\rho_{DM} = 4.5\rho_{baryon}$  from cosmological observation. Therefore, similarly to what has been postulated to explain the baryon-antibaryon asymmetry in the Universe, that cannot be consistent with a thermal freeze-out production, a possible explanation for the measured dark matter abundance arises from a dark matter particle-antiparticle asymmetry, related to the baryon number ( $B$ ) and lepton number ( $L$ ) asymmetry. Models that foresee a DM interaction carrying a non-zero  $B - L$  charge may account for this asymmetry and explain the non-thermal production of Asymmetric Dark Matter [21]. Since the dark matter relic density is set by the baryon asymmetry, the numerical density for baryon and DM candidates is predicted to be the same,  $n_{DM} \sim n_B$ , and therefore  $\rho_{DM} \sim (m_{DM}/m_B)\rho_B$ , which gives a candidate with a mass of order  $m_{DM} \sim 5 \text{ GeV}/c^2$ .

Another paradigm to explain the observed relic density is given by a class of theories that introduce a number changing  $3 \rightarrow 2$  annihilation of Strongly Interacting Massive Particles (SIMPs) [22] in a secluded dark sector. They predict a DM mass that belongs to the sub-GeV range and couplings within the expected sensitivities of DM direct production at accelerators.

## 1.3 Light Thermal Dark Matter and possible SM extensions

The thermal production scenario can account for light DM candidates and explain the observed relic abundance only in presence of DM mediators, which are required to enhance the DM annihilation rate and avoid DM overproduction, as exemplified in Figure 1.6, a). In that scenario, the annihilation cross section able to reproduce the measured relic abundance can be written as a function of the SM and DM couplings and the masses of the DM candidate  $m_\chi$  and the mediator  $m_\phi$ , as

$$\langle\sigma v\rangle_{relic} \sim \frac{g_D g_{SM} m_\chi^2}{m_\phi^4}.$$

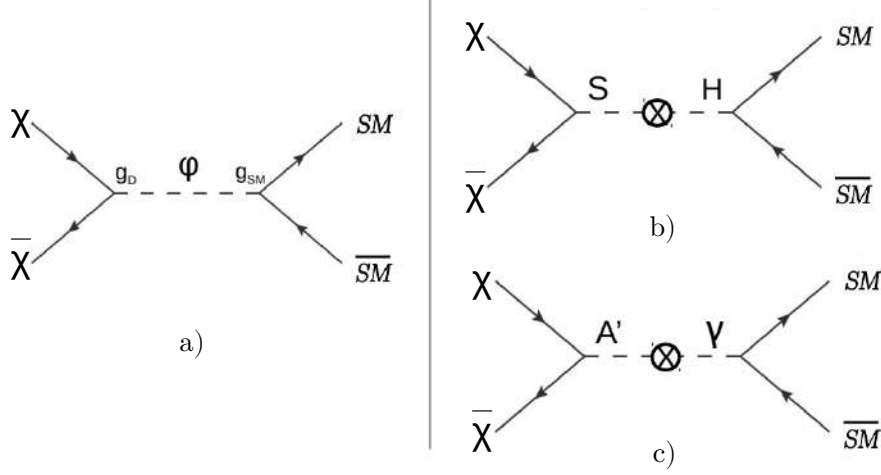


**Figure 1.6:** On the left, a) the Feynman diagram representation of a DM annihilation process involving a mediator  $\phi$  is shown. On the right, the processes depicting DM-SM interactions through b) a scalar and c) a vector portal are reported.

Being  $g_D < O(1)$ , the mediator mass appears to be constrained by the DM candidate mass and the measured relic abundance,  $m_\phi^4 < m_\chi^2 / \langle \sigma v \rangle$ . As a consequence, below a certain DM mass threshold, the required mediator mass is lighter than any other known SM gauge boson masses, therefore requiring the existence of a new mediator. The possible mediators must be neutral under the SM and have dimensionless coupling, hence acting as a renormalisable portal between dark sectors and SM particles. Given the allowed symmetries of the SM, the parity and spin of the mediators, three different portals can be postulated:

- the *neutrino portal* is of particular interest since it may explain a rich DM-neutrinos phenomenology while accounting for the observational results coming from indirect searches related to charged leptons. The basic ingredient is a sizable mixing between SM neutrinos and new sterile neutrinos which mediate the DM interactions. The SM Lagrangian can be therefore extended as:

$$\mathcal{L} = \mathcal{L}_{SM} + \bar{N}(i\partial^\mu\gamma_\mu - m_N)N - y_L\bar{e}_L\tilde{\phi}N$$

where  $N$  is the fermionic field associated to the right-handed sterile neutrino portal, which mixes with the  $SU(2)_L$  leptonic doublet  $e_L$  through the SM Higgs  $\phi$  (here  $\tilde{\phi} = i\sigma_2\phi$ , is the Hermitian conjugate of the Higgs complex scalar field), with interactions proportional to the Yukawa coupling  $y_L$ . The existence of a scalar field is required for such kind of interaction and some model introduces also a dark scalar field  $\Phi$ . Possible DM-SM processes mediated by a right-handed neutrino field  $N$  are shown in Figure 1.7. Existing experiments limit the allowed mass of the fermionic mediator to the range  $\text{MeV}/c^2$ - $\text{GeV}/c^2$ , constraining theoretical models dealing with sterile neutrinos [23];

- the *scalar portal* assumes the existence of a new spin-0 boson  $S$  coupled to a fermionic DM candidate  $\chi$  and which mixes with the SM Higgs field  $\phi$  as described by the phe-

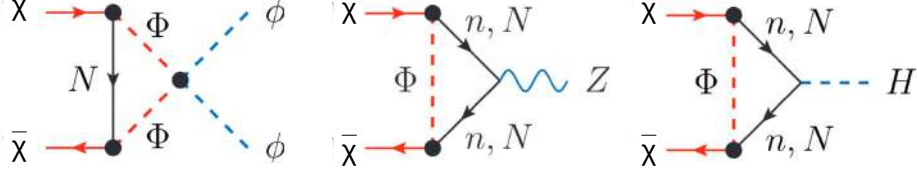


**Figure 1.7:** Feynman diagrams for processes involving a right-handed sterile neutrino  $N$  acting as portal between DM fermionic candidates ( $\chi$ ) and SM particles. Here  $\Phi$  denotes the dark scalar field, while  $\phi$  stands for the Higgs isodoublet;  $n, Z, H$  are the SM left-handed neutrinos,  $Z$  and Higgs bosons respectively. The center and right diagrams show possible one-loop couplings to SM neutral bosons induced by neutrinos coupled to the dark scalar.

nomenological Lagrangian:

$$\mathcal{L}_{\phi,S} = (\mu S + \lambda S^2)\phi^\dagger\phi.$$

The Feynman diagram for a possible process involving such interaction is depicted in Figure 1.6, b). According to the mass regime for the dark scalar and the DM candidate, several signatures may be searched for. Invisible SM Higgs decays are a suitable scenario for these searches at LHC. Given that the DM candidate does not interact directly with the SM particles, it would remain undetected and a typical signal at LHC may be a reconstructed final state with missing energy that accompanies dijet production in proton-proton collisions. Other interesting possibilities, especially at  $B$  factories, are the searches for invisibly decaying mediators in rare mesons decays. A smoking gun could be the process  $B^+ \rightarrow K^+\phi$ , which is mainly constrained by the branching fraction for the decay  $B^+ \rightarrow K^+\nu\nu$ . However, the paradigm of a scalar mediator decaying to Dirac fermion DM is already constrained for most of the available phase space by a combination of limits from above mentioned searches at colliders, rare meson decays and direct detection experiments. The visible final state addressing the mass regime with a scalar mediator lighter than the DM and thus decaying to visible SM particles is still a viable option, despite also in this case tight constraints can be derived from supernovae cooling data, beam dump experiments and direct searches (more details can be found in [24]);

- the *vector portal* relies on a new massive spin-1 boson  $A'$  associated to a  $U(1)_D$  gauge invariance of the dark sector [25, 26, 27]. A possible way to couple to the SM is through the kinetic mixing [28] mechanism, with  $\epsilon$  being the kinetic mixing strength. The mentioned process mixes the dark boson  $A'$  with the SM photon as represented in

Figure 1.6, c), and the corresponding term in the phenomenological Lagrangian can be shown to be parity-conserving and proportional to the kinetic mixing strength  $\epsilon$ :

$$\mathcal{L}_{A',\gamma} = \frac{\epsilon}{2} B_{\mu\nu} F'^{\mu\nu},$$

with  $B_{\mu\nu}$  the strength tensor associated to the SM hypercharge field  $B_\mu$ , and  $F'^{\mu\nu}$  the strength tensor of the new dark gauge boson  $A'$ , defined as  $F'_{\mu\nu} = \partial_\mu A'_\nu - \partial_\nu A'_\mu$ . After fields redefinition, the interaction term can be written as  $\mathcal{L}_{A',\gamma} \sim \epsilon e A'_\mu J_{EM}^\mu$ , where the mixing between the electromagnetic current  $J_{EM}^\mu$  and the new gauge boson is made explicit. The coupling is possible only to electrically charged particles and is naturally suppressed due to the smallness of  $\epsilon$ , which may be due to both perturbative and non-perturbative effects. The former involve quantum loop corrections that can account for  $\epsilon$  in the range  $10^{-8} - 10^{-2}$ , due to heavy messengers that are charged under both the  $U(1)_Y$  hypercharge symmetry and the dark  $U(1)_D$  gauge invariance. If large volume non-perturbative effects are also considered (such as in many string theories), the possible values of  $\epsilon$  can be made even smaller, reaching  $10^{-12} - 10^{-3}$ . In many dark sector scenarios, the vector portal through the boson  $A'$  may represent the only non-gravitational interaction of DM with SM particles. The new gauge boson is often called *dark photon* and usually it acquires mass through the Higgs mechanism. Beside the kinetic mixing mechanism to couple to the SM photon, other types of vector couplings can be foreseen, which still requires dark sectors containing a new massive gauge boson. Alternative SM extensions will be introduced later in this chapter (Section 1.6). According to the specific model, the dark photon can couple only to quarks, only to leptons, or to both types of fermions, and possibly with different strength to down-type and up-type quarks.

To conclude the mediator overview, axions can also be considered as pseudo-scalar portal which results from a *non-renormalisable* SM extension via the Lagrangian term:

$$\mathcal{L}_a = \frac{1}{f_a} a F^{\mu\nu} \tilde{F}_{\mu\nu},$$

where  $\tilde{F}_{\mu\nu}$  is the dual tensor of the strength tensor  $F^{\mu\nu}$ , built from the SM photon field  $A_\mu$ ,  $F_{\mu\nu} = \partial_\mu A_\nu - \partial_\nu A_\mu$ . The pseudo-scalar axion field  $a$  couples to the SM model through the dimensional axion decay constant  $f_a$  as determined in the Peccei-Quinn work [10], inversely proportional to the axion mass.

These portal interactions result in specific DM signatures that can be searched for at different experimental facilities and with different techniques. The next section introduces the existing methods and experiments looking for thermal DM candidates and for rich dark sectors.

## 1.4 Dark Matter detection methods

There are three possible detection methods currently exploited to investigate the particle nature of DM, whose main techniques and related experiments are summarized below.

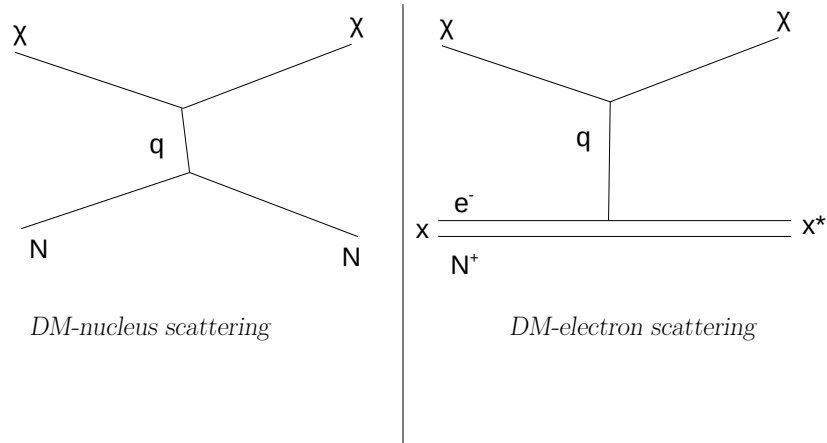


**Figure 1.8:** The scattering processes of WIMPs interacting with nuclei (left) or electrons (right) of the detector medium are shown.

### Direct detection

Direct detection of dark matter relies on low-background underground experiments which aim at detecting the SM particles scattered by the incoming dark matter. This technique mainly targets the WIMP-nucleon interactions which consist in the WIMP scattering on the nucleus of the detector atoms. The expected rate per unit mass of detector material depends on the WIMP density and velocity distribution in the galaxy and on the estimated interaction cross section. WIMP-nucleon interactions are depicted in Figure 1.8 (left) and the observable is the energy released by the nuclear recoil in the detector medium, usually of order of few keV. It can be computed assuming a Boltzmann velocity distribution for the DM candidate which transfers a momentum  $q$ , corresponding to an energy of  $E_r = \frac{|q|^2}{2m_N}$ . Interactions may depend on the spin of the hit particle, being proportional to the factor  $J(J+1)$ , while for the spin-independent cross section ( $\sigma_{SI}$ ) there is an enhancement factor due to its dependence on the square atomic mass  $A$ , being  $\sigma_{SI} \sim A^2$ . An annual modulation of the observed signal rate may be also expected, due to the earth relative motion with respect to a WIMP wind coming uniformly from the galactic halo. This modulation can be exploited to reject background in direct detection experiments [29]. Results from DAMA/LIBRA experiment, which exploits the equivalent of  $\approx 250$  kg of radio-pure Na(Tl) target detectors, report about the observation of an annual DM modulation at a confidence level that exceeds  $9\sigma$ , over the 14 year cycles of data collected during phase 1 and 2. However, no other direct search experiment have been able to confirm those results yet.

To detect the nuclear recoil there are two main experimental techniques which correspond to two different categories of experiments: the detection of ionization induced by the nuclear recoil through the scintillation light produced in iodide crystals or in noble gas detectors; the detection of phonons and/or ionization produced by WIMP-SM particle interactions in solid state detectors exploiting cryogenic devices. Large mass detectors based on the concept of dual-phase time projection chambers (TPCs), such as Xenon1T and DarkSide, belong to the first type of experiments; low threshold bolometers based on germanium or silicon sensors are

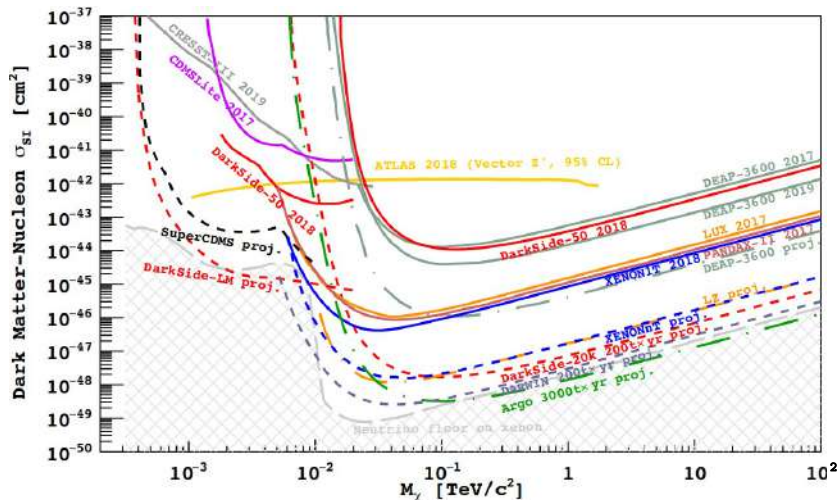


**Figure 1.9:** Upper limits and sensitivity curves to the WIMP-nucleon spin-independent cross section as a function of the mass of the DM candidate from various direct search experiments are reported. Credit to X.Li for the picture (European Strategy in Granada, 2019).

instead exploited by SuperCDMS and CRESST experiments, which are an example of the second category. The status and prospects of direct detection searches are summarized in the plot in Figure 1.9.

### Indirect detection

Indirect detection searches aim at measuring the flux of visible particles (mainly positrons, anti-protons and photons) produced through three main mechanisms, depicted in Figure 1.10: the DM self-annihilations, the DM decays and the DM conversions. DM annihilations in the galaxy can be detected by space-based experiments as an excess of the measured positron fraction in cosmic rays, not accompanied by a visible excess of the anti-proton flux. This may be interpreted as the interactions with light mediators that couple only to leptons among the SM particles. Such an excess has been observed for the energy range 20 – 200 GeV by both FERMI and PAMELA experiments [30, 31] and also confirmed by AMS [32]. The latter extended the observation up to 500 GeV, reporting the evidence of a possible change in the positron flux power law above the threshold of 350 GeV, which seems to indicate the positron flux start decreasing again. The main challenge for these measurements is to supply models that reliably predict the SM positron fraction expected to come from pulsars and other astrophysical objects. DM annihilations may be detected also via the observation of gamma rays from galactic sources: for this purpose, it is more suitable to arrange satellite experiments, since observations made from the earth have to deal with the photon conversion and the reconstruction of their electromagnetic shower. In fact, with typical energy of GeV-TeV, photons would have a not negligible interaction probability to convert into electron-positron pairs passing through the terrestrial atmosphere, losing much information about their original energy and directionality.

DM decays may be due to right-handed sterile neutrinos decaying into photons and SM neutrinos, as shown in Figure 1.10, which can be constrained by X-ray imaging and

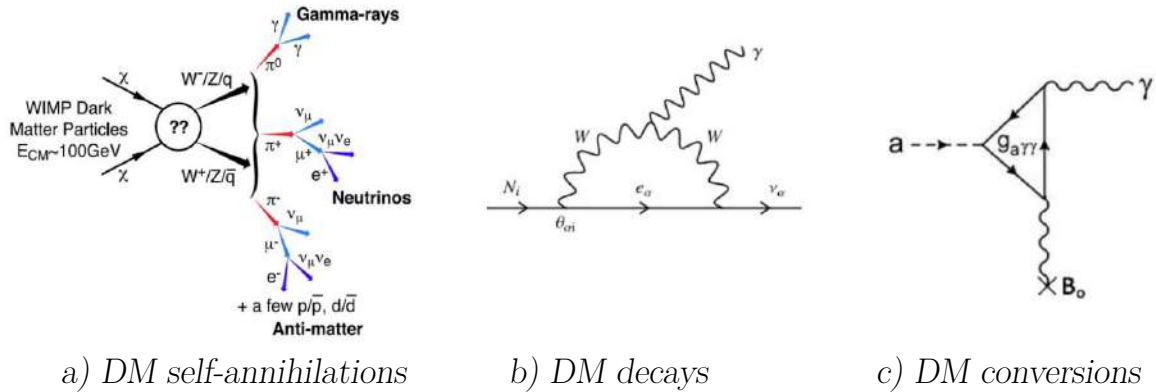


**Figure 1.10:** Three main mechanisms of interactions between DM candidates and SM particles exploited by dark matter indirect searches.

spectrometer-based experiments. An interesting result is the so called 3.5 keV feature, which is an excess observed independently by four detectors (XMM-MOS, Chandra, NuStar and Suzaku) that could point to such kind of sterile DM neutrino interactions. However, a better understanding of the analysis-dependent and target-dependent systematics has to be provided for the correct estimate of the expected backgrounds.

Finally, experiments devoted to search for axion conversions into photons in presence of a magnetic field or axions decays and stimulated emission complete the scenario of the indirect search techniques. Giving a list of the many experiments devoted to axion detection is beyond the scope of this work, the interested reader can find more details in [33]. The state of the art about the current parameter space investigation for Peccei-Quinn axion searches is reported in Figure 1.11. The possibility to probe axion conversion also from gravitational waves detection and radio observations is mainly unexplored yet, but it has gained much interest recently [34].

### Direct production

DM candidates can be produced in SM particle annihilations resulting in several signatures which involve DM mediators. The search for such hidden particles mediating the interaction between DM and SM has been actively pursued by both fixed-target experiments and colliders. As regards the former, electron-beam and proton-beam experiments on fixed target are sensitive to different mass ranges and have both unique discovery potentials in DM production searches. Electron fixed-target detectors allow to investigate the vector portal scenario, with dark photons within the mass range  $2m_e < m_{A'} < \text{GeV}$  and kinetic mixing larger than  $10^{-10}$ . The production process is the  $A'$  bremsstrahlung off an electron beam impinging a fixed tar-

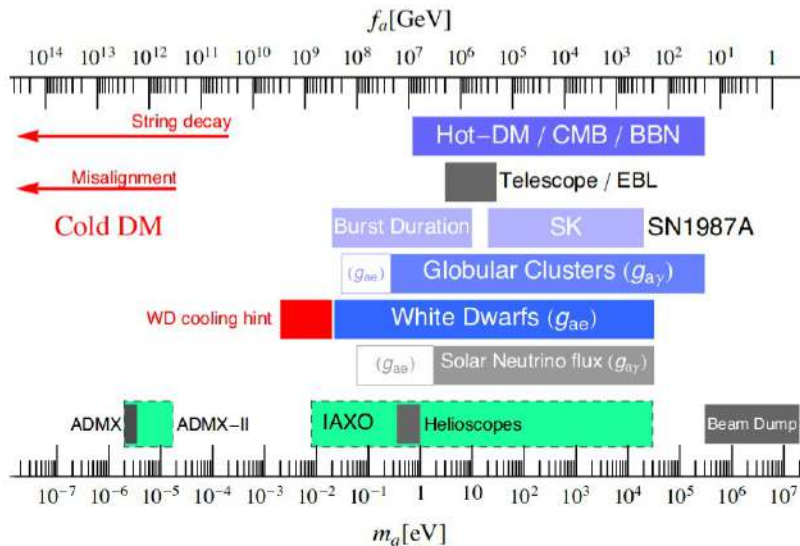


**Figure 1.11:** The parameter space for the Peccei-Quinn axion searches is shown, picture taken from [33].

get, as depicted in Figure 1.12 (top). The advantages of fixed-target experiments compared to lepton colliders are the larger luminosity, the scattering cross section enhancement due to the nuclear charge coherence and a resulting boosted final state that can be revealed by compact special-purpose detectors of three different types: the dual-arm spectrometers (for example Hall A at Jefferson Lab and MAMI at Mainz); the forward vertexing spectrometers, such as the silicon based project developed by the Heavy Photon Search (HPS) collaboration; full final-state reconstruction detectors (DarkLight project at JLAB FEL). However, the signal signatures already explored at beam dump experiments mainly look for dark photon decays into a pair of SM fermions (mostly electrons). The main source of backgrounds are illustrated in Figure 1.12 (bottom) and consists of QED radiative production (a) and Bethe-Heitler trident (b) processes.

Proton beam fixed-target experiments can also be exploited to look for new light, weakly coupled mediators from dark sectors. Neutrino facilities are suitable for this purpose, as for example MiniBooNE, T2K, LSND, MINOS experiments [33, 35], which share the common setup made of an intense proton beam impinging on a target and producing a shower of secondary hadrons, which then decay into neutrinos and other particles. The decay products are left to propagate through shields or earth: all particles are absorbed except for neutrinos whose flux can be measured by downstream detectors. Similarly, one can expect to produce a beam of dark sector particles leaving detectable signatures at near detectors. The reaction of interest consists of neutral pions produced in primary collisions decaying into a pair of photons  $\gamma$  which are allowed to couple to the dark photon  $A'$  through the kinetic mixing. The dark photon can either travel through the detector or interact decaying into electron-positron pairs. The observation of such signature is optimized at near-detector neutrino facilities and

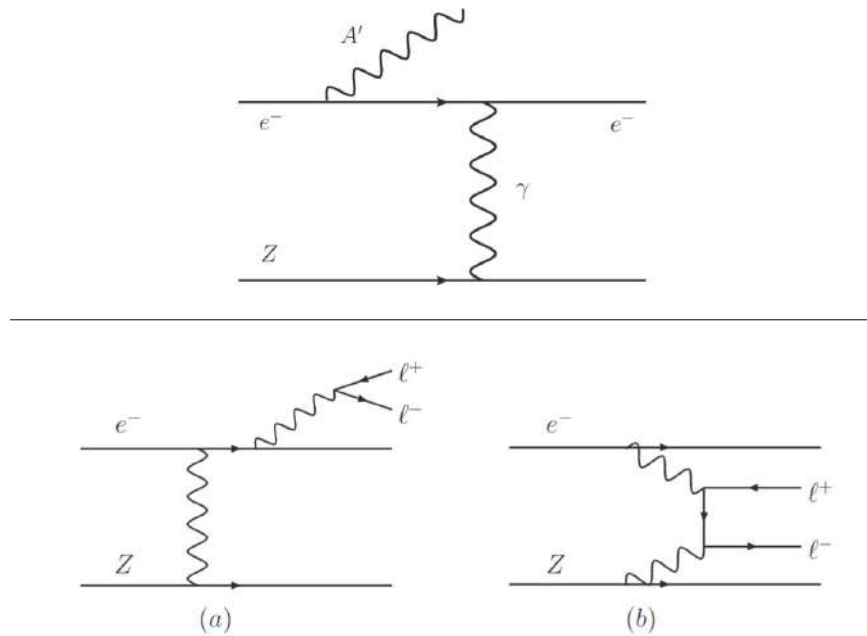


**Figure 1.12:** The Feynman diagram for the reaction of  $A'$  bremsstrahlung off electrons that scatter on target nuclei with atomic number  $Z$  is shown (top). The radiative (a) and Bethe-Heitler trident (b) reactions, being the main QED backgrounds expected for DM searches at electron fixed-target experiments are also illustrated (bottom).

can provide unique constraints in the  $m_{A'}\text{-}\epsilon$  parameter space.

The first two detection methods will not be addressed in this work and further details may be found in the comprehensive review on DM searches and direct detection experiments in [16]. The DM production at colliders is instead the main topic of the next Section 1.5, where an overview of the strategies to search for dark sector signatures at particle accelerators is given.

## 1.5 Dark sector searches at accelerators

A complementary experimental tool to DM direct and indirect detection is the DM production at colliders in SM particle annihilations. Colliders equipped with well-understood detectors could shed new light on the existence of invisible particles and their interactions with the SM matter, which may be very feeble, due to the small couplings or the heavy mass of the new mediators. Since the new particles are expected to be highly elusive, the most promising signature is an invisible final state that can be searched for as *missing energy*. Both high-luminosity and high-energy machines are important to investigate BSM physics, especially for this missing energy searches, where their complementarity is crucial to cross-check experimental results and ensure an efficient interplay with different theoretical models.

### 1.5.1 Search for invisible particles at accelerators

The success in measuring at accelerator invisible particles production is well-established, starting from the determination of the invisible width of the SM  $Z$  boson, at LEP [36]. The direct measurement has been performed by looking at invisible decays of the  $Z$  boson, associated to Initial State Radiation (ISR) photon emission. The signal signature in this case is the detection of a single high energetic photon and missing transverse energy  $\cancel{E}_T$  reconstructed as the recoil against the visible particles in the event. The shape of this variable (and of the related missing transverse momentum) is known for SM processes and the event rate is well predictable, being mainly dominated by the decay  $Z \rightarrow \nu\nu$ . Any measured deviations could be interpreted as a sign for the existence of a new invisible particle with mass lower than half the mass of the  $Z$  boson. Also invisible decays of the SM Higgs boson of the type  $h \rightarrow ZZ, Z \rightarrow \nu\nu$  may be enhanced by the presence of new invisible particles. Invisible decays mediated by the  $Z$  or Higgs bosons are specific cases of the more generic BSM mediation of invisible particle, that includes also heavier BSM mediators. This latter case is indeed interesting to be looked for at hadron colliders, since the distribution of  $\cancel{E}_T$  is expected to be very different from that determined by SM processes. Moreover, to be model-independent and test simultaneously a large variety of DM theoretical frameworks, only very few assumptions on the visible objects in the recoil are tolerable: the ISR +  $\cancel{E}_T$  search first exploited by LEP has become the most promising signature to detect invisible particles.

At hadron colliders, interesting signatures consist of jets, photons or massive gauge bosons +  $\cancel{E}_T$ , also known as mono-X searches, and have to face many experimental challenges. All the physics objects belonging to the hard scatter event contribute to the missing energy measurements and it is crucial to reject the contamination from debris coming from additional proton-proton interactions which happen simultaneously to the hard scatter process (*pileup*). In this regard, only a fraction of proton-proton collision events can be recorded for further processing and a very fast and efficient hardware-based selection (trigger) to keep only the most interesting ones is required. A key ingredient for these selections is a substantial  $\cancel{E}_T$  and for example an isolated ISR photon or very collimated jets. Further details on the selection criteria applied in these searches and other viable signatures at hadron colliders are provided in [37]. Other interesting channels to be studied at LHC for light DM searches are:

- Dilepton and  $b$ -quark resonances in Higgs decays investigated by both ATLAS and CMS experiments [38, 39];
- semileptonic  $B$  meson decays that allow to search for new lepton resonances as for examples the study of  $B \rightarrow K^{0*} \mu^+ \mu^-$  performed by LHCb [40];
- the searches for long-lived particles which open a very promising scenario to look for DM production by exploiting the displaced-vertex signatures [41].

The current exclusion limits constraining the light DM scenario and combined projections from accelerator searches which rely on missing energy/momentum/mass measurements are shown in Figure 1.13. The lower mass region is effectively investigated by proton and electron fixed-target experiments, while at higher masses, for mediators of few GeV, the mono-photon searches at  $B$  factories provide more stringent limits. Specific mass ranges can be constrained by searching for invisible pion, kaon and rare meson decays, while mono-jet searches, despite being less constraining, are relevant in testing the leptophobic nature of these mediators and

their couplings to quarks. The above mentioned results and more details on accelerators constraints can be found in [42].

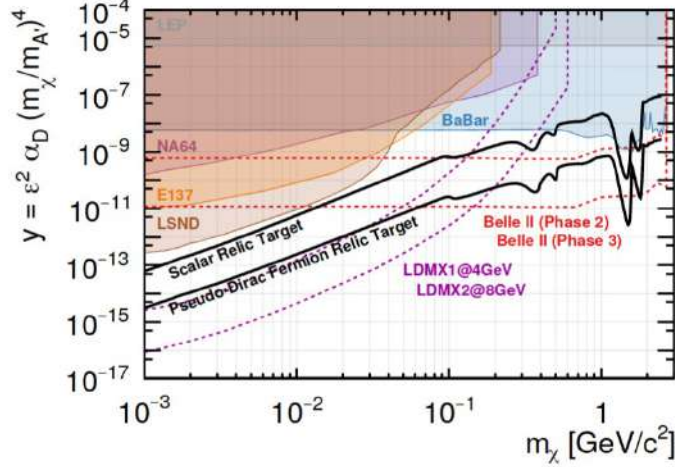


**Figure 1.13:** Constraints and projected limits (LDMX, Belle II) on DM yields ( $y$  displayed on the vertical axis) from searches dealing with kinetically mixed dark photons that couple to (nearly) elastically scattered light DM at beam-dump, missing mass and missing momentum experiments, as a function of the DM candidate mass. Common assumptions for the presented limits are: the mass of the vector mediator satisfies  $m_{A'} = 3m_\chi$ ; the dark photon coupling is  $g_\chi = 0.5$ , where applicable. Picture taken from [43]

### 1.5.2 Dark photon searches at lepton colliders

One of the strongest motivations for dark photon searches at lepton colliders comes from the famous tension measured in the muon magnetic moment that could be explained by the presence of a new vector boson. The gyromagnetic moment of the muon is one of the best known quantities, both experimentally and theoretically, and very sensitive to new physics through loop corrections. Vector mediator exchange could induce corrections to the muon (and also electron) anomaly  $a_{\mu(e)} = g - 2$ : the contribution arising from the additional exchange term due to the dark photon is a positive one and would go in the right direction to explain the observed deviation of  $3.6\sigma$  in the current measurement of  $a_\mu$  with respect to the SM prediction. Therefore, a favored region in the parameter space  $\epsilon^2 - m_{A'}$  can be identified, as shown in Figure 1.14, and a dark photon of a mass within 20-200 MeV and a coupling of order  $\epsilon \sim 2 - 4 \cdot 10^{-3}$  could effectively solve the measured  $(g - 2)_\mu$  discrepancy.

#### Dark photon production processes

A light vector mediator with a mass in the range  $\text{MeV}/c^2$ -  $\text{GeV}/c^2$  can be radiatively produced in  $e^+e^-$  collisions, resulting in detectable signatures at electron-positron colliders [37]. The interesting reaction is schematically given in Figure 1.15, where the main feature of the signal detection is the presence of a high energetic ISR photon. Previously the *BABAR* experiment explored this possibility [45, 46, 47], raising new theoretical interest which turns out in a

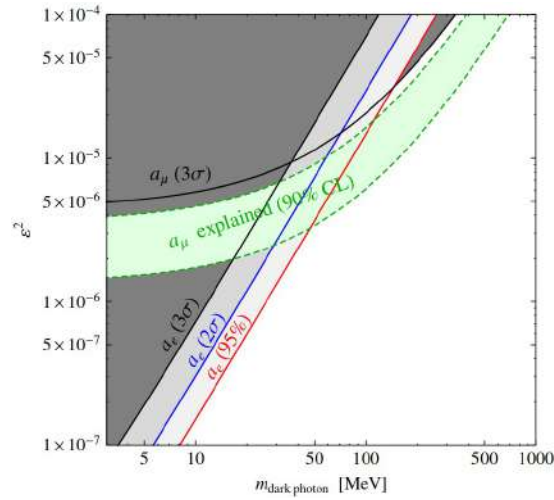


**Figure 1.14:** Dark photon parameter space with bounds that are independent from the dark photon decay branching ratio. The green band is the region within which the  $3.6\sigma$  deviation in  $a_\mu$  can be explained by the dark photon at 90% CL. The three  $a_e$  curves represent respectively the  $3\sigma$ ,  $2\sigma$ , and 95% CL bounds coming from the anomalous magnetic moment of the electron. Figure taken from [44].

rich phenomenology accessible to the  $B$  factories [48]. Several mechanisms at  $e^+e^-$  colliders

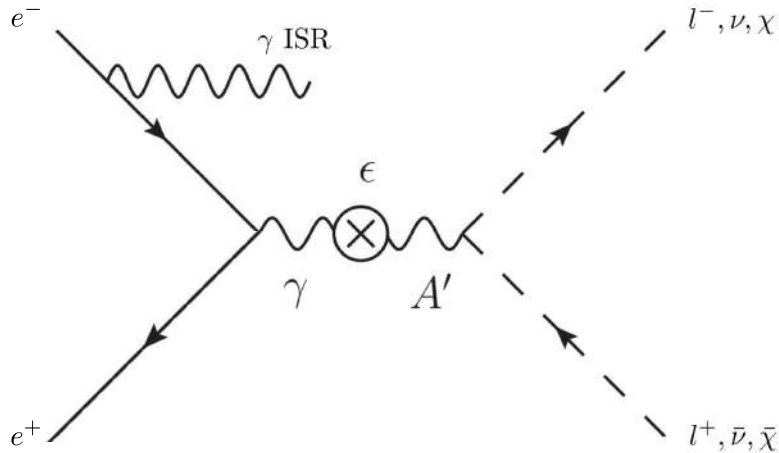


**Figure 1.15:** The Feynman diagram representing the ISR production of a dark photon in  $e^+e^-$  collisions is shown. According to the dark photon mass regime, different final-states are considered.

may contribute to dark photon production, but for the purposes of this work, only the direct production from electron-positron pair annihilations, excluding therefore the study of  $\Upsilon(nS)$  resonances invisible decays to DM, is relevant. This production mode relies on the coupling to electrons and naturally favor the vector portal searches. The cross section for the process  $e^+e^- \rightarrow \gamma A'$  increases with the square of the kinetic mixing coupling  $\epsilon$  and decreases with the reverse of the square CM energy  $s$ , being proportional to  $\epsilon^2 \alpha^2 / s$ , where  $\alpha$  is the fine-structure constant. Depending on the mass range of the mediator, different final states may be taken into account:

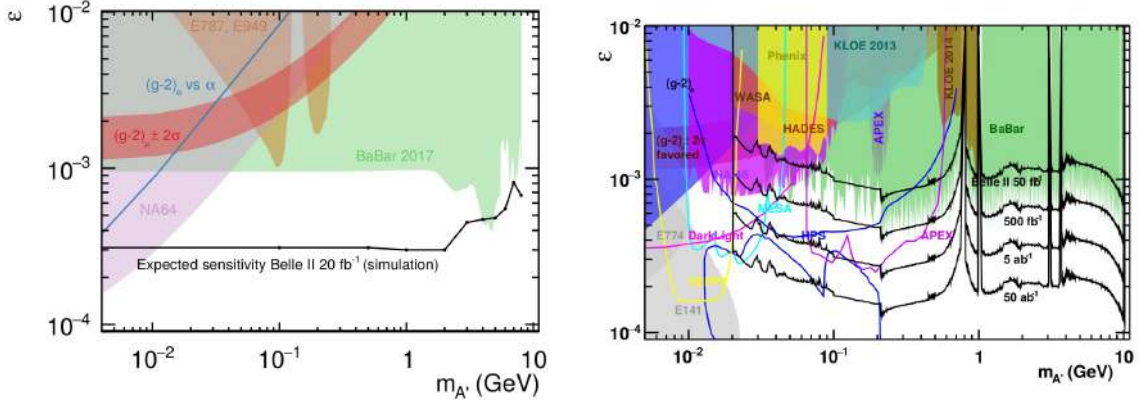


**Figure 1.16:** Expected limits for Belle II dark photon search in the single photon and dilepton channels for different size of the Belle II data set. On the left, projected upper limits on  $\epsilon$  for the process  $e^+e^- \rightarrow \gamma A'$ ,  $A' \rightarrow \text{invisible}$ , for a  $20 \text{ fb}^{-1}$  Belle II data set (solid black curve). On the right, existing exclusion regions (90% Confidence Level) on the dark photon mixing parameter  $\epsilon$  and mass  $M_{A'}$  (solid regions) for  $A' \rightarrow ll$ , with projected limits for Belle II and other future experiments. Figures taken from *The Belle II Physics Book* [43].

- the mediator mass  $m_{A'}$  is at least twice the mass of a lighter DM stable particle ( $m_\chi$ ) and it will decay into invisible final states  $A' \rightarrow \chi\bar{\chi}$ ;
- the mediator mass satisfies  $m_{A'} < 2m_\chi$  and only decays to SM particles are allowed; a cleaned signature is given by the two-lepton final state, if at least  $m_{A'} > 2m_e$ .

The dilepton channel has been already searched for by the *BABAR* experiment on a data set of  $514 \text{ fb}^{-1}$  and the resulting upper limits are reported in [46]. However, despite the dilepton resonance signature  $A' \rightarrow l^+l^-$  would be less challenging and easily detectable as a peak in the dilepton invariant mass distribution, there are no clear hints to assume that  $A'$  is the lightest DM candidate. Searches for invisible decays  $A' \rightarrow \chi\bar{\chi}$  are complementary to visible ones, have unique sensitivity below the dilepton invariant mass threshold and complete the full phase space investigation. Experimentally, the most challenging aspect of these searches is the dedicated trigger that must be implemented for these specific signatures. The ISR production of a dark photon invisibly decaying [49], i.e. the process  $e^+e^- \rightarrow \gamma A'$ ,  $A' \rightarrow \text{invisible}$ , which can be detected as a single photon associated with missing energy, is a promising signature to be searched at lepton colliders. Moreover, the good acceptance coverage and the detector hermeticity make this search perfectly suitable for *B* factory experiments and an improved sensitivity is expected with the Belle II experiment, due to its more efficient first level trigger for single-photon event detection. This trigger was only partially available at *BABAR*, which already performed the search for an invisible dark photon on  $53 \text{ fb}^{-1}$   $e^+e^-$  collision data [47]. The current exclusion limits and sensitivity projections for both the invisible and visible decay modes of the dark photon are shown in Figure 1.16.

Besides the above mentioned ISR production, the search for the dark photon can exploit also the reaction  $e^+e^- \rightarrow \mu^+\mu^-A'$ , where the dark photon (usually denoted as  $Z'$  in this context) decays into a variety of final states [50], including invisible ones. The *BABAR* experiment has performed the search for a muonic dark force as a dark photon decaying to two

muons [51], which together with the limits from the neutrino trident production studies [52] are the only constraints currently existing on such production channel. The search for the invisible dark photon decay in the above mentioned reaction hasn't been performed yet, being however a viable option for DM searches at the second generation of  $B$  factories (Chapter 2). The Belle II experiment has an interesting potential in detecting such processes, which would consist in  $e^+e^-$  collisions where just a pair of muons has been produced and nothing else is detected. This reaction may be sensitive to higher  $Z'$  masses than the single ISR photon search and to mixing parameter values at the level of  $10^{-4}$ – $10^{-3}$ . The physics motivations and a theoretical framework overview for the search  $e^+e^- \rightarrow \mu^+\mu^-Z'$ ,  $Z' \rightarrow invisible$  are given in the next section.

## 1.6 Alternative SM extensions: the $L_\mu - L_\tau$ model

The search for an invisibly decaying  $Z'$  refers to the class of viable extension of the SM which deal with a new light boson associated to an additional  $U(1)$  gauge symmetry. The analysis presented in this work is performed in a model-independent approach, nonetheless two interesting theoretical frameworks have been considered:

1. a  $Z'$  boson belonging to the  $L_\mu - L_\tau$  symmetry;
2. a  $Z'$  coupling to all leptons and violating Lepton Flavor conservation (LFV  $Z'$ ).

The first case deals with a light vector boson in the mass range of  $\text{MeV}/c^2$ – $\text{GeV}/c^2$  and with a new coupling constant  $g' \sim 10^{-6}$ – $10^{-3}$ , which gained a lot of attention from a theoretical point of view thanks to the minimal  $U(1)_{L_\mu - L_\tau}$  model, achievable by gauging the  $L_\mu - L_\tau$  current. This model predicts a dark photon candidate coupled only to the heaviest generations of leptons ( $\mu, \tau$  and their corresponding neutrinos  $\nu_\mu, \nu_\tau$ ), free of gauge anomalies without any extension of particle content [50, 53, 54].

Moreover, it can solve many open issues in particle physics, like the well-known discrepancy associated with the anomalous magnetic moment of the muon and simultaneously, it could explain the high energy cosmic neutrino spectrum, since the same region in the parameter space favored by the muon  $(g-2)_\mu$  anomaly, corresponding to  $M_{Z'} \simeq [5 \cdot 10^{-3}, 2 \cdot 10^{-1}] \text{ GeV}/c^2$  and  $g' \simeq [3 \cdot 10^{-4}, 1 \cdot 10^{-3}]$ , could also solve the gap in the distribution of the high-energetic cosmic neutrinos observed by the IceCube experiment [55]. Additionally, this search can target the problem of DM abundance, since the  $Z'$  may provide a way to balance the annihilation rate to sterile neutrinos in the early universe and explain the observed DM relic density [56]. Furthermore, it may explain the rare  $B$  decay anomalies [57] observed in the  $B \rightarrow Kl^+l^-$  analyses and specifically in the angular observables of the  $B \rightarrow K^*\mu^+\mu^-$  decays [58].

Existing limits for the low mass range are provided by visible  $Z'$  decay searches, as for example the one performed by the *BABAR* experiment [51], which looked for a visible final state with the  $Z'$  decaying into a pair of muons and cannot therefore provide any information below the dilepton invariant mass threshold ( $212 \text{ MeV}/c^2$ ). A similar search for four-muon events production at  $\sqrt{s} = 13 \text{ TeV}$  has been performed also by the CMS experiment [59], but no signal for a  $Z'$  boson was found. The region in the  $Z'$  parameter space constrained by the visible searches is shown in Figure 1.17. Limits on the visible  $Z'$  decays can be derived also from neutrino-nucleus scattering processes at neutrino beam dump experiments (*neutrino trident production* processes [52]), as measured, for instance, by the CCFR experiment [60].

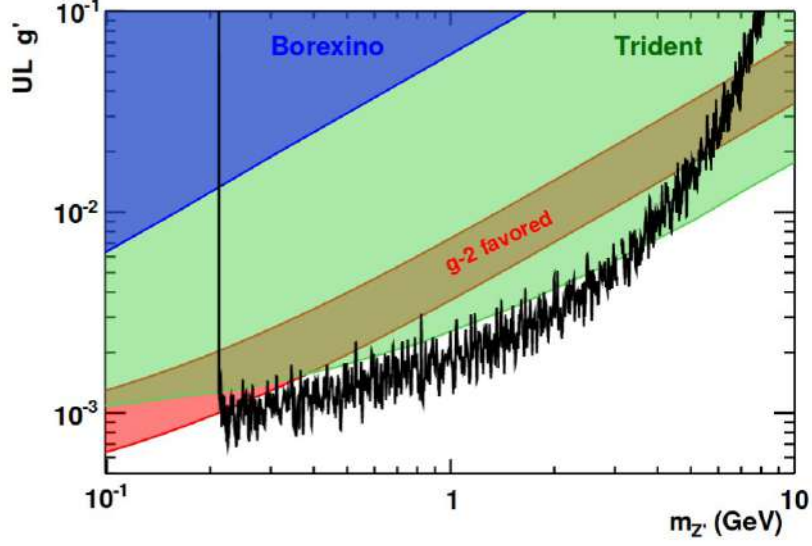


**Figure 1.17:** Existing limits at 90% CL on the new gauge boson coupling  $g'$  as a function of the  $Z'$  mass, together with the constraints derived from the production of neutrino nucleus scattering in neutrino trident production processes [52, 60]. The parameter space that could explain within  $2\sigma$  the observed discrepancy between experimental and theoretical values of the anomalous magnetic moment of the muon is shaded in red. Picture taken from [51].

The first search for an invisibly decaying  $Z'$  is reported here in this thesis: it can constrain new parameter space and mass regions lower than the dimuon threshold; moreover, it has a unique sensitivity to models that allow light dark matter with mass  $m_{DM} < M_{Z'}/2$ , due to the assumption of  $BF(Z' \rightarrow \chi\bar{\chi}) = 1$ , if kinematically accessible dark matter candidates exist. In this case, all the branching fraction for SM final states would turn out to be largely suppressed and consequently, the invisible search result is not directly comparable to the existing limits from visible decays and rather complementary to them. The Feynman diagram depicting the process of interest for this search based on  $e^+e^-$  collision data is shown in Figure 1.18. The interaction Lagrangian in the  $L_\mu - L_\tau$  model can be written as:

$$\mathcal{L} = \sum_l \theta g' \bar{l} \gamma^\mu Z'_\mu l \quad (1.13)$$

where the sum include the heaviest leptons species and their associated (left-handed) neutrinos, for  $l = \mu, \tau, \nu_\mu^L, \nu_\tau^L$ , and  $\theta = -1$  if  $l = \mu, \nu_\mu^L$ , or  $\theta = 1$  if  $l = \tau, \nu_\tau^L$ . The partial decay widths derived from [61, 54] are also given:

$$\Gamma(Z' \rightarrow l^+l^-) = \frac{(g')^2 M_{Z'}}{12\pi} \left( 1 + \frac{2M_l^2}{M_{Z'}^2} \right) \sqrt{1 - \frac{4M_l^2}{M_{Z'}^2}} \theta(M_{Z'} - 2M_l); \quad (1.14)$$

$$\Gamma(Z' \rightarrow \nu\bar{\nu}) = \frac{(g')^2 M_{Z'}}{24\pi}; \quad (1.15)$$

where it can be noticed that the probability to decay to one neutrino species is half the probability for decaying to one charged lepton flavor, due to the fact that the dark force

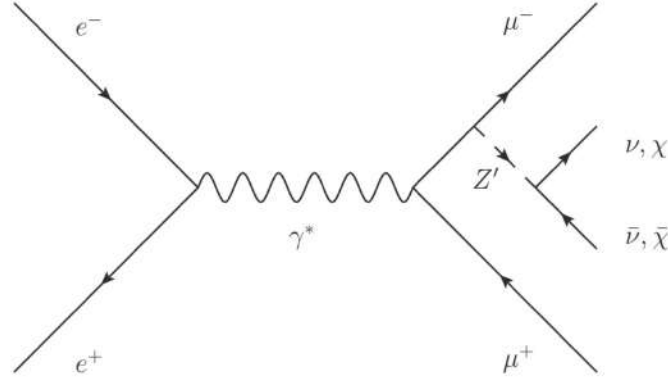


**Figure 1.18:** The Feynman diagram for the production of a light  $Z'$  in  $e^+e^-$  annihilations into a pair of muons is shown, accompanied by the subsequent  $Z'$  decay to neutrinos ( $\nu\bar{\nu}$ ) or DM candidates ( $\chi\bar{\chi}$ ).

mediator couples only to left-handed neutrino chiralities, while it couples to both left- and right-handed charged leptons. The branching fraction for the process  $Z' \rightarrow invisible$  can be computed:

$$BF(Z' \rightarrow invisible) = \frac{2\Gamma(Z' \rightarrow \nu_l\bar{\nu}_l)}{2\Gamma(Z' \rightarrow \nu_l\bar{\nu}_l) + \Gamma(Z' \rightarrow \mu^+\mu^-) + \Gamma(Z' \rightarrow \tau^+\tau^-)}. \quad (1.16)$$

Therefore, the expected branching fractions of final states with neutrinos, according to the considered mass regime, are:

$$\begin{aligned} M_{Z'} < 2M_\mu &: BF(Z' \rightarrow invisible) = 1 \\ 2M_\mu < M_{Z'} < 2M_\tau &: BF(Z' \rightarrow invisible) \simeq \frac{1}{2} \\ M_{Z'} > 2M_\tau &: BF(Z' \rightarrow invisible) \simeq \frac{1}{3} \end{aligned}$$

If DM candidates with mass  $2m_\chi < M_{Z'}$  exists, it is then assumed that the dark photon will decay to DM with a branching fraction  $BF(Z' \rightarrow \chi\bar{\chi}) = 1$ .

As far as the second theoretical framework is concerned, the  $Z'$  is allowed to couple to all leptons and charged lepton flavor violation is also embedded, resulting in possible final states for which almost no SM background is expected [62, 63]. The proposed model in the work referred to in [62] suggests a scalar light mediator that couples chirally to different flavor lepton pairs and may solve the  $\gamma$ -ray excess from the galactic center observed by Fermi-LAT [64] and also be a viable portal for DM self-interaction explanations of small scale structure anomalies, while still providing a solution for the anomalous magnetic moment of the muon.

The processes of interest being investigated are the following:

$$e^+e^- \rightarrow \mu^+\mu^-Z', \quad Z' \rightarrow \textit{invisible} \quad (1.17)$$

$$e^+e^- \rightarrow e^\pm\mu^\mp Z', \quad Z' \rightarrow \textit{invisible} \quad (1.18)$$

where the most sensitive variable for the experimental search is the recoil mass squared, defined as the square invariant mass of the system recoiling against the muon (electron-muon) pair in the center-of-mass (CM) frame:

$$M_{rec}^2 = s + M_{\mu^+\mu^-}^2 - 2\sqrt{s}(E_{\mu^+}^* + E_{\mu^-}^*) \quad (1.19)$$

being  $s$  the square CM energy,  $M_{\mu^+\mu^-}^2$  the invariant mass of the combined four vector of the detected muon pair and  $E_{\mu^{+(-)}}^*$  the energy of the positive (negative) muon in the CM frame; similarly for the LFV case:

$$M_{rec}^2 = s + M_{e^\pm\mu^\mp}^2 - 2\sqrt{s}(E_{e^\pm}^* + E_{\mu^\mp}^*). \quad (1.20)$$

The recoil mass squared can have negative values due to experimental resolution effects in the reconstruction of track momenta and deposited energies. Therefore, not to lose this information, whenever the recoil mass is used hereafter, it is meant the *signed* recoil mass, defined as

$$M_{rec} = \sqrt{M_{rec}^2}, \quad \text{if } M_{rec}^2 > 0;$$

$$M_{rec} = -\sqrt{-M_{rec}^2}, \quad \text{if } M_{rec}^2 < 0.$$

The signal signature in both searches would be an excess of event in the recoil mass distribution peaking at the mass of the invisible  $Z'$ .

### 1.6.1 Invisible $Z'$ produced in dimuon plus missing energy events in $e^+e^-$ collisions at Belle II

The goal of the thesis is to define and optimize the analysis strategy to search for an invisible  $Z'$  produced in association with muon pairs in  $e^+e^-$  collision data collected by the pilot run of the Belle II experiment, taken in April-July 2018 (Phase 2, see Section 2.3.2). The only existing limit on the  $Z'$  production in association to muons have been provided by the *BABAR* experiment [51] with a search on the full collected data set of  $514 \text{ fb}^{-1}$  for the visible decays  $Z' \rightarrow \mu^+\mu^-$ . The invisible signature explored in this thesis is motivated by the lack of any direct constraints on this specific channel, being it investigated here for the first time. Furthermore, given the reduced size of the Belle II 2018 sample (less than  $500 \text{ pb}^{-1}$ ), only a search that has not been performed yet on the *BABAR* or Belle data sets can produce competitive results, due to the low statistics available. Nonetheless, the invisible  $Z'$  analysis can already investigate an unexplored corner of the  $Z'$  parameter space in the mass region below the dimuon threshold and is sensitive to models involving light dark matter candidates with masses smaller than half the  $Z'$  mass.

This search is performed as a model-independent analysis and the signal signature is generic enough to be interpreted by a wide range of different dark sector models. According to the theory chosen when interpreting the results from the data, it may give limits on the

newly introduced parameters related to the specific model or also put new constraints to light DM candidates. A null results, consisting in a measured event rate compatible with the SM expectation, would still allow to provide the first upper limit at 90% confidence level (CL) on the cross section for the process  $e^+e^- \rightarrow \mu^+\mu^-Z'$ ,  $Z' \rightarrow invisible$  and, in the lepton flavor conserving (*standard*  $Z'$ ) case, within the  $L_\mu - L_\tau$  symmetry model this can also be interpreted as exclusion limit in the parameter space of the new coupling constant  $g'$  and the mass of the  $Z'$  boson. For the LFV  $Z'$  search, at the time this work has been accomplished, the Monte Carlo generator model embedded in the simulation software is not mature enough to provide reliable information regarding the main features of the signal distribution to compare to the background expectation. Therefore, the search has been fully optimized on the standard  $Z'$  case, for which reliable signal simulations were available, and it has been applied to the LFV case with the needed adjustments, to provide a measurement of the observed background cross section for the process  $e^+e^- \rightarrow e^\pm\mu^\mp + \text{missing energy}$ , constraining the product of the cross section times signal efficiency ( $\sigma \times \epsilon$ ).

To summarize the physics motivations for this thesis, the search for an invisibly decaying  $Z'$  boson produced in association to muon pairs in  $e^+e^-$  collisions has never been investigated before and is a well motivated analysis program to pursue at the Belle II experiment, which already with the data collected in 2018 can constrain a new corner in the  $Z'$  parameter space. This study may help to solve several tensions observed in particle physics, and especially the dark matter puzzle, which remains one of the most compelling issue pointing to the existence of new physics beyond the SM. Therefore, it deserves to be looked for with all the available experimental tools, data and analysis efforts.

## Chapter 2

# SuperKEKB accelerator

The strategy to look for new physics at accelerators is double: a viable way is to achieve the highest energy in order to produce directly new heavy particles, which is known as *energy frontier*. A complementary option consists in indirectly looking for new physics by performing precision measurements at lower energy, with the highest luminosity, known as the *intensity frontier*. The Large Hadron Collider at CERN, with the ATLAS and CMS experiments, is an example of the first category, while electron-positron colliders at  $B$  factories belong to the intensity frontier class.  $B$  factories have been crucial in the the past decades to establish the CKM mechanism and to provide precision tests of the SM as well as a complementary tool to the energy frontier experiments for the search of forbidden processes and new physics. The Belle II detector operates at the SuperKEKB asymmetric-energy electron-positron collider, at KEK laboratory in Tsukuba (Japan), will continue exploring the intensity frontier and investigating flavor and BSM physics thanks to an unprecedented luminosity. This will allow Belle II to collect a data set which is 50 times that recorded by its predecessor.

In the next Section 2.1 a brief introduction to the experiments at  $B$  factories will be provided, focusing on the asymmetric energy concept and on the first generation experiments. In Section 2.2 the overview on the upgrade to the second generation  $B$  factory SuperKEKB will be given and the last part of the chapter (Section 2.3) will be devoted to the description of the commissioning results and the three running phases of SuperKEKB, concluding with the luminosity prospects and future plans for the accelerator, which plays a crucial role in determining the physics reach of Belle II.

### 2.1 Introduction on experiments at the $B$ factories

Before 1964, it was known that the fundamental symmetries of charge conjugation ( $C$ ) and parity ( $P$ ) were individually violated by the weak interaction, but no evidence for a  $CP$  violation had been found. The revolutionary result of the experiment by Cronin and Fitch on the neutral  $K$  system provided the first experimental evidence that the laws of nature are not the same for matter and antimatter and  $CP$  symmetry is violated. In 1973, Kobayashi and Maskawa showed in their paper that  $CP$  violation could naturally arise in the Standard Model thanks to the irreducible complex phase in the weak interaction quark-flavor-mixing matrix, if only the quark flavors were six [3]. At that time, only the three lightest quarks— $u$ ,  $d$ ,  $s$ —were experimentally known. By 1980, after the *charm* and *beauty* quark discovery, the Cabibbo-

Kobayashi-Maskawa quark-flavor-mixing matrix was embodied in the Standard Model, providing predictions for the size of  $CP$  violation in the charm and beauty sectors. Large  $CP$  violation was expected in neutral  $B$  meson decays to  $CP$  eigenstates (*e.g.*,  $B^0 \rightarrow J/\psi K_s^0$ ), but no evidence could be found due to a branching fraction lower than 0.1%. Observations could have been provided only with data sets equivalent to millions of  $B\bar{B}$  pairs, and with this purpose in mind the  $B$  factory concept was born and the BABAR (1999-2008) and Belle (1999-2010) experiments were built [65]. The main features of those colliders and detectors were dominated by their primary goal, which was measuring the the time-dependent  $CP$  asymmetries in the  $B$ -meson system. In addition, they also performed precise measurements of the CKM matrix elements and several branching fractions of rare  $B$  meson decays, allowing to constrain the SM parameters with the highest experimental precision. These experiments also allow the study of the charm,  $\tau$  lepton and two-photon physics, and to indirectly search for new physics beyond the SM.

There are unique features in a  $B$  factory which make it an attractive and competitive alternative to the energy frontier approach, starting from the cleaner environment at lepton colliders with respect to hadron colliders, which implies lower track multiplicity and detector occupancy, and finally results in a higher  $B$ ,  $D$  and  $\tau$  reconstruction efficiencies, especially for what concerns neutral final states.

### 2.1.1 The asymmetric $B$ factory concept

Beauty hadrons can be produced both in  $e^+e^-$  interactions and in hadronic interactions, and while the production at high energy (for instance in  $p\bar{p}$  collisions at 13 TeV at LHC) offers a large cross-section and a full spectrum for beauty mesons and baryons, electron-positron colliders provide instead an extremely clean environment and a well known and coherent initial state. In order to have a large amount of  $B\bar{B}$  mesons, these colliders operate at a center-of-mass energy of 10.58 GeV, corresponding to the invariant mass of the  $\Upsilon(4S)$  resonance, which is a bound state (*bottomonium*) of the beauty quark  $b$  and its antiparticle, the antiquark  $\bar{b}$ , with quantum number  $J^{CP} = 1^{--}$ . The  $\Upsilon(4S)$  resonance is the first one of the bottomonium family above the threshold for  $B$ -meson pair production and mainly decays to neutral or charged  $B\bar{B}$  pairs, roughly in the same proportion. Since the mass of the  $B$  meson is 5.279 GeV/c<sup>2</sup> [66], they are produced almost at rest in the CM frame and because of their short lifetime ( $\tau = 1.519 \times 10^{-12}$  s [66]), they travel a very reduced distance in the laboratory. Therefore, the measurement of their decay vertices separation ( $\sim 60 \mu\text{m}$ ) would be hardly achievable, given the state-of-the-art of vertex detectors. The original asymmetric  $B$  factory concept, which was proposed by P.Oddone in 1988 [67], uses different energies for the electron and positron beams so that the  $\Upsilon(4S)$  acquires a boost in the laboratory frame and the decay products are pushed forward in the direction of the electron beam. From the now measurable decay lengths  $\Delta z = \beta\gamma c\tau$ , proper decay times can be inferred. These machines also required unprecedented luminosities, of order  $10^{33} \text{ cm}^{-2} \text{ s}^{-1}$  and for this reason they were called *factories*.  $B$ -meson production at  $B$  factories has several advantages:

1. The high signal-to-background ratio,  $\sigma_{\Upsilon(4S)}/\sigma_{had} = 0.28$ , where  $\sigma_{had}$  is the sum of the production cross sections at the CM energy  $\sqrt{s} = 10.58$  for continuum hadronization processes of the type  $e^+e^- \rightarrow q\bar{q}$ . The total production cross section of various physics processes from collisions at  $\sqrt{s} = 10.58$  is shown in Table 2.1.

2. Clean events with a higher mean charged multiplicity ( $\sim 11$ ) with respect to the backgrounds are expected, as shown in Figure 2.1. The event rate (10 Hz) is also quite low and allows relatively simple trigger strategies.
3. The possibility to build hermetic detectors with excellent reconstruction of neutrals, which result in a very high detection efficiency for final states involving  $\pi^0$  and photons and consequently in the possibility to close the event kinematics. This feature is crucial to perform missing energy searches and look for invisible particles that may be hint of new physics.
4. The absence of fragmentation products and the kinematics of the  $\Upsilon(4S)$  decay also reduces the combinatorial backgrounds. In fact, the initial state and also the momentum magnitudes of  $B$  mesons in the CM frame are completely known, allowing therefore to set kinematic constraints on reconstructed candidates, which results in a very powerful tool for suppressing backgrounds. Off-resonance data sets, collected at a center-of-mass energy 40 MeV below the peak of the  $\Upsilon(4S)$  are also relevant to study continuum background coming from  $q\bar{q}$  hadronization processes and subtract it from the  $B\bar{B}$  signal yields.

$e^+e^- \rightarrow$	Cross-section (nb)
$\Upsilon(4S)$	1.05
$u\bar{u}(\gamma)$	1.61
$d\bar{d}(\gamma)$	0.40
$s\bar{s}(\gamma)$	0.38
$c\bar{c}(\gamma)$	1.30
$\tau^+\tau^-$	0.94
$\mu^+\mu^-$	1.16
$e^+e^-$	$\sim 40$

**Table 2.1:** Production cross-sections for the main processes in  $e^+e^-$  collisions at a center-of-mass energy  $\sqrt{s} = m(\Upsilon(4S)) = 10.58$  GeV.

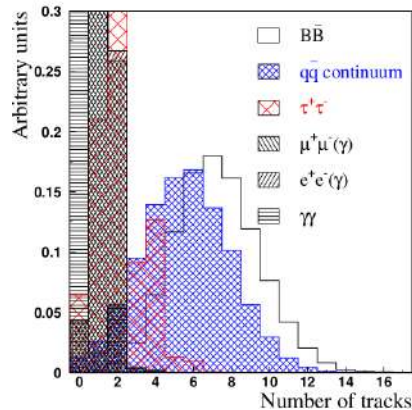


**Figure 2.1:** The number of charged tracks per event is shown, for different processes. Histogram taken from *The physics at B Factories*, Ch. 7,  $B$ -meson reconstruction [65].

### 2.1.2 The first generation of $B$ factories: PEP-II and KEKB

The *BABAR* and *Belle* experiments were installed respectively at the high luminosity  $e^+e^-$  colliders PEP-II at SLAC, in California, and KEKB at KEK, in Tsukuba (Japan) and collected data for about a decade, starting from 1999 until 2008 and 2010, respectively. At both the accelerators, in order to achieve asymmetric energies, two dedicated rings were needed: the High Energy Ring (HER) for electrons, and the Low Energy Ring (LER) for positrons. A schematic view of PEP-II and KEKB colliders is shown in Figure 2.2. For luminosity optimization, both facilities had a single Interaction Region (IR): unusual beam optics very close to the Interaction Point (IP) became necessary to accommodate for high luminosity

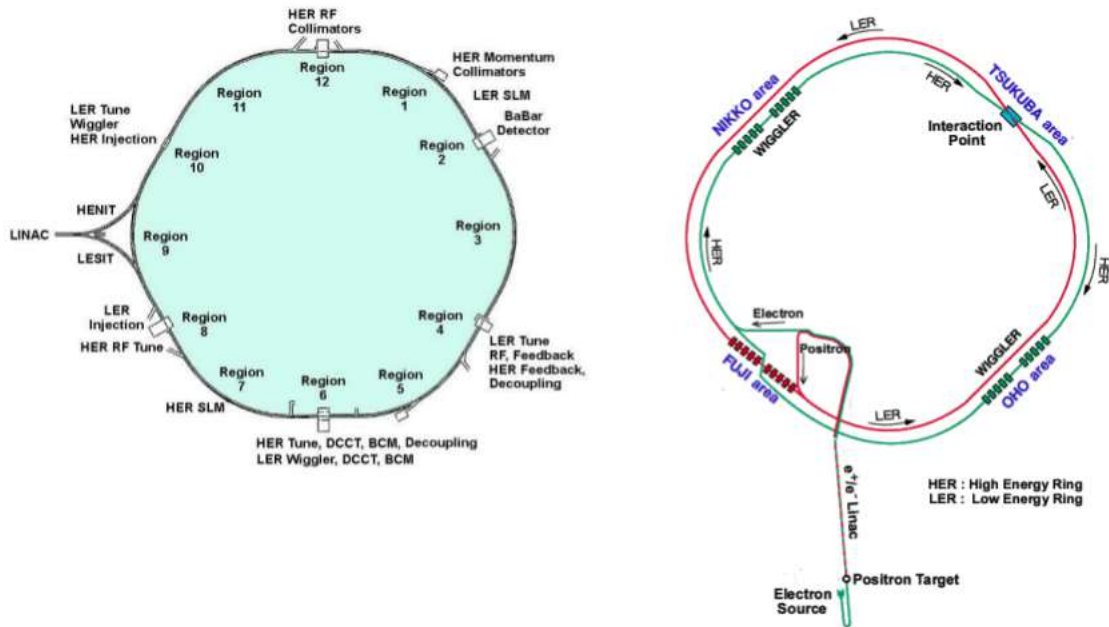


Figure 2.2: PEP-II (left) and KEKB (right)  $e^+e^-$  storage rings.

requirements, needed to compensate cross sections of order of  $\sim nb$  and to collect the necessary statistics. In terms of the collider parameters, the luminosity is expressed by:

$$\mathcal{L} = \frac{N_b n_{e^-} n_{e^+} f}{A_{eff}} \quad (2.1)$$

where  $N_b$  is the number of bunches,  $n_{e^-}$  and  $n_{e^+}$  respectively the numbers of electrons and positrons per bunch,  $f$  the circulating frequency, and  $A_{eff}$  the effective overlapping in the transverse area of the two beams at the interaction point. To ensure good performances and limit the damaging effect of synchrotron radiation and high beam currents, a high quality vacuum was needed throughout all the beampipe.

In addition, it was fundamental to introduce the beam-separation scheme, in order to handle the short bunch spacing in a two ring machine. At PEP-II interaction point, after the head-on collision the separation was achieved thanks to the bending magnets, which diverted the electron and positron bunches soon after their intersection, protecting the beams from parasitic interaction, while KEKB introduced a small crossing angle ( $\sim 22$  mrad), which simultaneously allowed to have shorter bunch spacing and more space available for detector components closer to the IP. This was not without risk, since the crossing angle induces coupling effect between transverse betatron oscillations and longitudinal synchrotron oscillations, inflating instabilities which were finally cured allowing KEKB to reach an instantaneous luminosity even twice as large as the originally designed nominal one, for a maximum peak of  $2 \times 10^{34} \text{ cm}^{-2} \text{ s}^{-1}$ .

In Figure 2.3 the luminosities achieved at PEP-II and at KEKB during different data-taking periods are shown and in Table 2.2 the major parameters of the machines for both the factories during their final stage of operation are given. The recorded data sets listed in

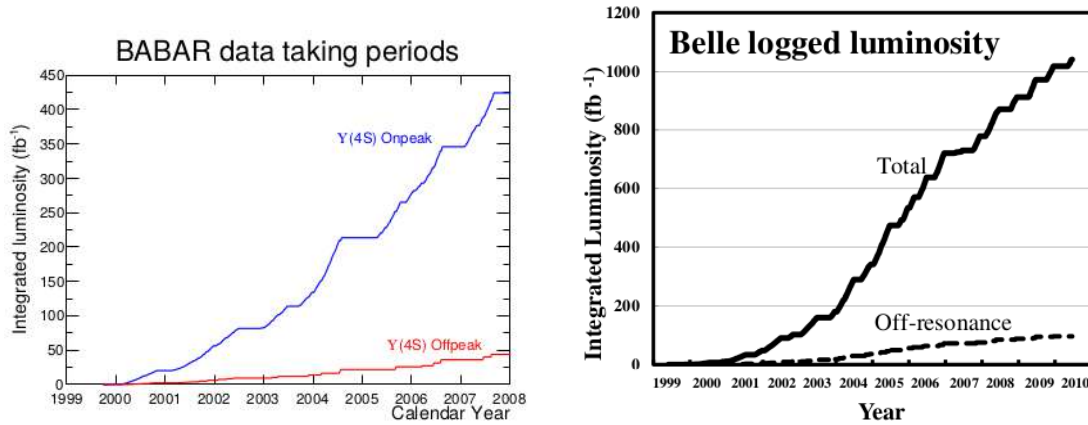


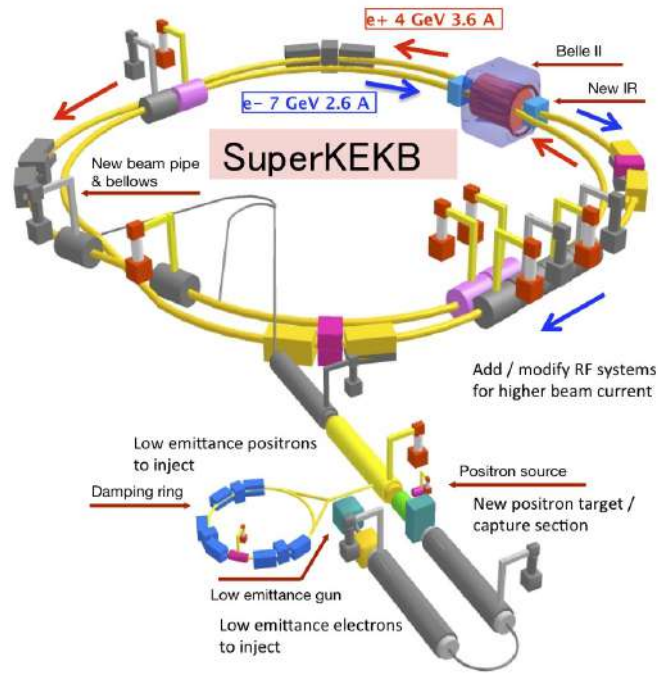
**Figure 2.3:** The *BABAR* (left) and *Belle* (right) luminosities integrated over the  $\Upsilon(4S)$  running period, for both the on- and off-resonance operational modes, are shown. Pictures are taken from *The physics of the B Factories* [65].

**Table 2.2:** Main machine parameters for PEP-II and KEKB during their final stage of operation; in the last column values from Belle II Technical Design Report [68] for SuperKEKB upgrade are listed.

Parameters	Units	PEP-II (HER/LER)	KEKB	SuperKEKB
Beam Energy	(GeV)	9.0/3.1	8.0/3.5	7.0/4.0
Beam Current ( $I$ )	(A)	1.8/2.7	1.19/1.64	2.62/3.60
Beam Size at IP ( $x$ )	( $\mu\text{m}$ )	140	80	11.2/10.2
Beam Size at IP ( $y$ )	( $\mu\text{m}$ )	3	1	0.0618/0.0483
Beam Size at IP ( $z$ )	(mm)	8.5	5	5/6
Luminosity	( $10^{34}\text{cm}^{-2}\text{s}^{-1}$ )	1.2	2.1	80
$\xi_y$			0.090/0.129	0.088/0.090
$\beta_y^*$	(mm)		5.9/5.9	0.41/0.27
Lorentz factor ( $\beta\gamma$ )		0.56	0.43	0.28
Half-crossing angle	(mrad)	0	11	41.5

**Table 2.3:** First generation  $B$  factory data sets. Integrated luminosity and equivalent amount of  $B\bar{B}$  pairs collected at the different  $\Upsilon$  resonances are given. Wherever two comma-separated values are specified, they correspond to the integrated luminosity and corresponding amount of  $B\bar{B}$  pairs.

$B$ factory	$\Upsilon(4S)$ 10580 MeV	off-res	$\Upsilon(1S)$ 9460 MeV	$\Upsilon(2S)$ 10023 MeV	$\Upsilon(3S)$ 10355 MeV	$\Upsilon(5S)$ 10876 MeV
	$\mathcal{L}, N_{\bar{B}B}$ [fb $^{-1}$ ], [10 $^6$ ]	$\mathcal{L}$ [fb $^{-1}$ ]	$\mathcal{L}, N_{\bar{B}B}$ [fb $^{-1}$ ], [10 $^6$ ]			
<i>BABAR</i>	433, 471	54	—	14, 99	30, 122	$R_b$ Scan
<i>Belle</i>	711, 772	11	6, 102	25, 158	3, 12	121, 36



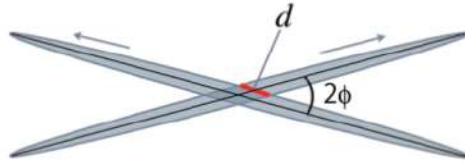
**Figure 2.4:** A schematic representation of the SuperKEKB asymmetric energy  $e^+e^-$  collider is given.

Table 2.3 are still unique and able to provide competitive results even more than 10 years later the end of the data taking. With these samples, the first generation of  $B$  factories observed the  $CP$  violation in the  $B$ -meson system [69, 70] which experimentally confirmed the CKM mechanism and led to the 2008 Nobel Prize in Physics awarded to Kobayashi and Maskawa. The measurement of the direct  $CP$  violation in  $B \rightarrow K\pi$  decays followed, and also the charm mixing [71] and several  $B$  and  $\tau$  rare decays were measured, as well as many predicted and unexpected new states, as for example the  $X(3872)$  [72] and the tetraquark candidate  $Z(4430)^+$  [73]. The future promise for flavor physics and BSM searches is now represented by the SuperKEKB accelerator and Belle II experiment.

## 2.2 The second generation: SuperKEKB design upgrades

The upgrade of the accelerator, whose schematic view is given in Figure 2.4, is the first necessary step for the second generation  $B$  factory project. The new SuperKEKB collider will achieve a design instantaneous luminosity 40 times larger than what achieved by its predecessor,  $8 \times 10^{35} \text{ cm}^{-2}\text{s}^{-1}$ , by applying the technology first proposed for Super  $B$  in Italy, the so-called *nano-beam* scheme. Essentially, it exploits the inverse proportionality that relates the luminosity to the vertical beta function  $\beta_y^*$ <sup>1</sup> at the Interaction Point (IP), which

<sup>1</sup>In Accelerator Physics, the betatron function  $\beta(s)$  describes the displacement of a particle beam due to oscillations in the transverse plane  $xy$  with respect to its nominal trajectory in a given point  $s$  along the orbit.  $\beta^*$  denotes the value of the  $\beta$  function at the interaction point. The  $\beta$  function relates to the transverse beam size according to the formula:  $x(s) = \sqrt{\epsilon} \sqrt{\beta(s)}$ , with  $\epsilon$  the emittance, being a constant of motion along the orbit.



**Figure 2.5:** The beam collision in the Nano-Beam scheme: the effective beam size  $d$  and the half-crossing angle  $\phi$  are illustrated. Picture taken from the Technical Design Report [68].

will be squeezed by a factor 20, from about  $1 \mu\text{m}$  to  $50 \text{ nm}$ , while the beam crossing angle will be increased from  $22$  to  $83 \text{ mrad}$ . At the same time, the beam currents will almost double, and as a result of both the squeezed beams and the increased currents, significantly higher backgrounds in the detector are expected. First, to reduce beam losses caused by Touschek scattering in the low energy ring and second, to limit the power consumption in the high energy ring, a smaller beam energy asymmetry was chosen, with a  $7 \text{ GeV}$  electron beam and  $4 \text{ GeV}$  positron beam energy. This results in a smaller boost  $\beta\gamma = 0.28$  and therefore in a reduced spatial separation between the  $B$ -meson vertices, which will be compensated by the new VerteX Detector (VXD). Furthermore, the reduced asymmetry will ensure a better hermeticity for missing energy decays, due to improvements in the solid angle acceptance.

Valuable improvements in several machine parameters are needed to achieve this goal, implying several interventions on the machine structure, on the ring lattices and a completely redesigned interaction region: a new electron injection gun, a new target for positron production, and a new additional damping ring for the positron beam are crucial to achieve the design luminosity. The upgrade of the accelerator also includes a redesign of the lattices of the low energy and high energy rings, replacing short dipoles with longer ones (LER), installing TiN-coated beampipes with ante-chambers and an important rearrangement of the Radio Frequency (RF) system, though using the same technology.

### 2.2.1 Nano beam scheme overview

The main modification in the *nano-beam* scheme approach regards the minimization of the longitudinal size of the beams overlap  $d$  (schematic view of the beam intersection is reported in Figure 2.5), which can be shown to be the lower bound for the  $\beta_y^*$ . The formula for  $d$  is the following:

$$d \simeq \frac{\sigma_x^*}{\phi} \quad (2.2)$$

The numerator  $\sigma_x^*$  represents the horizontal beam size at the IP and  $\phi$  is the half-crossing angle ( $\sim 41.5 \text{ mrad}$ ). If the assumption of flat beams is verified, the luminosity formula at the IP can be written as:

$$\mathcal{L} = \frac{\gamma_{\pm}}{2er_e} \left( 1 + \frac{\sigma_y^*}{\sigma_x^*} \right) \left( \frac{I_{\pm}\xi_{y\pm}}{\beta_{y\pm}^*} \right) \frac{R_L}{R_{\xi_y}} \quad (2.3)$$

where  $\gamma, e, r_e$  are respectively the Lorentz factor, the elementary electric charge and the electron classical radius, while  $R_L, R_{\xi_y}$  are the luminosity and vertical beam-beam reduction

factors, whose ratio can be approximately considered 1. Since the ratio  $\sigma_y^*/\sigma_x^*$  is order  $10^{-3}$ , the term into brackets can be approximated to one as well. Indices (+, -) refer to electron and positron beam, respectively. From this formula, it can be noticed that there are three fundamental parameters for manipulating the luminosity and they are the beam current ( $I$ ), the vertical beam-beam parameter ( $\xi_y$ ) and the beta function ( $\beta_y^*$ ) at the IP. A comparison of the major upgraded parameters between KEKB and SuperKEKB is given in Table 2.2.

### Beam background sources

The measurement of the beam backgrounds and the estimation of their expected rates with the final optics at the design luminosity is crucial to assess the safety of the Belle II detector and its good performance. The main beam background sources at SuperKEKB are five. The first is the Touschek scattering which is highly enhanced due to the nano-beam scheme technique and squeezed beams. It is an intra-bunch process which consists in the Coulomb scattering of two particles within the same bunch, implying as result a shift in the energies of the particles involved, one getting higher and one decreasing of the same amount, therefore deviating from the nominal energy and from the stable orbit. This effect depends inversely on the beam size and on the third power of the beam energy. The scattered particles are usually lost at the beampipe inner wall during propagation through the ring and if the loss happens at the IP, the detector might be hit by the shower. To prevent this and mitigate Touschek background both vertical and horizontal movable collimators are used, as well as metal shields. The expected rate is  $\sim 20$  times higher than KEKB, just applying a simple re-scaling.

The second source of background is the beam-gas scattering, due to remaining gas molecules in the beampipe which interact with the beam particles through two main processes: the Coulomb scattering, which changes the direction of the particles, and the bremsstrahlung scattering, responsible for decreasing the particle energy through photon emission. The rate is proportional to the beam current and to the vacuum pressure, and for the Coulomb scattering component, which is the dominant one, it is expected to be  $\sim 100$  higher than at KEKB, due to the reduced beampipe radius. As for the Touschek scattering the countermeasure is to apply collimators able to shield the IP and protect the detector, absorbing particle losses. However, the width of vertical collimators is the result of a trade off between the necessity to close them to avoid beam losses and not to incur in Transverse Mode Coupling instabilities.

The third type of background is the synchrotron radiation (SR) emitted by accelerated particles, which increases with the square of the particle energy and magnet field strength squared. The synchrotron radiation spectrum goes from few to tens of keV and it may severely damage the vertex detector. It mainly affects the HER ring and the most relevant contribution, contrary to what happened in Belle, is due to the final focusing magnets, since the synchrotron radiation produced in the bending magnet far from the interaction point cannot reach the detector. To avoid SR photons to hit the detector, the inner wall of the incoming beampipe is specifically structured to prevent scattered photons to reach the interaction point. Nonetheless, the beryllium beampipe inner wall is covered with a gold layer to absorb the photons which propagate to the direction of Belle II innermost detectors.

The last two types of beam background are generated during collisions and are luminosity dependent. The radiative Bhabha scattering produces a copious amount of low energy photons and through the photo-nuclear resonance mechanism also a huge amount of neutrons.

The production rate is proportional to the luminosity, therefore it is expected to be 40 times the background level at KEKB. Neutrons are a background mainly for the outermost detectors and a dedicated shielding system in the accelerator tunnel is required to absorb them. As a consequence of the radiative scattering, electron and positron energies decrease: for KEKB, which used a shared final focus quadrupole magnet (QCS) system for both beams, this caused an over-bending of the beam orbits due to the non-null dipole component far from the quadrupole center. Deviated beams may hit the magnets wall and produce additional electromagnetic showers. In SuperKEKB, the QCS system is separate for electrons and positrons, so that the beams can stay centered in their quadrupole magnets and the losses due to the over-bending caused by the dipole component out of the quadrupole center are largely mitigated. Moreover, the beam parameter tuning can be done independently for the two rings.

The last beam background source consists of low-momentum electron-positron pairs resulting from two-photon processes in  $e^+e^- \rightarrow e^+e^-e^+e^-$  reactions. These pairs can spiral inside the solenoid field and produce additional hits in the Belle II inner detectors.

Finally, when new charge is injected to a circulating beam, it perturbs the particles in the bunch, causing for few milliseconds a higher background rate which is called injection background. To prevent the possible data stream corruption due to too large occupancies of the Belle II subdetectors, a trigger veto is applied for a time window of  $\sim 2\mu\text{s}$ , whose shape is tuned according to the measurement of the injection background time structure provided by the BEAST II monitoring.

## 2.3 SuperKEKB commissioning and running phases

The commissioning of SuperKEKB has been carried out in three phases. In Phase 1 (2016) the accelerator rings have been commissioned without the final focusing system at the interaction point and without the Belle II detector. The main goal was to perform sufficient vacuum scrubbing before the Belle II detector was rolled in, tune the basic feedback system and perform machine studies for low-emittance and optics optimization.

During the Phase 2 commissioning (2018), the final focusing and the positron damping ring were also in place, together with the Belle II detector, except for the vertex detector, replaced by another system of devices dedicated to the beam background study. Also, additional collimators to protect the Belle II detector have been installed before the beginning of the data taking. The first physics collisions were detected on April 26<sup>th</sup>, 2018. The data taking continued until July 2018, with a maximum achieved instantaneous luminosity of  $0.5 \times 10^{34} \text{ cm}^{-2}\text{s}^{-1}$  and a total integrated luminosity of around  $0.5 \text{ fb}^{-1}$ . These data have been used to prove the understanding of the detector through performance measurements and several rediscoveries. Dark sector searches which were previously limited by inefficient trigger conditions can be also performed on this data set.

In Phase 3, the full vertex detector has been installed and started taking data with Belle II in March 2019. The application of the final nano-beam scheme will allow to reach the design luminosity and collect in the next ten years  $50 \text{ ab}^{-1}$ . Thanks to such a data set a very rich physics program can be pursued, which includes the measurement of time dependent  $CP$  violation and CKM parameters with a precision below the current threshold of percent level, hadronic charmless  $B$  decays and direct  $CP$  violation, charm and quarkonium physics,  $\tau$  and

low multiplicity studies as well as the search for physics beyond the SM through precision measurements.

### 2.3.1 Phase 1: first beam background measurements

Phase 1 operation had three main goals: first to ensure beam background levels are safe to install Belle II; second, to provide feedback for the accelerator optimization on how the machine parameters affect background levels; third, to validate the simulation studies on expected backgrounds, which are crucial to reliably estimate detector lifetimes. These goals have been achieved thanks to the BEAST II detectors system, which is described in detail elsewhere [74].

#### The BEAST II detector

The complete description of the BEAST II detector is beyond the purposes of this work, and hereby only an introduction will be provided. The BEAST II detector is composed of eight sub-detectors devoted to the measurement of many properties of SuperKEKB backgrounds at the interaction region. The PIN diodes serve as dosimeter at various location of the interaction region, while diamonds provide fast dose rates at the IP and have been used in the next phases to implement the beam abort system. The crystals and BGO systems measure instead the electromagnetic background and in the fast readout mode they provide information on the time structure of injection backgrounds. Also CLAWS, which couple plastic scintillators to silicon photo-multiplier (SiPM) readout, are important to capture the time structure of backgrounds during injection and provide feedback for accelerator tuning. Finally, to measure the very challenging neutron background two systems have been included in the BEAST II detector: the  $^3\text{He}$  tubes for thermal neutron counting and the time projection chambers (TPC) for the counting and tracking of faster, high-energy neutrons. The QCSS plastic scintillators system was not yet part of BEAST II during Phase 1, but it is a good prototype for background monitors based on plastic scintillators that are small enough to be placed between the final focus quadrupoles and the Belle II detector, and it has been integrated in the BEAST-II monitoring system during Phase 2.

#### Summary of main Phase 1 findings

The detailed description of the results achieved during Phase 1 commissioning is reported in [74]. The BEAST II detector recorded data in spring 2016 and was able to observe all the main background sources, beam-gas, Touschek, beam-dust and injection backgrounds, except for the two background types due to colliding beams, whose measurement have been postponed to Phase 2. A limit on the expected synchrotron radiation dose rate at the IP was also set. Based on these measurements, the expected background rates for Phase 2 have been also extrapolated and judged to be safe for proceeding with further commissioning and the Belle II installation, despite the safety factors have been found to be low for almost all the detectors and highly dependent on the machine parameter tuning, especially collimators and magnets alignment.

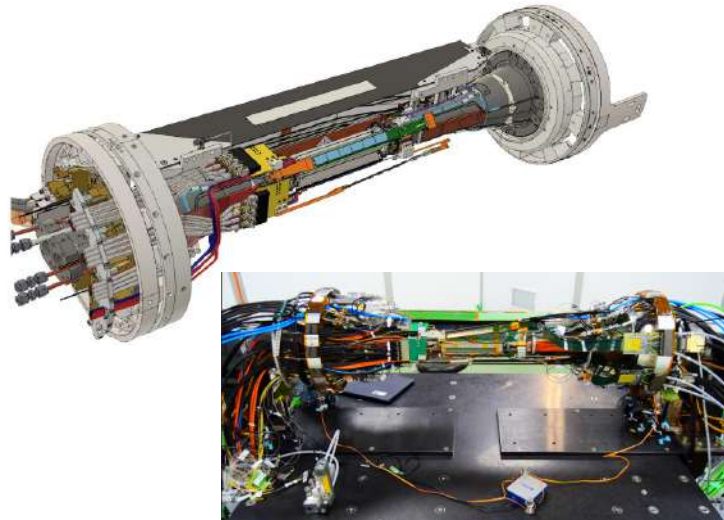


**Figure 2.6:** The CAD rendering and a real image of the vertex detector cartridge and BEAST II monitoring setup installed during Phase 2 at the interaction point.

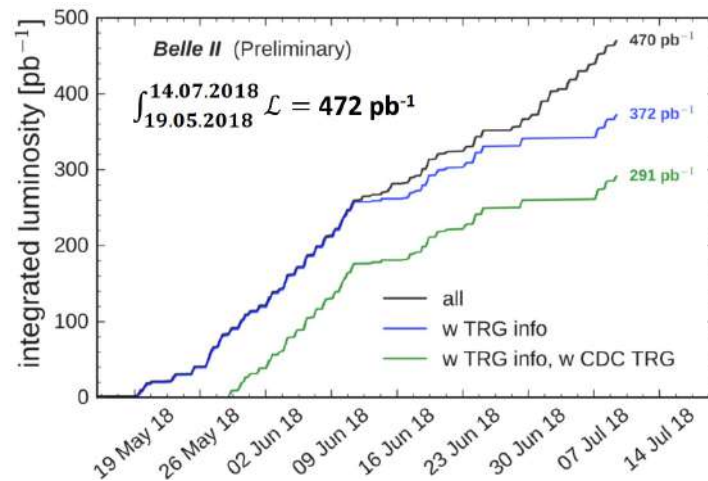


**Figure 2.7:** The integrated luminosity collected during the Phase 2 run, April-July 2018, is shown. The various curves refer to the trigger information available for each data set.

### 2.3.2 Phase 2: first collisions

At the beginning of February 2018, the second commissioning Phase 2 started and operations at SuperKEKB were resumed with the final focusing system in place and the Belle II detector rolled in, except for the vertex detector (detailed description is given in the next chapter). Instead of the final PiXel Detector (PXD) and Silicon Vertex Detector (SVD), a special

cartridge was installed close to the interaction region, which included the BEAST II detectors and one single ladder per each layer of PXD and SVD detectors (equivalent to roughly one octant of the full vertex detector), a schematic view is provided in Figure 2.6. The goal for such a configuration was double: to commission the machine by measuring beam background rates and providing feedback for accelerator tuning and to ensure the radiation safety of Belle II to run at higher luminosity with the final vertex detector installed, without damaging it. After the first collisions achieved on April 26<sup>th</sup> 2018, the data taking continued until July 17<sup>th</sup> 2018, reaching a peak luminosity of  $5 \times 10^{33} \text{ cm}^{-2}\text{s}^{-1}$  and collecting a total data set of  $\sim 500 \text{ pb}^{-1}$ . The main goals of Phase 2 were to verify the nano-beam scheme technique

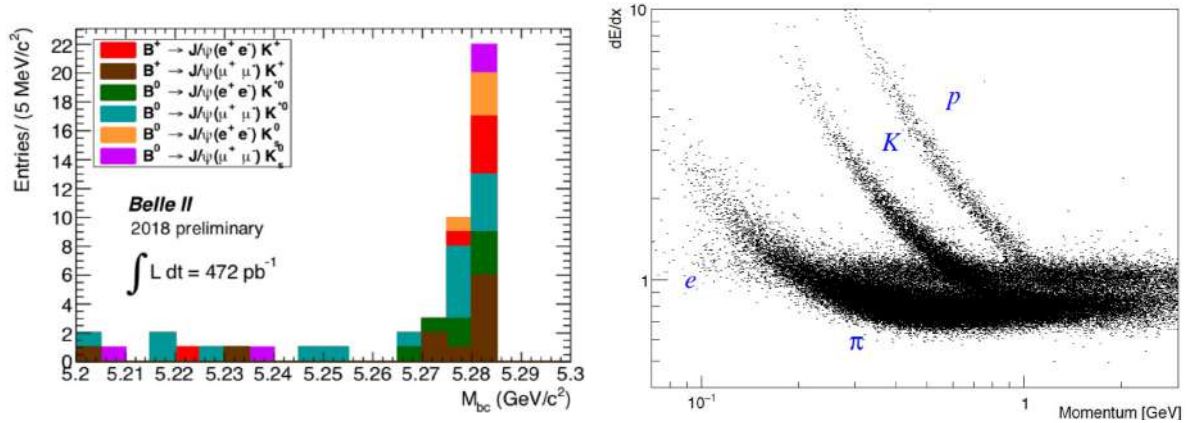


**Figure 2.8:** The distribution of the beam-constrained mass  $m_{bc}$  showing the peak of the 88 reconstructed  $B$  mesons from the analysis of  $472 \text{ pb}^{-1}$  collected during Phase 2 (left plot) and the energy loss per path length distribution for charged particles detected by Belle II (right plot). Black dots are collision data recorded during Phase 2.

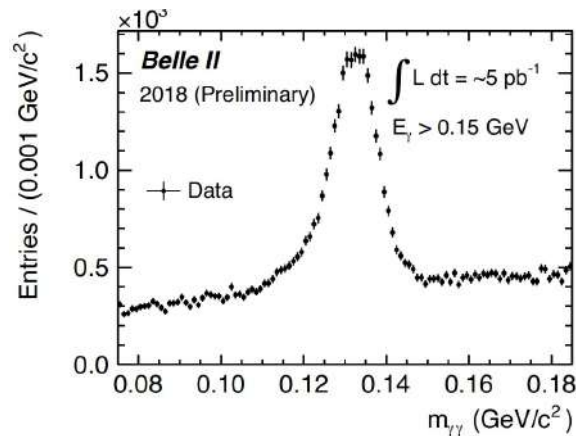


**Figure 2.9:** The two photon invariant mass distribution is shown, with the peak corresponding to the reconstructed  $\pi^0 \rightarrow \gamma\gamma$  decays on  $5 \text{ pb}^{-1}$  of Phase 2 collision data.

achieving the target luminosity of  $10^{34} \text{ cm}^{-2}\text{s}^{-1}$  and to prove the understanding of a new

detector operating at a new machine. Thanks to the total integrated luminosity recorded during Phase 2 (Figure 2.7), the first beam-constrained mass distribution <sup>2</sup> was provided, showing the peak at the  $B$ -meson mass which comes from the reconstructed 88  $B\bar{B}$  events (Figure 2.8). Particle identification capability as well as neutral reconstruction were also tested on the Phase 2 data set. In particular, the distribution of the energy loss per path length for charged particles traversing the Belle II tracking devices (Figure 2.8) is exploited for particle identification, while in Figure 2.9 the two photon invariant mass distribution shows the peak of the  $\pi^0$  mass, reconstructed only after one day of data taking with  $5 \text{ pb}^{-1}$ , proving the excellent detection capability of the electromagnetic calorimeter. During Phase 2 the relaxed hardware trigger conditions and the pass-through applied to the software trigger allowed to collect a data set particularly suitable for dark sector searches dealing with missing energy measurements and requiring nothing in the event except two charged tracks, as it is the case for the work presented in this thesis. The capability to efficiently reconstruct photons and veto them has been crucial for such study.

### 2.3.3 Phase 3: first physics with the full vertex detector

The third commissioning phase with the full vertex detector installed inside Belle II resumed the operations in March 2019. Phase 3 goal is to collect up to  $50 \text{ ab}^{-1}$  of data in the next 10 years, by achieving the world highest luminosity of  $8 \times 10^{35} \text{ cm}^{-2}\text{s}^{-1}$  (Figure 2.10), and provide a competitive data set to pursue a rich physics program in a wide range of areas in  $b$ -quark and  $c$ -quark physics, in  $\tau$ -lepton, two-photon, quarkonium and exotic studies. The new accelerator has sufficient power to deliver  $e^+e^-$  collisions at a center-of-mass energy in the range from just below  $\Upsilon(1S)$ , 9.46 GeV, to just above  $\Upsilon(6S)$ , 11.24 GeV. The majority of data will be collected at the center-of-mass energy of  $\Upsilon(4S)$ , which is a well motivated choice, nonetheless energy scans and running periods at other resonances are also foreseen and still topic of discussion for the possibility to collect unique data sets for dark sector and exotic searches (further details on the Belle II physics program can be found in [43]).

#### Early Phase 3: main issues and recorded data set

The first data of Phase 3 have been collected since March 25<sup>th</sup> until June 30<sup>th</sup> 2019, corresponding to a total integrated luminosity which is less than the  $\sim 20 \text{ fb}^{-1}$  of data originally expected for the spring run, reaching barely  $7 \text{ fb}^{-1}$  (Figure 2.11).

Several issues have slowed down the early Phase 3 data taking, starting from a fire accident happened at the beginning of April near the injector linear accelerator (Linac). The Linac provides the first acceleration boost to electrons and positrons and its accelerating units were forced to stay off for more than two weeks, preventing SuperKEKB to resume beam collisions before the April 22<sup>nd</sup>. Beside the external causes, other issues with the new machine and the implementation of the nano-beam scheme technique when squeezing the beta function at the interaction point have been responsible for the lower achieved luminosity and the smaller collected data set. Background rates which have been measured to be one order of magnitude higher than the simulated expectation required further caution in the increasing of the beam

<sup>2</sup> The beam-constrained mass is defined as the mass of the reconstructed  $B$ -meson  $m_B = \sqrt{E_{\text{beam}}^{*2} - p_B^{*2}}$  where the reconstructed energy is constrained to equal the measured beam energy in the center-of-mass frame,  $E_{\text{beam}}^* = \sqrt{s}/2$ . It is one of the most useful kinematic variables in  $B$ -meson reconstruction, as explained in [65].

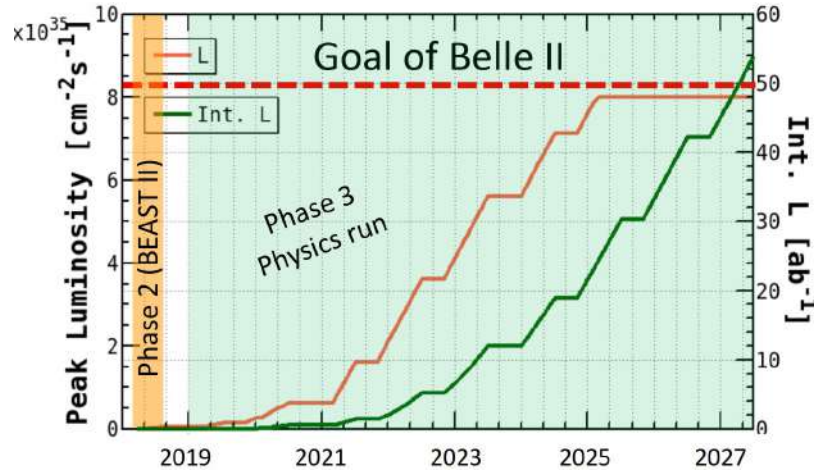


**Figure 2.10:** The luminosity projections for the Belle II experiment, which aims at the world highest instantaneous luminosity of  $8 \times 10^{35} \text{ cm}^{-2}\text{s}^{-1}$  for a total collected data set of  $50 \text{ ab}^{-1}$  in its ten years of operation. The months of running corresponding to Phase 2 are highlighted in yellow shade, the years of running belonging to Phase 3 are in green shade.

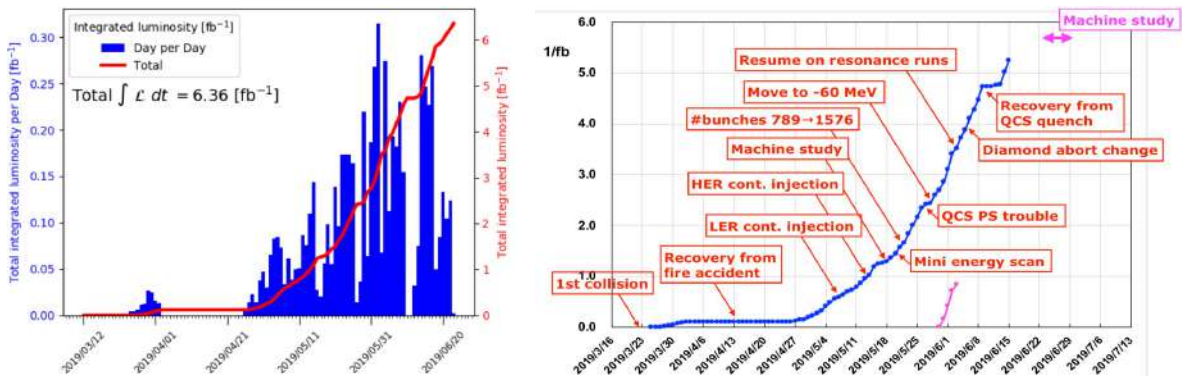


**Figure 2.11:** The online luminosity measured during early Phase 3, which sums up to a total of more than  $6.5 \text{ fb}^{-1}$  collected data is reported in the left plot. On the right, the main events of the spring run are shown on the integrated luminosity curve. Energy scans and off-resonance data have also been recorded, as well as data from beam background studies.

currents and additional studies to control the beam blow-up and the injection noise were also needed. The latter is related to short beam lifetimes at the SuperKEKB, whose running mode is therefore based on continuous injections. This implies a refill of the bunches every 20 ms, slightly perturbing the already circulating charges which are measured to remain noisy for the next 400 turns. As a consequence, at every accelerator turn when the noisier bunches hit the detector (every  $10 \mu\text{s}$ ), the background rates dramatically increase, affecting the performance of Belle II, especially for what concerns the sustainability of the PXD occupancy. Therefore it is crucial to silence the noisy bunches by applying a trigger veto ( $2 \mu\text{s}$ ) every  $10 \mu\text{s}$  in the 4 ms time window which follows the injection, to avoid any impact of this injection noise effect on

**Table 2.4:** Achieved machine parameters during Phase 3 commissioning. The snapshot of July 1<sup>st</sup> provides the latest achieved tuning at the end of the spring running.

Machine Parameter	June 20 <sup>th</sup>	July 1 <sup>st</sup>
$\beta_x^*$ (mm)	100	80
$\beta_y^*$ (mm)	3	2
$I_{LER} / I_{HER}$ (mA)	396/398	799.7/821.2
$n_B$	1576	1576
$I_{bLER} / I_{bHER}$ (mA)	0.314/0.317	0.507/0.521
$\xi_{yLER}/\xi_{yHER}$	0.0335/0.0189	0.0355/0.0197
$\mathcal{L}$ ( $\times 10^{33}$ /cm <sup>2</sup> /s <sup>-1</sup> )	0.479	12.294

the data stream.

Also the magnets of the final focusing system showed instabilities that in the worst cases resulted in a certain number of quenches, also related to background burst events. These episodes are particularly dangerous for the safety of the vertex detector, and for all the Belle II sub-systems in general and a better understanding of the machine background is crucial not to compromise the detector. The main events characterizing the 2019 spring runs are shown in Figure 2.11 and the final parameters achieved are reported in Table 2.4.

Nonetheless, thanks to the hard work of all the people involved in the first running period operations and in the analysis of the collected data, already with less than  $10 \text{ fb}^{-1}$  it has been possible to assess the improved performance of the Belle II detector in its final configuration, especially regarding tracking efficiency and the impact parameter resolution, thanks to the full VXD installation. Also particle identification, and especially muon detection, has largely improved due to the recovery of a well performing muon detector (KLM), now able to provide dedicated muon identification variables with much higher and reliable efficiency with respect to Phase 2. The early Phase 3 data set has been used to start new physics analyses and provide detector performance as well as rediscovery studies, as proof of concept of the good behavior of the detector and of the capability to understand the collected data.

After the summer shutdown, SuperKEKB resumed operation in October 2019 for the autumn run, which is expected to provide further  $20 \text{ fb}^{-1}$  of collision data by the end of the year, in order to reach  $200 \text{ fb}^{-1}$  by summer 2020. First beams were circulated on October 15 with the same machine configuration achieved at the end of the 2019 spring run, as shown in Table 2.4. Restarting from the same optics which allowed to achieve  $\beta_y^* = 2 \text{ mm}$ , the betatron function at the IP needs to be decreased by at least another order of magnitude to reach the nominal design value. The main goal for the autumn run is to squeeze down the beta function at the IP to 1 mm, with decreased beam currents around 300 mA. The injection background is now better controlled thanks to the installation of additional feedback systems and new collimators achieved during summer 2019, but in order to reach higher currents further beam background reduction is required and to that extent the collimator optimization will be crucial.

The integrated luminosity increase (prospects shown in Figure 2.10) will be the key ingredient to open new doors and achieve the benchmarks in flavor physics and BSM searches and with that purpose in mind an efficient interplay between the delicate machine tuning and the

detector performance is needed. In the following Chapter, the experimental apparatus that allows to detect the products of  $e^+e^-$  collisions delivered by SuperKEKB is described, as well as the software framework needed to analyze the collected data set.

## Chapter 3

# Belle II experiment

The Belle II detector is described in detail in the Technical Design Report [68], for the purposes of this work only a general overview will be given in Section 3.1. The main changes and improvements with respect to the Belle detector are highlighted and a brief description of each sub-detector is provided. In Section 3.2 the Belle II trigger system is described, followed by an overview of the software framework developed to analyze the collected data sets (Section 3.3), which are finally described in the last Section of this chapter, 3.4.

### 3.1 Belle II upgrade overview

The aim of the Belle II upgrade is to maintain the same good performance of Belle detector in the new experimental environment with much higher background levels. A schematic comparison of the longitudinal view of the new Belle II spectrometer with respect to the old Belle detector is shown in Figure 3.1. Since the SuperKEKB boost is reduced with respect to KEKB (0.28 instead of 0.43) achieving the same proper time resolution requires better vertex resolution, that can be achieved with the reduction in radius of the first active detector layer. Studies estimate a conservative 20 times increase of the expected background hit rate, due to 50 times higher event rates (proportional to the increase of the instantaneous luminosity) and to double beam currents. The modifications studied to ensure a comparable or even better performance for the Belle II detector are the following:

- the inner part of the vertex silicon strip detector, next to the beam pipe, is replaced by a two-layer silicon pixel detector based on DEPFET technology, placed at smaller radius and with a very light material budget;
- the silicon strip detector starts from just outside the pixel detector and reaches a larger radius than in Belle;
- the silicon strips readout is based on APV25 chips which have a shorter shaping time with respect to Belle VA1TA chips to cope with higher background;
- the central drift chamber, the main tracking device, extends to a larger radius and it has a larger number of small-cell layers compared to its predecessor;

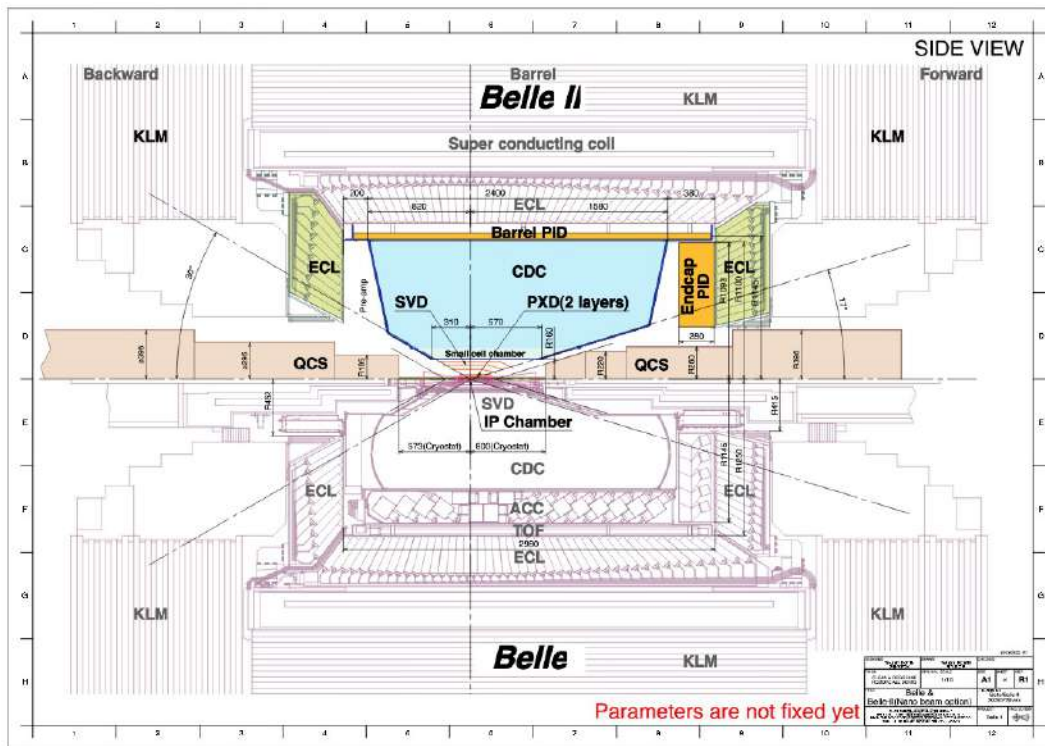


**Figure 3.1:** The top half shows the upgraded Belle II spectrometer as designed in the TDR[68]; in the bottom half the longitudinal view of the old Belle detector is shown.

- the new particle identification devices, both in the barrel and in the endcaps, are more compact and highly performing, exploiting the Cherenkov image detection method and a very fast readout electronics;
- the electronics of the electromagnetic calorimeter is replaced with a fast wave-form-sampling circuit;
- in the first two layers of the barrel part and in the endcaps of the muon and  $K_L$  detector, Resistive Plate Chambers (RPCs) are replaced by scintillators readout with wavelength shifting fibers and Silicon Photomultiplier (SiPM) called MPPC and produced by Hamamatsu;
- a new data acquisition system for handling the higher event rate is provided.

The improvements foreseen for Belle II performance are various, first of all the vertex resolution which benefits from the two innermost pixel layers; second, a better reconstruction efficiency for the  $K_S$  decaying to charged pions, which is crucial for the analysis of the golden mode  $B \rightarrow J/\psi K_S$  exploited in  $CP$  asymmetries measurements. In addition, the new particle identification devices ensure a better pion/kaon separation in the whole kinematics range of the experiment. Finally, a better performing electronics for the calorimeter readout reduces the pile up, improving missing energy measurements.

### 3.1.1 The Pixel Detector

The expected background rate makes the use of silicon strip sensors at small radius ( $\sim 20$  mm) not feasible because of the high occupancy. Pixel detectors have a much finer segmentation and therefore smaller occupancy (3%), while strips detectors at SuperKEKB can be safely located at larger radii.

The PiXel Detector (PXD) concept implemented at Belle II is based on the DEPFET (DEPLETED Field Effect Transistor) technology. It allows to have very thin pixel ( $50 \mu\text{m}$ ) with readout electronics moved outside the acceptance region, therefore reducing the material budget that contributes to the multiple scattering. The only part of the electronic readout being inside the tracking volume are the switcher ASICs for which very thin gas pipes have been devised to provide the necessary active cooling by means of nitrogen flow. Also radiation tolerance can be achieved engineering the sensors in a dedicated radiation-hard technology.

DEPFET is a semiconductor detector concept able to combine detection and amplification in one device. A DEPFET pixel consists in a p-channel MOSFET structure integrated onto a fully depleted silicon substrate. The MOSFET has an internal gate where the electrons generated when a charged particle passes through the device are collected. The internal gate modulates the current at readout time allowing the detection of the collected charge.

The DEPFET sensors are organized into planar modules, the ladders, which compose the two layers of the PXD, with radii respectively of 14 and 22 mm. The sensitive lengths of each layer are determined by the acceptance requirements of the detector: a polar angular coverage from  $17^\circ$  to  $155^\circ$  is ensured. The total amount of pixels composing the PXD is around 8 million organized into arrays. Each DEPFET pixel represents a cell, a monolithic structure with internal amplification, therefore much thinner than other devices which need additional amplification. Typical pixel sizes have to meet the vertex resolution requirement,

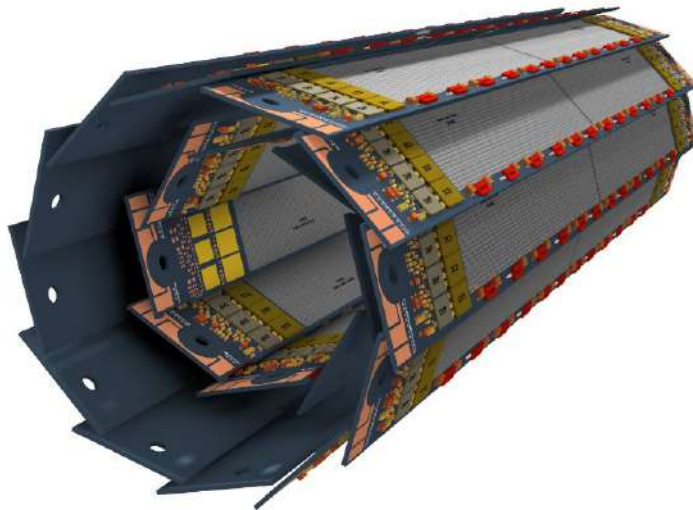


**Figure 3.2:** A CAD rendering of the two-layer pixel detector is shown.

which is  $20\ \mu\text{m}$ , and also the thinning feasibility, resulting in a  $50\times 50\ \mu\text{m}^2$  and  $50\times 75\ \mu\text{m}^2$  cells respectively for the inner and outer layers.

Another challenging requirement is the short frame readout time, that is achieved by splitting the readout on both sides of the pixel matrix and introducing high level of parallelization (a four-row simultaneous readout): the processing time for each pixel row is then manageable, of order of 100 ns, and all the 1600 rows can be read in a total frame time of 20  $\mu\text{s}$ .

The sensors are finally mounted on the supporting structure which is able to slide on the beam pipe to accommodate for thermal expansion. A schematic view of the total structure of PXD is reported in Figure 3.2. For the early Phase 3 started in March 2019 after the installation of the vertex detector, due to problems in the assembling of the PXD ladders, only half of the designed PXD has been installed, consisting in the full first layer and 2 ladders of the second one. The PXD installation is expected to be finalized in 2021.

### 3.1.2 The Silicon Vertex Detector

Low-momentum particles are crucial for the physics at the  $B$  factories, but also a challenge for the track finding system, since they are heavily affected by multiple scattering. Consequently, one of the fundamental requirements for the Silicon Vertex Detector (SVD) is a very low material budget, as long as a short shaping time to limit the occupancy under few percent and help the track finding algorithms to reject background. These features determine the geometrical shape of the sensors and also the choice of the readout electronics. The former issue is solved by adopting the largest possible silicon wafers and equipping the forward region with trapezoidal slanted sensors, while for the latter, the solution came from inheriting the APV25 chips first used in the tracker of the CMS experiment (LHC), equipped with 128

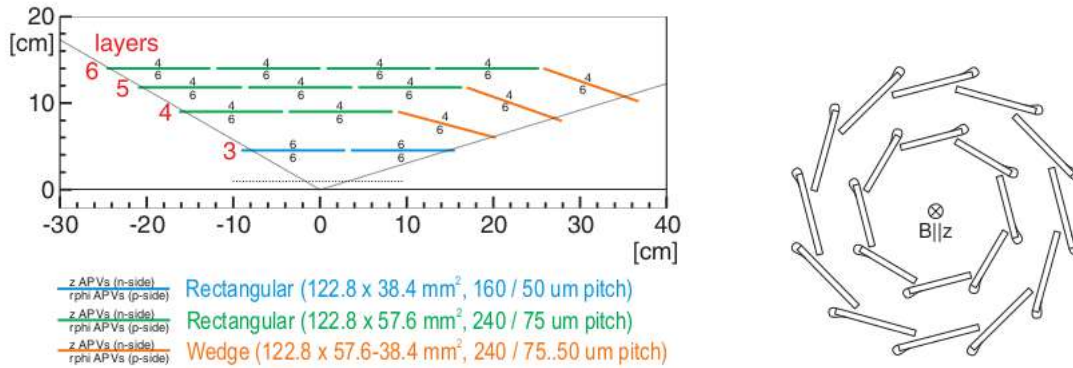


**Figure 3.3:** Left: Schematic view of the SVD longitudinal section, showing the sensors geometry for each layer and the number of APV25 chips on each side of the sensors. Right: the windmill structure of the inner sensors, with the Origi concept applied on the upper edge of silicon modules, is shown. The solenoidal  $\vec{B}$  field parallel to the  $z$ -axis is also indicated in the picture.

channels each and a shaping time of 50 ns. Moreover, the multi-peak operational mode of the APV25, where six (or three) consecutive samples along the shaping curve are recorded with each trigger, ensures a time resolution of order of 3 ns. The excellent SVD performance results in a innermost layer occupancy smaller than 1%.

The SVD is composed of four layers of Double-sided Silicon Strip Detectors (DSSDs), located respectively at radii of 39 mm (*layer 3*), 80 mm (*layer 4*), 104 mm (*layer 5*) and 135 mm (*layer 6*). The azimuthal angular coverage goes from  $17^\circ$  (the *forward* region) to  $150^\circ$  (*backward* region). The asymmetry is due to the Lorentz boost in the laboratory frame, which favors events boosted in the forward direction.

There are three different types of sensors used for the SVD: the rectangular ones (big and small) are produced by Hamamatsu Photonics (HPK), while the trapezoidal ones are produced by the Micron Semiconductor (UK). The first step for sensor production are six-inches, 300  $\mu\text{m}$ -thick silicon wafers, from which the rectangular sensors are developed in two sizes: for layer 3, which has only the barrel section, smaller sensors are adopted, while for layers 4 to 6 larger sensors are used for the barrel region. The forward region of layers 4 to 6 is covered by trapezoidal slanted sensors which minimize the material budget, simultaneously optimizing the acceptance. The long strips measuring the  $r\phi$ -coordinate on the  $p$ -side are in total 768, readout by six APV25 chips per sensor. For rectangular sensors they are parallel to and facing the beam axis. The short strips on the  $n$ -side, which measure the  $z$ -coordinate, are instead 512 for the large rectangular sensors and the trapezoidal ones ( while they are 768 as on  $p$ -side for the small rectangular sensors used for layer 3), therefore they need only four APV25 chips for readout. They are located on the sensor side towards the outside (except for layer 3, which has an inverted side structure, with the  $n$ -side facing the Interaction Point). For the slanted sensor of the forward region the geometry is the same, except for the  $p$ -side strips which are not parallel to  $z$ -axis anymore. Dimensions are given in mm in Figure 3.3 and a picture of the real SVD installed in Belle II is provided in Figure 3.4.

The *Origami chip-on-sensor* concept is a readout modification introduced in Belle II for the inner sensors, while the forward and backward sensors are readout by conventional APV25 chips located outside the acceptance. The Origi concept refers to flexible pitch adapter



**Figure 3.4:** The Belle II SVD already matched with the PXD and ready to be installed in at the Interaction Point of the detector (December 2018).

circuits connecting the sensor strips to APV25 chips applied on the outer edge of the sensors in the windmill structure, as shown in Figure 3.3. The strips on the outer side are read by a planar pitch adapter, while for the strips on the inner side, a flexible pitch adapter bent around the upper edge of the sensor is needed. This technique aligns all the chips on the outer side, enabling to use only a single cooling system for all the ladder. The cooling is provided by a dual phase CO<sub>2</sub> system, whose design aims at minimizing the material budget, adopting 1.4 mm-diameter tubes with 0.05 mm-thick walls.

### 3.1.3 The Central Drift Chamber

The Central Drift Chamber (CDC) fulfills three main functions. First, it contributes with the SVD and PXD to charged track reconstruction and measures the momentum. Second, it helps in particle identification thanks to the measurements of the characteristic energy loss of charged particle due to ionization in the gas volume. Finally, it provides reliable trigger signals for charged particle events.

The CDC follows the successful design of its predecessor in Belle: the same structure is implemented and the same material and gas mixture are used. The main modifications regard:

- the readout electronics, which needs to be much faster in order to handle higher trigger rates;
- the cylinder radii, where the innermost ones has to be larger to account for a bigger SVD, while the outermost radius has to deal with the more compact barrel detector for particle identification, resulting in a 160 mm and 1130 mm radii respectively. The

acceptance in azimuthal angle goes from  $17^\circ$  to  $150^\circ$ . Also the wire configuration has to be adapted.

- the three-dimensional trigger information, providing a  $z$  trigger (see Section 3.2) which efficiently helps in reducing beam backgrounds without losing physics events.

The CDC consists in 56 layers organized in 9 super-layers. The length of the squared cells varies from 10 mm for the innermost super-layer to 18.2 mm for the outermost ones. The 50% helium-50% ethane gas mixture is filled with a total of 14336 tungsten sense wires of 30  $\mu\text{m}$  diameter. For the generation of the needed electric field gradient, aluminum wires of 126  $\mu\text{m}$ -diameter are used. The structure is supported by two carbon-fiber reinforced cylinders, terminating with aluminum end-plates. Finally, the measured spatial resolution of the CDC is about 100  $\mu\text{m}$ , while the relative precision on the  $dE/dx$  measurement for particles with an incident angle of  $90^\circ$  is around 12%.

### 3.1.4 Particle Identification devices

Two sub-detectors in Belle II are specifically devoted to particle identification: the *Time-Of-Propagation* counter in the barrel region and the *Aerogel Ring-Imaging Cherenkov counter* for the end-cap. Both the sub-detectors exploit the Cherenkov effect to identify the charged particle traversing the spectrometer.

#### The Time-Of-Propagation counter

The Time-Of-Propagation (TOP) counter, shown in Figure 3.5, measures the time of propagation of the Cherenkov photons internally reflected in the quartz bar. Together with the detected arriving position along the  $x$  coordinate of the quartz bar as represented in the picture, the arrival time allows to reconstruct the Cherenkov angle  $\theta_C$  from which the particle velocity  $v$  can be inferred and the likelihood for different mass assignment hypothesis is calculated.

The TOP consists in 16 modules surrounding the outer wall of the CDC. Each module is a quartz radiator composed of two quartz bars glued together for a total length of 2500 mm and a transverse area of  $44 \times 20 \text{ mm}^2$ . Photons emitted in the forward direction are reflected backward by a mirror placed at the forward end of the quartz bar. Photons propagating in the backward direction are collected by different PMT channels, depending on their reflection angles. The critical issue in the TOP performance for PID is the broadening of time resolution due to the photons chromaticity, which is cured by a focusing system consisting in a slightly concave-shaped mirror, aimed at compensating the chromaticity dispersion of Cherenkov photons: the parallel rays are focused into the same pixel of a photo-sensor, while the chromatically-dispersed one are detected by separate channels.

The required time resolution for a single-photon detection is around 50 ps. The goal is achieved by employing as photon detectors the Multi-Channel Plate Photo Multipliers (MCP PMTs), two-stage amplification devices, with a gain of  $10^6$  and a very fast response.

#### The Aerogel Ring-Imaging Cherenkov counter

In the forward end-cap, the particle identification is provided by the proximity focusing Aerogel Ring-Imaging Cherenkov counter (ARICH), whose schematic view is shown in Figure 3.6.

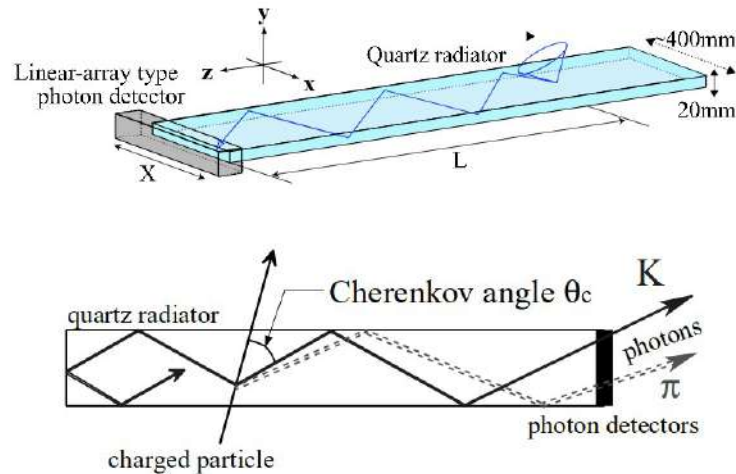


**Figure 3.5:** Conceptual representation of the time-of-propagation counter, which measures both the arriving time and position of the internally reflected Cherenkov photons.

It consists of an aerogel radiator producing Cherenkov photons when a charged particle passes through its volume; an expansion volume of 20 cm divides the aerogel tile from the photon detector surface and allows the Cherenkov photons to enlarge into rings. The array of position sensitive photon detectors provides single photon detection in a high magnetic field (1.5 T) with optimal resolution in two dimensions.

The main parameters describing the detector are the number of detected photons  $N_\gamma$  and the resolution on the Cherenkov angle  $\sigma_\theta$ . Increasing the radiator thickness, the number of detected photons increases and the resolution per charged track improves as  $\sigma_\theta/\sqrt{N_\gamma}$ , but the angular resolution on the single photon ( $\sigma_\theta$ ) degrades due to the uncertainty of the emission point. Combining two layers with appropriately tuned refractive indices in order to have two overlapping rings will reduce the spread due to the emission point uncertainty, achieving a resolution on the Cherenkov angle  $\sigma_\theta \simeq 16$  mrad. The performance is optimized for charged tracks with momentum larger than 3.5 GeV/c, but no significant degradation is shown also for lower momentum tracks. A non-homogeneous aerogel radiator ( see Figure 3.6) has been devised, with a global acceptance covering the azimuthal angular region from  $15^\circ$  to  $30^\circ$ . The proximity focusing technique is applied by choosing as upstream layer the aerogel with lower refractive index ( $n_1 = 1.046$ ) and increasing the refractive index of the downstream layer ( $n_2 = 1.056$ ). Studies have shown that a twice as thick layer of homogeneous aerogel radiator would provide the same number of photons, but with a worse resolution  $\sigma_\theta \simeq 20$  mrad. The development of reliable photo sensors with good efficiency for single-photon detection in the high magnetic field is achieved with the *Hybrid Avalanche Photo-Detectors* (HAPD) by Hamamatsu Photonics. Finally, considering the studies on Cherenkov angle resolution and on average 12.7 detected Cherenkov photons as measured during for Phase 3, the precision

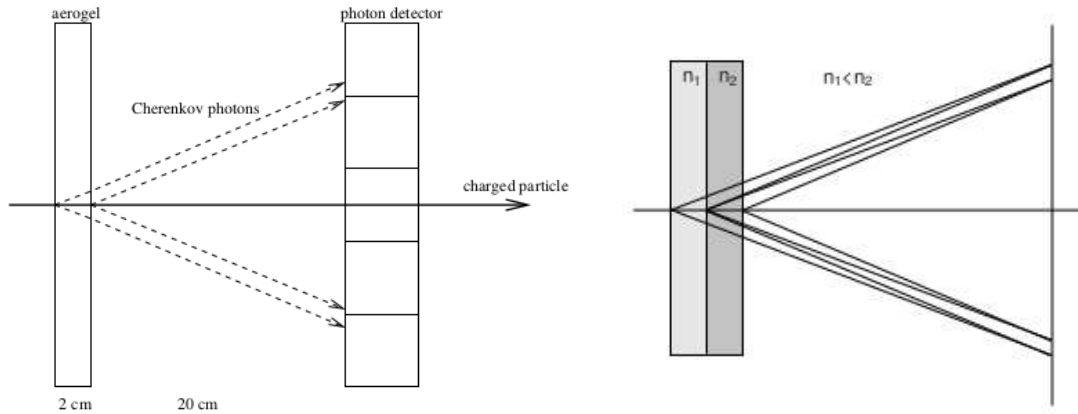


**Figure 3.6:** Left: a schematic drawing of the ARICH is shown. Dimensions are given in cm and from left to right the arrangement of the aerogel radiator, the expansion volume and the position sensitive photon detector surface is illustrated. Photons trajectory are reported in dashed lines. Right: the proximity focusing system with non-homogeneous dual-layer aerogel is shown. The two rings coming from the different aerogel layers, with an appropriate choice of the refractive indices ( $n_1 = 1.046$ ,  $n_2 = 1.056$ ), totally overlap on the photon detector surface.

achieved is:

$$\sigma_{track} = \sigma_{\theta} / \sqrt{N_{\gamma}} \sim 4.5 \text{ mrad.}$$

### 3.1.5 The Electromagnetic Calorimeter

The electromagnetic calorimeter (ECL) in Belle II covers many important tasks: it has to provide a high energy resolution, since more than a third of the  $B$  meson decay products consist of  $\pi^0$  and neutral particles. The calorimeter needs to detect with high efficiency photons over a wide energy range, from 20 MeV to 4 GeV, and it has to precisely determine their energies and angular coordinates. It must provide electron identification, luminosity measurements and proper trigger signal generation; finally, the calorimeter and KLM combined performance ensures kaon detection.

The choice for the Belle II detector has been to exploit the Belle calorimeter, replacing the readout electronics in order to cope with the increased background rates. The calorimeter is composed of a barrel section of 3 m length and 1.25 m inner radius, with an azimuthal angular coverage of  $32.2^\circ < \theta < 128.7^\circ$ , which together with the forward and backward endcaps covers all the range from  $12.1^\circ$  to  $155.03^\circ$ . The total structure contains 8736 CsI(T) crystals shaped as truncated pyramid with a  $6 \times 6 \text{ cm}^2$  cross section and of 30 cm length, corresponding to 16.1 radiation lengths ( $X_0$ ). In the Belle experiment, the energy resolution observed with the same calorimeter was  $\sigma_E/E = 4\%$  at 100 MeV, 1.6% at 8 GeV, and the angular resolution was 13 mrad (3 mrad) at low (high) energies;  $\pi^0$  mass resolution was  $4.5 \text{ MeV}/c^2$ ; in absence of backgrounds a very similar performance would also be expected in Belle II. To cope with considerably elevated background levels and larger pile-up noise, scintillator photo-sensors are equipped with wave-form-sampling readout electronics. The scintillation light is detected by two Hamamatsu Photonics photodiodes glued onto the crystal with a 1-mm plexiglass plate. A LED is attached on this plate and it injects light pulses for monitoring the optical stability of the crystal. Each photodiode terminates in a preamplifier producing an independent signal

and the two pulses are then summed at an external shaper board. The crystals in the barrel section are structured in multi-cell units divided by 0.5 mm thick aluminum septum walls which go from the inner to the outer supporting cylinders. The overall support structure is flushed with dry air to provide a low humidity (5%) environment for the crystals and the heat generated by the preamplifiers (about 3 kW in total) is extracted by a water cooling system. The support structure for the endcaps is similar to that of the barrel section.

From calibration with cosmic muons it is known that the average output signal of the current crystals gives 5000 photo-electrons per 1 MeV of deposit energy, with an average noise level of 200 keV. The higher background rate is handled with a new readout electronic based on the signal sampling method.

The intrinsic energy resolution of the calorimeter from a prototype test is given by the approximated formula:

$$\frac{\sigma_E}{E} = \sqrt{\left(\frac{0.066\%}{E}\right)^2 + \left(\frac{0.81\%}{\sqrt[4]{E}}\right)^2 + 1.34\%^2}, \quad (3.1)$$

where  $E$  is the energy in GeV and the first term refers to the electronic noise contribution.

### 3.1.6 The neutral kaon and muon detector

The  $K_L$  and muon detector (KLM), consisting of alternating 4.7-cm thick iron plates and active material detectors, is located outside the superconducting solenoid which provides the 1.5 T magnetic field used for particle momentum measurements. A schematic overview is shown in Figure 3.7. The iron is needed as magnetic flux return for the solenoid and it also provides the material budget for 3.9 interaction lengths, allowing the  $K_L$  to hadronically shower in its volume. The octagonal barrel section covers the azimuthal region  $45^\circ < \theta < 125^\circ$ . Adding the endcaps coverage, the KLM reaches the angular acceptance of  $20^\circ < \theta < 155^\circ$ . The outer layers of the barrel are equipped with glass electrode Resistive Plate Chambers (RPCs), while in the inner two layers and in the endcaps scintillators readout by SiPMs are installed. This replacement is needed to avoid the RPCs efficiency drop in a high rate environment.

The use of scintillator strips equipped with SiPMs ensures an optimal time resolution, which is measured with a trigger provided by cosmic ray events; the time dispersion difference gives  $\sigma_t \sim 0.7$  ns. The good timing performance enables to exploit the KLM endcaps as time of flight detector for  $K_L$ . In the barrel section the  $K_L$ -reconstruction efficiency is measured to be linearly increasing with the particle momentum up to a plateau of around 80% for momenta higher than 3 GeV/c.

As far as muon identification is concerned, the main strategy is to extrapolate outward the tracks reconstructed in the CDC with the mass hypotheses of a pion and checking if, on the outermost KLM layer crossed by the predicted extrapolation, the actual measured hit can also be found. In this case, the extrapolation of the track restarts at the entry point in the first KLM layer, assuming a muon mass hypothesis. The likelihood for being a muon is then computed according to the comparison between the predicted and measured ranges and the goodness of the track fit, based on Kalman filtering fitting technique. For high-purity samples of muons (for example from the reactions  $e^+e^- \rightarrow \mu^+\mu^-(\gamma)$  and  $J/\psi \rightarrow \mu^+\mu^-$ ), it has been estimated that the barrel section of the KLM provides a  $\mu$ -reconstruction efficiency of 89% for particle momenta above 1 GeV/c.

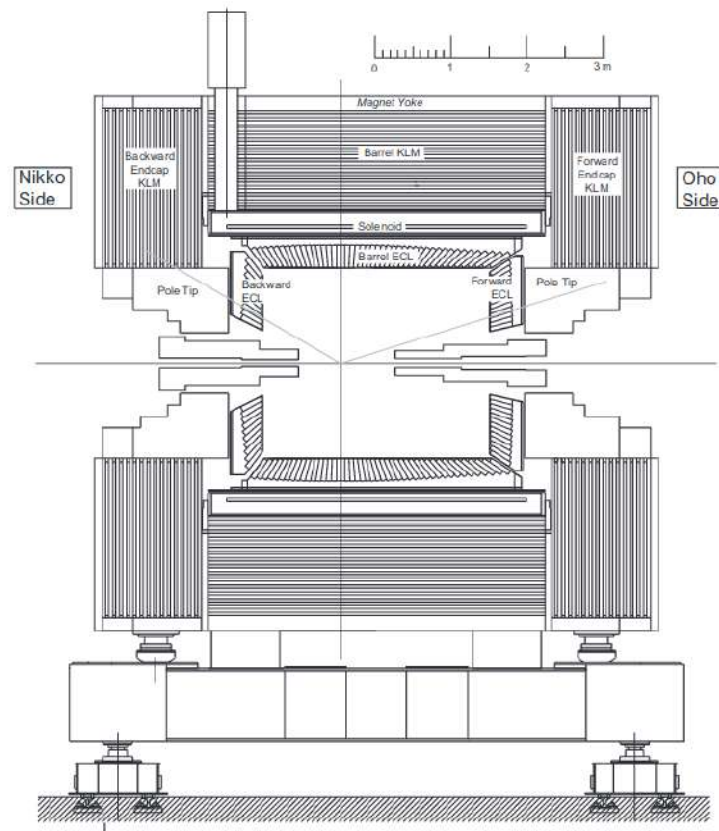


**Figure 3.7:** A schematic overview of the neutral kaon and muon detector at Belle II is given in the picture.

## 3.2 The trigger system at Belle II

The high luminosity upgrade will increase the total event rate to almost 20 kHz, requiring a robust and at the same time flexible trigger for discriminating the signal events from the background rates, which are expected 20-30 times larger than at KEKB. Considering the high charged track multiplicity in  $B\bar{B}$  event final states, an obvious trigger requirement is on the number of tracks in the event. However, there are physics processes, *e.g.*,  $\tau$  leptonic decays and dark matter searches, that have zero or two tracks only in their final state, which causes much more difficulties in signal and background discrimination. In addition, some low multiplicity processes have the same topology as the Bhabha scattering events, which have a huge cross section at  $\Upsilon(4S)$  CM energy ( $\sim 300$  nb) compared to the typical signal cross sections (1 nb). Therefore, when vetoing Bhabha events for reducing the total event rate, large part of the trigger efficiency on low multiplicity events is also lost. To preserve high efficiencies on the processes of interest, an effective trigger system is essential. Its implementation follows the same principle successfully adopted for Belle, but with totally new technologies able to support the increased event rates. The trigger system is composed of the Level 1 trigger (L1), implemented in hardware, and the software implementation of the High Level Trigger (HLT).

### The L1 Trigger

The L1 trigger system gathers many sub-trigger systems which provide information from various subdetectors, merged by the global reconstruction logic (GRL), whose output is sent to the global decision logic (GDL), responsible for issuing the trigger signal. In Belle II, all the trigger system components are based on the Field Programmable Gate Array (FPGA) technology, which makes the logic configurable rather than hard-wired. The first combination of detector information is performed by the GRL and it is mainly based on the drift chamber trigger and on the ECL trigger.

The CDC trigger finds and characterizes the tracks detected in the drift chamber. The 2D tracking basically follows the same implementation as Belle. The Belle II CDC detection improvement with the 3D tracking, which adds the information on the  $z$ -coordinate, allows to reject the most part of the background coming from Touschek intra-bunch scattering. In fact, these scattering events show a large displacement in their  $z$ -position with respect to the nominal interaction region. The maximum 5  $\mu$ s latency of the L1 trigger system requires a very fast  $z$ -vertex reconstruction, to be performed in no more than 1  $\mu$ s, which is achieved thanks to neural networks techniques.

The calorimeter trigger system adopts two complementary trigger schemes: a total energy trigger and an isolated cluster counting technique, the former being sensitive to events with high electromagnetic energy deposition, the latter to multi-hadronic physics events with low energy clusters and/or minimum ionizing particles. Moreover, the ECL trigger is able to recognize the back-to-back topology of Bhabha scattering with a high purity, which is fundamental for ensuring a high trigger efficiency of low multiplicity processes.

The single calorimeter cluster trigger, in association with at least one non-electron track in the opposite direction, is fundamental for the detection of radiative two-track processes, which include the background studies for the dark photon search and for the ALPs search as well. The trigger for non radiative dimuon events  $e^+e^- \rightarrow \mu^+\mu^-$  exploits instead the combination of two-track triggers based on one single detector sub-system (CDC), plus single high-energetic

track triggers provided by the KLM, for penetrating muons. Finally, a more efficient Bhabha veto, based on both polar and azimuthal angle information, largely improves the background suppression. The L1 trigger can sustain a maximum instantaneous rate of 30 kHz, however the goal is to keep the trigger rate as low as possible, while ensuring a high efficiency (larger than 99%) for physics targets, mainly hadronic events. The L1 output is then forwarded to the High Level Trigger for further background rejection based on fully reconstructed objects.

### The High Level Trigger

The HLT is a software trigger developed to improve the backgrounds suppression and relies on the *physics trigger*, whose main purpose is to reduce the load of data written on permanent storage at a maximum design output event rate of 10 kHz. Events preselected by using only the information provided by CDC and ECL triggers undergo the full offline reconstruction, involving all output from the subdetectors except the PXD. The physics trigger is then able to classify the event category ( $B\bar{B}$ ,  $e^+e^- \rightarrow \tau^+\tau^-$ , etc.) and once this has been assigned, the HLT processing results containing the event tag and the track parameter estimate are combined with the information from the PXD, which enables to calculate the Region of Interest (ROI). Only the pixels belonging to that region are readout and the selected PXD hits are used to complete the event reconstruction.

During Phase 2 the HLT was in pass-through and no software filter was applied to the triggered events, resulting in a very favorable condition to collect events with topologies interesting for dark sector searches, that may be suppressed by the HLT filtering necessary for the Phase 3 running at higher luminosity.

## 3.3 Overview of the *Belle II analysis software framework*

The upgrade of the detector has been crucial to maintain Belle II performances similar to, if not even better than, the ones achieved by Belle, despite the much higher background environment. Likewise, the development of a dedicated core software for online and offline data handling, with improved reconstruction algorithms is fundamental to pursue the goal. The core software of Belle II includes three main parts which are the specific *Belle II analysis software framework* (basf2) providing all the tools to perform physics analysis; the *externals*, consisting in third-party code on which basf2 depends; the *tools*, providing scripts for basf2 installation and configuration. More information about the core software and the details of the reconstruction algorithms implementation can be found in [75, 76], hereby only a general description of basf2 structure and purposes is provided.

### 3.3.1 The *basf2* code

A typical way to process data is building a chain of smaller processing blocks with very specific tasks, which go from reading the data to the full detector simulation. These small units are called modules and can be assembled in paths. Basf2 is a modular analysis framework whose flexibility relies on two ingredients, the modules to process the data and the data store to share the data between modules, as schematically represented in Figure 3.8.

The container where the modules live and perform their task is the path, which execute one at the time all the registered modules, in the order specified by the user through dedicated

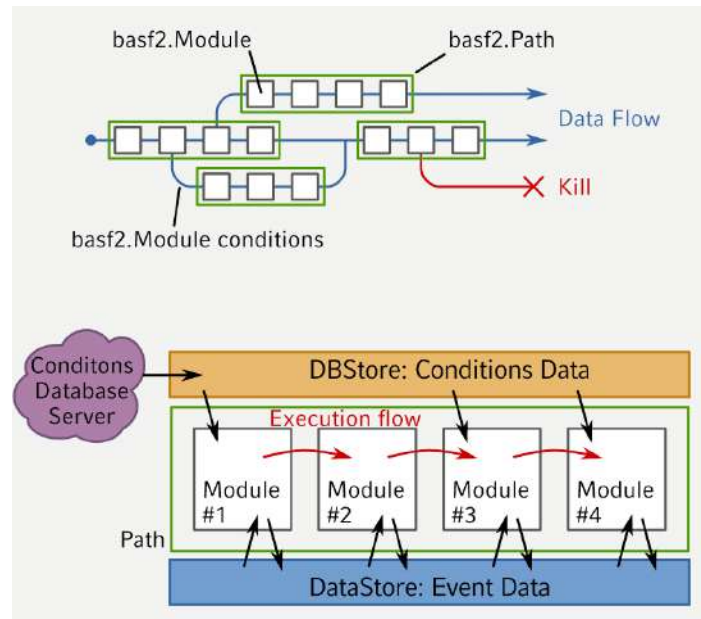


**Figure 3.8:** The data processing flow as handled by basf2 is represented in the scheme.

Python scripts. Data processing can be steered in a customized way by the user, thanks to the module parameters, which can tailor the module execution and be set at runtime through the python steering scripts.

As regards data either from Belle II detector or from the simulation, they are organized in a set of *runs* with variable duration, containing a sequence of independent *events*. Each event is defined as the set of measurements produced by an electron-positron collision or the passage of a cosmic ray. A set of runs sharing similar hardware state and operational features defines an *experiment*. Each single independent event is then identified in Belle II through three unsigned integers standing for the experiment, run and event numbers.

Basf2 modules can be written either in C++ or Python and are derived from the `Module` base class which defines five interface methods: `initialize()` called before the processing of the path; `beginRun()` called every time a sequence of events belonging to a new run starts, to properly initialize the run-dependent parameters, `event()` which is called for each processed event; `endRun()`, called at the end of the sequence of events which belong to the same run, to collect the run-summary information; `terminate()` called at the end of all events processing. The sequence of modules to be executed is provided by an instance of the `Path()` class, that can be called through the steering Python script providing a user-friendly interface to set the values of modules parameters and their execution sequence. During execution, modules are able to access and modify the data provided by the Data Store either as single object (`StoreObjPtr`) or as an array of objects (`StoreArray`), which also keeps track of the relationships between the various objects per each event.

### 3.3.2 Input/output: simulation and reconstruction in *basf2*

Object persistency is implemented using ROOT, which implies all objects stored in the Data Store need a ROOT dictionary. The `RootOutputModule` writes the Data Store content to a file with two `TTrees` with permanent and event durability, where each branch corresponds to a Data Store entry. The permanent-durability tree in each output file is the `FileMetaData`, containing the metadata related to the processed events, which are run, experiment and event numbers, as well as the steering file content. Similarly, ROOT files can be read by the `RootInputModule`.

No assumption is made for the event data model which can be very flexible in its dynamical implementation, determined by the modules execution and the creation of objects in the Data Store. The only mandatory object is the `EventMetaData`, which uniquely identifies an event given the event, run and experiment numbers and a production identifier to distinguish simulated events from real experimental data.

The *raw data* format to provide physical quantities from detector information like track hits or calorimeter clusters, is instead defined by each detector readout. Dedicated unpacker modules are responsible for the conversion of raw data to digit objects, as first step to build high-level objects such as charged tracks and ECL clusters. At that point the hit and cell information is discarded and the event size can be reduced by a factor of 40, which however is not the final result. High level-objects, like tracks, ECL and KLM clusters which are the final output of the reconstruction process are used to produce particle-level information, such as four momenta and event-shape variables, which compose a subset of data-objects needed for physics analyses and written in root files as mini data summary tables (`mDST`).

The tracks reconstruction relies on the information collected by the tracking devices of the Belle II detector (CDC, VXD), from which track parameters and their errors are extrapolated thanks to dedicated fits implemented in the *basf2* reconstruction modules and based on the Kalman filter fit technique [77], a track finding procedure which correctly takes into account effects of multiple scattering and the energy loss in the material. From reconstructed tracks, their associated momenta are measured, while clusters are reconstructed from adjacent over-threshold crystals in the ECL detector or from the number of hits and longitudinal penetration length in the KLM and can be associated to charged tracks or identified as neutral objects. Particle identification algorithms based on likelihood ratios are then applied to establish particle identities. The event reconstruction continues with the combination of stable particles to form a common vertex which indicates composite particle decays. Several techniques of vertexing are in place in the *basf2* packages and they allow to fit different types of decay chains, also dealing with neutrals. Finally, the particle lists are filled and available in the `mDST` files, where all the information for physics analyses is stored.

For what concerns data from Monte Carlo simulations, the digit objects are produced by the digitizer modules of each detectors from the energy deposition generated through GEANT4 [78] and stored in the common class framework of `SimHits`. This allow to easily add the hits from energy deposition produced by the simulated machine-induced background on those coming from the simulated physics signal process, which is defined as *background mixing*. After digitization, the simulated digits follow the same reduction path to higher-level objects described for real data from the Belle II detector and at the end of the analysis chain they are also written as `mDST` objects in rootfiles.

### 3.3.3 Condition Data

The information about the specific running conditions during data acquisition are also fundamental to be stored, in order to properly calibrate the data recorded by the detector when performing physics analysis. Condition data are saved in the Belle II Conditions Database as a sequence of payloads reproducing the time evolution of the conditions changing during the experiment (but not on a per-event base) thanks to an associated *Interval of Validity (IoV)*, uniquely identified by the run and experiment numbers. A collection of payloads with their associated IoVs specifying when they are valid is called a *Global Tag (GT)*. The Condition Database design was determined by the main goal of easy and scalable maintainability and therefore based on the standard industry software tools. Its implementation won't be discussed in this work and further details can be found in the reference [79].

Finally, a `release-XX-YY-ZZ` of the basf2 software is a snapshot of basf2 as frozen at a specific time and unchangeable anymore in its reconstruction and simulation algorithms and calibrations. Several releases have been produced to reprocess experimental data and produce new Monte Carlo samples with new features, including modifications of the software in the online fabrication system, and better calibrations. Each data reprocessing is called `prodX` and to analyze a specific reprocessing of the experimental data set the proper release version and global tag must be used, to grant the highest performance, efficiency and repeatability of the analysis results.

## 3.4 Data sets

For this work two types of data sets have been exploited: the 11<sup>th</sup> campaign of the official Monte Carlo (MC) production MC11 for the simulated samples and the sixth reprocessing of Phase 2 data `prod6` for the experimental data set.

The MC samples are exploited to optimize the event selection and background rejection, to compute the signal efficiency and study the signal shape and resolution, and finally to tune the upper limit calculation strategy with different statistical approaches.

The experimental data set is used to provide the physics results from this search, as well as for all the validation and performance studies needed to evaluate the systematic uncertainties.

### 3.4.1 Monte Carlo samples

Monte Carlo simulation uses event generators, which consist of several packages in the basf2 framework that according to theoretical models of particle interactions produce sets of four-vectors describing the final state of  $e^+e^-$  collisions. A particle identity is associated by the generators to each four-vector. A combination of both background and signal generators is required to properly mimic the event stream of real data.

### Background simulation

The production of leptonic event from  $e^+e^-$  collisions is handled by several generators whose detailed description can be found elsewhere [76]. The muon and  $\tau$  pair productions are generated with the KKMC [80] package and the  $\tau$  decays simulation is then handled by TAUOLA [81], while QED background processes like  $e^+e^- \rightarrow e^+e^-(\gamma)$  are simulated using BabaYaga@NLO [82]

and four-lepton final states exploit instead AAFH [83]. Finally, radiative decays to two-pion final states  $e^+e^- \rightarrow \pi^+\pi^-(\gamma)$  have been simulated by using the package PHOKHARA [84]. The generators to produce each background sample used in the analysis are referenced in the last column of Table 3.1. The propagation of particles in the detector and the physics processes of the interactions between the particles and the detector materials are finally handled by the GEANT4 software package [78], through the specific physics lists recommended by the GEANT4 group for high energy physics experiments and embedded in basf2.

The official MC11 samples which have been used for background studies are listed in Table 3.1. They have been simulated using the Phase 2 geometry and adding the officially produced beam background samples. In order to compare the MC results to the experimental data, the generated samples have been always normalized to the effective integrated luminosity  $\int Ldt_{\text{good runs}}$  reported in Table 3.2 and corrected for the trigger efficiency, according to the weights:

$$w_i = \frac{\int \mathcal{L}dt_{\text{goodruns}} \cdot \epsilon_{\text{trg}}}{\int \mathcal{L}dt_{\text{gen},i}} \quad (3.2)$$

where the index  $i$  stands for each generated process and  $\epsilon_{\text{trg}}$  correspond to the measured efficiency for a given trigger line. Additional background contamination due to continuum hadronization events from  $e^+e^- \rightarrow q\bar{q}$  processes have been checked to give a negligible contribution already at the event reconstruction level. Further discussion on a specific veto devised for hadronic interaction suppression is reported in Section 4.3.

**Table 3.1:** Phase 2 MC11 samples used for background studies with the number of generated events  $N_{\text{evts}}$  and the equivalent integrated luminosity  $\int Ldt$ .

Process	$N_{\text{evts}}$ [ $10^6$ ]	$\int Ldt$ [ $\text{fb}^{-1}$ ]	Reference
$e^+e^- \rightarrow \mu^+\mu^-(\gamma)$	65	56.621	KKMC [80]
$e^+e^- \rightarrow \tau^+\tau^-(\gamma)$	36.8	40.044	KKMC
$e^+e^- \rightarrow e^+e^-\mu^+\mu^-$	140	7.406	AAFH [83]
$e^+e^- \rightarrow \pi^+\pi^-(\gamma)$	210	1372.539	PHOKHARA [84]
$e^+e^- \rightarrow e^+e^-(\gamma)$	60	0.198	BabaYaga@NLO [82]
$e^+e^- \rightarrow e^+e^-e^+e^-$	260.6	6.562	AAFH [83]

### Signal simulation

The Monte Carlo samples for the signal simulation does not belong to the same official MC11 production campaign from which the background samples have been taken and have been self-produced due to technical difficulties in the integration of the external packages for the MadGraph 5 generator [85] and basf2 [75]. The Phase 2 geometry and beam background have been added to the simulation of the signal process  $e^+e^- \rightarrow \mu^+\mu^-Z'$ ,  $Z' \rightarrow \text{invisible}$  by exploiting the `release-02-00-01` basf2 release and with the MadGraph 5 generator [85], according to the model described in Section 1.6. In total, 18 signal MC samples of 20000 events each have been generated, for  $Z'$  boson masses from  $0.5 \text{ GeV}/c^2$  up to  $9 \text{ GeV}/c^2$ , with a mass step size of  $0.5 \text{ GeV}/c^2$ .

### 3.4.2 Experimental data set

All the results based on real data are derived from the analysis of the mDST files from `prod6` reprocessing of Phase 2 runs 0 – 5613, which correspond to an integrated luminosity of  $\int Ldt = 496.7 \text{ pb}^{-1}$  measured with Bhabha events,  $\int Ldt = 493.1 \text{ pb}^{-1}$  with  $\gamma\gamma$  events.

Only data which fire the CDC two-track trigger for the standard  $Z'$  and the ECL trigger for LFV  $Z'$  respectively, are used in this work. Due to the trigger configurations and data quality selections used for the analysis optimization, the effective integrated luminosity of the data is then reduced to  $276 \text{ pb}^{-1}$ , with an average trigger efficiency of  $\epsilon_{CDC(ECL)} = 79(96)\%$  for the standard (LFV)  $Z'$ . Further details about trigger efficiencies are discussed in Section. 7.2. In Table 3.2, a summary of the information about the experimental data set is provided.

The software release version used for the this analysis is the release-02-01-00 of `basf2` and the applied condition data are those provided by the `data_reprocessing_prod6` global tag.

**Table 3.2:** Sixth Phase 2 reprocessing, `prod6`, used for producing all the physics results of this work, with the measured integrated luminosities (uncertainties are statistical only [86]) and trigger efficiencies. In the last column, in bracket also the measured efficiency for the trigger line used for the LFV  $Z'$  search (Section 1.6.1) is given.

Reprocessing	$\int Ldt$ [ $\text{pb}^{-1}$ ]	$\int Ldt_{\text{good runs}}$ [ $\text{pb}^{-1}$ ]	Trigger efficiency $\epsilon_{CDC} (\epsilon_{ECL})$
<code>prod6</code>	$496.7 \pm 0.3$ (Bhabha) $493.1 \pm 0.7$ ( $\gamma\gamma$ )	276	0.79 (0.96)

### 3.4.3 Belle II detector during Phase 2

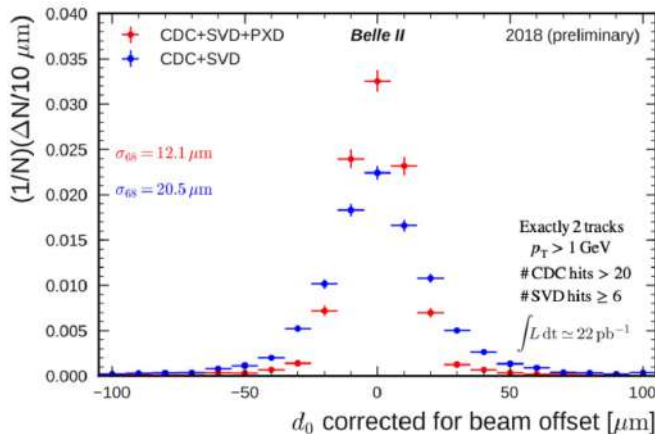


**Figure 3.9:** The distribution of the transverse impact parameter  $d_0$  using Belle II 2018 data is shown here with two different selection: in blue without any specific requirement on the number of PXD hits per track, in red selecting only tracks with at least one PXD hit, which shows the improved resolution ( $\sim 12 \mu\text{m}$ ) achievable thanks to the PXD accuracy.

An important feature of the Phase 2 pilot run which has a direct impact on the data analyzed for this work was the malfunctioning of the kaon and muon detector (KLM), which due to technical problems was turned off for most of the time. Consequently, the standard particle identification variables for muons which exploit the information provided by this sub-detector were not reliably applicable to Phase 2 data and the muon identification has been based on calorimeter information, as it will be explained in detail in Section 4.3 in the analysis description chapter. This resulted in a higher misidentification rate for pions wrongly identified as muons and therefore contaminating the Phase 2 muon sample. Moreover, firmware and hardware-related issues compromised the performances of the CDC two-track trigger, reducing the average plateau efficiency and the usable runs, as it will be discussed in more details in Section 7.2. Also, it has to be noticed that the absence of the VXD during Phase 2 affected the tracking efficiency and resolution performance: the expected improvement with the full vertex detector installed will be also addressed as final prospect of this work in Chapter 8. However, preliminary results on VXD performances have been studied on Phase 2 data and the achievable resolutions are shown in Figure 3.9.

The muon detection for Belle II 2018 data has been sub-optimal, due to the above mentioned issues, for which a deep investigation has been devised during this thesis work to understand the main feature of such a data set and correct accordingly the results from the simulation. Nonetheless, this is expected to be cured in 2019 data thanks to the overall detector and performance improvement.



# Chapter 4

## Analysis overview and event selection

This chapter starts with a brief overview of the analysis strategy, its goal and the search technique, and continues with the description of the candidate reconstruction (Section 4.2), the event selection (Section 4.3) and the background suppression strategy (Section 4.4), providing the number of surviving background events and the measured signal efficiencies. The binning scheme of the recoil mass spectrum, crucial for the selection optimization and the bin by bin evaluation of the expected background yields is also discussed in this chapter, and the specific format developed for real data analysis is provided.

### 4.1 Analysis Strategy

The goal of this work is to search for an invisible  $Z'$  boson by looking for bumps in the mass distribution of the system recoiling against two muons for the standard  $Z'$ , or an electron-muon pair for the LFV  $Z'$ , where an excess in data peaking at the mass of the new boson represents the signal signature for these searches. The analyzed channels are reported below:

$$e^+e^- \rightarrow \mu^+\mu^-Z', \quad Z' \rightarrow \textit{invisible} \quad (4.1)$$

$$e^+e^- \rightarrow e^\pm\mu^\mp Z', \quad Z' \rightarrow \textit{invisible}. \quad (4.2)$$

For the LFV  $Z'$ , a model-independent search on the expected background rate for the analyzed channel is provided, being the quantity constrained by this study the product of the cross section times the efficiency ( $\sigma \times \epsilon$ ), since no robust signal simulation is at the moment available, as explained in the first chapter. For the standard  $Z'$ , assuming the  $L_\mu - L_\tau$  model as discussed in Section 1.6, the predicted cross section for the signal process is quadratic in the coupling constant  $g'$  and decreases at higher  $Z'$  masses, vanishing when approaching the CM energy. The simulated signal cross section as a function of the  $Z'$  mass  $M_{Z'}$ , assuming a coupling constant of  $g' = 0.01$ , is shown in Figure 4.1. At an integrated luminosity of about  $0.5 \text{ fb}^{-1}$ , the total number of expected signal events for  $g' = 0.01$  and  $M_{Z'} = 1 \text{ GeV}/c^2$ , assuming a branching fraction  $BF(Z' \rightarrow \textit{invisible}) = 1$ , is

$$N = \sigma L \sim 11 \cdot 0.5 \sim 6,$$

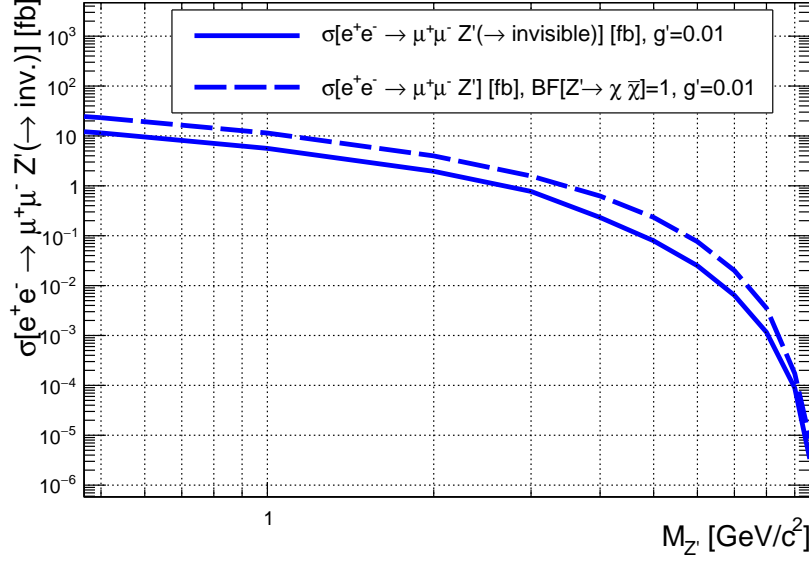


**Figure 4.1:** Numerical cross sections for  $e^+e^- \rightarrow \mu^+\mu^- Z'(\rightarrow \text{invisible})$  obtained with MadGraph 5. The solid line assumes the  $L_\mu - L_\tau$  predicted rates for  $Z' \rightarrow \text{invisible}$  while the dashed line assumes  $BF(Z' \rightarrow \text{invisible}) = 1$ . For  $Z'$  masses approaching the CM energy  $\sqrt{s}$ , the cross section vanishes, limiting the sensitivity to the parameter space region for  $M_{Z'} > 8 \text{ GeV}/c^2$ .

while it increases to 600 for  $g' = 0.1$  at the same mass, given the quadratic dependence on the coupling constant. The impact of the event selection and the background suppression procedure on the signal yield will be analyzed in the this chapter. The expected backgrounds mainly come from SM processes producing final states with two muons and missing energy that can mimic the signal signature, namely  $e^+e^- \rightarrow \mu^+\mu^-(\gamma)$  with one or more photons lost due to inefficiency of the detection or acceptance constraints;  $e^+e^- \rightarrow \tau^+\tau^-(\gamma)$  events involving missing energy because of the undetected neutrinos, with  $\tau \rightarrow \mu$  or  $\tau \rightarrow \pi$ , where the latter involves sub-optimal particle identification (PID);  $e^+e^- \rightarrow e^+e^-\mu^+\mu^-$ , which are two photon processes where the electrons and positrons usually are out of acceptance escaping along the beampipe.

Events are thus selected by requiring two charged tracks identified as muons and no reconstructed photons above a minimum energy in the direction opposite to the dimuon momentum. This veto is an example of the Rest Of Event selection procedure which is required for this analysis. Any other detected clusters or tracks that are not used for the dimuon (electron-muon) candidate reconstruction belong to the Rest Of Event (ROE), to which also the recoil momentum belongs. Since the goal of this analysis is to reveal a boson decaying to invisible, it is crucial to have a good control of the ROE, where no known physical object is left. Once it has been cleaned from the beam background contamination that do not come from the primary collision, the ROE has to contain nothing that could be responsible for the detection of a non-null recoil and could be ascribed to known SM signature. Furthermore, the transverse momentum of the dimuon system is required to be above some threshold which depends on the recoil mass, as this selection is very effective against  $\mu^+\mu^-(\gamma)$  and  $e^+e^-\mu^+\mu^-$  backgrounds. An additional selection (described in Section 4.4) is then applied to further

suppress the  $\tau^+\tau^-(\gamma)$  background, which is the dominant contamination for this search. Signal efficiency and background rejection are evaluated from simulations as a function of the recoil mass. The estimate of the surviving background is validated with an extensive use of signal-free control samples, from which correction factors are measured to compensate the observed discrepancy between experimental data and simulations and the associated systematic effects to both the expected number of background events and the signal efficiency are evaluated. The recoil mass distribution in real data which is expected to contain the signal has been kept hidden through all the analysis optimization procedure in order not to introduce any bias, according to the *blind analysis* principle. Care must be taken to avoid unintentional unblinding for instance by applying control sample selections with high efficiency for the signal. In all the data validation studies, as discussed in Chapter 6, it has always been verified that the various procedures would not accidentally reveal the signal mass distribution in real data. Finally, through a statistical analysis of the number of selected events, the 90% CL upper limit to the  $Z'$  cross section is computed by applying a Poisson counting experiment technique for each bin of the recoil mass distribution (Section 8.1).

For what concerns the LFV  $Z'$ , the same considerations hold with the obvious change of the particle identification requirements when identifying two tracks, one of which has to be identified as a muon and the second as an opposite-sign charge electron. Due to the lack of a robust signal generator and with the aim to provide a model-independent limit, except for the above mentioned changes on PID requirements, the same selections as in the standard  $Z'$  case are applied and 90% CL upper limit is interpreted in terms of the cross section times the efficiency  $\sigma \times \epsilon$ .

## 4.2 Candidate Reconstruction

The event is reconstructed by requiring two opposite charge tracks coming from the Interaction Point (IP), satisfying the following criteria which define the *CleanedTracks* selection:

- the signed distance  $d_r$  of the perigee<sup>1</sup> of the track helix from the origin, in the transverse plane  $r/\phi$ , should satisfy  $|d_r| < 0.5$  cm;
- the longitudinal signed distance  $d_z$  of the perigee from the origin should be  $|d_z| < 2$  cm;
- the selected track must have at least one hit in the CDC.

The muon identification is performed by applying a loose selection based on calorimetric information provided by ECL variables:

- the energy deposit of the detected cluster must be below a certain threshold, since muon are not expected to loose much energy due to electromagnetic shower,  $\text{clusterE} < 0.75$  GeV
- consequently, also the ratio of the energy deposit and the muon momentum in the laboratory frame must be below 0.5,  $\text{clusterE}/p < 0.5$

---

<sup>1</sup>A track propagating in vacuum in a constant magnetic field moves along a helix described by five parameters defined at a point  $\vec{P}$  of the trajectory, which in Belle II is identified with the perigee, the point of closest approach (POCA) to the origin in the  $r/\phi$  plane

The selected tracks are combined to form a dimuon candidate and the recoil momentum against the dimuon candidate with respect to the center of mass (CM) momentum is computed, being the  $Z'$  candidate for that event. The Rest Of Event (ROE) is built, which is defined by all the physics objects and reconstructed particles belonging to the Data Store for the processed event and not used for the specific decay reconstruction, meaning in this case all charged tracks in the event which do not combine into a dimuon candidate; ECL and KLM clusters not associated with the two selected tracks. A selection on the reconstructed ECL clusters in the event to clean up the ROE from the beam background photons, which are not coming from physics processes and should not be taken into account for event rejection, has been also applied, based on some standard requirements on cluster shape hypothesis [87], angular acceptance, error on the cluster timing and minimum energy deposit per cluster to be larger than 100 MeV. Furthermore, for the vetoing procedure, only tracks in the ROE with at least one hit in the CDC (*cdcTracks* selection) are considered. As last step, for each reconstructed  $Z'$  candidate the kinematic information of the photon closest to the recoil momentum, including the opening angle with respect to the  $Z'$  candidate momentum, polar angle and energy in both the laboratory and CM frames, the kinematic information of the most energetic photon and the information of the most probable  $\pi^0$  candidate reconstructed in the event ( see next Section 4.3 for details) is stored, to allow further background rejection implemented as veto on certain events.

### LFV $Z'$ to invisible

For the LFV  $Z'$  search the same event reconstruction is applied as far as the *CleanedTracks* selection is concerned. For the particle identification, the dimuon candidate must be replaced by an electron-muon candidate, therefore one track is required to be identified as a muon, as in the standard  $Z'$  case, and a second good <sup>2</sup> track to be identified as an electron according to the following ECL-based selection:

1.  $\text{clusterE} > 1 \text{ GeV}$
2.  $0.7 < \text{clusterE}/p < 1.3$

Then the electron-muon candidate is obtained by combining the electron and muon tracks (with opposite charge) and the reconstruction flow continues exactly as for the standard  $Z'$  case, with the ROE and the recoil reconstruction.

In both cases, the produced *ntuples* undergo the event selection as described in the next section.

## 4.3 Event Selection

To further reject the background contamination, a tighter selection is applied to each reconstructed candidate, which has to satisfy the following criteria:

1. the number of *CleanedTracks* must be exactly two and the opening angle between the two muon candidates in the transverse plane must exceed  $90^\circ$ , in order to emulate the

---

<sup>2</sup>In this work a track is defined good if it satisfies the requirements which define the *CleanedTracks* selection.

functionality of the CDC two-track trigger which will be described in more details in Section 7.2. Its logical implementation (`ffo`, trigger bit 7 of the Phase 2 trigger lines) which requires two 2D-tracks with an opening angle larger than  $90^\circ$  is not simulated in the MC samples and therefore these additional selection requirements have to be satisfied to correctly reproduce the data. Furthermore, the same opening angle is required to be less than  $172^\circ$ , in order to follow the prescriptions provided by the performance study on Phase 2 data for the trigger efficiency estimate [88], for which the systematic effects are evaluated;

2. the polar angle of the muon tracks must be within a restricted barrel ECL angular acceptance,  $37^\circ < \theta_\mu < 120^\circ$ , for a good cluster-matching efficiency and a reliable control of the systematic uncertainties;
3. the recoil momentum must point to the barrel ECL acceptance region,  $33^\circ < \theta_{\text{rec}} < 128^\circ$ , to grant a better hermeticity and exclude inefficient regions where photons can pass undetected and mimic the signal recoil. This selection is applied only for recoil masses below  $3 \text{ GeV}/c^2$ , as for larger masses the photon hypothesis is very unlikely; possible distortions in the recoil mass spectrum induced by this selection have been checked and found to be negligible;
4. a tighter ECL-based muon selection,  $0.15 < \text{clusterE} < 0.4 \text{ GeV}$  and  $\text{clusterE}/p < 0.4$ ;
5. all events with the closest reconstructed photon within a  $15^\circ$  cone from the recoil momentum are discarded;
6. the ROE, after cleaning up from beam induced background hits and energy depositions, must not contain any physical objects as follows:
  - (a) it must have no additional tracks with hits in the CDC ( $N_{\text{cdcTracks}} = 0$ ); only very poor quality tracks not coming from the IP and not detected by the CDC are tolerated, since they are mainly remnants of beam-induced backgrounds not associated to any physics event;
  - (b) as most of the physical background comes from  $\tau$  pair production and  $\pi^0$  are among the most common  $\tau$  decay products, a  $\pi^0$  veto has been devised. All the photons in the ROE which pass the beam-background rejection are used to reconstruct the decay  $\pi^0 \rightarrow \gamma \gamma$ , requiring in addition that the invariant mass of the two photon system is below 200 MeV. Only one  $\pi^0$  candidate per event is selected, by choosing the one with the invariant mass closest to the nominal  $\pi^0$  mass. The event is then discarded if the following conditions are both satisfied: the mass of the candidate is in the range  $125 < M_{\pi^0} < 145 \text{ MeV}/c^2$  and the remaining energy detected in the ROE exceeds 0.20 GeV (see Figure 4.2);
  - (c) the extra energy in the ECL, which is the energy deposit not associated to any particles in the cleaned ROE, is required to be below 0.4 GeV.
7. the transverse momentum of the dimuon candidate in the LAB frame satisfies  $p_{\mu\mu}^T > p_{\text{cut}}^T$ , where  $p_{\text{cut}}^T$  is a linearly decreasing function of the recoil mass and its value is 1.03 GeV/c at a recoil mass of  $0.5 \text{ GeV}/c^2$  and 0.43 GeV/c at a recoil mass of  $9 \text{ GeV}/c^2$ . This requirement is efficient in removing the dominating background at very low recoil mass

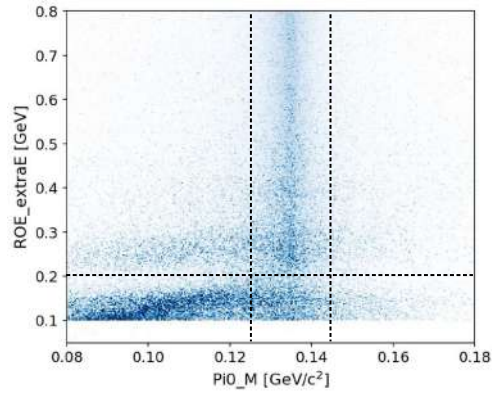


**Figure 4.2:** Extra Energy in the ROE as a function of the reconstructed  $\pi^0$  candidate mass for simulated background events. The veto region is highlighted in black dashed lines. The structure observed at an extra energy in the ROE of around 0.25 GeV is a result of the selection requirement  $E_\gamma > 100$  MeV on the photons used to reconstruct the  $\pi^0$  candidate.

coming from radiative dimuon events  $e^+e^- \rightarrow \mu^+\mu^-\gamma$ , anyway in most events is superseded by tighter selections based again on the momentum of the dimuon candidate and described in the next Section 4.4, which are also effective against the  $e^+e^- \rightarrow \tau^+\tau^-(\gamma)$ .

At this point of the analysis, the main background contributions still come from the three SM processes  $e^+e^- \rightarrow \mu^+\mu^-(\gamma)$ ,  $e^+e^- \rightarrow \tau^+\tau^-(\gamma)$ ,  $e^+e^- \rightarrow \mu^+\mu^-e^+e^-$ , which can mimic the signal if the photon is not detected and, in the case of the four lepton final state, if the electron-positron pair escapes the detector acceptance. The simulated backgrounds affect differently the recoil mass spectrum: the  $e^+e^- \rightarrow \mu^+\mu^-(\gamma)$  events are more relevant in the low recoil mass range  $M_{Z'} < 2$  GeV/ $c^2$ , while the process  $e^+e^- \rightarrow \tau^+\tau^-(\gamma)$  dominates most of the phase space available, especially the central region  $2 < M_{Z'} < 7$  GeV/ $c^2$ , and, finally, the main contamination at higher recoil masses  $M_{Z'} > 7$  GeV/ $c^2$  is due to  $e^+e^- \rightarrow \mu^+\mu^-e^+e^-$  decays. The other sources of background are found to be negligible. The number of background

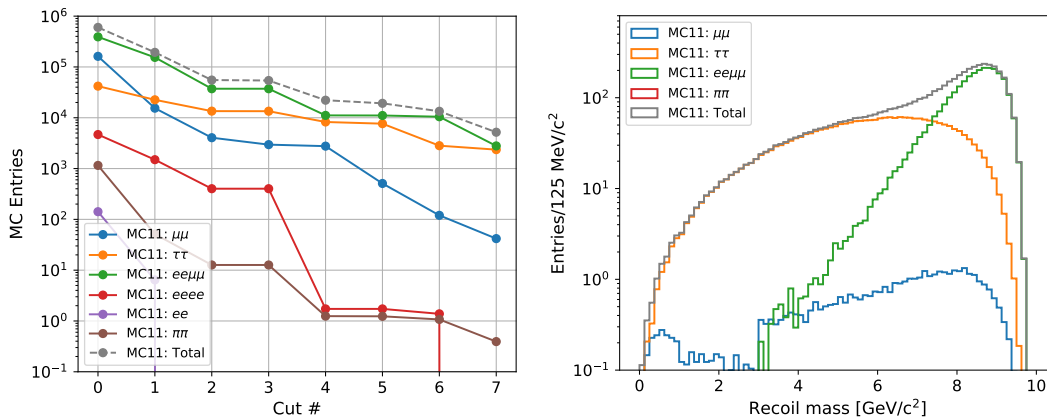


**Figure 4.3:** Surviving background events as a function of the selection steps (left) and the recoil mass distribution (right) for background simulations. The background yields have been normalized to an integrated luminosity of  $276 \text{ pb}^{-1}$  and scaled by the trigger efficiency factor 0.79.

events after every selection step listed above and the background spectrum achieved after the candidate reconstruction and the event selection, as a function of the recoil mass, are shown in Figure 4.3 (legend in the plots uses a notation for dilepton events without ( $\gamma$ ) in the final state, but radiative contribution are also considered, as listed in the text). All the backgrounds are normalized to an integrated luminosity of  $276 \text{ pb}^{-1}$  and scaled by a trigger efficiency of 0.79 (estimated as discussed in Section 7.2), not simulated in the Monte Carlo. The signal efficiencies for each generated  $Z'$  mass hypothesis corresponding to every analysis step listed before are shown in Figure 4.4; they have been computed as the ratio between the selected and the generated events and finally have been also scaled by the 0.79 trigger efficiency factor which is not implemented in the Monte Carlo simulation.

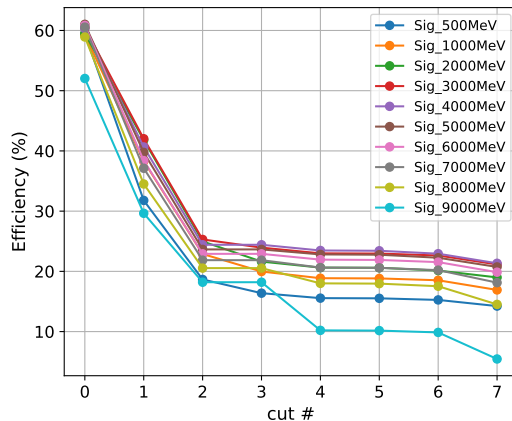


**Figure 4.4:** Signal efficiencies for different simulated  $Z'$  masses as a function of the selection step.

## 4.4 Background Rejection: $\tau$ suppression and analysis optimization

To suppress the  $\tau$  pair background, several discriminating variables have been studied at the various recoil masses. The first step for the optimization of the background rejection has been to define the signal regions where to count the surviving events and the signal efficiency. To this purpose, recoil mass windows are computed for each  $Z'$  generated mass, centered at the simulated nominal mass and with a width, defined in term of multiples of the recoil mass resolution  $\sigma$ , such that it maximizes the Punzi Figure of Merit  $\text{FOM}_{\text{Punzi}}$  [89] over all the spectrum at the end of the analysis procedure. The optimal value turns out to be a width of  $\pm 2\sigma$ , as shown in Figure 4.5 (see also Figure 4.12). Recoil mass resolutions are computed according to the results from the signal shape study on MC samples described in the next Chapter 5. Mass window widths vary from  $1150 \text{ MeV}/c^2$  at  $M_{Z'} = 0.5 \text{ GeV}/c^2$  to  $53 \text{ MeV}/c^2$  at  $M_{Z'} = 7 \text{ GeV}/c^2$ , due to the different recoil mass resolution. Only events within the mass windows are considered and the signal inefficiency due to the mass window definition (signal events outside the window) is mostly caused by the Initial State Radiation (ISR) tail, however the partial signal loss has been found not to affect the analysis optimization procedure.

The guiding principle in discriminating signal from background is that the  $Z'$  production is a Final State Radiation (FSR) process from a muon leg, while the invisible missing momentum

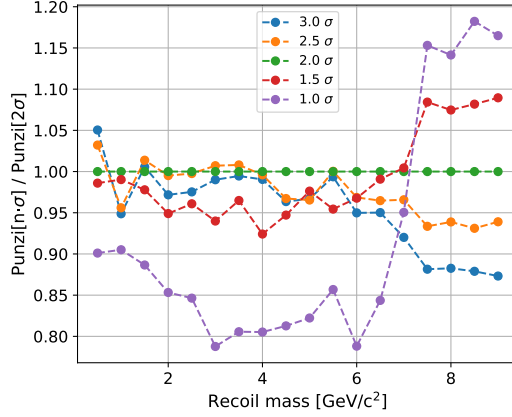


**Figure 4.5:** Ratio of the Punzi FOM at the end of the analysis computed for different recoil mass window widths in units of recoil mass resolutions  $\sigma$ . All curves are normalized with respect to that computed for a mass window of  $\pm 2\sigma$  ( reported in Figure 4.12).

in  $\tau$  pair events, which can mimic the presence of a  $Z'$ , comes from neutrinos from  $\tau$  decays on both legs. Therefore the idea is to exploit kinematic variables that can quantify this different level of asymmetry in the event topology. Hereafter, the longitudinal direction corresponds to the  $z$  axis, which is defined along the bisector of the angle between the direction of the electron beam and the reversed direction of the positron beam, while the transverse direction is the projection onto the plane perpendicular to the  $z$  axis. All the following variables have been computed in the CM frame: the longitudinal and transverse recoil momentum (which coincides with the  $Z'$  momentum in the signal case) projected onto the directions of the maximum and minimum lepton momenta  $p_{rec}^{l,lmax}$ ,  $p_{rec}^{T,lmax}$ ,  $p_{rec}^{l,lmin}$ ,  $p_{rec}^{T,lmin}$ , respectively; opening angles between the recoil momentum and directions of the maximum and minimum momentum of the selected leptons; longitudinal and transverse components of the momenta of the two lepton candidates with respect to the recoil momentum direction; asymmetry of the modulo of the momenta of the two leptons; modulus of the sum of the two lepton momenta; transverse momentum of the dilepton candidate  $p_{\mu\mu(e\mu)}^T$ .

A Multivariate Analysis (MVA) software package (`scikit-learn` Python library [90]) available in the `basf2` framework is used with the only goal to rank the variables in order of discriminating power. The final choice is based on discriminating power criteria and the simplicity of the selection implementation in terms of linear cuts. In fact, at the very beginning of the data taking of an almost newborn experiment, the use of more performing MVA algorithms based on high-level variable is avoided. The goal is to allow a more straightforward evaluation of systematic uncertainties and detector effects affecting the physics results and produced by the difference in the shape of the variable distributions exploited in the analysis between Monte Carlo and actual data. With these purposes in mind, the chosen variables are the transverse recoil momentum with respect to the directions of the minimum and maximum lepton momenta  $p_{rec}^{T,lmax}$ ,  $p_{rec}^{T,lmin}$  and the transverse momentum of the dilepton pair  $p_{\mu\mu(e\mu)}^T$ .

Bidimensional distributions of  $p_{rec}^{T,lmax}$  versus  $p_{rec}^{T,lmin}$  and distributions of  $p_{\mu\mu}^T$  for the events in the mass windows corresponding to three different generated samples,  $M_{Z'} = 2, 5, 7$  GeV/ $c^2$  respectively, are shown in Figure 4.6, 4.7, 4.8 for both signal and background MC samples.

An optimal separating line defined by two parameters, its slope  $m$  and the intercept  $q$ , in the  $p_{rec}^{T,max} - p_{rec}^{T,min}$  plane and an optimal selection threshold on the  $p_{\mu\mu}^T$  distribution are searched by independently varying the three parameters (the slope  $m(M_{Z'})$ , the intercept  $q(M_{Z'})$  and the  $p_{\mu\mu}^T(M_{Z'})$  threshold) which define the selection requirements. For each variable, a one-dimensional binning has been used and values have been simultaneously varied in nested loops to find numerically the maximum of the  $FOM_{Punzi}$ . The ensemble of variable values that maximize the  $FOM_{Punzi}$  thus define the optimal selections. The Punzi figure of merit has the

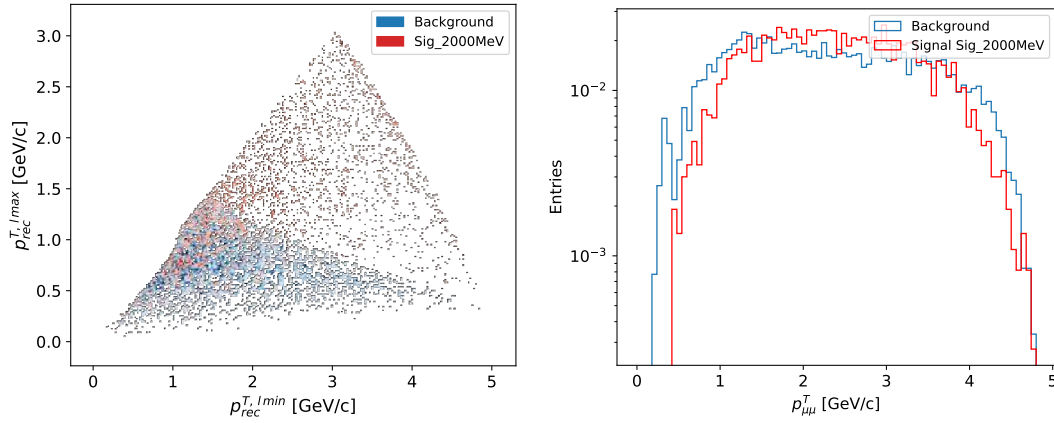


**Figure 4.6:** The  $p_{rec}^{T,max}$  Vs.  $p_{rec}^{T,min}$  (left) and  $p_{\mu\mu}^T$  (right) distributions of the simulated events for the signal (red) and background MC samples in the mass window corresponding to a generated  $Z'$  mass  $M_{Z'}=2$   $\text{GeV}/c^2$ .

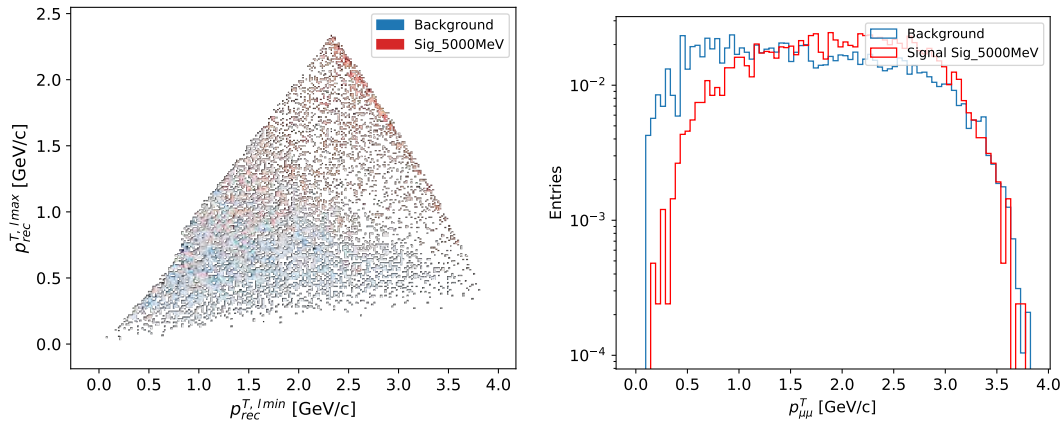


**Figure 4.7:** The  $p_{rec}^{T,max}$  Vs.  $p_{rec}^{T,min}$  (left) and  $p_{\mu\mu}^T$  (right) distributions of the simulated events for the signal (red) and background (blue) MC samples in the mass window corresponding to a generated  $Z'$  mass  $M_{Z'}=5$   $\text{GeV}/c^2$ .

important advantage to be independent from the unknown signal cross section on which the limit has to be measured and optimize the exclusion region in the parameter space of  $(g', M_{Z'})$  to be constrained. The  $FOM_{Punzi}$  allows to easily handle two fundamental ingredients of a search, maximizing the significance and simultaneously ensuring the minimum coverage for a

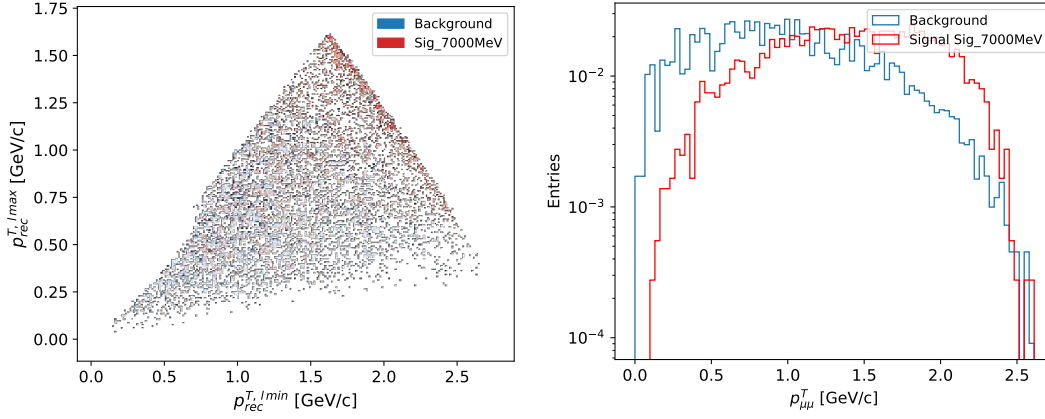


**Figure 4.8:** The  $p_{rec}^{T,max}$  Vs.  $p_{rec}^{T,min}$  (left) and  $p_{\mu\mu}^T$  (right) distributions of the simulated events for the signal (red) and background (blue) MC samples in the mass window corresponding to a generated  $Z'$  mass  $M_{Z'}=7$   $\text{GeV}/c^2$ .

given confidence level (CL):

$$\text{FOM}_{\text{Punzi}} = \frac{\epsilon(t)}{a/2 + \sqrt{B(t)}} . \quad (4.3)$$

In the above definition,  $a$  is the desired CL in units of sigmas corresponding to the one-sided Gaussian test for a given significance,  $t$  is set of observables which defines the selection, and  $\epsilon(t)$ ,  $B(t)$  are respectively the signal efficiency and the number of remaining background events as a function of the applied selection  $t$ . A 90% CL is chosen ( $a = 1.64$ ) to compare to the *BABAR* search. Figure 4.9 shows, for the 2, 5 and 7  $\text{GeV}/c^2$  mass samples, the

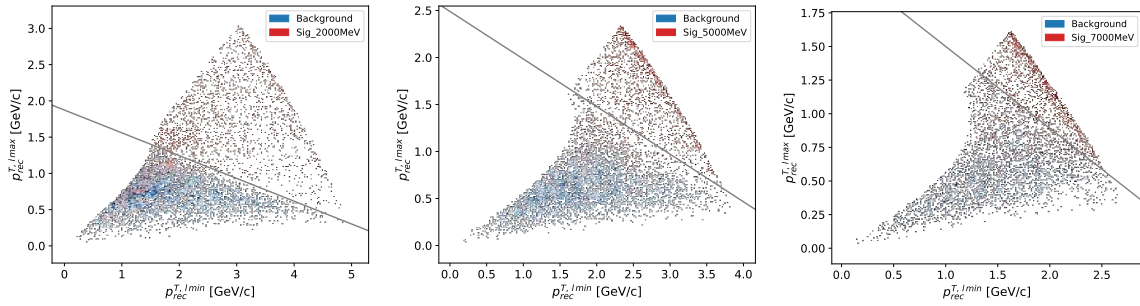


**Figure 4.9:** The scatter plot of  $p_{rec}^{T,max}$  versus  $p_{rec}^{T,min}$  distributions after the optimal  $p_{\mu\mu}^T$  selection for  $M_{Z'} = 2, 5, 7$   $\text{GeV}/c^2$  signal (left, middle and right respectively, red) and for background (blue). The optimal separation line is superimposed.

bidimensional  $p_{rec}^{T,max}$  -  $p_{rec}^{T,min}$  distributions after the optimal  $p_{\mu\mu}^T$  selection, with the optimal separation line superimposed. Events above the optimal line are classified as signal, below as background and therefore discarded. The two line parameters and the values of the  $p_{\mu\mu}^T$  cut are independently fitted (neglecting mutual correlations arising from the optimization procedure) with a linear interpolation technique as a function of the recoil mass, implemented with the Interpolation ROOT class [91], in order to get values of these parameters for a

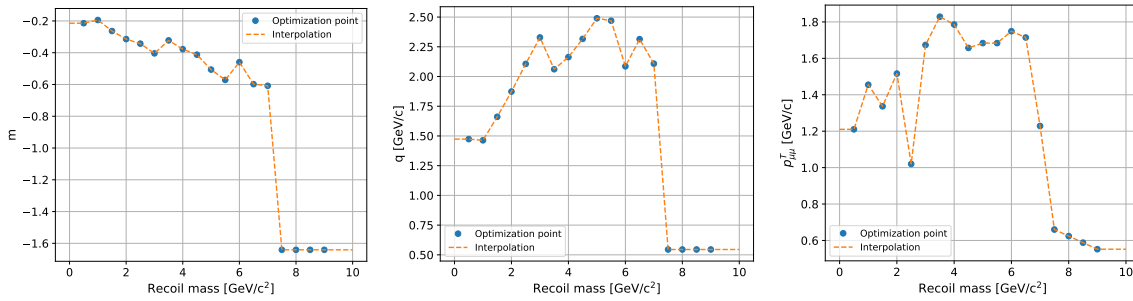


**Figure 4.10:** Optimal line parameters (left: slope; middle: intercept) and optimal  $p_{\mu\mu}^T$  selections (right) as a function of the recoil mass. The interpolated values (orange dashed line) in a continuum range of recoil mass are also shown.

generic recoil mass. Figure 4.10 shows the separation line parameters and the  $p_{\mu\mu}^T$  optimal selections determined by the optimization procedure, together with the interpolated values from the linear interpolation technique. Figure 4.11 shows the signal efficiency and the

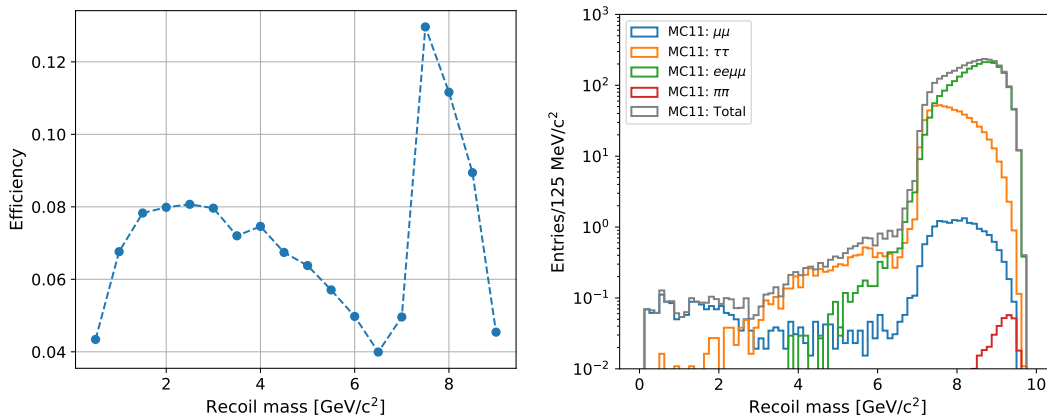


**Figure 4.11:** Signal efficiency (left) and number of surviving background events (right) computed on the generated MC samples after the final analysis selections, as a function of the recoil mass. Background MC samples have been normalized to an integrated luminosity of  $276 \text{ pb}^{-1}$ .

surviving background spectrum as a function of the recoil mass. The background rejection factor achieved by the  $\tau$  suppression procedure only, defined as the bin by bin ratio in the recoil mass spectrum of the number of events before and after the described selections, and the Punzi FOM as a function of the recoil mass are displayed in Figure 4.12. The residual background originating from  $\tau$  pair production is composed by only 15% of events in which both taus decay leptonically into muons, all the remaining fraction being dominated by  $\tau$  decaying to pions. This shows a potentially big margin of improvement of this analysis when a more performing, KLM-based muon identification selection will be available (Phase 3 data, see Section 8.3). As a final remark, it should be noticed that this procedure has been specifically devised for suppressing the  $\tau$  background, which means that the variables have been chosen based on the topology of pure  $\tau$  pair events and their full rejection power applies to the kinematic range where the  $\tau$  pairs contamination is the dominant source of background (3–7  $\text{GeV}/c^2$  recoil mass range). However, to find their selection optimal values, all the simulated background

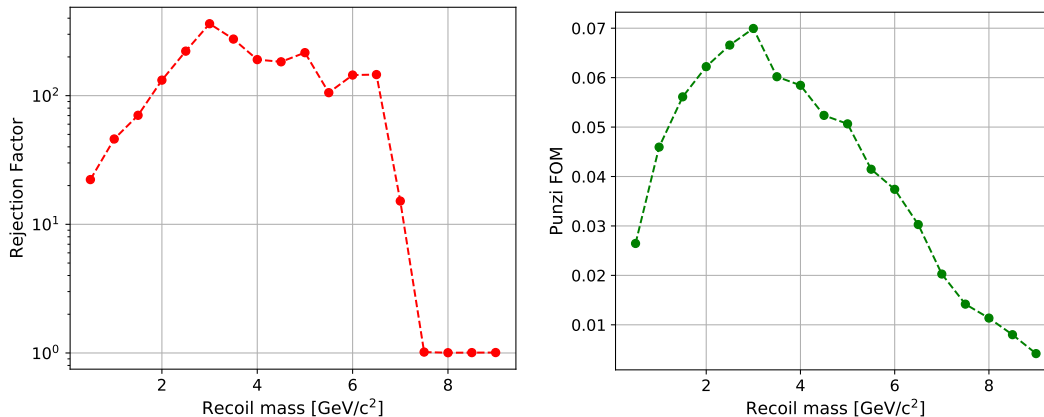


**Figure 4.12:** Background rejection factor defined as the bin by bin ratio in the recoil mass spectrum of the number of events before and after the  $\tau$  suppression procedure only (left). Punzi FOM as a function of the recoil mass after the optimization process (right).

samples have been included when studying the number of surviving events in the recoil mass spectrum. The loss of rejection power for masses above 7  $\text{GeV}/c^2$  (Figure 4.12, left) is thus due to kinematics reasons related to the change of the dominant background source (now being  $e^+e^- \rightarrow e^+e^-\mu^+\mu^-$  events), against which the procedure is less effective. Above that mass threshold, no further optimization could be found and the optimal selection values for the parameters  $m, q$  are therefore fixed to those found at 7  $\text{GeV}/c^2$ .

The full analysis chain is run on all the signal and the background MC samples. Recoil mass bins, signal efficiencies and number of background events surviving the selections are shown in Table 4.1. Errors therein are Monte Carlo statistical uncertainties only.

The bin choice in Table 4.1 corresponds to the pattern of generated  $Z'$  masses and is not suited for an analysis on real data, as it doesn't cover all the possible recoil mass values. A new choice with contiguous mass intervals is thus made, based again on the signal width study reported in Chapter 5. Recoil mass bin widths and signal efficiencies are interpolated at the center of each bin and background contributions recomputed in this new defined binning scheme. The new resulting bins with the corresponding signal efficiencies and expected background yields are shown in Figure 4.13 and Figure 4.14. The complete set of numbers is also reported in Appendix A as supplementary material, in Table A.1. The statistical analysis on simulation results (Chapter 8) which provides the expected sensitivities is performed on these numbers. On real data, an additional binning scheme is defined as a sanity check with a half bin shift in order to conveniently cover hypothetical signals located at the border of two contiguous bins.

**Table 4.1:** Signal efficiencies and number of background events after all the analysis selections in  $Z'$  mass bins. Background normalized to an integrated luminosity of  $276 \text{ pb}^{-1}$ . Errors on efficiency and background events are Monte Carlo statistical uncertainties only. Signal efficiencies and background yields include the 0.79 trigger efficiency (see Section 7.2)

$M_{Z'}$ [GeV/ $c^2$ ]	Mass range [GeV/ $c^2$ ]	Efficiency [%]	Background events
0.50	-0.15 - 1.15	$4.34 \pm 0.12$	$0.67 \pm 0.05$
1.00	0.63 - 1.37	$6.76 \pm 0.15$	$0.42 \pm 0.04$
1.50	1.28 - 1.72	$7.82 \pm 0.16$	$0.33 \pm 0.04$
2.00	1.84 - 2.16	$7.98 \pm 0.16$	$0.21 \pm 0.03$
2.50	2.37 - 2.63	$8.06 \pm 0.16$	$0.15 \pm 0.03$
3.00	2.90 - 3.10	$7.96 \pm 0.16$	$0.10 \pm 0.02$
3.50	3.42 - 3.58	$7.20 \pm 0.16$	$0.14 \pm 0.03$
4.00	3.93 - 4.07	$7.46 \pm 0.16$	$0.21 \pm 0.04$
4.50	4.44 - 4.56	$6.74 \pm 0.15$	$0.22 \pm 0.03$
5.00	4.95 - 5.05	$6.37 \pm 0.15$	$0.19 \pm 0.03$
5.50	5.47 - 5.53	$5.70 \pm 0.14$	$0.31 \pm 0.06$
6.00	5.97 - 6.03	$4.97 \pm 0.13$	$0.26 \pm 0.05$
6.50	6.47 - 6.53	$3.99 \pm 0.12$	$0.25 \pm 0.06$
7.00	6.97 - 7.03	$4.96 \pm 0.13$	$2.65 \pm 0.23$
7.50	7.46 - 7.54	$12.96 \pm 0.20$	$69.26 \pm 1.13$
8.00	7.97 - 8.03	$11.16 \pm 0.19$	$81.07 \pm 1.36$

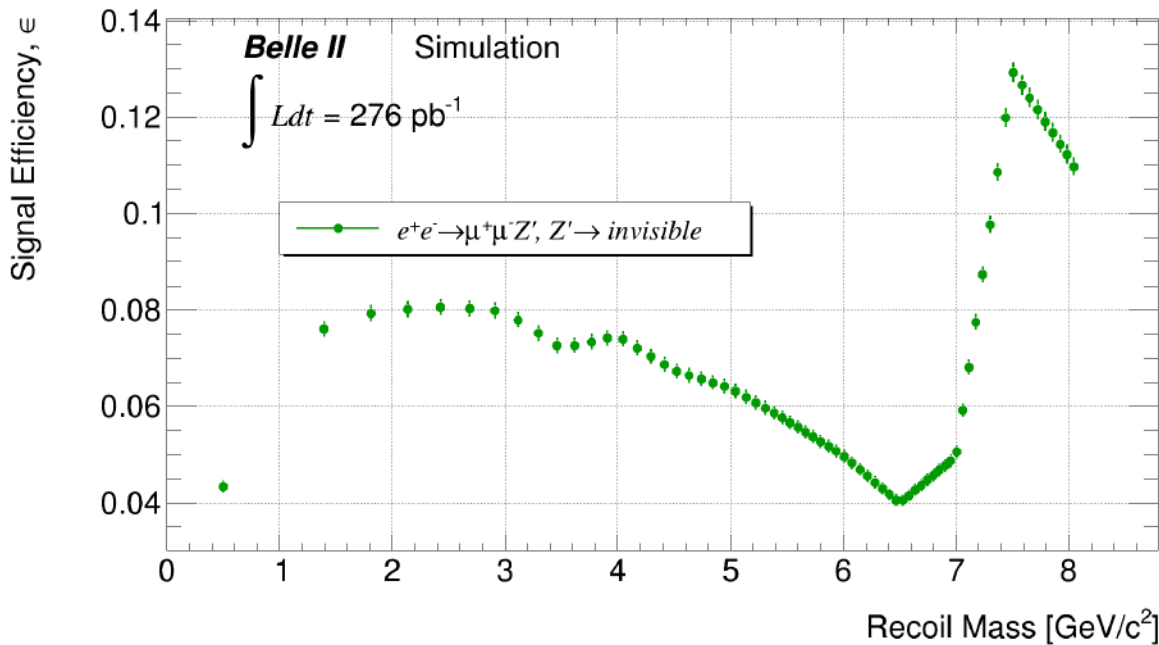


**Figure 4.13:** Signal efficiencies resulting from the interpolation procedure on the contiguous binning scheme are reported as function of the recoil mass, after the  $\tau$  suppression selection. This format provides the numbers to be used in the analysis on real data. The complete list of numbers is also shown in Table A.1

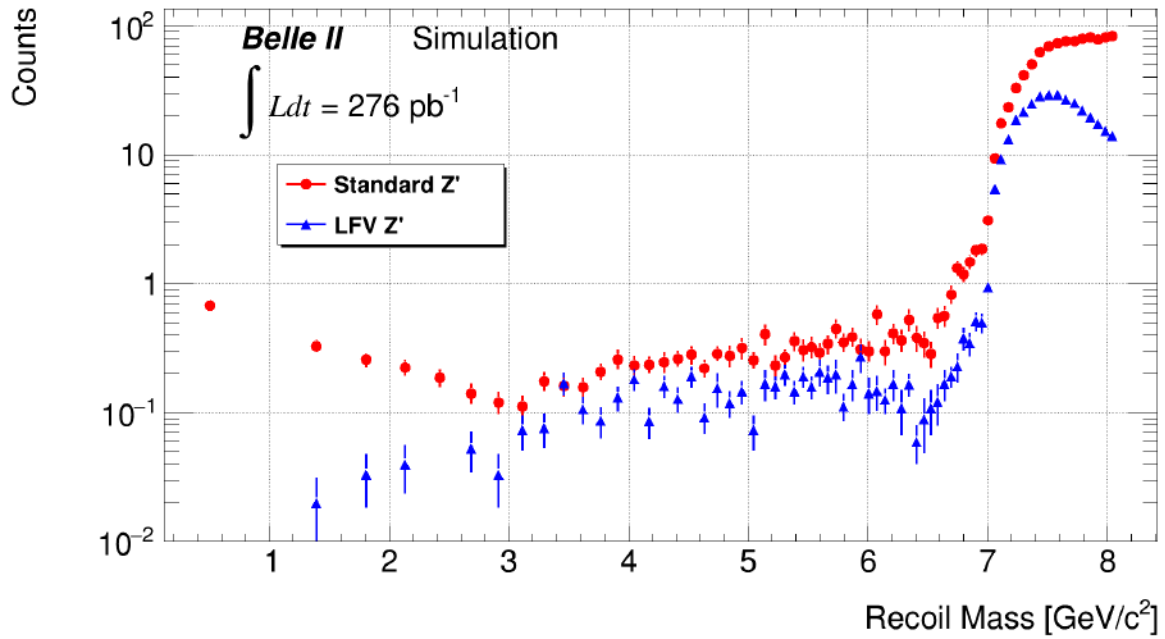


**Figure 4.14:** Expected background yields for the standard (red dots) and the LFV (blue triangles)  $Z'$  after the  $\tau$  suppression selection as a function of the recoil mass in the contiguous binning scheme are reported. These background yields are recomputed after interpolating the generated mass bins centers and width according to the results from the signal shape study discussed in Chapter 5, which provide the format to perform the analysis on real data.

#### 4.4.1 LFV $Z'$ to invisible

As a byproduct of the analysis optimized for the standard  $Z'$  search, it may be possible to apply a similar selection also to an electron-muon candidate and look for a LFV  $Z'$ , with a minimum set of changes:

- the number of *CleanedTracks* must be equal to 2 and the energy deposit in the calorimeter associated with the electron track must satisfy  $\text{clusterE} > 1.5$  GeV to emulate the functionality of the ECL trigger 7.2 (trigger logic `hie`, corresponding to the bit 8);
- a tighter ECL-based muon selection is applied to the muon candidate, which has to satisfy  $0.15 < \text{clusterE} < 0.4$  GeV and  $\text{clusterE}/p < 0.4$ , and a tighter ECL-based electron selection is required for the electron candidate,  $0.8 < \text{clusterE}/p < 1.2$ .

All the other selections are left unchanged, with the obvious replacement of the subscript  $\mu$  with  $e$  where appropriate (e.g.  $p_{e\mu}^T$ ).

The surviving background yields after the various analysis steps and the background spectrum achieved after the candidate reconstruction and the event selection, as a function of the recoil mass, are shown in Figure 4.15: as for the standard  $Z'$  case,  $\tau$  pair events ( $\tau^+\tau^-(\gamma)$ ) are largely the main source of background for most of the available phase space, with the exception of a small region at low recoil masses, where radiative dimuon events ( $\mu^+\mu^-(\gamma)$ ) give some contribution. All the background sources are normalized to the same integrated luminosity of  $276 \text{ pb}^{-1}$ , as in the standard  $Z'$  analysis, but with a trigger efficiency of 96% (see Section 7.2 for the complete discussion). At the moment of the writing of this work, no reliable

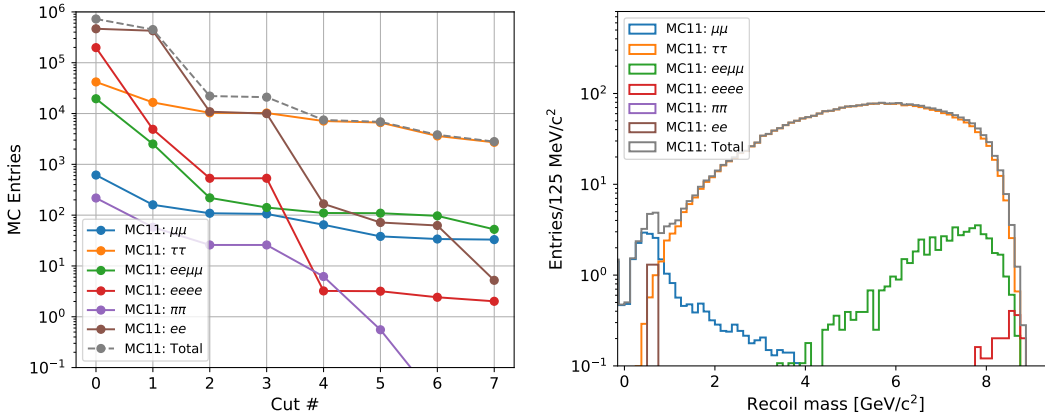


**Figure 4.15:** Surviving background events as a function of the analysis selection step before  $\tau$  suppression (left) and the resulting recoil mass spectrum (right) are displayed. Background yields are normalized to an integrated luminosity of  $276 \text{ pb}^{-1}$  and scaled for a trigger efficiency of 0.96.

LFV  $Z'$  signal simulation is available as mentioned in Section 1.6 and no signal efficiency due to these selections can be computed. For the same reason, any further signal-like selection optimization being impossible, the same  $\tau$  suppression procedure studied in Section 4.4 for the standard  $Z'$  has been applied to the surviving background events. Figure 4.16 shows for the 2, 5 and 7 GeV/c<sup>2</sup> sample masses for background events only the bidimensional  $p_{\text{rec}}^{T, \text{max}}$  -  $p_{\text{rec}}^{T, \text{min}}$  distributions after the  $p_{e\mu}^T$  selection, with the separation line as computed from the standard  $Z'$  optimization superimposed. Figure 4.17 shows the background rejection factor

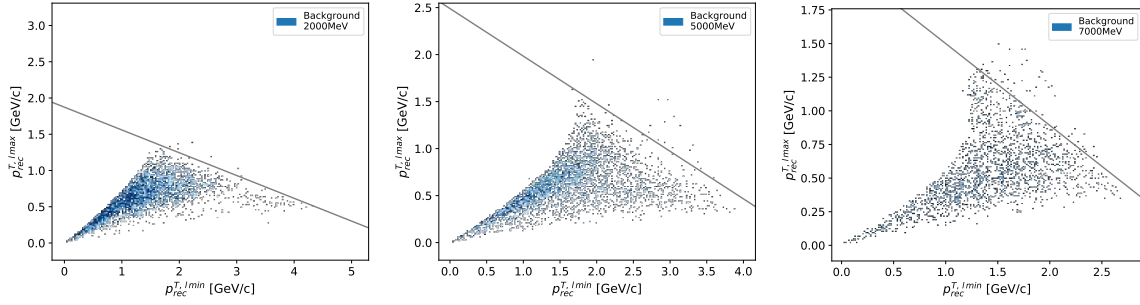


**Figure 4.16:** The bidimensional distributions of  $p_{rec}^{T,max}$  versus  $p_{rec}^{T,min}$  after the  $p_{e\mu}^T$  optimal selection for background events in the recoil mass windows centered around the simulated masses of 2, 5, 7  $\text{GeV}/c^2$  (left, middle and right respectively) are shown. The signal-from-background separation line (from standard  $Z'$  optimization) is also shown for each mass case.

achieved by the  $\tau$  suppression procedure only and the surviving background spectrum as a function of the recoil mass. The full analysis chain is run on all the the background sam-

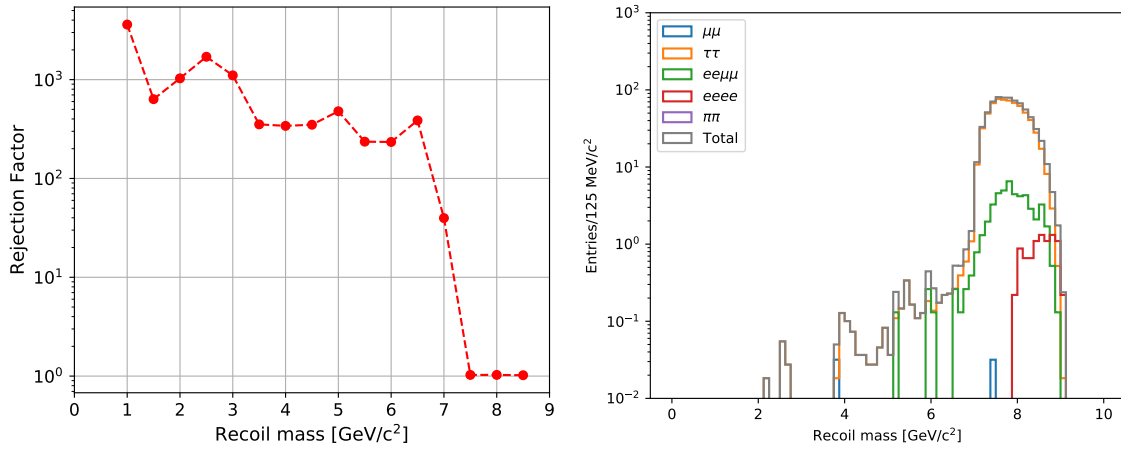


**Figure 4.17:** Background rejection factor achieved by the  $\tau$  suppression procedure only is reported on the left. Values at 0.5 and 3  $\text{GeV}/c^2$  could not be computed since no background events survived the final selection. The number of surviving background events after final selection as a function of the recoil mass is shown on the right plot. Background yields are normalized to an integrated luminosity of  $276 \text{ pb}^{-1}$  and scaled for a trigger efficiency of 0.96.

ples by grouping events in the same recoil mass bins as for the standard  $Z'$  and results for each generated mass are provided in Table 4.2. Recoil mass bins and number of background events surviving the selections are shown in the final contiguous binning scheme providing the analysis-ready format in Figure 4.14 and the complete list of numbers is reported in Table A.2 in Appendix A.

**Table 4.2:** Recoil mass bin center (first column), recoil mass range (second column) and number of background events surviving the selection (third column). Background yields are normalized to an integrated luminosity of  $276 \text{ pb}^{-1}$  and scaled for a trigger efficiency of 0.96. Errors on background events are Monte Carlo statistical uncertainties only.

$M_{Z'}$ [GeV/ $c^2$ ]	Mass range [GeV/ $c^2$ ]	Background events
0.50	-0.15 - 1.15	$0.00 \pm 0.01$
1.00	0.63 - 1.37	$0.01 \pm 0.01$
1.50	1.28 - 1.72	$0.04 \pm 0.02$
2.00	1.84 - 2.16	$0.03 \pm 0.01$
2.50	2.37 - 2.63	$0.03 \pm 0.01$
3.00	2.90 - 3.10	$0.05 \pm 0.02$
3.50	3.42 - 3.58	$0.16 \pm 0.03$
4.00	3.93 - 4.07	$0.17 \pm 0.03$
4.50	4.44 - 4.56	$0.17 \pm 0.03$
5.00	4.95 - 5.05	$0.12 \pm 0.03$
5.50	5.47 - 5.53	$0.18 \pm 0.03$
6.00	5.97 - 6.03	$0.18 \pm 0.06$
6.50	6.47 - 6.53	$0.09 \pm 0.04$
7.00	6.97 - 7.03	$0.69 \pm 0.07$
7.50	7.46 - 7.54	$29.02 \pm 0.48$
8.00	7.97 - 8.03	$14.72 \pm 0.36$



# Chapter 5

## Signal study

The strategy to extract the signal yield in each defined recoil mass bin is based on a Poisson counting experiment technique, for which the definition of the bin width is crucial and has to be studied on the recoil mass distributions of the simulated signal samples and validated on data to take into account any resolution effects introduced by the detector. In the following chapter, the signal yield extraction procedure will be explained and the needed studies on the signal shape performed both on simulation and real data will be reported.

### 5.1 Signal yield extraction

The fit to the recoil mass distribution would have improved the sensitivity to a hypothetical observed signal, but due to the low statistics expected after the final selections (less than one event per bin for most of the spectrum below  $6 \text{ GeV}/c^2$ , as previously shown in Figure 4.14), this option had to be discarded. Based on the Poisson counting experiment technique, the signal yields per each recoil mass bin are extracted by counting the number of observed events in the recoil mass window corresponding to a given  $Z'$  mass hypothesis and by comparing the results of the observation to the background yield expectations. The binning scheme on which the counting technique is applied has been optimized as a function of the recoil mass resolution as explained in Section 4.4. It is found to be optimal when corresponds to a  $4\sigma$ -wide window centered at the simulated  $Z'$  mass, with  $\sigma$  being the width of the signal peak distribution which varies as a function of the recoil mass.

#### 5.1.1 Signal shape study

To find the width of the signal distribution for various mass points, an unbinned maximum likelihood fit (using RooFit v3.6 [92]) has been performed on the recoil mass distribution of the signal samples generated for various  $Z'$  masses, after the final selections, including the  $\tau$  suppression procedure, are applied. The signal shape is modeled by a Probability Density Function (PDF) which includes two contributions: a Crystal Ball (CB) shape function describes the rightmost radiative tail of the recoil mass distribution; a Gaussian is added to model the remaining part of the distribution and account for the reconstruction resolution effect. As far as the former is concerned, the Crystal Ball Shape function [93] with parameters

$m_0, \sigma, \alpha, n$ , can be written as:

$$\begin{aligned}
 CB(x; m_0, \sigma, \alpha, n) &= N \cdot \begin{cases} e^{-\frac{(x-m_0)^2}{2\sigma^2}} & \text{for } \frac{x-m_0}{\sigma} > -\alpha \\ A \cdot (B - \frac{x-m_0}{\sigma})^{-n} & \text{for } \frac{x-m_0}{\sigma} \leq -\alpha \end{cases} \\
 A(n, \alpha) &= \left( \frac{n}{|\alpha|} \right)^n \cdot e^{-\frac{|\alpha|^2}{2}}; \\
 B(n, \alpha) &= \frac{n}{|\alpha|} - |\alpha|,
 \end{aligned} \tag{5.1}$$

where  $m_0$  is the mean of the distribution;  $A, B$  are constants depending on the parameters

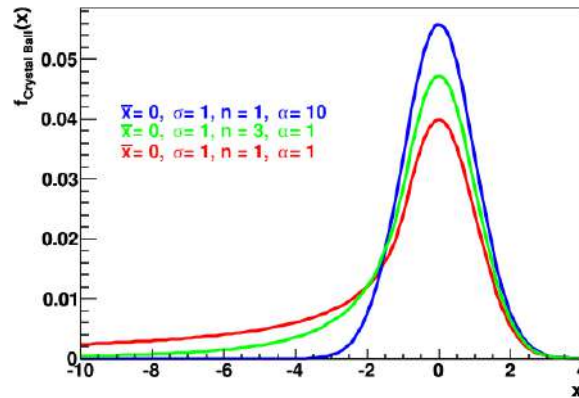


**Figure 5.1:** The Crystal Ball shape function. Various plots are shown for different values of  $n, \alpha$ .

$n, \alpha$ . In Figure 5.1 examples of the Crystal Ball shape function are plotted at varying of  $n$  and  $\alpha$ . The difference with respect to an ordinary Gaussian is the power-law tail on the left side which models the side band of the distribution. It should be noticed that for what concerns the  $Z'$  case, being an example of final state radiation and being the  $Z'$  mass reconstructed as the recoil with respect to the dimuon candidate, the typical CB shape is mirrored ( $\alpha < 0$ ), having the radiative tail not on the left, but instead on the right side. The resulting PDF consists of five parameters, because the means of both the CB and the Gaussian are fixed to the value of the generated  $Z'$  mass under study:  $\sigma_{\text{CB}}$  and  $\sigma_{\text{Gauss}}$ , being the width of the CB and of the Gaussian respectively;  $\alpha_{\text{CB}}$  and  $n_{\text{CB}}$ , the remaining CB parameters;  $frac$ , the fraction of the CB function with respect to the normalized sum of both. The recoil mass distribution for every generated signal sample as well as the corresponding fitted PDF model distribution are shown in Figure 5.2. To cope with the negative values and the double-peaked profile (due to a dip at zero) obtained for the signed recoil mass distribution of the signal sample for  $M_{Z'} = 0.5 \text{ GeV}/c^2$ , the square recoil mass  $m_{\text{rec}}^2$  has been used only for the mass point at  $0.5 \text{ GeV}/c^2$  and the fit algorithm has been applied to this variable. The extracted widths have then been used to compute the signal resolution as for the other mass points. In general, good fit results have been observed, concluding that the chosen PDF model is able to well describe the recoil mass distribution.

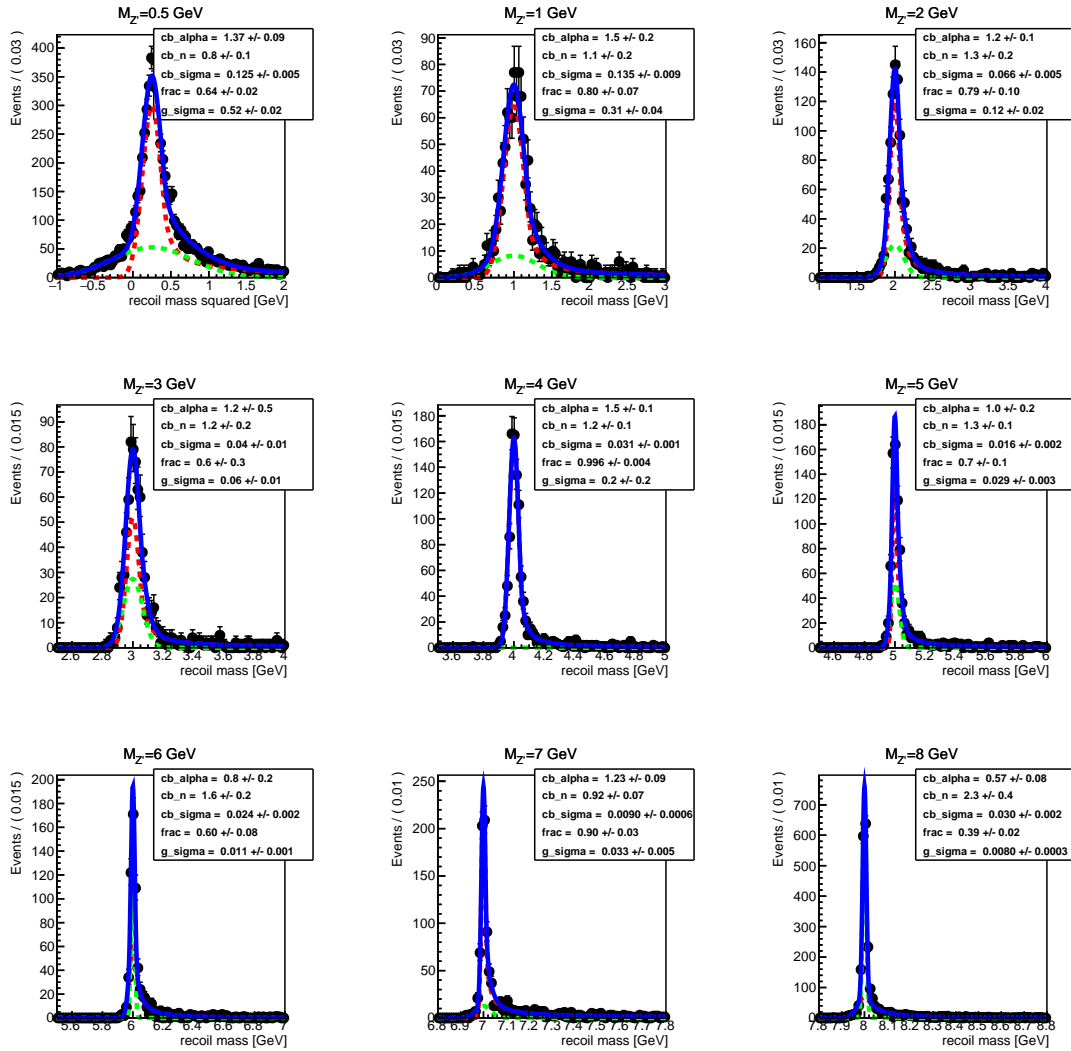


**Figure 5.2:** The recoil mass distribution and the fitted PDF model superimposed (blue line) are reported for every generated signal sample. The contribution of the CB and the Gaussian functions are shown with a red and green dotted line respectively. The resulting fit parameters are shown in the top right corner of each graph.

## Toy MC studies

For the validation of the fit, a toy MC study with 1000 samples of 10000 events each has been implemented. The events in each of the toy sample were generated according to the resulting PDF model with parameters fixed to the values extracted from the above described signal shape study. By looking at the parameter distributions of the toy MC samples, in particular the mean, the associated uncertainty and the resulting pull distribution of the two widths  $\sigma_{\text{CB}}$  and  $\sigma_{\text{Gauss}}$  for each studied mass point, it is possible to assess that there is no bias in the fit procedure and the uncertainties provided by the fit are correctly estimated. The pull distributions have been fitted with Gaussian functions and since the resulting mean (*pullMean*) and width (*pullSigma*) are consistent with 0 and 1 for the studied parameters, the fit algorithm and the chosen PDF model are considered validated and unbiased, and the signal peak widths can be reliably extracted from this method. All the generated  $Z'$  mass points have been tested with this validation procedure and results consistent with normal distributions are shown in Appendix A in Figure A.2 and in Table A.3 and Table A.4.

### 5.1.2 Signal width

The selection optimization described in Section 4.4, as well as the signal yield extraction strategy require to define a signal window for the event counting. The optimal value for the signal window width as optimized by maximizing the  $\text{FOM}_{\text{Punzi}}$  is found to be  $4\sigma$ , where  $\sigma$  is the computed signal resolution as a function of the recoil mass. The width of the mass window is thus a function of the signal peak width for each simulated recoil mass distribution, taking into account the different contributions of the CB and Gaussian functions and it is calculated according to formula:

$$\sigma_w = \sqrt{\text{frac} \times \sigma_{\text{CB}}^2 + (1 - \text{frac}) \times \sigma_{\text{Gauss}}^2}, \quad (5.2)$$

using as input values for each mass point the  $\sigma_{\text{CB}}$ ,  $\sigma_{\text{Gauss}}$  and *frac* from the fit results shown in Figure 5.2. The weighted widths computed for every generated  $Z'$  mass point are given in Table 5.1 and shown in Figure 5.3 as a function of the generated  $Z'$  mass,  $M_{Z'}$ .

## 5.2 Recoil mass resolution

The recoil mass resolution may differ in real data from what observed in the simulation due to unknown detector effect and it is necessary to validate the signal resolution results on real data control samples, taking care not to unblind the signal recoil mass distribution in data. The strategy is to measure the recoil mass resolution on data by selecting a pure sample of  $e^+e^- \rightarrow \mu^+\mu^- \gamma$  events, where the presence of the photon prevents any unblinding issue, and then compare to MC results on the same simulated process. The control sample on real data and on simulated events has been selected by applying the same analysis requirements as described in Section 4.3 for steps 1, 2, 3, 4 and 6, while the selection 5 has been reversed, by explicitly requiring the presence of a photon within a  $15^\circ$  cone with respect to the recoil momentum direction. In addition, to reject contamination from radiative  $\tau$  pair events, it was required that the sum of the energies of the two muons and of the photon lies between 10 and 12 GeV and no additional photons with energy larger than 100 MeV are detected in the event.

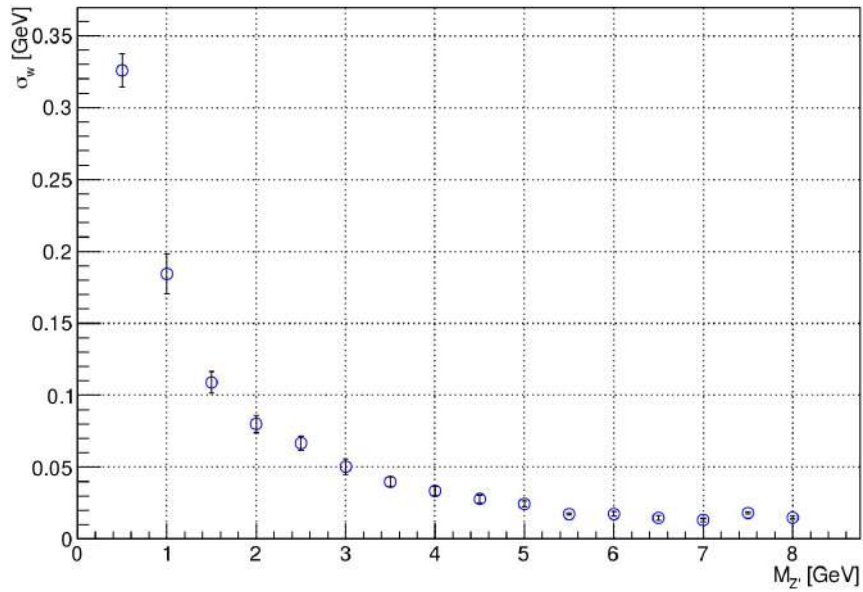


**Figure 5.3:** The signal width  $\sigma_w$  computed according to Equation 5.2 is shown as a function of the generated  $Z'$  mass.

**Table 5.1:** The weighted width for every generated  $Z'$  mass point has been computed according to Equation 5.2 and with the fit results given in Figure 5.2.

$M_{Z'}$ [GeV/c <sup>2</sup> ]	$\sigma_w$ [GeV/c <sup>2</sup> ]
0.5	$0.3257 \pm 0.0115$
1.0	$0.1844 \pm 0.0138$
1.5	$0.1089 \pm 0.0075$
2.0	$0.0799 \pm 0.0060$
2.5	$0.0667 \pm 0.0050$
3.0	$0.0504 \pm 0.0055$
3.5	$0.0398 \pm 0.0033$
4.0	$0.0335 \pm 0.0031$
4.5	$0.0278 \pm 0.0028$
5.0	$0.0245 \pm 0.0019$
5.5	$0.0174 \pm 0.0007$
6.0	$0.0175 \pm 0.0017$
6.5	$0.0147 \pm 0.0015$
7.0	$0.0132 \pm 0.0012$
7.5	$0.0182 \pm 0.0008$
8.0	$0.0149 \pm 0.0009$

The selected events on both data and MC samples are then weighted to match the kinematic distribution expected for the signal process. The weights have been produced from the bidimensional muon momenta distribution in  $0.5 \text{ GeV} \times 0.5 \text{ GeV}$  bins for  $e^+e^- \rightarrow \mu^+\mu^- Z'$  events at different  $Z'$  masses (distributions are reported in Figure 5.4) and then applied to

the selected control samples from  $\mu^+\mu^-\gamma$  events, on both data and MC simulations, to reproduce the same kinematic dependence in the recoil mass distribution as expected for signal processes. The weighting procedure has been repeated for all the generated  $Z'$  mass points, with optimal results for the low recoil mass region, while for increasing  $Z'$  masses it suffers of the low statistics in the  $\mu^+\mu^-\gamma$  spectrum and the matching between the bidimensional dimuon momentum distributions becomes highly inefficient, due to obvious kinematic reasons (see Figure 5.4).

The weighted recoil mass distributions produced on the control samples are expected to be centered at zero, since the recoil mass against the dimuon candidate for  $e^+e^- \rightarrow \mu^+\mu^-\gamma$  events coincides with the invariant mass of the radiated photon: the ratio of the width measured in data and in Monte Carlo can be used as a correction factor to the recoil mass resolution. Distributions are fitted as described in the previous Section 5.1.1, with the sum of a Crystal Ball function and a Gaussian. Figure 5.5 and Figure 5.6 show the results for the studied  $e^+e^- \rightarrow \mu^+\mu^-\gamma$  events on both Monte Carlo and data, including the fitted PDF model. Correction factors defined as the ratio of the values of the weighted widths (Equation 5.2) in data and in Monte Carlo recoil mass distributions,  $\frac{\sigma_{\text{weighted,data}}}{\sigma_{\text{weighted,MC}}}$ , computed from the fit results, are shown in Table 5.2. For all the generated  $Z'$  masses studied within the weighting procedure, the correction factors are smaller or compatible with unity within their fit uncertainty and it can be concluded that the effect of the detector resolution is well described in simulations and its impact on the signal yield extraction procedure is negligible.

**Table 5.2:** An overview of the values of the weighted width including the number of events for the fitted data and MC recoil mass distributions is given. The ratio of both values is calculated in order to determine the correction factor due to the detector resolution.

$M_{Z'}$ [GeV/c <sup>2</sup> ]	$\sigma_{\text{weighted,data}}$ [GeV/c <sup>2</sup> ]	$\sigma_{\text{weighted,MC}}$ [GeV/c <sup>2</sup> ]	$\frac{\sigma_{\text{weighted,data}}}{\sigma_{\text{weighted,MC}}}$	$N_{\text{events,data}}$	$N_{\text{events,MC}}$	$\frac{N_{\text{events,data}}}{N_{\text{events,MC}}}$
0.5	$0.263 \pm 0.012$	$0.298 \pm 0.021$	$0.88 \pm 0.07$	$4432 \pm 275$	$4498 \pm 287$	$0.99 \pm 0.09$
1	$0.282 \pm 0.020$	$0.355 \pm 0.028$	$0.79 \pm 0.08$	$4220 \pm 374$	$4309 \pm 371$	$0.98 \pm 0.12$
1.5	$0.305 \pm 0.018$	$0.325 \pm 0.022$	$0.94 \pm 0.08$	$3958 \pm 291$	$4099 \pm 375$	$0.97 \pm 0.11$
2	$0.329 \pm 0.018$	$0.302 \pm 0.024$	$1.11 \pm 0.11$	$3655 \pm 200$	$3819 \pm 323$	$0.96 \pm 0.09$
2.5	$0.329 \pm 0.013$	$0.314 \pm 0.023$	$1.05 \pm 0.08$	$3510 \pm 236$	$3787 \pm 313$	$0.93 \pm 0.10$
3	$0.355 \pm 0.010$	$0.356 \pm 0.027$	$1.00 \pm 0.08$	$3065 \pm 134$	$3575 \pm 392$	$0.86 \pm 0.10$

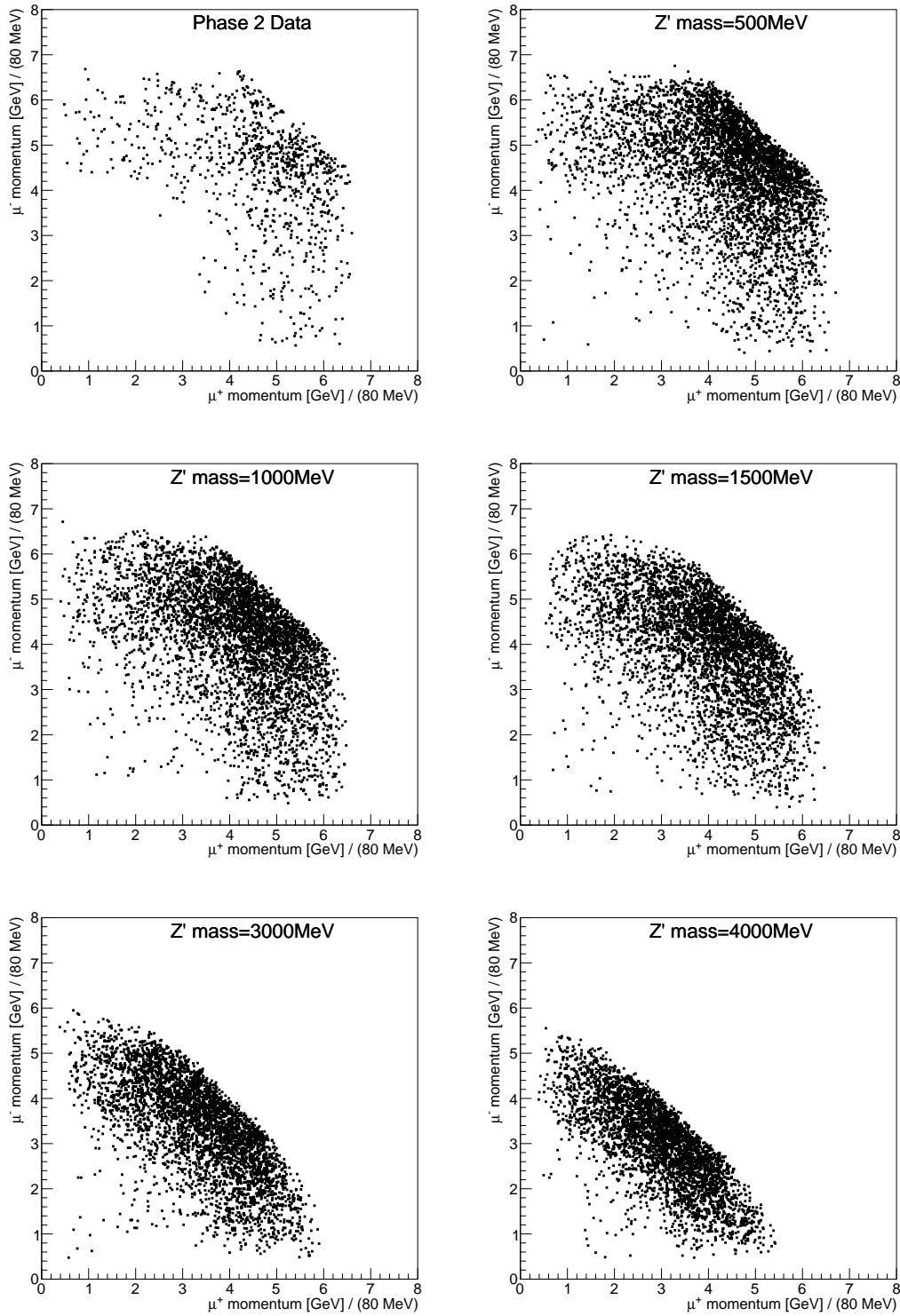


**Figure 5.4:** Bidimensional distributions of muon momenta for  $\mu^+\mu^-\gamma$  events in data (top left), and the same distributions for simulated events of  $e^+e^- \rightarrow \mu^+\mu^- Z'$  processes, for different  $Z'$  masses, are shown: 0.5 GeV (top right), 1 GeV (middle left), 1.5 GeV (middle right), 3 GeV (bottom left), 4 GeV (bottom right).

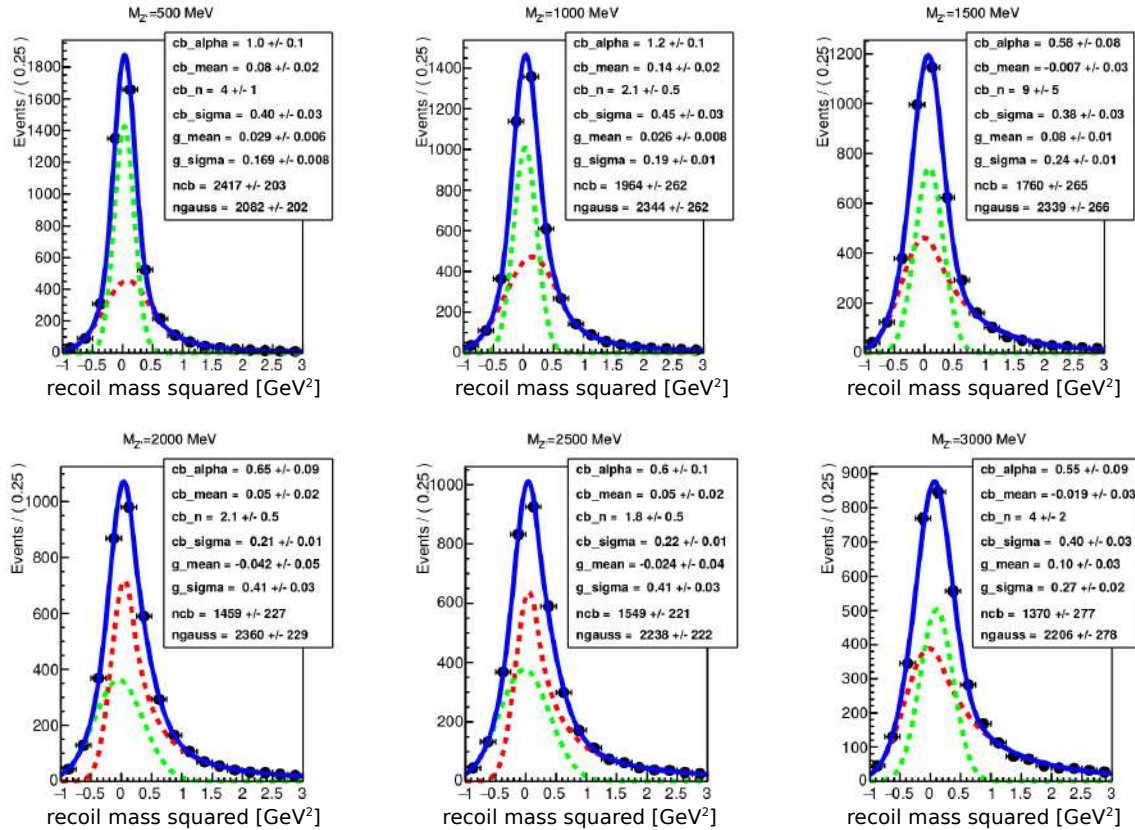


**Figure 5.5:** The weighted MC recoil mass distributions and the fitted PDF model superimposed (blue line) are shown for different  $Z'$  mass point hypothesis. The contribution of the CB and the Gaussian function are highlighted with a red and green dotted line respectively. The resulting fit parameters are provided in the top right corner of each graph.

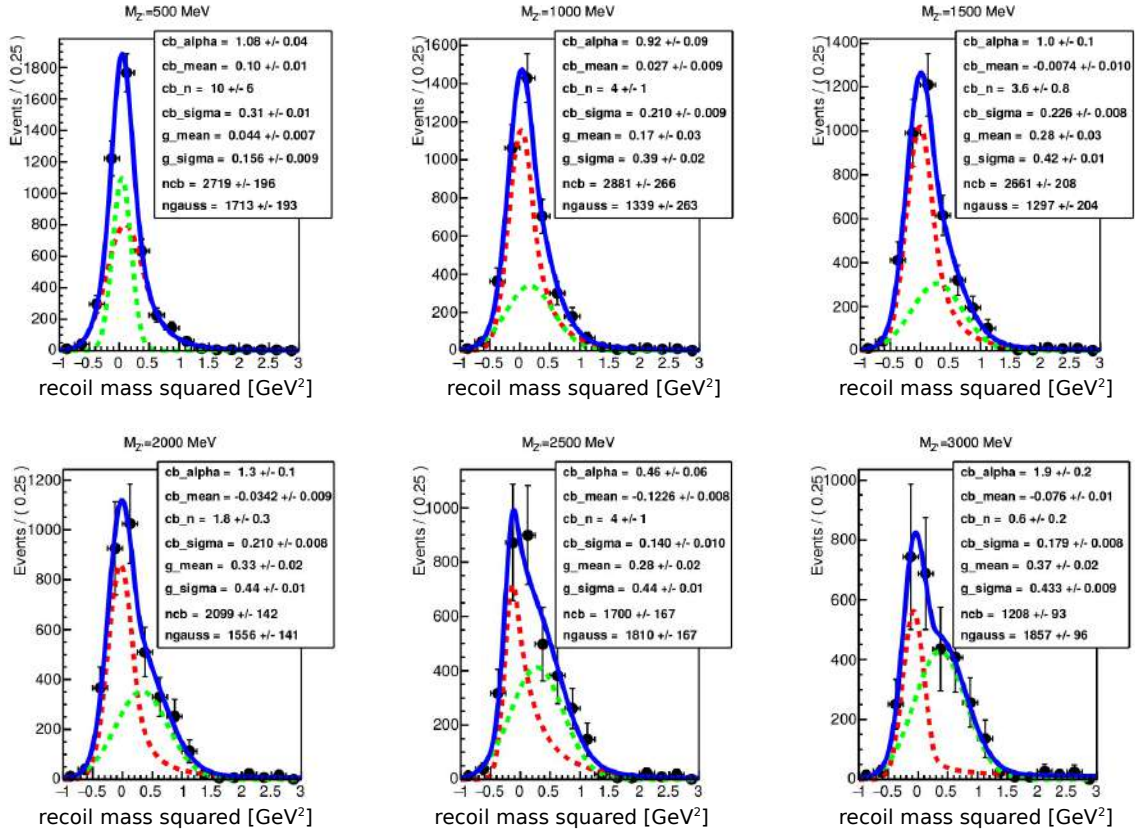


**Figure 5.6:** The weighted data recoil mass distributions and the fitted PDF model superimposed (blue line) are shown for different  $Z'$  mass point hypothesis. The contribution of the CB and the Gaussian function are highlighted with a red and green dotted line respectively. The resulting fit parameters are provided in the top right corner of each graph.



## Chapter 6

# Data validation studies

The goal of the validation procedure is twofold, first to obtain an estimate of the total background yield based on real data and compare to the result of the Monte Carlo simulation and second, to evaluate on real data the effect of the individual analysis selections optimized on MC samples as described in Chapter 4 for the candidate reconstruction, the event selection and the  $\tau$  suppression procedure, without unblinding the signal in the data sample. The blind analysis principle still holds and for any control samples mentioned below, careful checks to ensure the probability to accidentally reveal the signal is negligible have always been performed, as it will be discussed in the following sections.

Three different data validation procedures, each corresponding to a differently selected control sample, were devised:

- *ee sample*. Beside the Bhabha and *eeee* backgrounds, this sample is dominated by  $\tau\tau(\gamma)$  events, with both  $\tau$ 's decaying to electrons, whose kinematics is almost identical to one of the the dominant  $Z'$  analysis background,  $\tau\tau(\gamma)$  events, with both  $\tau$ 's decaying to muons. All the analysis selections, with the exception of the PID requirements, and including the  $\tau$  suppression procedure, can thus be checked. Requiring two identified electrons avoids any unblinding issue since the ECL-based identification of electrons is complementary to that used for muons and applied for the signal selection;
- *$\mu\mu\gamma$ ,  $e\mu\gamma$ ,  $ee\gamma$  samples*. The presence of a photon with a reconstructed energy above 1 (or 1.5) GeV decreases the signal efficiency by a factor  $\sim \alpha_{\text{QED}}$ , thus avoiding any unblinding issue. This sample is particularly useful in checking the low recoil mass region, being dominantly composed by the ISR QED process  $e^+e^- \rightarrow \mu^+\mu^-\gamma$ . These events are referred to hereafter as the  $\mu\mu\gamma$  sample. Similarly, the  $e\mu\gamma$  and  $ee\gamma$  samples are used to cross check the  $\mu\mu\gamma$  one;
- *$\mu\mu$ ,  $e\mu$  samples*, after the application of a partially reversed  $\tau$  suppression procedure. This technique allows to strongly suppress any hypothetical signal contributions, thus leaving an almost unbiased background sample, very similar to the one expected for the  $Z'$  analysis before the  $\tau$  suppression procedure, with no unblinding risk.

For these procedures extensive comparisons between data and MC on the most important analysis variables were performed as shown hereafter. Beside checking the overall number of events in data and in simulations, for each validation sample, the level of agreement was measured in

three different recoil mass regions, as they correspond, for events with two identified muons, to different sources of contributing background: the low recoil mass region  $-2 < M_{rec} < 3$   $\text{GeV}/c^2$ , dominated by  $\mu\mu(\gamma)$  processes; the intermediate spectrum for  $3 < M_{rec} < 6$   $\text{GeV}/c^2$ , dominated by  $\tau\tau(\gamma)$  events; the high recoil mass region  $6 < M_{rec} < 11$   $\text{GeV}/c^2$ , dominated by four-lepton final state events, i.e.  $e^+e^- \rightarrow e^+e^-\mu^+\mu^-$ .

Unless differently and explicitly stated, data events are selected by requiring the CDC two-track trigger (line `fbo`, known as bit 7 among the Phase 2 trigger options) to be fired, whose efficiency evaluated to be 0.79 in Bhabha events as explained later on in Section 7.2 is used to scale all the expected background MC yields. Samples with electrons or photons with a reconstructed energy above 1 GeV can be triggered by the ECL trigger line `hie` too, thus providing the possibility of additional cross-checks on the trigger effects, including alternative measurements of the CDC trigger efficiency.

## 6.1 Data validation with $ee$ sample

The  $ee$  sample is selected by applying all the requirements described in Section 4.2 on both data and Monte Carlo, except for the PID selection for a loose ECL-based muon candidate, replaced by the loose ECL-based electron candidate requirement,  $\text{clusterE}/p > 0.75$ . Similarly for the analysis steps described in Section 4.3, they have been applied on data and Monte Carlo, by replacing the tight-muon PID requirement with  $0.8 < \text{clusterE}/p < 1.2$  for tight-electron selection. Recoil mass distributions for data and Monte Carlo before the application

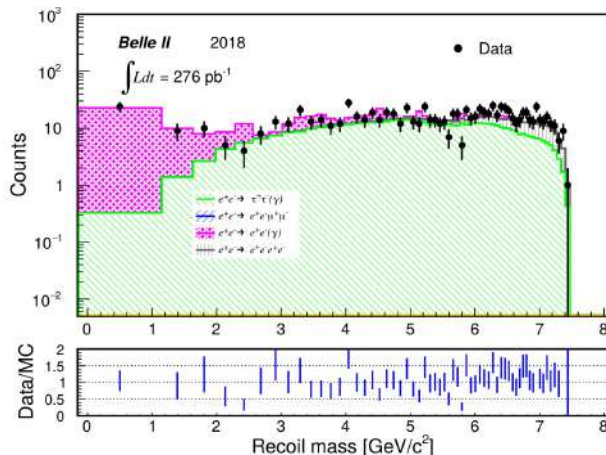


**Figure 6.1:** The recoil mass spectrum for the  $ee$  validation and the data/MC ratio as a function of the recoil mass in the final binning scheme, before the  $\tau$  suppression procedure, are plotted.

of the  $\tau$  suppression procedure are reported in Figure 6.1. The agreement between data and simulation has been measured and results in a data/MC ratio of  $0.97 \pm 0.01$  averaged overall the spectrum. After the application of the  $\tau$  suppression procedure, 20 events are found in data in the first two recoil mass windows while 18.4 are expected in Monte Carlo. These numbers can be interpreted as a validation of the  $\tau$  suppression procedure with a statistical precision of 22%, which is used as input only in the upper limit calculations as described in Section 8.1 for assessing the systematic error on the background level knowledge coming from the  $\tau$

suppression procedure. The statistical significance of such a check can be slightly improved by adding the results coming from the  $e\mu$  sample, largely dominated by  $\tau\tau(\gamma)$  background, which is also the LFV  $Z'$  sample. About 5 events are expected from the simulation after the luminosity normalization and assuming a similar number of events in data at the moment of unblinding, that can be justified from the above measured data/MC agreement, the statistics for the combined  $ee + e\mu$  sample would bring the statistical uncertainty of the  $\tau$  suppression procedure precision at  $\approx 20\%$  level.

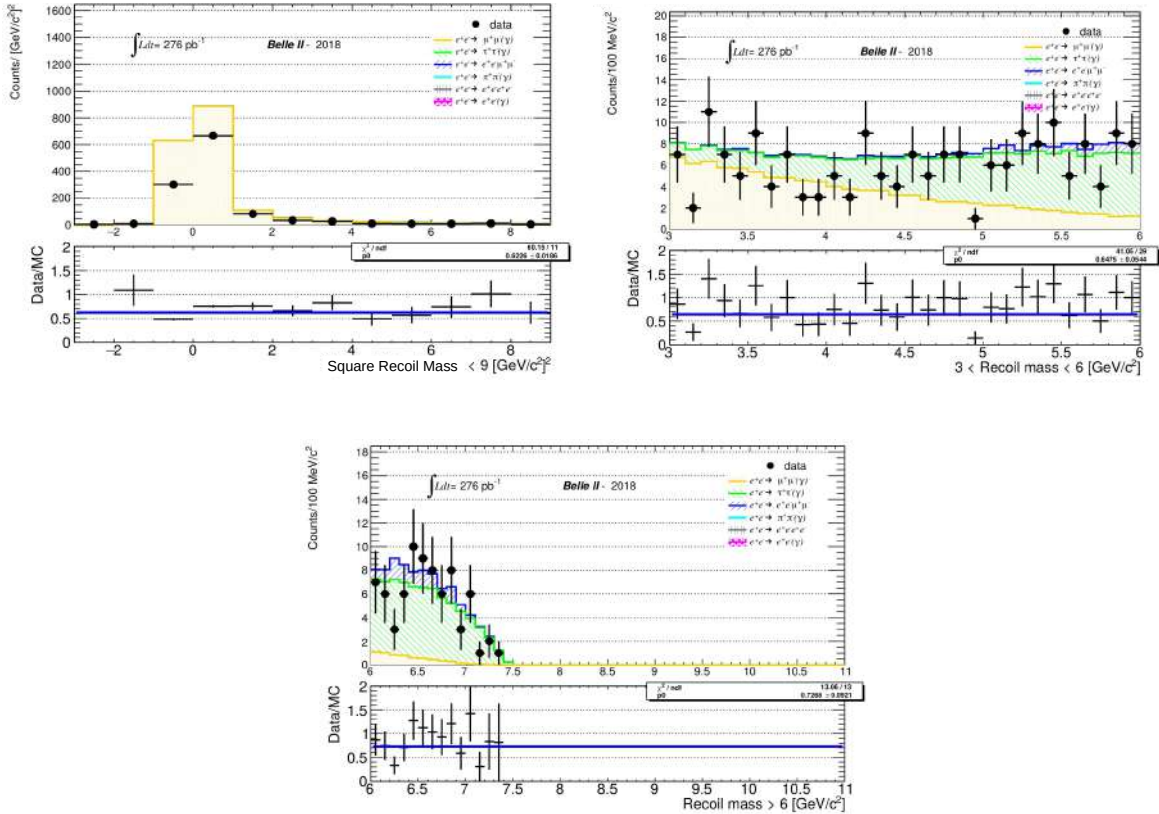


**Figure 6.2:** Distributions for the  $\mu\mu\gamma$  validation sample, in the three analyzed mass ranges (clockwise):  $-2 < M_{Z'} < 3$ ,  $3 < M_{Z'} < 6$  and  $M_{Z'} > 6$ . Note for the first recoil mass region for  $M_{Z'} < 3 \text{ GeV}/c^2$ , the square recoil mass is plotted, to cope with negative reconstructed masses due to resolution effects.

## 6.2 Data validation with $\mu^+\mu^-\gamma$ sample

The default selection described for the standard  $Z'$  analysis as explained in Section 4.3 is applied on data with some modifications: a detected photon in the barrel ECL with a reconstructed energy  $E_\gamma > 1 \text{ GeV}$  has been required; the veto on events with a reconstructed photon within a  $15^\circ$  cone centered on the recoil momentum direction has been removed; the requirement to have an energy deposit in the cleaned ROE (extraEnergy) smaller than  $0.4 \text{ GeV}$  is replaced by the requirement to have  $(\text{extraEnergy} - \text{cluster}E_\gamma) < 0.4 \text{ GeV}$ , all the rest

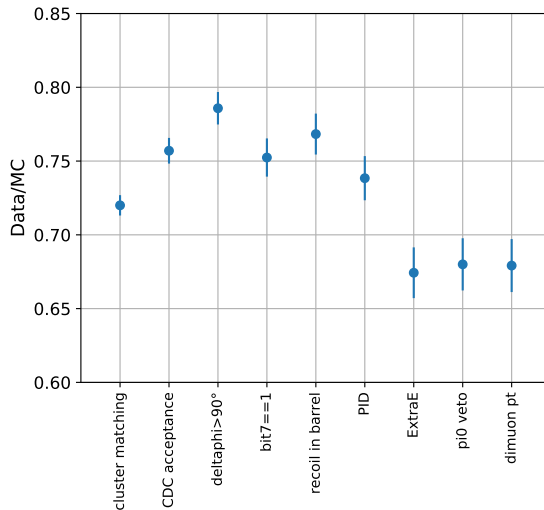


**Figure 6.3:** Data/MC ratio as a function of each selection step for the  $\mu\mu\gamma$  validation. The 0.79 efficiency correction due to the trigger applies only when the requirement of having the CDC trigger bit fired is effective (from the fourth point on).

being the same as described in Section 4.3. The contributing sources of background are the same as in the standard  $Z'$  analysis, but it has to be noticed that the generator **AAFH**, used to simulate the  $ee\mu\mu$  background, has no ISR implemented. To reduce its importance in the selected control sample and reject this contamination on real data, the direct dimuon mass has been constrained to  $M_{\mu\mu} > 3 \text{ GeV}/c^2$ . Even with such countermeasure, the  $ee\mu\mu$  appears still relevant, especially for high recoil masses  $M_{rec} > 6 \text{ GeV}/c^2$  for which other validation samples are more suitable (see next sections). Recoil variables are always referred to the dimuon system, regardless the presence of a reconstructed photon. Data and Monte Carlo recoil mass distributions are compared after the event selection, before applying the  $\tau$  suppression procedure as shown in Figure 6.2, for the three different mass intervals. Discrepancies of the order of 30% are visible, with data consistently below Monte Carlo expectations (final results reported in summary Table 6.1 at the end of the chapter). This is particularly evident, for statistical reasons, for the first recoil mass window, largely dominated by the radiative  $\mu\mu\gamma$  QED background. It has been checked if the discrepancy might be originated by the  $\mu\mu\gamma$  event generator by producing a special sample with the **BabaYaga@NLO** generator, which has been analyzed through the same analysis chain: differences within 1% level are found with respect to the standard **KKMC** generated sample and therefore it has been concluded the discrepancy could not be ascribed to the MC generator.

The effect of the individual selections is also studied, as shown in the plot in Figure 6.3, which summarizes the data/MC ratio as a function of the applied selection requirement. For the background yield considered in the data/MC ratio, the 0.79 efficiency correction due to the CDC trigger is applied only at the moment in which the requirement of having the **ffo** bit fired is made on data and applied in the simulation as further selection conditions that mimic trigger requirements (fourth point in figure); before that analysis step, a 100% trigger efficiency is assumed, which allows to conservatively study the observed discrepancy. In Figure 6.4, Figure 6.5, Figure 6.6 distributions of the most relevant variables for the analysis

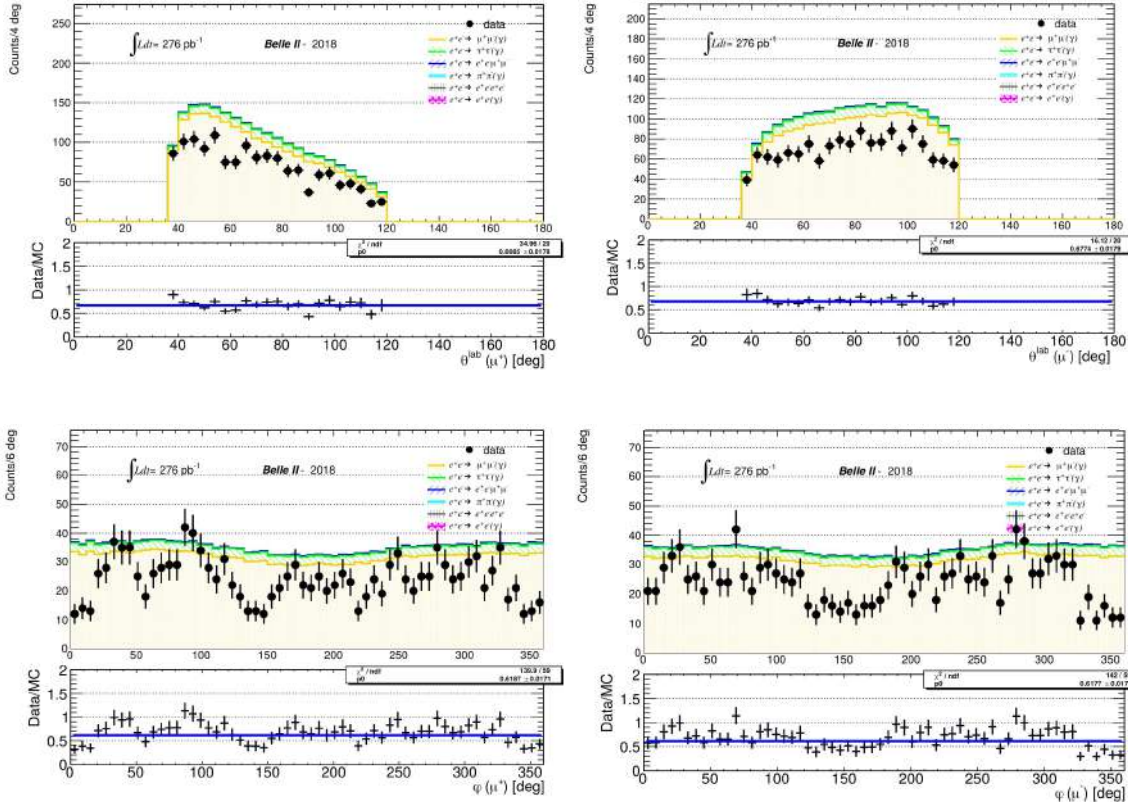


**Figure 6.4:** Most relevant angular variables exploited in the analysis are shown for  $\mu\mu\gamma$  validation sample, as follows (row order):

- (1) the Polar angle (in the laboratory frame) of the two muons, positive charge (left), negative charge (right);
- (2) Azimuthal angle (in the laboratory frame) of the two muons, positive charge (left), negative charge (right).

are shown, from which no evident indication of a possible source of discrepancy comes out: most distributions look reasonably flat within the statistical fluctuations, with the exception of the data/MC comparison as a function of the azimuthal track angle (see Figure 6.4). The CDC trigger line `ffo` in Phase 2 is known to produce strong  $\phi$  dependencies due to hardware issues. The presence of the photon with energy above 1 GeV allows one to measure the CDC trigger efficiency by using the calorimeter trigger line `hie` (bit 8) as a reference, which has been systematically checked as reported in Section 6.4. The entire data/MC validation with the  $\mu\mu\gamma$  sample can be repeated by requiring only the ECL trigger line to be fired, and thus ruling out the possibility that the observed discrepancy may be ascribed to the CDC trigger  $\phi$ -dependencies. The result of the ECL trigger cross-check is in agreement with that obtained with the CDC trigger `ffo`, as reported in Table 6.1. The  $e\mu\gamma$  and  $ee\gamma$  final states have also been studied, using both the CDC `ffo` trigger and the ECL `hie` trigger. The  $e\mu\gamma$  sample contains much less background from  $\mu\mu$  and  $ee$  final states, due to the PID requirement, and is dominated by radiative  $\tau$ -pair production, i.e.  $e^+e^- \rightarrow \tau^+\tau^-\gamma$  events. For these validation samples, when the statistics is high enough, the agreement looks much better than for  $\mu\mu\gamma$

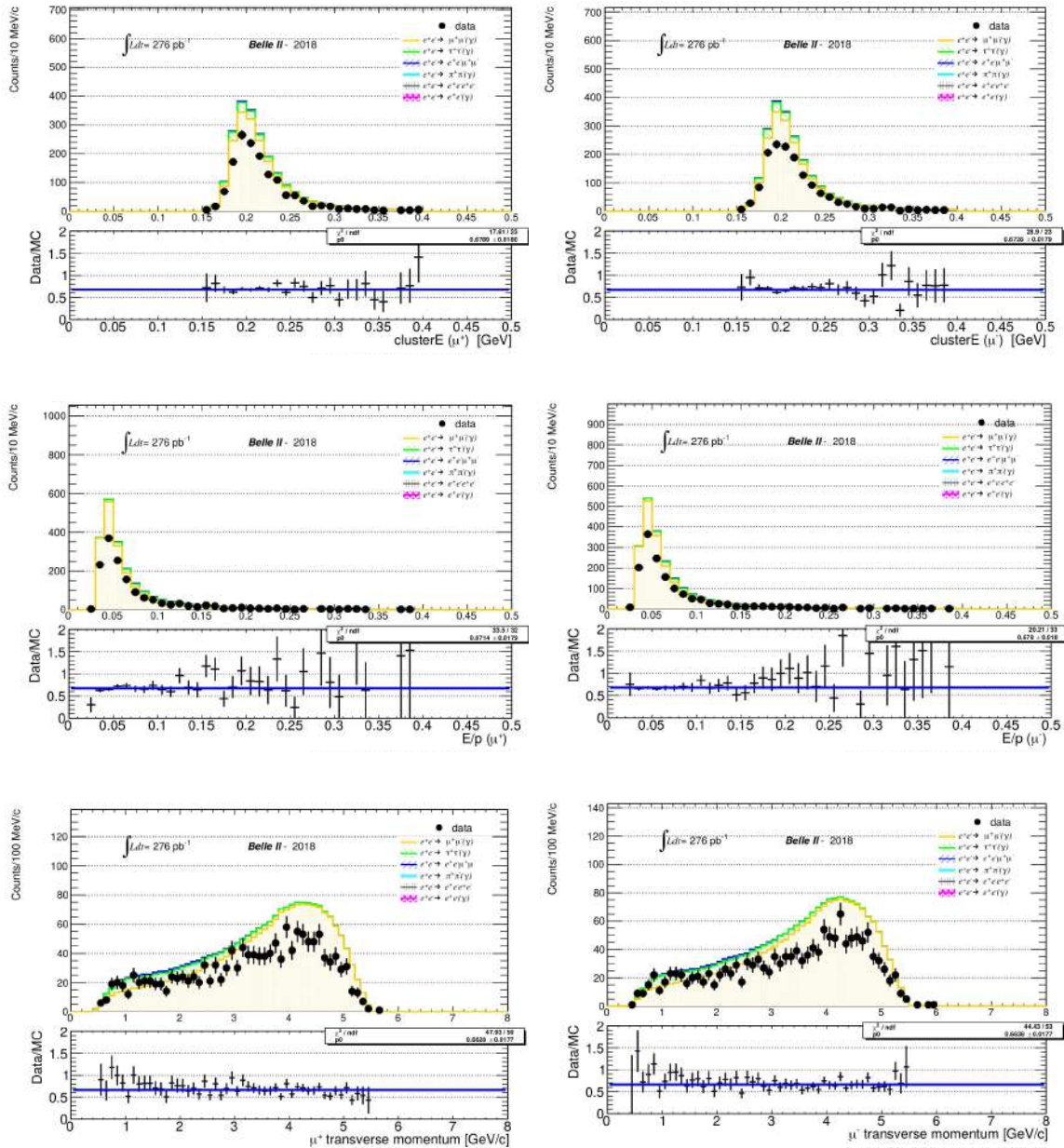


**Figure 6.5:** Most relevant kinematic variables exploited in the analysis are shown for  $\mu\mu\gamma$  validation sample, as follows (row order):

- (1) Cluster energy of the two muons, positive charge (left), negative charge (right);
- (2) Ratio of the muon cluster energy and the muon track momentum, positive charge (left), negative charge (right);
- (3) Transverse momentum of the two muons, positive charge (left), negative charge (right).

events (see Table 6.1), thus suggesting the possibility that the problem is related to muon detection in Phase 2 data. Being the statistical significance either much higher in the first recoil mass window or not very high overall the spectrum for the selected control sample (see

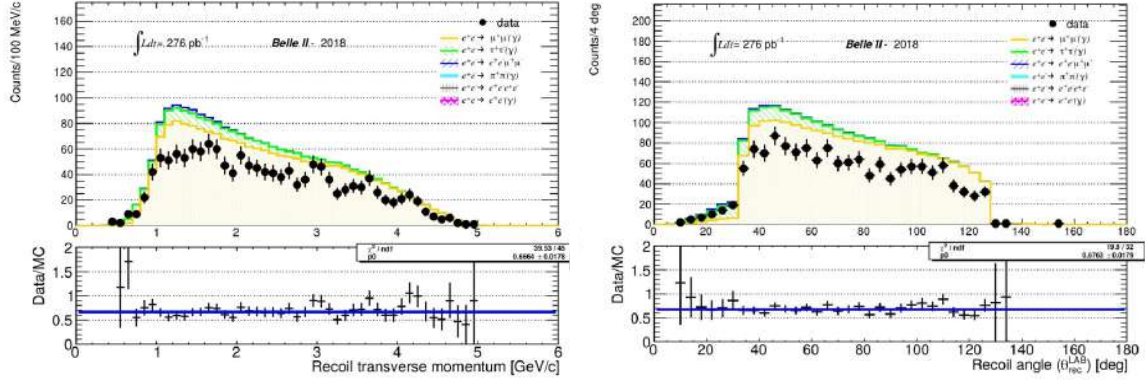


**Figure 6.6:** Transverse momentum (left) and polar angle (right) of the system recoiling against the two muons for the  $\mu\mu\gamma$  validation sample.

Table 6.1), a complementary validation procedure able to check the full interesting recoil mass region is required and described in the next Sections.

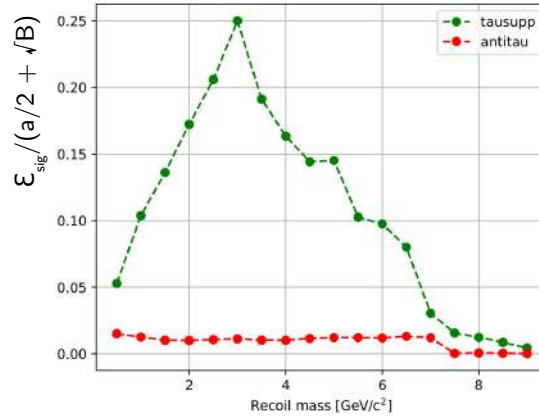


**Figure 6.7:** Punzi FOM as a function of the recoil mass for the final selection applied in the standard analysis (green) and with a partially reversed  $\tau$  suppression procedure (red).

### 6.3 Data validation with a reversed $\tau$ suppression procedure

A partially reversed  $\tau$  suppression procedure is used to select a background sample very close to that expected for the standard analysis of the  $Z'$  search, for the medium-high recoil mass region. Referring to the procedure described in Section 4.4, the selection on  $p_{\mu\mu}^T$  is not considered, while the optimal separation line in the bidimensional  $p_{rec}^{T,max}$  versus  $p_{rec}^{T,min}$  plane is used in a reversed way, by accepting only events below it (see for example Figure 4.9), which means rejecting the signal and selecting the background. Any hypothetical  $Z'$  signal is strongly suppressed, as shown in Figure 6.7, where the Punzi FOM following the application of such a procedure is compared with the one obtained at the end of the standard analysis. The distortion in the recoil mass distribution for the background induced by this procedure,

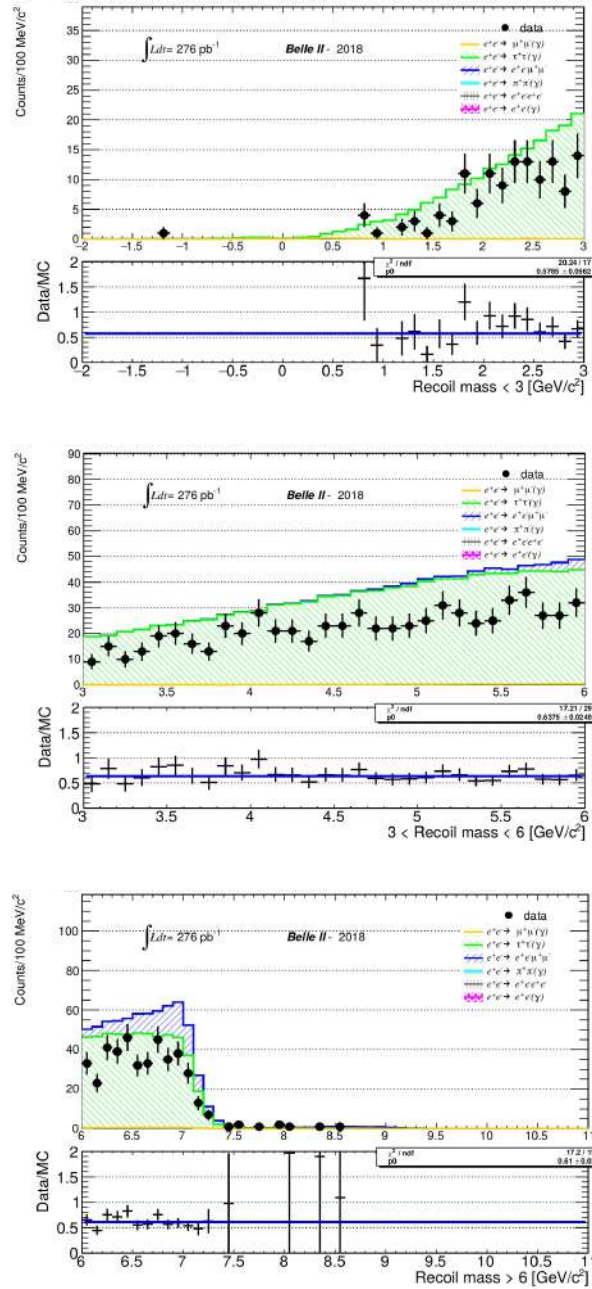


**Figure 6.8:** The recoil mass distribution for the  $\mu\mu$  sample with a partially reversed  $\tau$  suppression procedure is shown, in the three different mass intervals. The data/MC ratio reported in the inset plots confirms the discrepancy observed in the  $\mu\mu\gamma$  analysis.

compared to the one in the analysis before the application of the standard  $\tau$  suppression, is studied on the  $ee$  sample and found to be negligible.

The partially reversed  $\tau$  suppression procedure is applied on the  $\mu\mu$  and  $e\mu$  samples after the default event selection  $\tau$  described in Section 4.3, in order to avoid any unblinding issue.

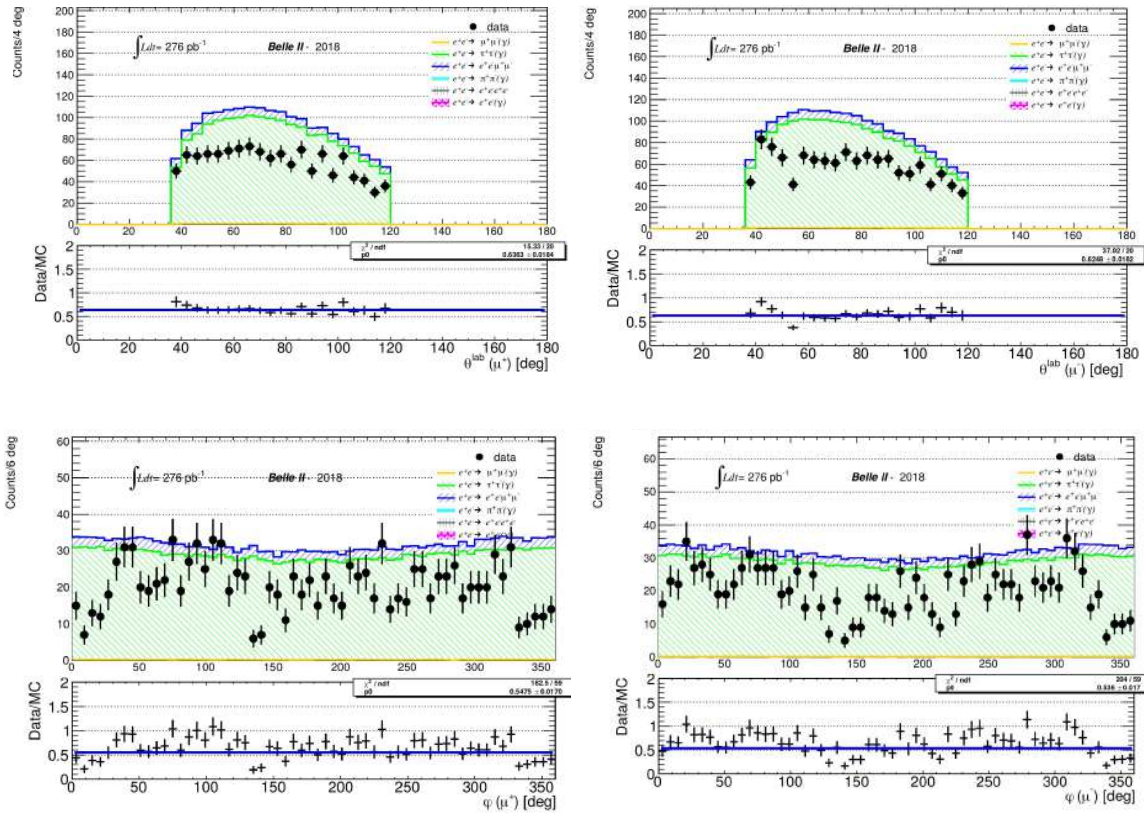


**Figure 6.9:** Most relevant angular variables exploited in the analysis are shown for  $\mu\mu$  validation sample with a partially reversed  $\tau$  suppression procedure, as follows (row order):

- (1) the Polar angle (in the laboratory frame) of the two muons, positive charge (left), negative charge (right);
- (2) Azimuthal angle (in the laboratory frame) of the two muons, positive charge (left), negative charge (right).

Results of the data/MC ratio on the full recoil mass spectrum gives  $(0.64 \pm 0.02)$  and  $(0.90 \pm 0.02)$  for  $\mu\mu$  and  $e\mu$  respectively and for the  $\mu\mu$  sample the comparison between data and Monte Carlo is reported in Figure 6.8, for the three different recoil mass intervals. These results fully confirm the data-Monte Carlo discrepancies observed with the  $\mu\mu\gamma$  sample (a summary is provided in Table 6.1 at the end of the chapter).

In analogy with the  $\mu\mu\gamma$  case in Figure 6.9, Figure 6.10, Figure 6.11 distributions of the important variables for the analysis are shown and no clear hint of a possible source of discrepancy comes out, being the data/MC ratio for all the distributions reasonably flat within the statistical fluctuations, with the exception of the data/MC comparison as a function of the azimuthal track angle (Figure 6.9), as already discussed for the  $\mu\mu\gamma$  case.

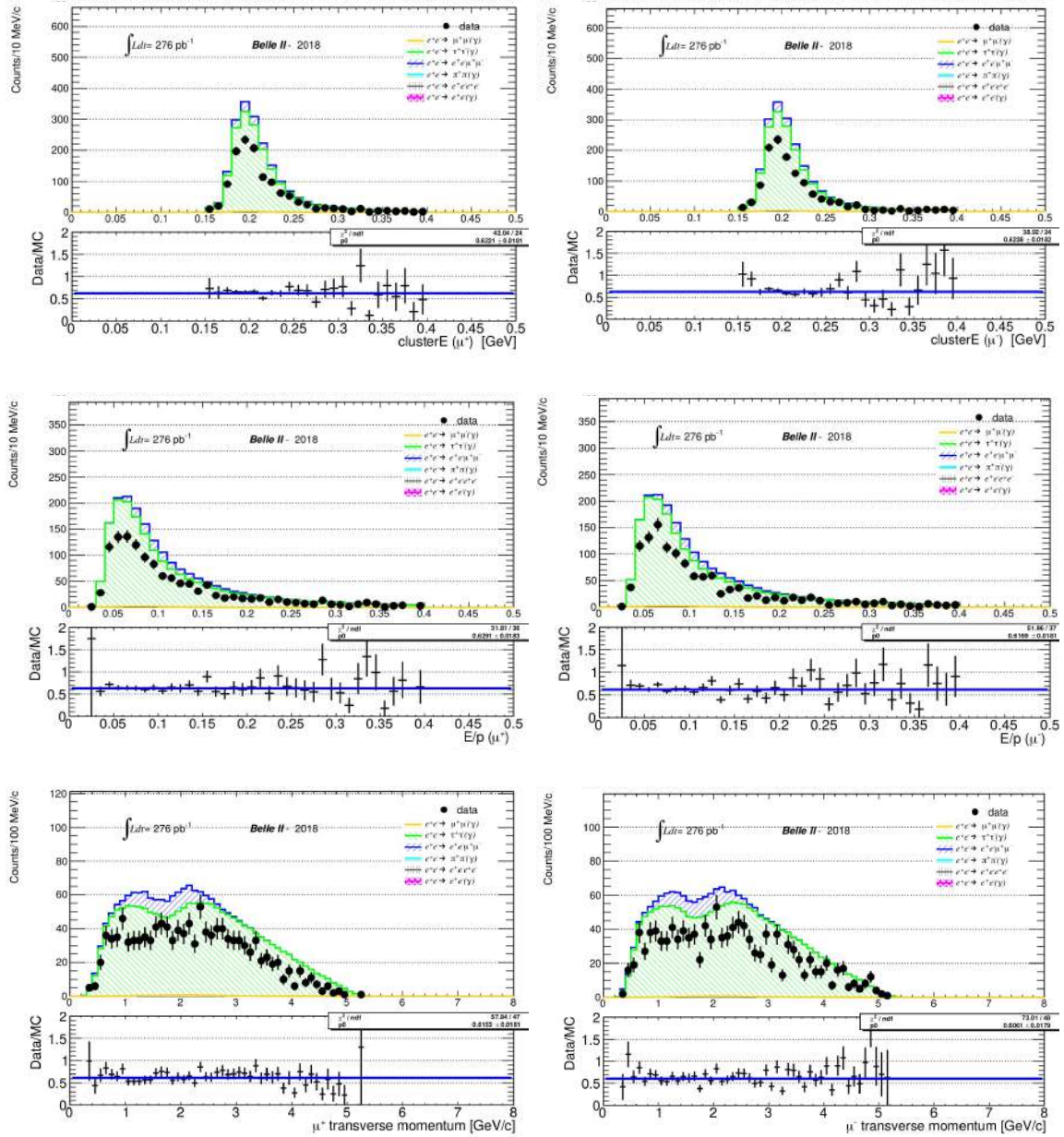


**Figure 6.10:** Most relevant kinematic variables exploited in the analysis are shown for the  $\mu\mu$  validation sample with a partially reversed  $\tau$  suppression procedure, as follows (row order):

- (1) Cluster energy of the two muons, positive charge (left), negative charge (right);
- (2) Ratio of the muon cluster energy and the muon track momentum, positive charge (left), negative charge (right);
- (3) Transverse momentum of the two muons, positive charge (left), negative charge (right).

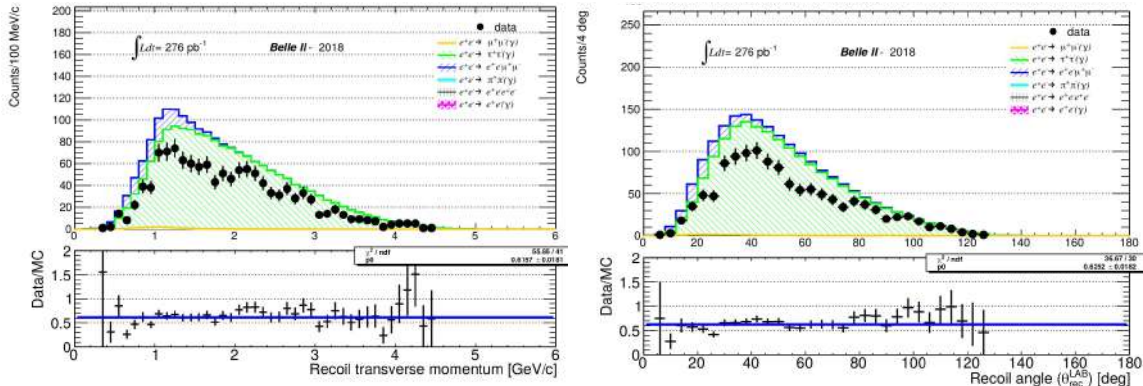


**Figure 6.11:** Transverse momentum (top) and polar angle (bottom) of the system recoiling against the two muons in the  $\mu\mu$  validation sample with a partially reversed  $\tau$  suppression procedure.

## 6.4 Trigger data validation

As already mentioned in the section regarding the  $\mu\mu\gamma$  validation sample, a possible cause of the data - Monte Carlo discrepancies could be the CDC `ffo` trigger, which had hardware issues during the Phase 2 data taking. Its efficiency is measured to be 0.79 with Bhabha events, using the ECL `hie` trigger as a reference, as documented in Section 7.2. Two muon events, due to the small energy depositions in the ECL, cannot be triggered by the ECL `hie` line, making the CDC trigger efficiency measurement statistically impossible on such sample. On the other hand,  $\mu\mu\gamma$  events as selected in Section 6.2 with photon energies above 1 GeV are able to fire the ECL trigger and thus allow the CDC trigger efficiency measurement, as independent cross-check of the results provided in Section 7.2. On the  $\mu\mu\gamma$  validation sample selected on data, the ECL trigger `hie` is required to be fired and the CDC trigger efficiency is defined as the ratio of the number of events where both the ECL and CDC trigger are fired and the number of triggered events, in which at least the ECL `hie` trigger fired. The result measured on  $\mu\mu\gamma$  events gives an efficiency  $\epsilon_{CDC} = 0.747 \pm 0.007$ , to be compared with 0.79 evaluated in Section 7.2. Since strong non-uniformities in the azimuthal angle distributions induced by the CDC trigger, as reported in Figure 6.4 and Figure 6.9, could be one of the causes of the data-MC discrepancy observed in both the  $\mu\mu\gamma$  and the  $\mu\mu$  validation samples, as additional check the trigger efficiency is measured as a function of the minimum and maximum track azimuth angle in the event, as shown in Figure 6.12: regions of higher trigger efficiencies are selected by requiring  $\phi_{min} < -1$  rad and  $(0.5 < \phi_{max} < 2)$  rad and for events belonging to these ranges the CDC trigger efficiency is recomputed to be  $\approx 0.88$ . Repeating all the validation analysis on the  $\mu\mu\gamma$  sample with this angular selection and using the corresponding trigger efficiency for normalization finally gives the same data-Monte Carlo discrepancy as measured in the  $\mu\mu\gamma$  sample without these additional angular selections and no real improvement is observed (results in the summary Table 6.1 ).

Furthermore, changing the energy threshold for the reconstructed photon from 1 GeV to 1.5 GeV does not affect the final results. As further validation, the CDC trigger efficiency is measured also in  $e\mu$  events, by requiring the presence of an electron with an energy larger than 1 GeV that can fire the orthogonal ECL trigger: very similar results both in terms

of efficiency and final data-Monte Carlo discrepancy have been found. By using the same technique of the conditional probability measured with two orthogonal trigger bits, the ECL trigger efficiency needed for the LFV  $Z'$  analysis is also provided, having as a reference the CDC trigger, in the  $\mu\mu\gamma$  sample and in the  $e\mu$  sample. Photon and electron reconstructed energies are required to be above 1.5 GeV in both cases. The results are consistent in both samples and give  $\epsilon_{ECL} = 0.96 \pm 0.01$ , where the uncertainty is statistical only.

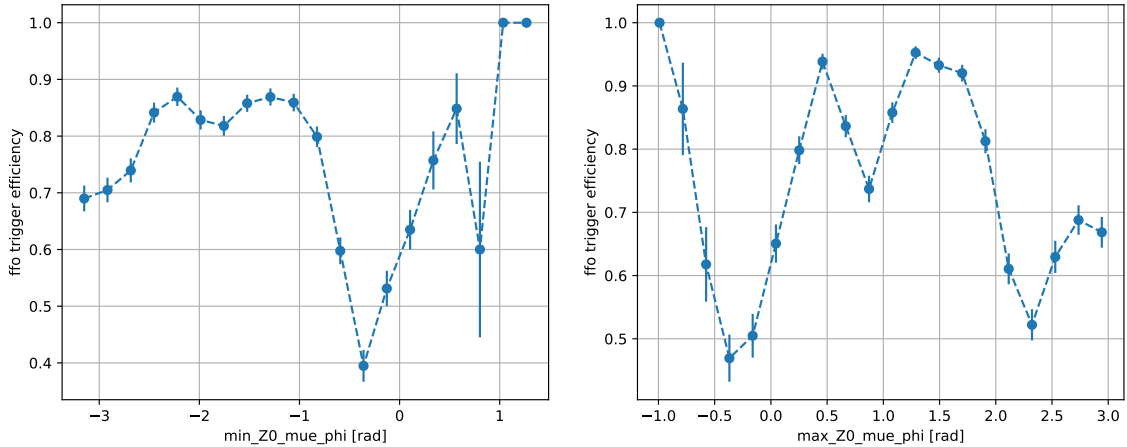


**Figure 6.12:** CDC trigger efficiency as a function of the minimum (left) and the maximum (right) track azimuth angle in  $\mu\mu\gamma$  events.

## 6.5 Data validation summary

The outcome of all data validation procedures discussed in the previous sections are summarized in Table 6.1. The results look coherent and point to a data-Monte Carlo discrepancy of  $\approx -35\%$  for  $\mu\mu$  events, which indicates the efficiency before  $\tau$  suppression selection is 35% lower in data than in simulation. Similarly for the  $e\mu$  events, the yield measured in data before the  $\tau$  suppression procedure is  $-10\%$  the yield measured in the simulation. The  $-10\%$  data-MC discrepancy in  $e\mu$  events is explained by the tracking inefficiency, as evaluated in Section 7.4. Therefore it is accounted as a measured inefficiency and the simulated samples are simply rescaled by 0.90 to match the yield observed in data control samples. No systematic uncertainty due to this discrepancy is additionally assigned to the  $e\mu$  events, since it is already accounted for in the systematic uncertainty ascribed to the tracking performance (see Section 7.4). For the standard  $Z'$  search, the results of the data validation studies consistently point to a residual  $-25\%$  unexplained deficit in the two-muon event yield observed in data with respect to the simulated background yield, which must be managed both in the background and signal efficiency estimate and in the evaluation of the systematic uncertainty in the background yield and in the signal efficiency, as it will be explained in the next chapters.

A deep investigation has been performed to understand the nature of such a discrepancy, but nothing relevant is found. The most probable explanation is related to the difficulties in muon detection experienced on several sides, in the trigger, tracking performances and in the ECL-based identification, that are expected to be cured in the Belle II 2019 data set.

---

Moreover, Phase 3 data sets will rely on a recovered KLM detector and a generally improved tracking system due to the full VXD in place and no actual issues are expected on muon detection from the preliminary performance studies on the new 2019 data. For the Phase 2 data analysis, to correctly and reliably account for the outcome of the data validation study, the background predictions from the simulation and the signal efficiency are corrected with a scaling factor of 0.65 for  $\mu\mu$  events, as further discussed in Chapter 8, where the associated systematic uncertainties will be also explained.

**Table 6.1:** Summary of the validation studies for the data/Monte Carlo ratio on the various samples. The second row shows the trigger line used in the corresponding study: hereafter the CDC ffo trigger line is defined as bit $_{CDC}$  and the ECL hie trigger line as bit $_{ECL}$ . Data/MC ratios are shown for three different recoil mass intervals and for the total mass range.

Mass window [GeV/ $c^2$ ]	$\mu\mu\gamma$	$\mu\mu\gamma$	$e\mu\gamma$	$e\mu\gamma$	$e\epsilon\gamma$	$e\epsilon\gamma$	$\mu\mu+\text{anti } \tau$	$e\mu+\text{anti } \tau$
-	bit $_{CDC}$	bit $_{ECL}$	bit $_{CDC}$	bit $_{ECL}$	bit $_{CDC}$	bit $_{ECL}$	bit $_{CDC}$	bit $_{CDC}$
-2 ÷ 3	0.65±0.02	0.67±0.02	0.8±0.3	1.3±0.3	0.88±0.01	0.99±0.01	0.66±0.06	0.94±0.07
3 ÷ 6	0.84±0.07	0.76±0.07	0.9±0.1	0.95±0.13	1.10±0.10	1.14±0.01	0.65±0.02	0.89±0.03
6 ÷ 11	0.9±0.1	0.72±0.13	0.9±0.2	0.93±0.15	2.13±0.12	1.3±0.1	0.63±0.03	0.89±0.03
Overall	0.68±0.02	0.68±0.02	0.92±0.09	0.96±0.10	0.90±0.01	0.99±0.01	0.64±0.02	0.90±0.02

## Chapter 7

# Detector studies and systematic uncertainty evaluation

In this chapter the evaluation of the main sources of systematic uncertainty which affect the measurement of the signal cross section and need to be taken into account for the upper limit calculation is discussed (Section 7.1). The systematic uncertainties come either from detector effects, as in resolutions and in efficiencies that have to be measured on real data, and from the differences between the simulation, used for analysis optimization and for the signal efficiency estimation, and data. Both types of contributions need to be estimated with dedicated performance and data validation studies.

The validation procedure already allowed to estimate the residual discrepancy observed between Monte Carlo and data, after the corrections for the measured efficiencies have been applied. This chapter will provide the overview of the methods developed to measure these efficiencies with their associated systematic uncertainties. Hereafter, the main results of these studies (Section 7.2, 7.3, 7.4), which have been described in details elsewhere in dedicated technical notes (see Appendix B), are reported. In the final Section 7.4 the measurement of the discrepancy in the track reconstruction efficiency on data and Monte Carlo will be addressed in more details, since it has been crucial to partially explain the observed deficit in data-MC comparisons. This study has been one of my major tasks for the  $Z'$  project, as well as the full validation procedure developed for the presented search.

### 7.1 Main systematic uncertainty sources

In each recoil mass bin, the  $Z'$  cross section can be computed from the measured event yield according to the formula:

$$\sigma_{Z'} = \frac{N_{\text{obs}} - B_{\text{exp}}}{L \times \epsilon_{\text{sig}}}, \quad (7.1)$$

where the inputs are the number of observed events  $N_{\text{obs}}$ ; the effective data integrated luminosity  $L$ ; the signal efficiency  $\epsilon_{\text{sig}}$  and the expected total background yield  $B_{\text{exp}}$ , which are both computed from the simulated samples, but corrected for the data-MC discrepancy observed in the validation studies. Their associated systematic uncertainties contribute to the total systematic error in the measured cross sections, which has to be accounted for when

computing the expected sensitivity (see Section 8.1, the details of the computation are given in Appendix C.1).

### Systematic uncertainty in the luminosity measurement

The effective luminosity  $L$  refers to the integrated data luminosity of the runs on which the trigger information could be retrieved and whose trigger efficiency could be measured, as explained in Section 7.2. The offline luminosity measurement in Phase 2 is performed independently on two different samples, radiative Bhabha and two-photon events. The overall measurement strategy and the techniques to estimate the associated uncertainty are explained in the Belle II paper for the offline luminosity measurement in [86]. The relative systematic uncertainty which is taken into account for the upper limit calculation is 1.5%.

### Systematic uncertainty in the signal yield

The systematic uncertainty in the number of observed events receives contributions from the applied signal yield extraction technique, which relies on a specific signal model for the estimation of the signal width. Dedicated studies reported in Chapter 5 have shown that the implemented fit procedure to extract the signal width, which is crucial for the binning scheme definition, is robust and unbiased. Moreover, the detector resolution effect is correctly taken into account in the simulations and has no additional impact on the estimation of the signal width and thus its systematic uncertainty contribution is found to be negligible.

### Systematic uncertainty in the background yield

As far as the expected background yield is concerned, its contribution to the systematic uncertainty is mainly due to the effect of the applied selections and to the residual discrepancy observed between data and Monte Carlo that has been measured on the validation control samples. It can be attributed to different sources, as the difference in the track reconstruction efficiency evaluated on data and on simulations and the muon detection in Phase 2 data, which also affect in a totally correlated way the signal efficiency.

After rescaling the expected background yield for the measured data-MC discrepancy as described in the previous chapter, the difference between the simulated number of events and the number of events observed in the recoil mass spectrum on data with a reversed  $\tau$  suppression procedure has been taken as systematic uncertainties on the expected background yield and it is assessed to be 2%.

The  $\tau$  suppression procedure adds a further contribution to the systematic uncertainty on the expected background yield, which is driven by the low statistics of the control samples in data and is evaluated to be 22% from the  $ee$  control sample as explained in Section 6.1. However, this uncertainty is not the dominant one when propagating on the signal cross section computation, since the background yield enters the formula in Equation 7.1 as a subtraction and therefore the associated error is not multiplicative in the estimation of the final uncertainty. Moreover, it is statistically driven, therefore it is expected to further reduce with larger data sets.

### Systematic uncertainty in the selection efficiencies

The main source of systematic uncertainty comes from the estimate of the signal efficiency, which receives contributions from the trigger efficiency, the track reconstruction efficiency, the particle identification efficiency, as well as from the applied requirements for background rejection ( $\tau$  suppression procedure). Regarding the latter, its contribution is evaluated through the validation procedure (see previous chapter). For the above mentioned efficiencies, a full program of performance studies has been devised on Phase 2 data. In the following sections, the strategy overviews and the results important for this analysis are reported.

### Systematic uncertainty summary

A summary of the systematic uncertainty contributions accounted for in the 90% CL exclusion upper limit computation is shown in Table 7.1. The systematic uncertainties due to trigger efficiency, tracking efficiency and particle ID selections are considered to affect in a completely correlated way the signal efficiency and the background yields and similarly for the luminosity measurement uncertainty, it is assumed to affect in a completely correlated way the background expectations.

**Table 7.1:** Systematic uncertainties affecting the  $\mu\mu$  and  $e\mu$  samples, referred to the standard and LFV  $Z'$ , respectively.

Source	Affected quantity	$\mu\mu$	$e\mu$
Trigger efficiency	$\epsilon_{sig}$	6%	1%
Tracking efficiency	$\epsilon_{sig}$	4%	4%
PID	$\epsilon_{sig}$	4%	4%
Luminosity	$L$	1.5%	1.5%
$\tau$ suppression (background)	$B_{exp}$	22%	22%
Background before $\tau$ suppression	$B_{exp}$	2%	2%
Discrepancy in $\mu\mu$ yield (signal)	$\epsilon_{sig}$	12.5%	-

The data validation procedure has shown a  $\approx -35\%$ (10%) discrepancy between data and simulations for the  $\mu\mu(e\mu)$  sample, of which  $\approx 10\%$  can be ascribed to the tracking inefficiency. Therefore, while for the  $e\mu$  sample the full observed discrepancy is understood and explained by means of performance measurements, for the  $\mu\mu$  sample after all the performed studies, no evident explanation could be advocated to explain the residual  $-25\%$  deficit observed in data when comparing to simulation. Therefore, both the background level and the signal efficiency for the  $\mu\mu$  case have been scaled by the factor 0.65 to match MC expectations to what observed in data and different systematic uncertainties have been assigned to the background yields and the signal efficiency, according to the following strategies:

- the validation procedure with a reversed  $\tau$  suppression selection (see Section 6.3) is assumed to provide a reliable estimate of the expected background yield and thus the statistical uncertainties of this measurement,  $\pm 2\%$  (Table 6.1), is assigned as associated systematic error, and later on confirmed from the results of the background measurement on real data (no reverse  $\tau$  suppression applied, Figure 8.4), after the approval for unblinding;

- an additional systematic uncertainty is assigned to the total number of expected background events only, due to the effect of the  $\tau$  suppression procedure measured on the  $ee$  control sample within a statistical accuracy of 22%. This statistical error is then assigned as systematic uncertainty in the background yield; no systematic uncertainty due to this effect is considered on the signal efficiency, as this selection is quite mild on the  $Z'$  side and the distributions on which it is based are well reproduced in the simulation;
- half the size of the discrepancy coming from an unknown source (residual  $-25\%$  data-MC discrepancy) is assigned as a systematic uncertainty in the signal efficiency of  $\pm 12.5\%$ . Unlikely to what has been devised for the uncertainty in the background yields due to the  $\tau$  suppression procedure (previous point), where the measured data-MC discrepancy is fully used as systematic uncertainty (100% of the dominating statistical error), since it applies directly to the measured background level, the quoted 12.5% uncertainty in the signal efficiency corresponds to 50% the measured unknown residual discrepancy in the muon yields. This choice is motivated by the fact that this systematic contribution refers to a correction factor (the 0.65 scaling applied to the efficiency), not directly to the data-MC difference itself. This is an arbitrary and widely established choice, commonly used in most of the correction procedures applied in high energy physics analyses. It is for example analogous to what usually happens for PID correction factors, where the bin-by-bin correction extracted from the measured MC-data discrepancy on well defined control samples (e.g. thanks to PID table as a function of the main kinematical distributions) is applied to the simulation and half of the measured discrepancy is additionally associated as systematic uncertainty in the selection efficiency due to the correction factor applied. Though this is an arbitrary choice, every step of the applied procedure has been clarified to the reader, who is thus fully informed on how the measured discrepancy affects the result.

A summary of the studies of detector effects and systematic uncertainties mentioned in this chapter is reported in the next sections. These studies refer to the standard  $Z'$  case only, unless where LFV  $Z'$  is explicitly mentioned.

## 7.2 Trigger efficiency

Two different trigger lines have been used for the standard and LFV  $Z'$ : the CDC two-track trigger and the ECL trigger respectively. The performances of the CDC two-track trigger are studied on data samples selected by means of orthogonal ECL lines. The CDC trigger corresponds to what has been defined in Table 6.1 as trigger  $\text{bit}_{\text{CDC}}$  to underline which detector is used to send the trigger. The trigger  $\text{bit}_{\text{CDC}}$  selects non-Bhabha events with at least two tracks in the CDC acceptance, with opening angle in  $\phi$ -plane of at least  $90^\circ$ . To emulate the effects of the trigger selection in simulations, the same criteria required to fire the CDC trigger on data have been added as a part of the event selection (see Section 4.3). The trigger selection efficiency is evaluated with respect to the orthogonal ECL trigger line ( $\text{bit}_{\text{ECL}}$ ) and it is computed as the ratio between the events which fired both the triggers and

the events firing at least the ECL trigger:

$$\epsilon_{CDC} = \frac{N(\text{bit}_{\text{CDC}} \text{ AND } \text{bit}_{\text{ECL}})}{N(\text{bit}_{\text{ECL}})}. \quad (7.2)$$

It has been found that  $\epsilon_{CDC}$  varies from runs to runs (the interested reader could see the dedicated trigger performance study summarized in Appendix B.1) and to ensure a reliable and stable estimate of the trigger efficiency only runs where the CDC trigger efficiency is validated and is higher than 50% have been used for this work. The final trigger efficiency is defined as the average of efficiencies measured in good runs weighted with the luminosity of the corresponding run and gives  $(79.0 \pm 0.1)\%$  for a total integrated luminosity of  $276 \text{ pb}^{-1}$ , where the uncertainty is statistical only. The systematic uncertainty in the trigger efficiency due to kinematic dependencies has also been evaluated as the relative variation of the average efficiency in bins of polar angle, transverse momentum, and number of track hits in the CDC. A 6% variation has been measured and it is assigned as systematic uncertainty in the measurement of  $\epsilon_{CDC}$ .

The LFV  $Z'$  search exploits Phase 2 data selected by the ECL trigger. As this is validated with the use of the two-track CDC trigger, the same integrated luminosity of  $276 \text{ pb}^{-1}$  is considered. The performances of the ECL trigger line have been studied using  $e^+e^- \rightarrow \mu^+\mu^-\gamma$  events selected with the CDC two-track trigger for photon energies larger than 1 GeV and the corresponding plateau efficiency is found to be  $(96 \pm 1)\%$ , flat in the ECL barrel region (see Sections 6.4).

### 7.3 Particle ID selection

Due to the already mentioned problem with the KLM firmware during Phase 2, no KLM-based muon identification variables are available for such data set, and the particle identification is performed through selections based on ECL variables (Section 4.2 and 4.3). The performance of these selections has been studied in a dedicated technical note, as reported in Appendix B.2. The efficiency of the particle identification selections has been estimated with a self-tagging technique on  $e^+e^- \rightarrow e^+e^-\mu^+\mu^-$  events on data and simulations. The deviation from unit of the measured correction factor, defined as the ratio of efficiencies computed on data and on simulations, is assigned as systematic uncertainty. In the fiducial kinematic region considered for this analysis, which corresponds to the ECL barrel region, the data-MC discrepancies per track have been measured to be of order 2%. A systematic uncertainty of 4% is assigned to both the signal efficiency and the total background yield due to the particle ID selection, where the error propagation assumes a 100% positive correlation between the two track probabilities. Though this is a conservative choice that may lead to overestimate the systematic uncertainty contribution, it has been tested that assuming no correlation and thus a reduced systematic of  $\sqrt{2}\sigma_{\text{track}} = 2.8\%$  has a negligible impact on the computation of the final result (see Section 8.1) and therefore the conservative approach has been preferred.

### 7.4 Tracking efficiency

The tracking efficiency has been measured by using tag-and-probe techniques in radiative Bhabha events and in  $e^+e^- \rightarrow \tau^+\tau^-$  events, for the latter exploiting a particular topology,

known as 3x1-prong decay<sup>1</sup>. The inefficiency of the tracking system was found to amount to 10% for two-track final states, with a 4% systematic uncertainty due to kinematic dependencies. Since the tracking efficiency study has been crucial to understand part of the observed data-MC discrepancy, the rest of the Section will be dedicated to explain the strategy and the main findings of the second method mentioned above, which exploits the  $e^+e^- \rightarrow \tau^+\tau^-$  event topology to infer the existence of a track and measure the detection efficiency of the track reconstruction algorithms in both real data and simulations.

The  $e^+e^- \rightarrow \tau^+\tau^-$  process provides an ideal test-bed for the performance of track reconstruction algorithms. The cross section for  $\tau$ -pair production is large and close to that of  $B$  meson pairs at the  $\Upsilon(4S)$  resonance energy. In addition, the jet-like topology of  $\tau$  decay products is suitable to study tracking performance in a low multiplicity but high-density track environment. Moreover, the  $\tau$ -pair kinematics cover a lower track momentum region compared, for example, to Bhabha events.

The tracking efficiency is measured using a tag-and-probe method, similar to the one developed previously by the *BABAR* collaboration [94]. The method targets  $e^+e^- \rightarrow \tau^+\tau^-$  events, where one  $\tau$  lepton decays leptonically ( $\tau \rightarrow \ell^\pm \nu_\ell \bar{\nu}_\tau$ ,  $\ell = e, \mu$ ) while the other decays hadronically into three charged pions ( $\tau \rightarrow 3\pi^\pm \nu_\tau + n\pi^0$ ). These decays will be referred to, hereafter, as the *1-prong* and *3-prong*  $\tau$ -decays, respectively.

Two channels according to the origin of the track from 1-prong  $\tau$ -decay have been defined:

- *electron channel* — the 1-prong track originates from an electron ( $\tau \rightarrow e^\pm \nu_e \bar{\nu}_\tau$ ).
- *muon channel* — the 1-prong track originates from a muon ( $\tau \rightarrow \mu^\pm \nu_\mu \bar{\nu}_\tau$ ) or from  $\tau \rightarrow \pi^\pm \nu_\tau + n\pi^0$ .

In fact, this channel contains a sizable contribution from  $\tau$  hadronic decays where the 1-prong track originates instead from a charged pion, due to the high misidentification rate for erroneously identify a pion as a muon. In Phase 2 data, with no muon ID available, it is not possible to distinguish between muons and pions being the ECL-based selection for muons the same as for pions.

The tree-level Feynman diagram for the targeted process can be seen in Figure 7.1.

Three good quality tracks with total charge  $\pm 1$  are used to tag  $\tau$ -pair events, in which the existence of the additional fourth track can be inferred from charge conservation, since in the event the total charge must equal to zero. This allows to probe the tracking performance and to compute the per track reconstruction efficiency  $\epsilon_{track}$  defined by:

$$\epsilon_{track} = \frac{N_4}{N_3 + N_4}, \quad (7.3)$$

where  $\epsilon_{track}$  also include the detector acceptance factor;  $N_4$  is the number of events where all four tracks are found, while  $N_3$  is the number of events where the fourth track is not found. The  $N_4$  and  $N_3$  samples will be referred to, hereafter, as the 4- and 3-track samples, respectively. Note that the 3-track sample do always include the 1-prong side track.

When performing physics analyses, it is essential to measure the tracking efficiency in data and compare to the results of the same measurement on the MC simulations for two

<sup>1</sup>The 3x1 prong topology refers to a specific final state of the process  $e^+e^- \rightarrow \tau^+\tau^-$  where one  $\tau$  decays leptonically to one charged lepton and its associated neutrino, and the other decays hadronically with exactly 3 charged pions among its decay products.

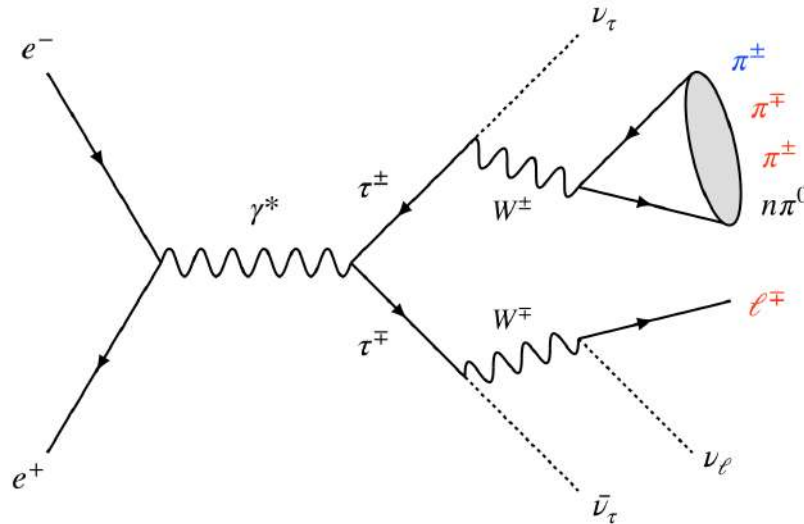


**Figure 7.1:** Feynman diagram for the  $e^+e^- \rightarrow \tau^+\tau^-$  process targeted by the tag-and-probe method. The tag objects ( $\ell^\mp\pi^\pm\pi^\mp$ ) are highlighted in red, while the probe pion is highlighted in blue.

reasons. First, to assign a systematic uncertainty for the mismodeling of the efficiency in MC simulation, which can be parameterized by the formula:

$$\begin{aligned} \delta &= 1 - \frac{\epsilon_{Data}}{\epsilon_{MC}} \\ &= 1 - \left( \frac{N_4^{Data}}{N_3^{Data} + N_4^{Data}} \right) \cdot \left( \frac{N_3^{MC} + N_4^{MC}}{N_4^{MC}} \right), \end{aligned} \quad (7.4)$$

where  $\delta$  stands for the data-MC discrepancy and  $\epsilon_{Data}$ ,  $\epsilon_{MC}$  are the tracking efficiencies measured in data and MC, respectively. Second, to apply kinematically dependent corrections using the scale factors  $SFs = \epsilon_{Data}/\epsilon_{MC}$  to match the results from simulations to what measured on data. Hereafter, only the discrepancy computation will be provided, due to the poor statistics of the Phase 2 data. The scale factor maps are not treated in this study and they will be available with larger statistics.

When computing  $\epsilon_{Data}$  the yields that enter Equation 7.3 are the background subtracted data described below, while for  $\epsilon_{MC}$  they come from  $\tau$ -pair MC simulation.

To correctly measure the tracking efficiency discrepancy, a specific calibration procedure to apply to the discrepancy estimator as computed in equation 7.4, which involves a full MC simulation study, has been developed, as described at the end of this Section.

### Data and MC Samples

The final results of this study have been produced on the eighth reprocessing of Phase 2 data, by using the basf2 software release `release-03-00-03` with the corresponding global tag for condition data GT528 (`data_reprocessing_proc8`). Selected events on data have been required to fire the ECL trigger line `hie` (see Section 7.2 for the trigger logic description), which corresponds to an integrated luminosity of  $381 \text{ pb}^{-1}$ .

For the simulation of the signal and background processes, the official MC11 productions were used (Table 7.2), which were produced with the nominal beam background conditions. Apart from the signal process  $e^+e^- \rightarrow \tau^+\tau^-$ , the analyzed MC samples correspond to the main sources of background expected for this study, which include the continuum hadronization processes  $e^+e^- \rightarrow q\bar{q}$ , with  $q = u, d, s, c$ , the two-lepton (Bhabha, dimuon) and two-pion radiative final-state processes and the four-lepton final state events.

**Table 7.2:** Summary of the simulated samples used in this study.

Process	Cross section ( $E^{CM} = \mathcal{T}(4S)$ )	Number of events
$e^+e^- \rightarrow \tau^+\tau^-$	0.92 nb	$36.8 \times 10^6$
$e^+e^- \rightarrow q\bar{q}$ ( $q = u, d, s, c$ )	3.69 nb	$7.38 \times 10^6$
$e^+e^- \rightarrow e^+e^-\gamma$	300 nb	$10 \times 10^6$
$e^+e^- \rightarrow \mu^+\mu^-\gamma$	1.148 nb	$10 \times 10^6$
$e^+e^- \rightarrow e^+e^-e^+e^-$	39.7 nb	$50 \times 10^6$
$e^+e^- \rightarrow e^+e^-\mu^+\mu^-$	18.9 nb	$40 \times 10^6$
$e^+e^- \rightarrow \pi^+\pi^-\gamma$	0.03 nb	$10 \times 10^6$

## Trigger

For both the electron and muon  $\tau$ -decay channels, events in data are required to fire the ECL trigger  $\text{bit}_{\text{ECL}}$ , which has the lowest Level 1 energy threshold among the ECL triggers (1 GeV) and includes a Bhabha veto requirement. CDC triggers were also considered, however they were shown to have a lower efficiency and to be correlated by construction to the track reconstruction efficiency itself, since they rely on the detection of CDC-tracks. Therefore they were discarded and only used as orthogonal trigger lines to measure the ECL trigger efficiency.

A significant fraction of runs in Phase 2 are missing the ECL trigger information. Because of this, only  $381 \text{ pb}^{-1}$  of the available  $504 \text{ pb}^{-1}$  data set is usable after the ECL trigger requirement.

In order to measure the ECL trigger efficiency in data, an orthogonal reference trigger ( $\text{bit}_{\text{CDC}}$ ) is used:

$$\epsilon_{ECL} = \frac{N(\text{bit}_{\text{CDC}} \text{ AND } \text{bit}_{\text{ECL}})}{N(\text{bit}_{\text{CDC}})}, \quad (7.5)$$

where the reference trigger requires at least two CDC tracks with an opening angle larger than  $90^\circ$  and a Bhabha veto requirement.

Figure 7.2 shows the measured ECL trigger efficiency in data as defined in equation 7.5. In this figure, all requirements that will be described below regarding the offline selections are applied, excluding the invariant mass selections, which were dropped to improve the usable statistics for this measurement.

Muons deposit less energy in the ECL compared to electrons, so it is more likely for events in the muon channel to have a total ECL energy value below the 1 GeV trigger threshold. This can be seen in Figure 7.2, where the ECL trigger efficiency in the muon channel is  $\sim 10\text{-}20\%$  lower than in the electron channel.

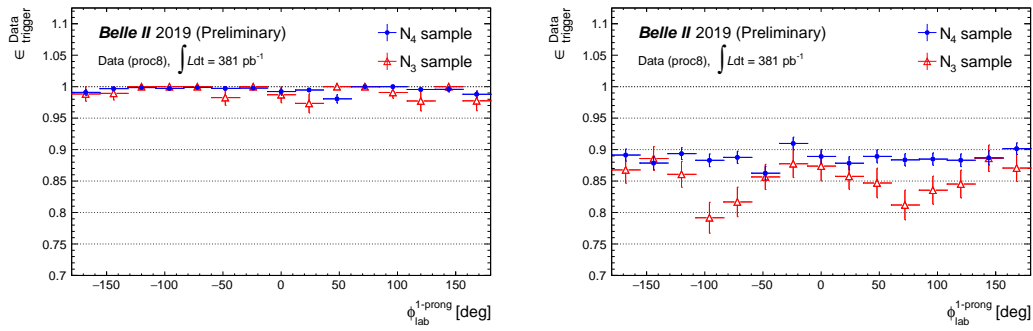


**Figure 7.2:** The measured ECL trigger efficiency in data as a function of the 1-prong track  $\phi$  for the electron channel (left) and the muon channel (right). The 4- and 3-track samples are shown in blue and red, respectively.

### Track selections

Since in the tag-and-probe approach  $\tau$ -pair events are tagged by the presence of three good quality tracks with total charge equal to  $\pm 1$ , it is important to define the different classes of selected tracks for this analysis: three categories of tag tracks depending on whether they originates from a pion, electron or muon have been exploited. Regarding the probe track, which belongs to a fourth separate category, a looser pion selection is also defined. The selections that define these four classes of tracks are summarized in Table 7.3. Depending

**Table 7.3:** Track selection criteria are listed below. The selection value which refers to the muon channel only is indicated in square brackets. Any selections that do not apply to a particular track type are indicated by a dash.

Track class	Probe pion	Tag pion	Tag electron	Tag muon
$p_T$ [MeV]	—	$> 200$ [400]	$> 200$	$> 400$
$\cos\theta$	(-0.8660, 0.9565)	(-0.8660, 0.9565)	(-0.8660, 0.9565)	(-0.8660, 0.9565)
$ d_z $ [cm]	$< 5$	$< 5$	$< 5$	$< 5$
$ d_r $ [cm]	$< 1$	$< 1$	$< 1$	$< 1$
$\frac{E_{\text{cluster}}}{p}$	$< 0.8$	(0, 0.6)	(0.8, 1.2)	(0, 0.4)
$E_{\text{cluster}}$ [MeV]	—	$> 0$	$> 0$	(0, 400)
nCDCHits	—	$> 0$	$> 0$	$> 0$

on the channel and sample, events are required to satisfy different track multiplicity requirements, summarized in Table 7.4. Note that the muon track selections are a subset of the tag pion selections, and that both are a subset of the probe pion selections. Due to the  $\frac{E_{\text{cluster}}}{p}$  requirement, the electron track selections are orthogonal to the other track types. Events are allowed to contain additional tracks that fail each of the four track selection criteria defined in Table 7.3.

**Table 7.4:** Track multiplicity criteria for the tagged event reconstruction are listed below. Any selections that do not apply to a particular channel and sample are indicated by a dash. Note that the muon and pion tag tracks are contained in the probe pion track ensemble, by definition of the respective track lists (see above Table 7.3).

	$N_{\text{pion}}^{\text{probe}}$	$N_{\text{pion}}^{\text{tag}}$	$N_{\text{electron}}^{\text{tag}}$	$N_{\text{muon}}^{\text{tag}}$
electron channel, 4-track sample	3	$\geq 2$	1	–
electron channel, 3-track sample	2	2	1	–
muon channel, 4-track sample	4	$\geq 3$	–	$\geq 1$
muon channel, 3-track sample	3	3	–	$\geq 1$

### Background suppression

After requiring events to pass the trigger and track selection requirements, there is still substantial background contamination coming mainly from the QCD continuum ( $e^+e^- \rightarrow q\bar{q}$ ,  $q = u, d, s, c$ ) and radiative dilepton processes ( $e^+e^- \rightarrow \ell^+\ell^-\gamma$ ,  $\ell = e, \mu$ ). Additional selections are applied to suppress the background contributions. Hereafter, the two tag-tracks from the 3-prong  $\tau$ -decay will be referred to as the *2-prong* tracks.

- *angular isolation:* the  $\tau$  leptons are produced back-to-back in the CM frame. Their momentum in this frame is approximately 2.8 GeV/c such that in most of the cases the decay products momenta are very collimated along the direction of flight of the parent  $\tau$  and almost back-to-back, with a large angular separation. To exploit this topology, the 1-prong track is required to have an opening angle in the CM frame with each 2-prong tracks that is at least  $120^\circ$ ;
- *1-prong momentum:* the 1-prong track is required to have a CM frame momentum that is less than 80% and more than 20% of the beam energy. The upper threshold significantly reduces the radiative dilepton background, while the lower threshold helps to suppress the QCD continuum;
- *invariant mass:* the invariant mass of the 2-prong tracks ( $m_{\pi\pi}$ ) is required to satisfy:
  - $|m_{\pi\pi} - m_\rho| < 100$  MeV, for events where the 2-prong tracks have opposite-sign electric charge (*OS charge*). This targets hadronic  $\tau$ -decays with an intermediate  $\rho$  meson ( $\rho \rightarrow \pi^+\pi^-$ ), and significantly reduces the QCD continuum.
  - $300 \text{ MeV} < m_{\pi\pi} < m_\tau$ , for events where the 2-prong tracks have same-sign electric charge (*SS charge*). This helps to reduce the QCD continuum for SS charge events.

The relevant variables used for background rejection are shown in Figure 7.3 for the MC samples. Note that only after the angular isolation requirement the 1-prong track is uniquely identified per each tagged event, due to the non-orthogonal track lists that are used for the muon channel (muons and tag pions are both sub-ensemble of the probe track list). Before this requirement, only with the track selections is not possible to distinguish the 2-prong pions from the 1-prong muon(pion) track. The angular isolation ensures that the candidate multiplicity in the N3 sample is exactly one, being this crucial to avoid multiple counting. This has been checked in both data and simulation. However, multiple N4 candidates per event are still allowed since they are produced by probe pion tracks which pass all the selections

applied also on the 2-prong pion tracks and therefore the 3-prong side tracks can be mutually exchanged. Since the choice of the best candidate would in this case imply a selection on the probe track and could potentially introduce a bias in the tracking efficiency measurement, all the possible N4 combinations, which from pure combinatorial counting, without considering the charge constraints and the applied track and background reduction selections, could be up to a maximum of three, are accepted and averaged with the weight  $w = 1/N_{cand}$ , where  $N_{cand}$  indicates the event candidate multiplicity after the final selections. Furthermore, any selections on variables that heavily depend on the existence of the probe track, such as the Thrust axis<sup>2</sup> related variables and the total visible energy in the CM frame, have been avoided. This is because such selections would have significantly different signal efficiencies in the 4- and 3-track samples, and thus bias the tracking efficiency measurement.

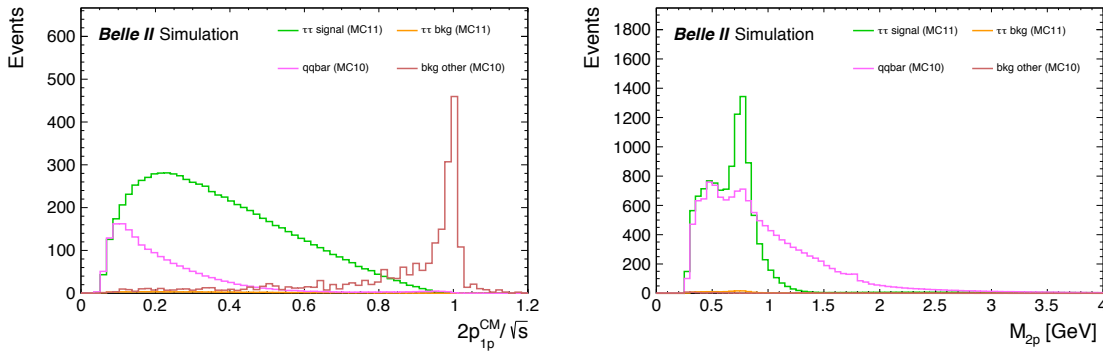


**Figure 7.3:** Distributions in MC simulation of the 1-prong track momentum in the CM frame relative to the beam energy  $\sqrt{s}/2$  (left) and the 2-prong track invariant mass for OS charge events, after the 1-prong momentum cut (right).

### Data-MC Comparison

Distributions of the 2-prong track invariant mass are reported in Figure 7.4 and 7.5, for the electron and muon channels respectively. The distributions of the 1-prong track  $p_T$ ,  $\theta$  and  $\phi$  have been also studied and the data/MC ratios have been shown to be flatly distributed. For the 4-track samples they are consistent with 1 within the uncertainty, indicating a good agreement between simulation and data. For the 3-track samples the data/MC ratios are uniformly distributed around a value above 1, where the fraction of data exceeding unity is due to the additional inefficiency which affects actual data. All the relevant plots are reported in Appendix B.3 for the electron and muon channels. All of the requirements previously described for track selections and background suppression are applied. Additionally, the MC yields are normalized to the effective luminosity of the sample  $\left(\frac{N_{gen}}{\sigma[pb]}\right)$ , scaled to  $381 \text{ pb}^{-1}$  and corrected in a bin-by-bin manner by the measured trigger efficiency in data (see Equation 7.5). This applies to all the subsequent plots that will be shown hereafter.

<sup>2</sup>The Thrust axis is defined as the direction which maximizes the sum of the projections of the decay product momenta; in analyses with  $\tau_s$ , it reliably estimates the direction of flight of the decaying lepton.

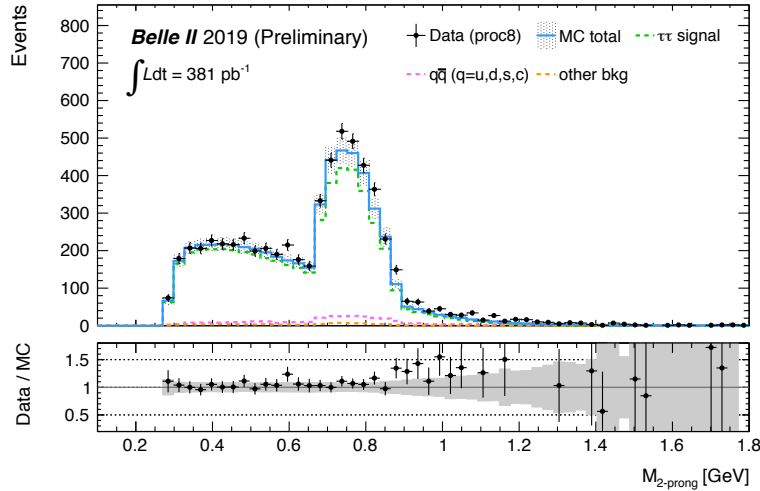


**Figure 7.4:** Distribution of the 2-prong track invariant mass in the electron  $\tau$ -decay channel. The 3- and 4-track samples as well as the OS and SS charge events are combined. The data (points) are compared to the signal + background expectation (solid blue line). The lower panel shows the Data-MC ratio, with the gray band centered around unity indicating the combined MC statistical and systematic (luminosity and trigger efficiency) uncertainties.

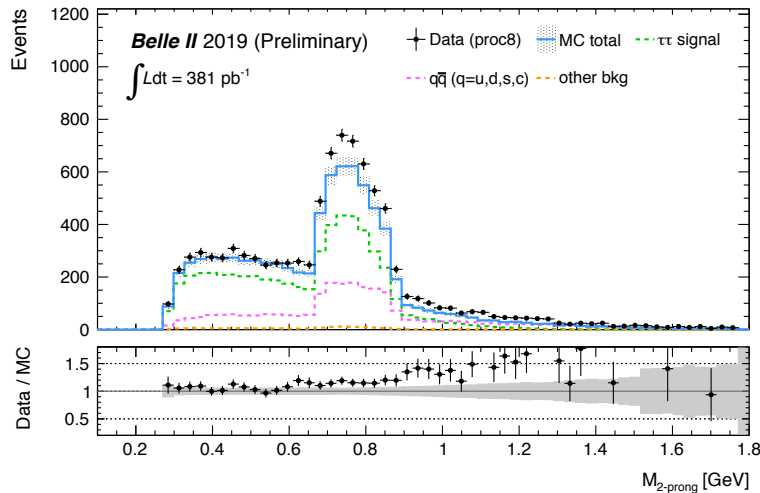


**Figure 7.5:** Distribution of the 2-prong track invariant mass in the muon  $\tau$ -decay channel. The 3- and 4-track samples as well as the OS and SS charge events are combined. The data (points) are compared to the signal + background expectation (solid blue line). The lower panel shows the Data-MC ratio, with the gray band centered around unity indicating the combined MC statistical and systematic (luminosity and trigger efficiency) uncertainties.

### Calibration of the efficiency estimator

By construction, the efficiency estimator as defined in Equation 7.3 is affected by some combinatorial effects that can introduce an overestimate of the tracking reconstruction inefficiency.

A purely statistical approach, assuming all tracks are equally exchangeable, allows to estimate the calibration factor by counting all the possible ways to loose one track. Indeed, one can write the  $N_4$  sample as  $\epsilon^4$  times some proportionality factors depending on branching fractions and luminosity that cancel out in the ratio defined in Equation 7.3. Here the efficiency  $\epsilon$  represents the probability to reconstruct a track. Similarly,  $N_3$  is proportional to  $\epsilon^3(1 - \epsilon)$ , where  $(1 - \epsilon) = q$  represents instead the probability to loose a track, therefore the track reconstruction inefficiency. The only relevant proportionality factor in  $N_3$  is the combinatorial one which accounts for the possible permutations of three tag tracks out of four, since all the other factors cancel out in the ratio. Assuming the only distinguishable tracks are those coming from orthogonal lists as defined at the track selection step in the analysis, the electron and muon channel are affected by a different combinatorial contribution:

- electron channel: the ambiguity regards only the 3-prong side tracks which is composed by two same-sign tracks with electric charge opposite to the 1-prong track and one track with the same electric charge as the electron; therefore, there are two ways to loose one opposite-sign track with respect to the 1-prong track, while there is just one possibility to loose the track with the same sign as the electron. From pure combinatorial effect, for the  $N_3$  sample, in the electron channel case the proportionality factors would be 2 for the OS charge or and 1 for the SS charge. The inefficiency overestimate due to the combinatorial contribution which enters the formula in Equation 7.3 can be made explicit by means of a linear approximation at first order in  $q$ , in the limit of a small inefficiency  $q = (1 - \epsilon)$ . Rewriting the equation for the track efficiency estimator one obtains:

$$\begin{aligned}
 \epsilon_{track} &= \frac{N_4}{N_4 + N_3} \\
 &= \frac{\epsilon^4}{\epsilon^4 + 2 \cdot \epsilon^3(1 - \epsilon)} \\
 &= \frac{1 - q}{1 - q + 2q} \\
 &\approx 1 - 2q + O(q^2),
 \end{aligned} \tag{7.6}$$

while for the SS charge case the combinatorial coefficient for the  $N_3$  sample being one, the same equation gives:

$$\begin{aligned}
 \epsilon_{track} &= \frac{N_4}{N_4 + N_3} \\
 &= \frac{\epsilon^4}{\epsilon^4 + \epsilon^3(1 - \epsilon)} \approx 1 - q.
 \end{aligned} \tag{7.7}$$

Note that only in the SS case for the electron channel one would expect to correctly estimate the probability to loose one of the four tracks, which allows to write the track reconstruction efficiency as  $1 - q$ , while in the OS case, the inefficiency seems to be overestimated by a factor 2.

- muon channel: due to non-orthogonal lists, the combinatorial factor in this case arises from the possible ways to select three out of four tracks, including also the 1-prong track

among the possible permutations of indistinguishable tracks. Since the charge situation is now completely symmetric, with two pairs of opposite sign tracks (the process  $e^+e^- \rightarrow \mu^+\mu^-$  must always have total null charge), the possible combinations to generate the N3 event are the same for the OS and SS charge candidates, and must be averaged on the sign of the 1-prong track in the final state, since we are not considering here different track reconstruction efficiencies for positive or negative charge tracks. Therefore, for the muon channel from pure statistical effects one would expect an overestimate of the track reconstruction inefficiency by a factor 2 for both SS and OS charge events, leading to the formula  $\epsilon \approx 1 - 2q + O(q^2)$ .

However, the applied offline selections discussed above for background rejection break the degeneracy and make the tracks distinguishable, depending on the result of the selections. Therefore the pure statistical treatment is no more sufficient to explain the N3 proportionality factor through the number of possible permutations and a deviation from the above computed factors for the inefficiency overestimate is expected, mainly due to three ingredients:

1. combinatoric due to the possible swapping among the probe and tag tracks on the 3-prong side, if the probe track passes the tighter pion tag selection criteria; moreover, the 1-prong track is uniquely identified after the angular isolation selection for both the studied channels (electron and muon);
2. the impact of the offline selections for background rejection, which are different for the OS and SS charge samples;
3. the impact of the weights associated to multiple N4 candidates ( $1/N_{cand}$ ).

The overall effect should generally go into the direction to reduce the N3 proportionality factor compared to the pure combinatorial effect, since the selections optimized to suppress the background contamination are expected to reduce the number of indistinguishable tracks per every tagged event and therefore to mitigate the inefficiency overestimate. A full simulation study has been devised to measure the calibration factors as a function of the channel (electron, muon) and the charge (OS, SS) of the selected samples, which provides the track reconstruction inefficiency overestimate and allow to correct the discrepancy estimator in Equation 7.4.

The calibration strategy consists in modifying the reconstructed MC samples by introducing a known per track inefficiency  $\delta_{MC}$  which mimics the additional inefficiency observed in data. The calibration study is performed on simulations, since it requires to know the additional inefficiency introduced in order to calibrate the estimator. The MC signal sample simulating the process  $e^+e^- \rightarrow \tau^+\tau^-$  has been reconstructed in four different cases, adding each time a different track reconstruction inefficiency for values of  $\delta_{MC} = 0.025, 0.05, 0.075, 0.1$ . Later on this sample will be called *modified* MC. For each of these values, the events are reconstructed and analyzed as described at the beginning of this section and the efficiency estimator on the modified MC is computed as in Equation 7.3,

$$\epsilon'_{MC} = N4/(N4 + N3)$$

and exploiting the definition of efficiency as the complementary to unit of the inefficiency, it can be written also as

$$\epsilon'_{MC} = \epsilon_{MC}(1 - \delta_{MC}),$$

from which the measured discrepancy estimator is calculated by comparing the efficiency of the modified MC to the one measured on the default reconstructed MC sample,  $\epsilon_{MC}$ :

$$\Delta^{meas} = 1 - \epsilon'_{MC} / \epsilon_{MC}. \quad (7.8)$$

The distributions for the efficiency estimator computed on the default and modified MC samples for OS and SS charge, for the electron and muon channel events have been studied, for different values of  $\delta_{MC}$ . The plots showing results as a function of the 1-prong  $\phi^{CM}, \theta_{lab}$  are reported as supplementary material in Appendix B.3.1. The measured discrepancy  $\Delta^{meas}$  calculated as in Equation 7.8 shows a deviation from the generated inefficiency  $\delta_{MC}$  which is flat over the studied kinematic range and indicates an overestimation of the track reconstruction inefficiency. The measured deviation varies depending on the charge (OS, SS) and channel of the studied sample. As already discussed, this can be explained as the interplay between a pure combinatoric effect and the impact of the applied selections. The calibration curve reported in Figure 7.6 shows the correlation for both the analyzed channels (electron, muon) between the measured discrepancy  $\Delta^{meas}$  plotted on the  $y$  axis and the simulated MC inefficiency  $\delta_{MC}$  reported on the  $x$  axis, known by construction.

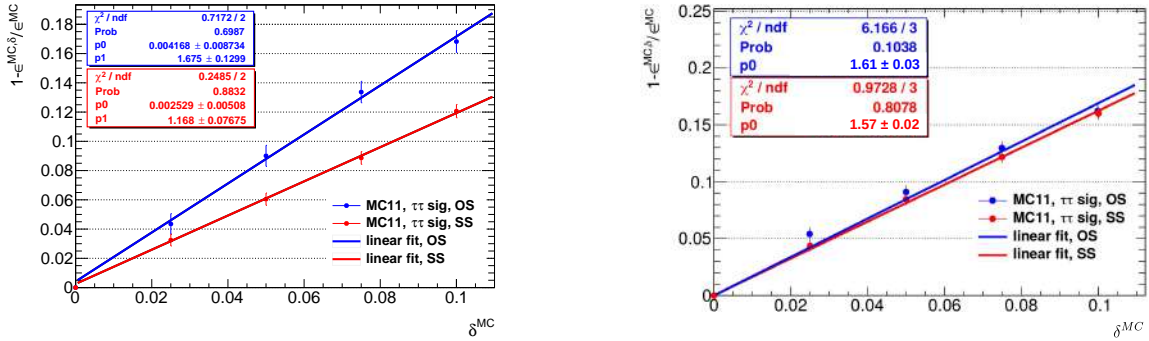


**Figure 7.6:** Calibration curves showing the measured discrepancy  $\Delta^{meas}$  as a function of the simulated one  $\delta_{MC}$ , for the electron (left) and muon (right) channels and for both charges OS (blue) and SS (red). The linear fit results reported in the top left box provide the calibration factors  $k$ .

In the same linear approximation for small inefficiencies used before ( $O(q^2)$ ), linear fits to scatter plots  $\Delta^{meas}$  Vs.  $\delta_{MC}$  reported in Figure 7.6 are performed and the four calibration factors,  $k$ , are extracted for each charge (OS, SS) and channel (electron, muon). The fit results with their associated uncertainties are reported in Table 7.5.

The expectation to observe a reduced calibration factor of the inefficiency overestimate compared to the pure statistical treatment, due to the impact of the background suppression, holds for the muon channel and the OS charge electron channel, where the calibration factor is measured from the simulation study to be reduced of about 20% with respect to what could be computed just from a statistical approach (see previous discussion of Equation 7.6). For the SS charge electron case, after subtracting the fit uncertainty, a calibration factor larger than unity (see Equation 7.7) is measured. This goes in the opposite direction of slightly increasing the inefficiency overestimate, despite the background rejection selections,

**Table 7.5:** Calibration results:  $k$  factors and their uncertainties from the fit are reported in the last column, per each analyzed channel, charge.

Channel	Charge	$k$ factor
electron	OS	$1.7 \pm 0.1$
electron	SS	$1.17 \pm 0.07$
muon	OS	$1.61 \pm 0.03$
muon	SS	$1.57 \pm 0.02$

and might be explained by the combination of several factors, as for example the invariant mass selection which is much milder for the SS charge sample and could be less effective in rejecting combinatorial background, or furthermore the associated event weight for the  $N_4$  candidate average.

Nonetheless, being these results produced as a final calibration step which is performed after the whole analysis chain has been applied, every possible overestimation effect that could be introduced by the analysis process and by the estimator computation is taken into account, and we correct for it by applying the calibration factors to the measured discrepancies, both in data and simulation. With this purpose in mind, the linear correlation between the measured discrepancy  $\Delta^{meas}$  and the generated MC inefficiency  $\delta_{MC}$  is inverted and allows to express the per-track data-MC *true* discrepancy  $\delta^*$  as a function of measured quantities:

$$\begin{aligned}
 \delta^* &= 1/k \cdot \Delta^{meas} \\
 &= 1/k \cdot \left( 1 - \frac{\epsilon_{meas}^{Data}}{\epsilon_{meas}^{MC}} \right) \\
 &= 1/k \cdot \left( 1 - \left( \frac{N_4^{Data}}{N_3^{Data} + N_4^{Data}} \right) \cdot \left( \frac{N_3^{MC} + N_4^{MC}}{N_4^{MC}} \right) \right).
 \end{aligned} \tag{7.9}$$

For the results presented hereafter, the calibration factors  $k$  resulting from the above described procedure are always used to correct the measured data-MC discrepancy  $\Delta^{meas}$  according to the formula described above.

### Systematic uncertainties

Systematic uncertainties have been assigned to the calibrated data-MC discrepancies, evaluated as the relative change in their value after varying the following up/down one standard deviation:

- *luminosity* — the difference between the Bhabha and  $\gamma\gamma$  luminosity measurements, as shown in Table 3.2.
- *trigger efficiency* — uncertainty on the trigger  $\text{bit}_{ECL}$  efficiency measurement, as shown in Figure 7.2.
- *calibration procedure* — uncertainty on the  $k$  factors from the calibration procedure, as shown in Table 7.5.
- *background subtraction* — uncertainty associated to the background MC, which enters during the background subtraction procedure on data.

The systematic variations measured as a function of the 1-prong track  $p_T$ ,  $\theta$  and  $\phi$  are shown in Appendix B.3.2.

### Data-MC discrepancy final results

The calibrated data-MC discrepancies for the combined electron and muon channels, including the systematic uncertainties added in quadrature, are finally computed. The discrepancies measured as a function of the 1-prong track  $p_T$ ,  $\theta$  and  $\phi$  are shown in Figure 7.7 below. The overall discrepancies integrated over the kinematic range are also displayed in Figure 7.8 and the final value of the calibrated data-MC discrepancy for Phase 2 data is measured to be:

$$3.17 \pm 0.54 \text{ (stat)} \pm 0.17 \text{ (sys)} \% . \quad (7.10)$$

From this result, which is consistent with what measured also on the radiative Bhabha events, it is conservatively assessed a 4% systematic uncertainty in the measurement of the  $Z'$  cross section related to the tracking performance.

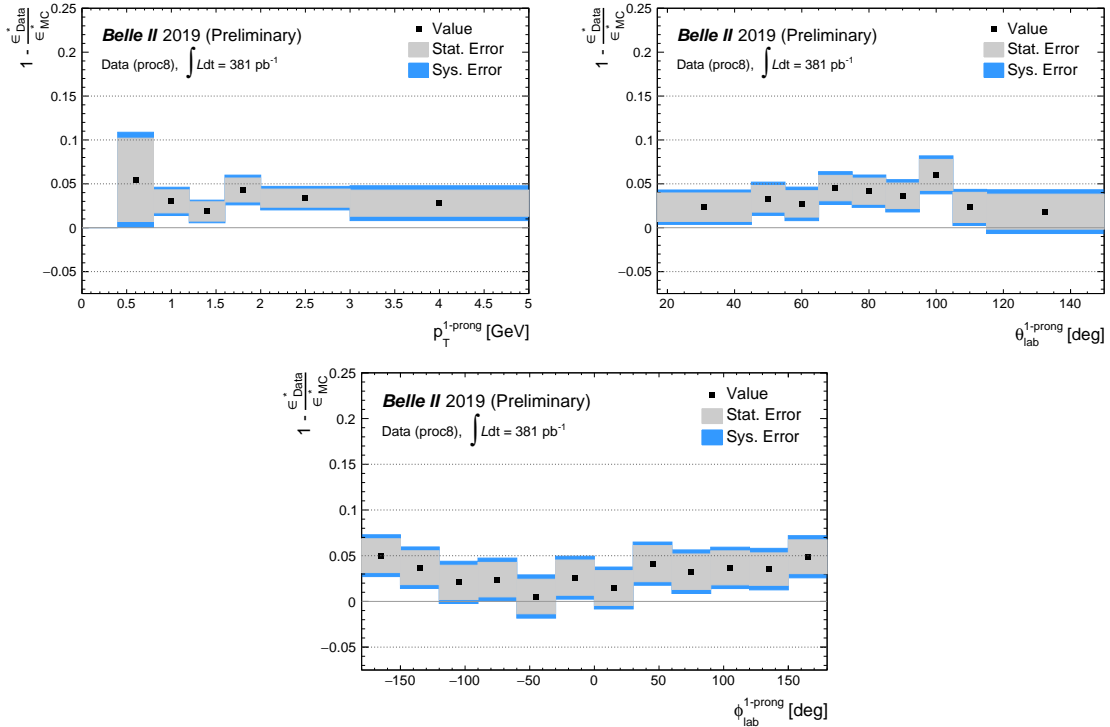


**Figure 7.7:** The calibrated data-MC discrepancies for the combined channels as a function of the 1-prong track  $p_T$  (top left),  $\theta$  (top-right) and  $\phi$  (bottom) are shown, with the associated statistical (gray) and systematic (blue) uncertainties.

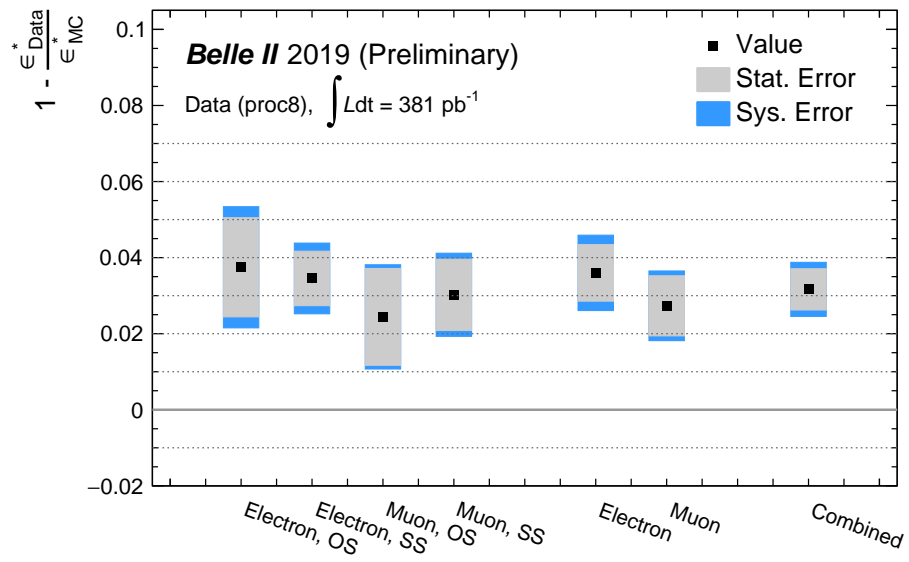


**Figure 7.8:** The overall data-MC discrepancies for (left to right): the four individual channels, the electron and muon combinations and, finally, the full combination. The statistical (gray) and systematic (blue) uncertainties are shown.

## Chapter 8

# Results and conclusions

This chapter addresses the statistical treatment of the yields found after the final selection with the continuous binning scheme applied and the strategy for the upper limit calculation. The procedures implemented to compute expected sensitivities based on the simulated background yields and on the data validation results, on a still blinded data set, are given in the first Section 8.1. After the approval for unblinding, the same techniques have been applied on the recoil mass yields measured on real data: no significant excess of events in neither the standard nor the LFV  $Z'$  cases has been found and limits on the production cross sections of both processes have been measured, as reported in Section 8.2. The upper limit to the cross section  $\sigma[e^+e^- \rightarrow \mu^+\mu^-Z'(\rightarrow \textit{invisible})]$  is then interpreted in terms of the new coupling constant  $g'$ , whose values larger than  $\text{few} \times (10^{-2} - 10^{-1})$  are excluded at the 90% confidence level for  $10^{-3} \leq M_{Z'} \leq 6 \text{ GeV}/c^2$ . To conclude, the final part of the chapter (Section 8.3) will give the prospects for this measurement on Phase 3 data, including the expected improvement due to luminosity and to the better performance of the complete detector, with the VXD installed and a functional muon identification system finally available.

### 8.1 Expected sensitivities

The statistical analysis of the selected events has been implemented in a Bayesian approach and cross-checked with frequentist techniques, as explained in detail in Appendix C. The primary aim with a still blinded data sample is to provide the expected sensitivity to the 90% Confidence Level (CL) exclusion curves for the Phase 2 data luminosity. Only simulated results from background MC samples are used, additionally taking into account the outcome of the data-MC validation studies and the systematic uncertainties as evaluated on real data. When computing the expected sensitivities, the results of the data validation studies affect both the background yields and the signal efficiency. Both have been rescaled for the measured data-MC discrepancy, by multiplying the background yields and the signal efficiencies for the standard  $Z'$  by the factor 0.65 and the background yields for the LFV  $Z'$  by the factor 0.90, respectively, as measured on the control samples. For the LFV case, being this discrepancy completely understood and ascribed to the tracking inefficiency, no additional systematic uncertainty due to the applied correction is assigned. On the other hand, for the standard  $Z'$  case, as discussed previously in Section 6.5, after considering the tracking inefficiency contribution, an unexplained data-MC discrepancy of  $-25\%$  remains and this has to be considered

differently when assessing the systematic uncertainties in the background expectation and in the signal efficiency. Since the level of agreement of the background yield between data and simulation can be directly measured in data control samples (see Section 6.1) and checked also after the unblinding, no further systematic uncertainty due to the residual 25% discrepancy is assigned to the number of expected background events. Unlikely, for the signal efficiency measurement there is no control sample available in data to measure the level of agreement with simulation, unless unblinding the data set, therefore half of the residual unexplained 25% discrepancy,  $\pm 12.5\%$  is assigned as systematic uncertainty in the signal efficiency. Moreover, the following considerations regarding the systematic uncertainties which enter the cross section estimation, as listed in Table 7.1, hold:

1. the uncertainties related to tracking, trigger and PID selection efficiencies affect both the background yields and signal efficiency;
2. half of the remaining unknown data-MC discrepancy ( $-25\%$ ) is assigned as systematic uncertainty in the signal efficiency for the standard  $Z'$  case only, 12.5%;
3. the 22% systematic contribution due to the  $\tau$  suppression procedure as estimated in Section 6.1 is assigned as uncertainty to the background yields only;
4. a 2% systematic uncertainty on the estimated background yields is assigned, as measured from the the data-MC agreement on the validation control samples before the  $\tau$  suppression application, after applying the data-MC discrepancy corrections as discussed above (0.65, 0.90 for the  $\mu\mu$ ,  $e\mu$  events, respectively).

The upper limit computation is performed within the Bayesian Analysis Tool (BAT) framework [95]. Flat priors are assumed for the  $Z'$  cross section up to  $10^5 \text{ fb}^{-1}$ . Each source of systematic uncertainty is modeled by a Gaussian function of unit mean and width equal to the estimated size of the effect, as evaluated from the detector and systematic uncertainty studies, and it is convoluted with a Poissonian likelihood modeling the number of expected background events. The final results are shown in Figure 8.1 as a function of the recoil mass (blue line) and compared to the ideal case (magenta solid line), which assumes no residual data-MC discrepancy after the validation study, and thus no additional systematic uncertainty in the signal efficiency due to remaining discrepancy and no correction factor applied to the expected yields.

In the LFV  $Z'$  case, being at present impossible to estimate a signal efficiency in absence of a robust model,  $(\sigma_{Z'} \times \epsilon_{\text{sig}})$  must be considered as a single parameter in the upper limit computation, as explained in Appendix C.1.1. The same procedures and similar considerations as in the standard  $Z'$  apply also to the LFV  $Z'$  case, except for a different correction factor (0.90) of the simulated yields. Systematic uncertainties have been treated as discussed previously, assuming Gaussian distributions and integrating them out. Moreover, differently from the standard  $Z'$  case, no additional systematic uncertainty is assigned due to the data-MC discrepancy, being this -10% mismatching ascribed to the measured tracking inefficiency, for which a systematic error is already considered. The 90% CL upper limit for the LFV  $Z'$  search is shown in left plot of Figure 8.2 as a function of the recoil mass.

Results on the sensitivity to the process  $e^+e^- \rightarrow \mu^+\mu^-Z'(\rightarrow \text{invisible})$  have been calculated also in a frequentist approach exploiting the Feldman-Cousins techniques [96], of which

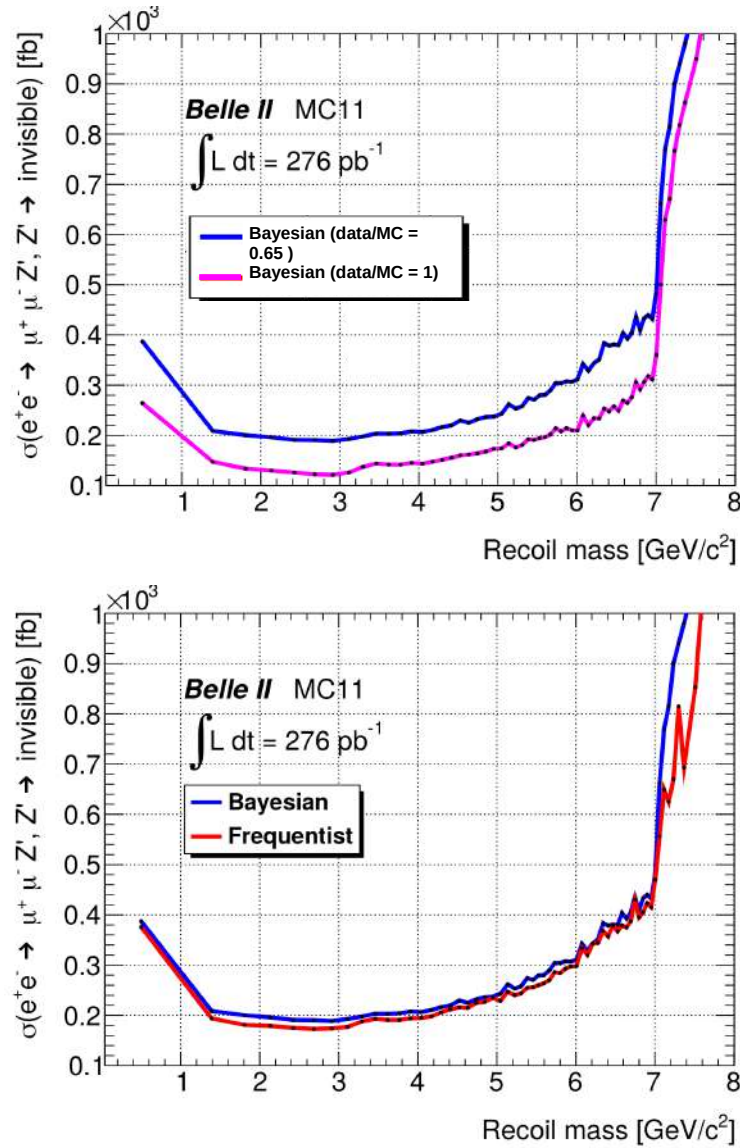


**Figure 8.1:** On the top, the expected Bayesian 90% CL upper limit to  $\sigma[e^+e^- \rightarrow \mu^+\mu^-Z'(\rightarrow \text{invisible})]$  at the corresponding luminosity of Phase 2 usable data, applying all the assumptions listed previously regarding the treatment of the systematic uncertainties (blue solid line). The expected improvement foreseen in an ideal case with no residual data-MC discrepancy, without any rescaling of the background yields and no additional systematic uncertainty of 12.5% in the signal efficiency is shown by the magenta solid line.

On the bottom, the curves for the expected frequentist based (red line) and Bayesian based (blue line) 90% CL upper limits to  $\sigma[e^+e^- \rightarrow \mu^+\mu^-Z'(\rightarrow \text{invisible})]$  are reported as a function of the recoil mass, showing consistent results.

the detailed implementation is given as supplementary material to this work, reported in Appendix C.2. The Bayesian and frequentist results are consistent with each other and compared in the right plot in Figure 8.1 as a function of the recoil mass. The Bayesian upper limit for the LFV  $Z'$  is also compared to the Feldman-Cousins results as shown in the right plot in

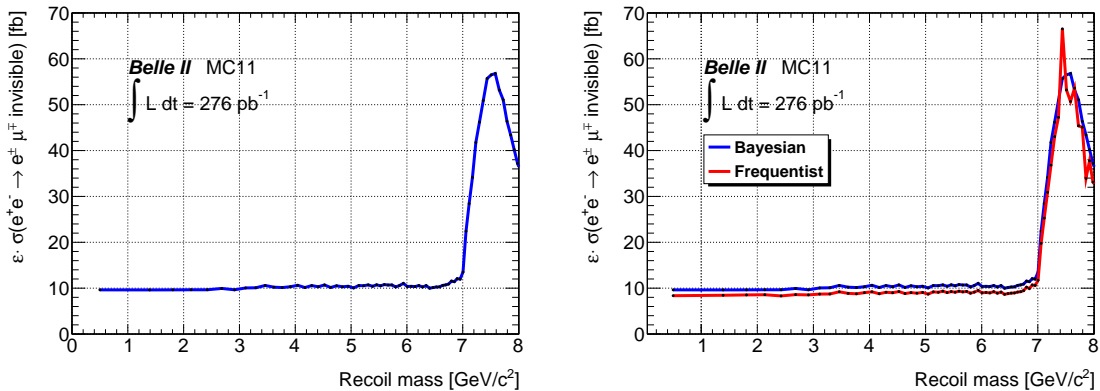


**Figure 8.2:** On the left, the expected Bayesian (blue line) 90% CL upper limit to  $\epsilon \times \sigma[e^+e^- \rightarrow e^\pm\mu^\mp + \text{invisible}]$  is reported as a function of the recoil mass. On the right, comparison with the frequentist results (red line) is shown.

Figure 8.2, as a function of the recoil mass.

Finally, to conclude the sensitivity studies, cross section results for the standard  $Z'$  search are translated in terms of upper limits on the new boson coupling constant  $g'$ , as interpreted in the framework of the  $L_\mu - L_\tau$  model. A numerical approach exploiting the MadGraph 5 generator has been implemented, being the analytical expression not available. The expected sensitivities for  $g'$  in both frequentist and Bayesian approaches are finally shown in Figure 8.3 (linear and logarithmic scales) as a function of the recoil mass, which corresponds to the mass of the reconstructed  $Z'$  candidate,  $M_{Z'}$  in the plots hereafter.

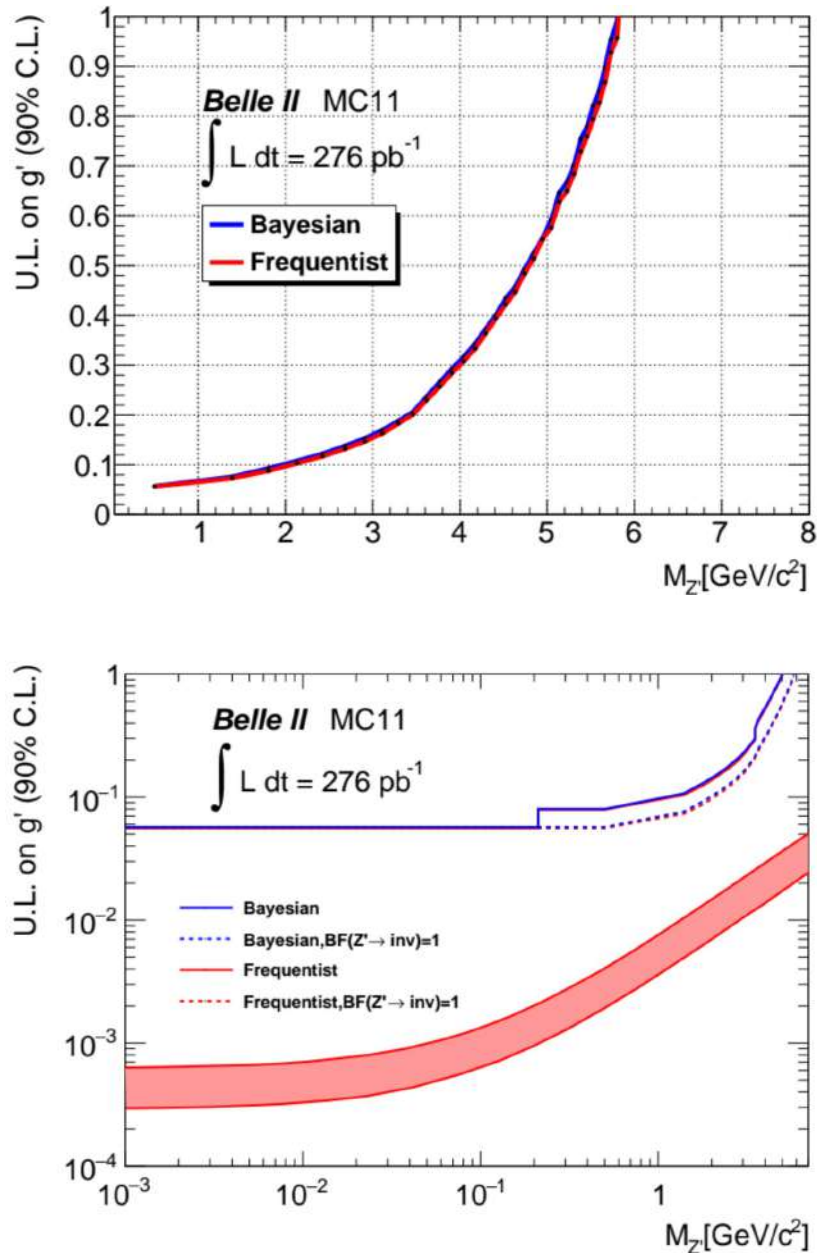


**Figure 8.3:** The expected frequentist based (blue line) and Bayesian based (red line) 90% CL upper limits to coupling constant  $g'$  as a function of the reconstructed  $Z'$  mass,  $M_{Z'}$ , in linear (top) and logarithmic (bottom) scales, are shown. The solid line assumes the  $L_\mu - L_\tau$  predicted branching fraction for  $Z' \rightarrow \text{invisible}$ , while the dashed line (bottom plot only) assumes  $BF[Z' \rightarrow \text{invisible}]=1$ . The red band shows the region that could explain the anomalous muon magnetic moment  $(g_\mu - 2) \pm 2\sigma$ , taken from the work referenced in [61].

## 8.2 Results on Phase 2 data

A first partial unblinding of Belle II 2018 data has been performed by comparing the recoil mass distribution measured on data and on simulations before the application of the  $\tau$  suppression procedure, with the application of the correction scale factors previously discussed. After rescaling respectively the MC yields for the 0.65, 0.90 discrepancy measured in the validation studies, the data-MC ratio is consistent with one within the statistical fluctuations for both the channels  $e^+e^- \rightarrow \mu^+\mu^-$ ,  $e^+e^- \rightarrow e^\pm\mu^\mp$  investigated in this analysis, as shown by the inset plots in Figure 8.4

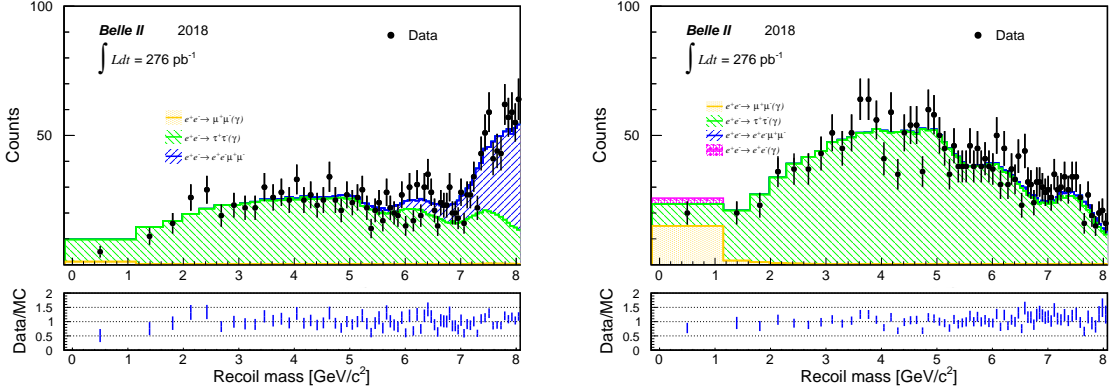


**Figure 8.4:** Recoil mass spectrum for the  $e^+e^- \rightarrow \mu^+\mu^-$  ( $e^\pm\mu^\mp$ ) sample before the  $\tau$  suppression procedure is shown on the left (right). The inset plots show the data-MC ratio computed after correcting the simulated yields as explained in Chapter 6 for the observed data-MC discrepancy (scaling factor of 0.65 applied to the simulated yields in the left plot, 0.90 applied in the right plot). The corrected distributions show a good data-MC agreement within statistical fluctuations.

The final recoil mass spectrum for the  $e^+e^- \rightarrow \mu^+\mu^-$  sample, which targets the standard  $Z'$  search, is shown in Figure 8.5 after the application of the  $\tau$  suppression procedure on data and rescaled simulation yields. To look for possible anomalies in data, under the assumption of the background only hypothesis,  $p$ -values have been computed as the probability to get a result (counts) greater than or equal to the observed one, with statistical and systematic uncertainties both taken into account (see Appendix C.3). No evidence of new signal has been found, being the computed  $p$ -values within the  $3\sigma$  equivalent for each recoil mass bin, both in the normal and in the shifted binning option. The previously discussed Bayesian procedure is applied to compute the 90% CL upper limit to the standard  $Z'$  cross section. Flat priors are used for all positive values of the cross section and Poissonian likelihoods are assumed for the number of observed and Monte Carlo generated events, while Gaussian smearings have been used to model the systematic uncertainties. Results are cross-checked with the frequentist procedure following the Feldman-Cousins approach, as reported in Appendix C.2, and found to be compatible between the two methods. The 90% CL upper limit to the standard  $Z'$  cross section  $\sigma[e^+e^- \rightarrow \mu^+\mu^- Z'(\rightarrow \text{invisible})]$  is shown in Figure 8.6 as a function of the recoil mass. Cross section results are then interpreted in terms of 90% CL upper limit on the coupling constant  $g'$ , shown in Figure 8.7.

Concerning the LFV  $Z'$  search, the final recoil mass spectrum for the  $e^+e^- \rightarrow e^\pm\mu^\mp$  sample is shown in Figure 8.8 (top) after the application of the  $\tau$  suppression procedure on

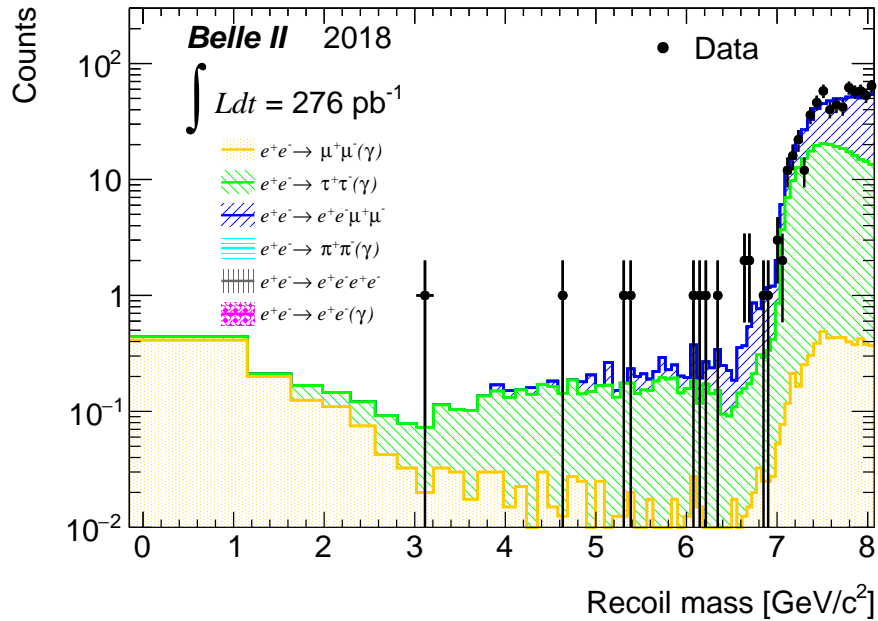


**Figure 8.5:** Recoil mass spectrum for the  $e^+e^- \rightarrow \mu^+\mu^-$  sample after the  $\tau$  suppression procedure. Monte Carlo values are rescaled for the luminosity, the trigger efficiency (0.79) and the validation procedure outcome (0.65). In the recoil mass interval  $-0.15 \div 6.5(7)$   $\text{GeV}/c^2$ , 8(17) events are found in data and 8.6(16.8) in Monte Carlo.

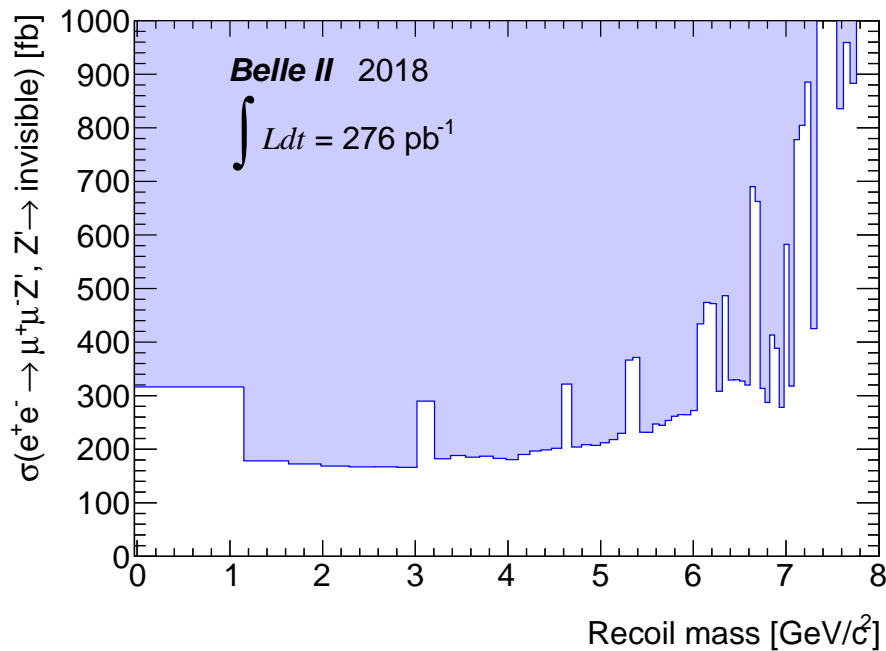


**Figure 8.6:** 90% CL upper limits to  $\sigma[e^+e^- \rightarrow \mu^+\mu^- Z'(\rightarrow \text{invisible})]$ .

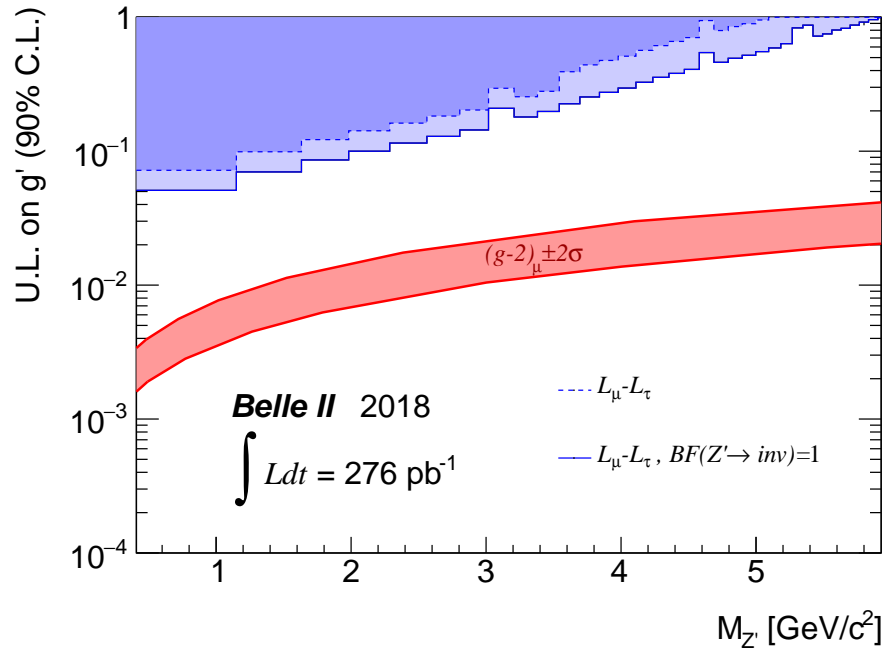


**Figure 8.7:** 90% CL upper limits to  $g'$ . The solid line assumes the  $L_\mu - L_\tau$  predicted branching fraction for  $Z' \rightarrow$  invisible while the dashed line assumes  $BF[Z' \rightarrow \text{invisible}]=1$ . The red band shows the region that could explain the anomalous muon magnetic moment  $(g - 2)_\mu \pm 2\sigma$ .

data and rescaled Monte Carlo. As for the standard  $Z'$ , the background only hypothesis is tested by computing  $p$ -values as a function of the recoil mass and the outcome is analogous to the standard  $Z'$  case, with no significant anomalies observed, neither in the normal nor in the shifted binning scheme. Model independent 90% CL upper limits to the quantity (cross section  $\times$  efficiency) for the LFV  $Z'$  search are computed in both the Bayesian and frequentist approaches and found to be consistent. The results are displayed in Figure 8.8 (bottom) as a function of the recoil mass.

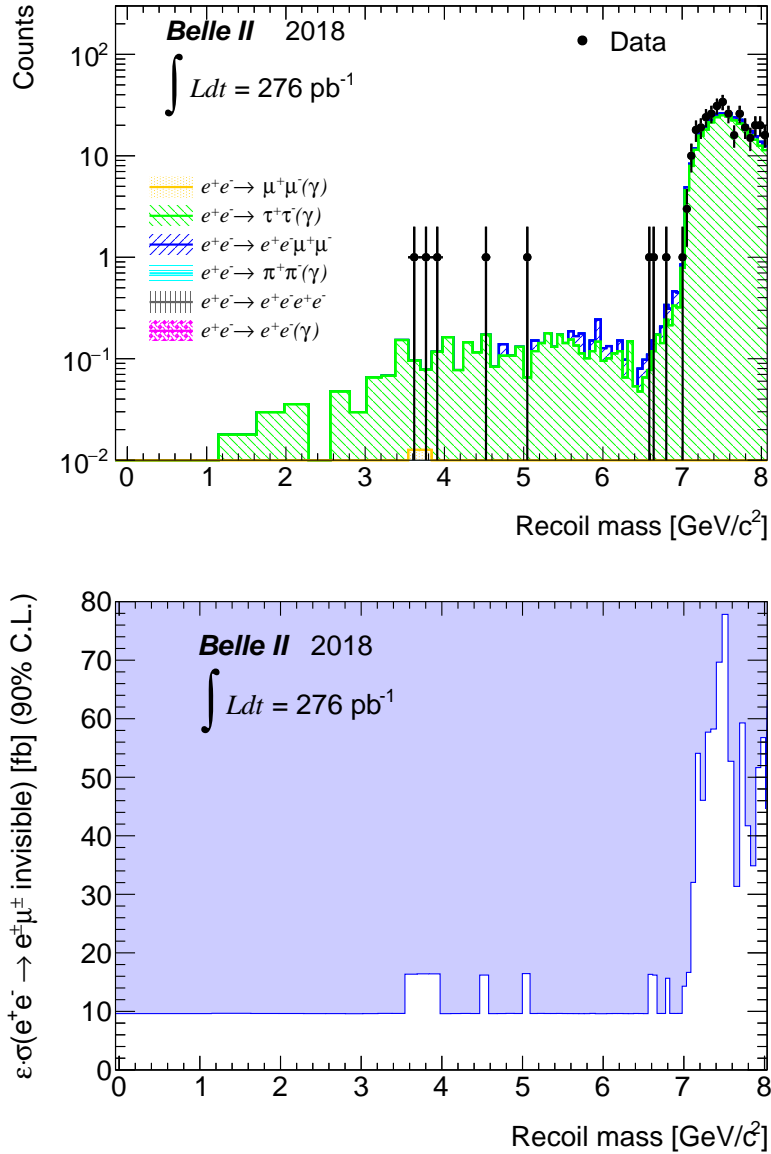


**Figure 8.8:** In the top plot, the recoil mass spectrum after the  $\tau$  suppression procedure on the unblinded  $e^+e^- \rightarrow e^\pm\mu^\mp$  data targeting the LFV  $Z'$  search is shown. Simulated yields values are rescaled for the luminosity, the trigger efficiency (0.96) and the validation procedure outcome (0.9). In the recoil mass interval  $-0.15 \div 6.5(7) \text{ GeV}/c^2$ , 5(9) events are found in data and 4.9(7.9) in Monte Carlo. In the bottom plot, the 90% CL upper limits to  $\epsilon \times \sigma[e^+e^- \rightarrow e^\pm\mu^\mp \text{invisible}]$  are reported.

### 8.3 Phase 3 improvement and prospects

The next step for this search is to repeat the analysis on the early data set collected during Phase 3 (Section 2.3.3), which provides three main factors of improvement:

1. the increased luminosity, at least ten times larger than the data set of  $276 \text{ pb}^{-1}$  used for the Phase 2 results, with improved trigger efficiency and performance;
2. the muon selection implemented with a KLM-based particle identification algorithm, which does not have to rely exclusively on the ECL acceptance and performance anymore;
3. the presence of the full VXD, with a main impact on the tracking performance and the recoil mass resolution.

An overall better data quality has been observed for early Phase 3 data. A full re-optimization on Phase 3 simulations is however needed to confirm the final selections on the Phase 3 data set, as well as a data validation program aimed at studying the data-MC discrepancy on the new samples. Preliminary studies show that the muon detection has much improved with respect to Phase 2 data and the observed discrepancy between data and simulations is found to be around  $-10\%$ , which might be explained by the tracking and muon ID inefficiencies (and related systematic uncertainties) assessed by the preliminary performance studies on Phase 3 data.

Within these assumptions, the expected sensitivities on the cross section for the process  $e^+e^- \rightarrow \mu^+\mu^-Z'$ ,  $Z' \rightarrow \text{invisible}$ , in different configurations of luminosity and detector performances, varying the above mentioned conditions, have been computed with the same Bayesian procedure implemented in the BAT framework [95], already described at the beginning of this chapter.

#### 8.3.1 The luminosity increase

A competitive result even with a null outcome of the search, that would be able to exclude at 90% CL all the region which still favors the  $Z'$  boson as possible explanation of the  $(g-2)_\mu$  anomaly, implies to reach a limit on the coupling constant  $g'$  of order of few  $\times (10^{-4}-10^{-3})$ . Since the cross section is proportional to the the square coupling constant, this would require four order of magnitude improvement on the measured sensitivities, which currently exclude values of  $g'$  larger than few  $\times (10^{-2}-10^{-1})$  for masses below  $6 \text{ GeV}/c^2$ . At first approximation, the sensitivity can be considered proportional to the luminosity in the low mass region, where no background is expected, while it goes as the luminosity to the one-half power in presence of background events and for the  $g'$  sensitivity an additional square root has to be considered, so it is proportional to the luminosity to the one-fourth.

Five different scenarios from  $2.7 \text{ fb}^{-1}$  to  $27 \text{ ab}^{-1}$  have been studied, with a luminosity each time multiplied by a factor 10 and an the expected total background yield increased accordingly.

#### 8.3.2 The muon ID improvement

The availability of a KLM-based particle identification in Phase 3 means a huge improvement in the purity of the selected muons. The development of the dedicated PID variable for muon

selection (defined as the normalized likelihood ratio of the muon hypothesis and the sum of all the other particle hypotheses) allows to better reject pion contamination, which has been estimated to contribute as 85% of the background yield coming from  $e^+e^- \rightarrow \tau^+\tau^-(\gamma)$  processes. The main advantage will be the possibility to reduce the expected background due to the misidentification rate, despite the higher luminosity. Preliminary studies on the data collected during the Phase 3 spring runs indicate a reduction of a factor 20 in the background rate due to pion misidentification when reconstructing the  $J/\psi \rightarrow \mu^+\mu^-$  peak on data with a tighter selection on the muon ID probability. Results from preliminary studies are shown in Figure D.1 reported in Appendix D. This has been taken into account in the projection studies as follow:

- 85% of the background yield coming from  $e^+e^- \rightarrow \tau^+\tau^-(\gamma)$  events is reduced by the factor 0.1, which is shown from preliminary performance studies to be a reasonable estimate of the rejection factor expected from a muon ID probability selection  $> 0.8$ ;
- 100% of the background yield from  $e^+e^- \rightarrow \pi^+\pi^-(\gamma)$  processes, only due to particle misidentification, is scaled by the factor 0.1.

While the latter is found to be a negligible contribution in Phase 2 data, the former is the main background component in the medium recoil mass region and therefore a significant improvement is expected from the muon ID selection on Phase 3 data.

### 8.3.3 The VXD impact on recoil mass resolution

For each mass point studied on Phase 2 data as reported in Section 3.4.1, signal MC samples generated with the MadGraph 5 generator and the Phase 3 detector geometry have been simulated. Studies on the improved signal width have been performed by fitting the recoil mass distribution for each generated sample (20000 events) with the same PDF model as described in Section 5.1.1, after selecting the events with exactly the same requirements listed in Section 4.2, 4.3, before the  $\tau$  suppression procedure. The results of the fit and the corresponding values of the shape parameters, particularly the Gaussian and CB function widths, are reported in Figure D.2 in Appendix D. From these results, the signal peak widths for Phase 3 simulations are computed accordingly to Equation 5.2 as explained in Section 5.1.1, and their values have been compared to those extracted from Phase 2 simulation, as a function of the recoil mass, shown in Figure 8.9. For recoil masses below  $4.5 \text{ GeV}/c^2$ , an average 40% improvement is observed in the signal resolution, mainly due to the better tracking performance coming from the full installation of the VXD detector. Above  $5 \text{ GeV}/c^2$  recoil masses, the tracking system has to deal with low momentum muons affected by multiple scattering which eventually dominates the resolution, due to the additional material budget introduced by the full VXD. For the large recoil mass case ( $> 5 \text{ GeV}/c^2$ ), no significant improvement is observed in the signal widths, which are comparable to Phase 2 results. In the reasonable assumption of a flat background in each recoil mass window, the resolution improvement would imply a correspondent 40% reduction of the background yields for recoil masses below  $4.5 \text{ GeV}$ . The above condition translates in a reduction factor of 0.60 applied to the expected background for recoil masses below  $4.5$ , that has been added as further improvement factor to the five luminosity scenarios studied within the new full VXD resolution hypothesis.

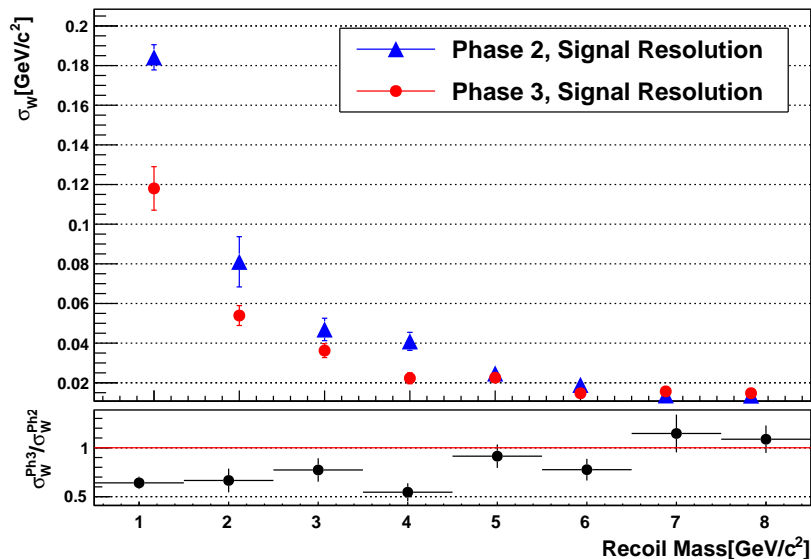


**Figure 8.9:** The signal width  $\sigma_W$  as computed according to Equation 5.2, as a function of the recoil mass, is compared between Phase 2 (blue triangles) and the Phase 3 (red dots) simulation results. The ratio between Phase 3 and Phase 2 widths per each mass point is shown in the inset plot. It can be noticed that for masses above 5 GeV/ $c^2$  the multiple scattering on low-momentum muons, due to the additional material budget of the full VXD, dominates the resolution and no significant improvement is gained with respect to Phase 2 results.

### 8.3.4 Projection results

The resulting sensitivities computed on the signal cross section and translated also in terms of the coupling constant  $g'$ , as a function of the reconstructed recoil mass, are shown in green lines in Figure 8.10, compared to the results from Belle II 2018 data, represented by the blue line. The 27  $\text{ab}^{-1}$  scenario is highlighted in magenta solid line.

As previously discussed, several factors of improvement expected on both the surviving background events and the associated uncertainties have been considered:

1. for each scenario, the luminosity has been increased by a factor 10 and the systematic uncertainties which are statistically driven (e.g.  $\tau$  suppression, background yield) have been reduced accordingly;
2. the background contamination from  $e^+e^- \rightarrow \tau^+\tau^-(\gamma)$  and  $e^+e^- \rightarrow \pi^+\pi^-(\gamma)$  processes, due to particle misidentification, has been scaled as described in subsection 8.3.2;
3. the total number of background events has been scaled by the factor 0.60 for  $M_{Z'} < 4.5 \text{ GeV}/c^2$ , as described in subsection 8.3.3;
4. the data-MC discrepancy has been reduced to  $-10\%$  and assumed to come from the inefficiencies of the track reconstruction algorithms and lepton ID selection performances; half of this residual discrepancy is conservatively assigned as systematic uncertainty in the signal efficiency;

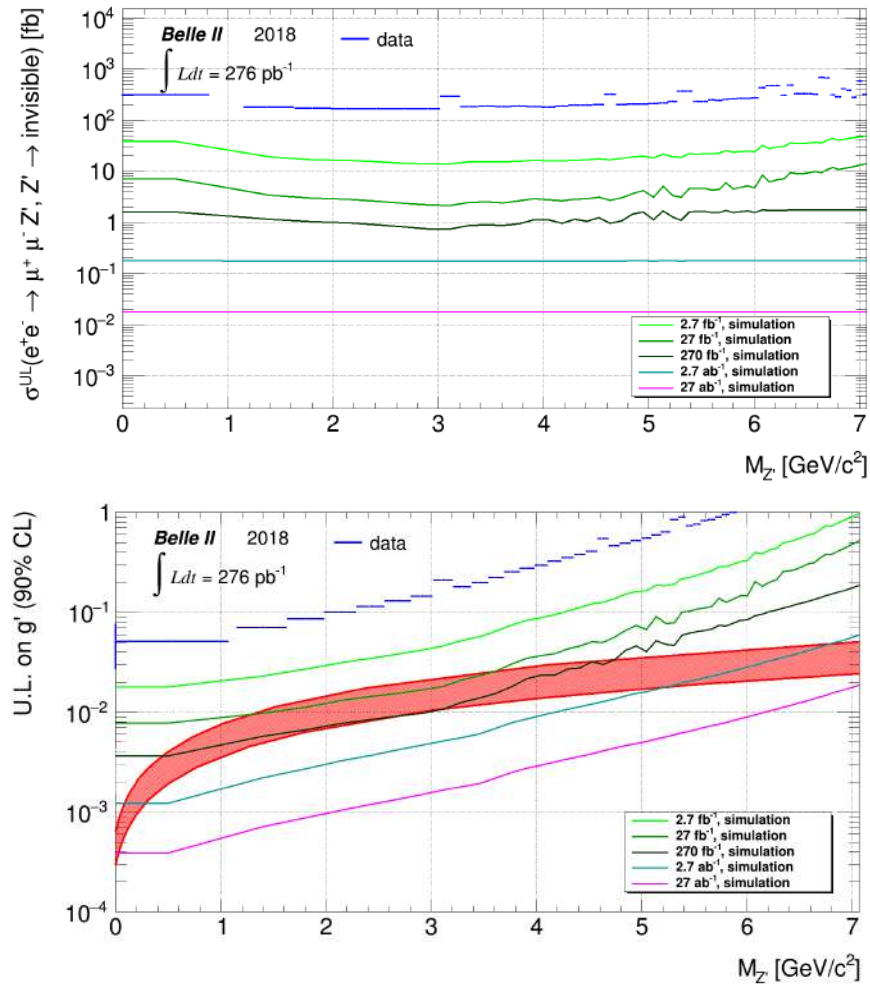


**Figure 8.10:** In the top plot, the 90% CL upper limit on the cross section of the process  $e^+e^- \rightarrow \mu^+\mu^-Z'$  as measured from Phase 2 data is shown (blue solid line), compared to the sensitivities computed for the 10 times increased luminosity scenarios evaluated in the study. The  $27 \text{ ab}^{-1}$  that may rule out completely the  $(g-2)_\mu$  band is shown in magenta solid line.

The same limits translated in terms of the  $g'$  coupling constant are reported in the bottom plot.

5. the discrepancy in the tracking efficiency as measured on data and simulation from preliminary studies on Belle II 2019 data is assessed to be of order 1% and it is assumed as associated systematic uncertainty due to the track reconstruction performance;
6. studies of the uncertainties associated to the muon ID selection and trigger performances have been already set up and official results on Belle II 2019 data are going to be released; for this projection study, 4% and 6% systematic errors due respectively to muon identification and trigger selections, as quoted in Table 7.1, are conservatively assumed.

The Phase 3 projections shown above have been computed in the same Bayesian approach exploited for the upper limit estimation within the BAT software framework and all the considerations listed previously apply to the studied curves in Figure 8.10.

It should be noticed that the sensitivity ratios between different curves do not scale as the the power of luminosity, since the luminosity effect combines in a not trivial way with the other scaling factors applied to simulate improved detector conditions and performances, as explained in the previous subsections.

### 8.3.5 Next plans

More specific studies are required for repeating the  $Z'$  analysis on Phase 3 data. Currently the analysis group is active on the new performance studies necessary to understand the Belle II 2019 data. The next steps can be summarized following the three main factors of improvement discussed previously:

- a run-dependent study of the trigger performances on Phase 3 data is under development and preliminary results show a higher and more accurate efficiency due to the overall improvement of the detector and firmware performances. Moreover, it will benefit from the larger statistics of at least  $10\times$ ( Belle II 2018 data);
- the new muon selection based on KLM-information requires a dedicated optimization and the associated efficiency with its systematic uncertainty needs to be measured on the new data set;
- the track reconstruction efficiency study exploiting the topology of the  $e^+e^- \rightarrow \tau^+\tau^-$  events will benefit of both the larger statistics and the improved detector and I am working on the new analysis on Belle II 2019 data which will provide the measurement of the scale factors and discrepancies for track reconstruction efficiencies measured on Phase 3 data and on simulations;
- the signal width study on Phase 3 simulation and the comparison with the recoil mass resolution evaluated on data must be repeated; these results will allow to define the new binning scheme for the recoil mass spectrum measured on Phase 3 data;
- given the overall better agreement between data and simulations, two point of the previous analysis strategy may change:
  - the background suppression strategy, and specifically the  $\tau$  suppression procedure, may benefit from a more sophisticated non-linear selection based on multivariate analysis methods. A re-optimization of the full selection chain with Boosted Decision Tree and Neural Network algorithms is currently under study; the same control samples exploited in the Phase 2 analysis, with larger statistics, will be used for data validation and the control of the systematic errors;
  - the larger statistics and the reduced data-MC discrepancy motivate the estimation of the expected background yields directly from data, by applying the sideband extrapolation technique. This method aims at estimating locally the expected background yield per each recoil mass bin by fitting the adjacent bin yields and extrapolating the result to the bin under study, before the application of the  $\tau$  suppression procedure, in order to have enough statistics for a good fit performance.
- a newly optimized linear-cut based selection for Belle II 2019 data is under development, to ensure also on the new data set a robust result produced with validated techniques.

Prospects for the  $Z'$  search on Phase 3 data are indeed promising. The analysis implemented for this doctoral thesis has been shown to have an important discovery potential in the search for a new massive boson coupled to muons and decaying in invisible, which is here performed for the first time on the Belle II 2018 data. No previous limits exist on the invisible signature results and the upcoming Belle II 2019 data will allow to set competitive constraints on the  $L_\mu - L_\tau$  model, profiting of the larger statistics and the better data quality. As reported from the upper limit projections on  $g'$  almost half the final Belle II data set is needed to completely rule out the  $(g-2)_\mu$  band, being this a strong motivation for keeping the  $Z'$  search constantly monitored.

## 8.4 Conclusions

The results presented in this thesis provide the first upper limit for the process  $e^+e^- \rightarrow \mu^+\mu^-Z'$ ,  $Z' \rightarrow$ invisible, and measure for the first time the quantity cross section multiplied by the efficiency for the reaction  $e^+e^- \rightarrow e^\pm\mu^\mp Z'$ ,  $Z' \rightarrow$ invisible, which searches for a LFV  $Z'$ . Both analyses for the standard and LFV  $Z'$  cases have been performed with the collision data collected during 2018 by the Belle II experiment and a paper [97] based on the main findings discussed in this doctoral project has been submitted to *Physical Review Letters*. Though previous limits from visible final-state searches for a  $Z'$  decaying into two muons exist and constrain the  $L_\mu - L_\tau$  framework, the search for an invisible  $Z'$  has unique sensitivity to models including light dark matter candidates with mass  $m_{DM} < M_{Z'}/2$  and, despite the reduced data set, can already explore a new region in the parameter space of the  $L_\mu - L_\tau$  model, especially for  $Z'$  masses below 212 MeV/ $c^2$ . This study is therefore a well motivated effort to look for a new hidden mediator that may explain how dark matter couples to heavy leptons and potentially solve several observed tensions, such as for example the  $(g-2)_\mu$  anomaly.

The upcoming Belle II data are the most suitable to periodically update the search, as it has been shown throughout this thesis, with the goal to improve and repeat the analysis, as soon as larger statistics is available, and complete the exploration of the  $Z'$  parameter space.



# Appendices



# Appendix A

## Event selection and signal shape study results

### A.1 The standard $Z'$ selection results

Hereby we report the complete list of final results for signal efficiencies and expected background yields in the contiguous binning scheme which is used for the statistical analysis of the data.

**Table A.1:** Signal efficiencies and number of background events after all the analysis selections in contiguous  $Z'$  mass bins, for the standard  $Z'$  analysis. Background normalized to an integrated luminosity of  $276 \text{ pb}^{-1}$ . Signal efficiencies and background yields include the 0.79 trigger efficiency (Section 7.2)

$M_{Z'}$ [GeV/ $c^2$ ]	Mass range [GeV/ $c^2$ ]	Efficiency [%]	Background events
0.50	-0.15 - 1.15	$4.34 \pm 0.13$	$0.67 \pm 0.05$
1.39	1.15 - 1.63	$7.60 \pm 0.16$	$0.33 \pm 0.04$
1.81	1.63 - 1.98	$7.93 \pm 0.17$	$0.26 \pm 0.03$
2.13	1.98 - 2.29	$8.01 \pm 0.17$	$0.22 \pm 0.03$
2.42	2.29 - 2.56	$8.06 \pm 0.17$	$0.19 \pm 0.03$
2.68	2.56 - 2.81	$8.03 \pm 0.17$	$0.14 \pm 0.03$
2.91	2.81 - 3.02	$7.98 \pm 0.17$	$0.12 \pm 0.02$
3.11	3.02 - 3.21	$7.79 \pm 0.17$	$0.11 \pm 0.02$
3.29	3.21 - 3.38	$7.51 \pm 0.16$	$0.17 \pm 0.03$
3.46	3.38 - 3.54	$7.26 \pm 0.16$	$0.16 \pm 0.03$
3.62	3.54 - 3.69	$7.26 \pm 0.16$	$0.16 \pm 0.03$
3.77	3.69 - 3.84	$7.34 \pm 0.16$	$0.21 \pm 0.03$
3.91	3.84 - 3.98	$7.41 \pm 0.16$	$0.26 \pm 0.05$
4.04	3.98 - 4.11	$7.40 \pm 0.16$	$0.23 \pm 0.04$
4.17	4.11 - 4.24	$7.21 \pm 0.16$	$0.24 \pm 0.04$
4.29	4.24 - 4.36	$7.04 \pm 0.16$	$0.25 \pm 0.04$
4.41	4.36 - 4.47	$6.87 \pm 0.16$	$0.26 \pm 0.04$
4.52	4.47 - 4.58	$6.72 \pm 0.16$	$0.28 \pm 0.05$

Continued on next page

Table A.1 – *Continued from previous page*

$M_{Z'}$ [GeV/ $c^2$ ]	Mass range [GeV/ $c^2$ ]	Efficiency [%]	Background events
4.63	4.58 - 4.69	$6.65 \pm 0.16$	$0.22 \pm 0.03$
4.74	4.69 - 4.79	$6.57 \pm 0.15$	$0.29 \pm 0.04$
4.85	4.79 - 4.90	$6.49 \pm 0.15$	$0.28 \pm 0.05$
4.95	4.90 - 5.00	$6.42 \pm 0.15$	$0.32 \pm 0.06$
5.05	5.00 - 5.09	$6.32 \pm 0.15$	$0.26 \pm 0.04$
5.14	5.09 - 5.18	$6.19 \pm 0.15$	$0.41 \pm 0.08$
5.23	5.18 - 5.27	$6.08 \pm 0.15$	$0.23 \pm 0.04$
5.31	5.27 - 5.35	$5.97 \pm 0.15$	$0.27 \pm 0.04$
5.38	5.35 - 5.42	$5.86 \pm 0.15$	$0.36 \pm 0.06$
5.46	5.42 - 5.49	$5.76 \pm 0.15$	$0.31 \pm 0.06$
5.53	5.49 - 5.56	$5.67 \pm 0.14$	$0.32 \pm 0.06$
5.60	5.56 - 5.63	$5.57 \pm 0.14$	$0.29 \pm 0.05$
5.66	5.63 - 5.70	$5.47 \pm 0.14$	$0.34 \pm 0.06$
5.73	5.70 - 5.76	$5.37 \pm 0.14$	$0.45 \pm 0.08$
5.80	5.76 - 5.83	$5.27 \pm 0.14$	$0.35 \pm 0.06$
5.87	5.83 - 5.90	$5.17 \pm 0.14$	$0.39 \pm 0.06$
5.94	5.90 - 5.97	$5.07 \pm 0.14$	$0.31 \pm 0.06$
6.01	5.97 - 6.04	$4.96 \pm 0.14$	$0.30 \pm 0.05$
6.08	6.04 - 6.11	$4.83 \pm 0.13$	$0.58 \pm 0.10$
6.15	6.11 - 6.18	$4.69 \pm 0.13$	$0.30 \pm 0.07$
6.21	6.18 - 6.25	$4.56 \pm 0.13$	$0.41 \pm 0.08$
6.28	6.25 - 6.31	$4.43 \pm 0.13$	$0.37 \pm 0.07$
6.34	6.31 - 6.38	$4.30 \pm 0.13$	$0.53 \pm 0.10$
6.41	6.38 - 6.44	$4.17 \pm 0.12$	$0.38 \pm 0.09$
6.47	6.44 - 6.50	$4.05 \pm 0.12$	$0.35 \pm 0.08$
6.53	6.50 - 6.56	$4.05 \pm 0.12$	$0.29 \pm 0.07$
6.58	6.56 - 6.61	$4.16 \pm 0.12$	$0.55 \pm 0.10$
6.64	6.61 - 6.67	$4.27 \pm 0.13$	$0.57 \pm 0.10$
6.69	6.67 - 6.72	$4.37 \pm 0.13$	$0.83 \pm 0.13$
6.75	6.72 - 6.77	$4.47 \pm 0.13$	$1.32 \pm 0.18$
6.80	6.77 - 6.83	$4.57 \pm 0.13$	$1.18 \pm 0.15$
6.85	6.83 - 6.88	$4.67 \pm 0.13$	$1.47 \pm 0.18$
6.90	6.88 - 6.93	$4.77 \pm 0.13$	$1.81 \pm 0.20$
6.95	6.93 - 6.98	$4.87 \pm 0.13$	$1.85 \pm 0.20$
7.01	6.98 - 7.03	$5.06 \pm 0.14$	$3.08 \pm 0.24$
7.06	7.03 - 7.09	$5.92 \pm 0.14$	$9.34 \pm 0.37$
7.12	7.09 - 7.14	$6.81 \pm 0.15$	$17.47 \pm 0.50$
7.17	7.14 - 7.20	$7.75 \pm 0.16$	$23.43 \pm 0.57$
7.24	7.20 - 7.27	$8.74 \pm 0.17$	$32.93 \pm 0.71$
7.30	7.27 - 7.33	$9.77 \pm 0.18$	$41.23 \pm 0.81$
7.37	7.33 - 7.40	$10.86 \pm 0.19$	$50.41 \pm 0.91$
7.44	7.40 - 7.47	$11.98 \pm 0.20$	$62.98 \pm 1.06$
7.51	7.47 - 7.55	$12.92 \pm 0.21$	$69.32 \pm 1.13$

Continued on next page

Table A.1 – *Continued from previous page*

$M_{Z'}$ [GeV/ $c^2$ ]	Mass range [GeV/ $c^2$ ]	Efficiency [%]	Background events
7.58	7.55 - 7.62	$12.66 \pm 0.20$	$73.16 \pm 1.19$
7.66	7.62 - 7.69	$12.40 \pm 0.20$	$76.22 \pm 1.24$
7.73	7.69 - 7.76	$12.15 \pm 0.20$	$76.07 \pm 1.25$
7.79	7.76 - 7.83	$11.91 \pm 0.20$	$79.03 \pm 1.30$
7.86	7.83 - 7.89	$11.67 \pm 0.20$	$80.55 \pm 1.33$
7.92	7.89 - 7.95	$11.44 \pm 0.20$	$77.66 \pm 1.32$
7.98	7.95 - 8.01	$11.22 \pm 0.19$	$80.99 \pm 1.36$
8.04	8.01 - 8.07	$10.97 \pm 0.19$	$83.10 \pm 1.39$

## A.2 The LFV $Z'$ selection results

Hereby we report the complete list of final results for expected background yields in the contiguous binning scheme which is used for the statistical analysis of the data.

**Table A.2:** Number of background events after all the analysis selections in contiguous mass bins, fro the LFV  $Z'$ . The number of background events is normalized to an integrated luminosity of 276  $\text{pb}^{-1}$ . Signal efficiencies and background yields include the 0.96 trigger efficiency (see Section 7.2)

$M_{Z'}$ [GeV/ $c^2$ ]	Mass range [GeV/ $c^2$ ]	Background events
0.50	-0.15 - 1.15	$0.00 \pm 0.01$
1.39	1.15 - 1.63	$0.02 \pm 0.01$
1.81	1.63 - 1.98	$0.03 \pm 0.01$
2.13	1.98 - 2.29	$0.04 \pm 0.02$
2.42	2.29 - 2.56	$0.01 \pm 0.01$
2.68	2.56 - 2.81	$0.05 \pm 0.02$
2.91	2.81 - 3.02	$0.03 \pm 0.01$
3.11	3.02 - 3.21	$0.07 \pm 0.02$
3.29	3.21 - 3.38	$0.08 \pm 0.02$
3.46	3.38 - 3.54	$0.17 \pm 0.03$
3.62	3.54 - 3.69	$0.11 \pm 0.03$
3.77	3.69 - 3.84	$0.09 \pm 0.02$
3.91	3.84 - 3.98	$0.13 \pm 0.03$
4.04	3.98 - 4.11	$0.18 \pm 0.03$
4.17	4.11 - 4.24	$0.09 \pm 0.02$
4.29	4.24 - 4.36	$0.16 \pm 0.03$
4.41	4.36 - 4.47	$0.13 \pm 0.03$
4.52	4.47 - 4.58	$0.19 \pm 0.04$
4.63	4.58 - 4.69	$0.09 \pm 0.02$
4.74	4.69 - 4.79	$0.15 \pm 0.05$
4.85	4.79 - 4.90	$0.12 \pm 0.03$
4.95	4.90 - 5.00	$0.15 \pm 0.03$
5.05	5.00 - 5.09	$0.07 \pm 0.02$
5.14	5.09 - 5.18	$0.17 \pm 0.05$
5.23	5.18 - 5.27	$0.16 \pm 0.03$
5.31	5.27 - 5.35	$0.20 \pm 0.04$
5.38	5.35 - 5.42	$0.15 \pm 0.03$
5.46	5.42 - 5.49	$0.19 \pm 0.04$
5.53	5.49 - 5.56	$0.16 \pm 0.03$
5.60	5.56 - 5.63	$0.21 \pm 0.05$
5.66	5.63 - 5.70	$0.19 \pm 0.05$
5.73	5.70 - 5.76	$0.20 \pm 0.06$
5.80	5.76 - 5.83	$0.11 \pm 0.03$
5.87	5.83 - 5.90	$0.17 \pm 0.05$
5.94	5.90 - 5.97	$0.27 \pm 0.07$
6.01	5.97 - 6.04	$0.14 \pm 0.04$

Continued on next page

Table A.2 – *Continued from previous page*

$M_{Z'}$ [GeV/ $c^2$ ]	Mass range [GeV/ $c^2$ ]	Background events
6.08	6.04 - 6.11	$0.15 \pm 0.04$
6.15	6.11 - 6.18	$0.13 \pm 0.03$
6.21	6.18 - 6.25	$0.17 \pm 0.05$
6.28	6.25 - 6.31	$0.11 \pm 0.04$
6.34	6.31 - 6.38	$0.17 \pm 0.03$
6.41	6.38 - 6.44	$0.06 \pm 0.02$
6.47	6.44 - 6.50	$0.09 \pm 0.04$
6.53	6.50 - 6.56	$0.11 \pm 0.04$
6.58	6.56 - 6.61	$0.12 \pm 0.04$
6.64	6.61 - 6.67	$0.17 \pm 0.05$
6.69	6.67 - 6.72	$0.19 \pm 0.04$
6.75	6.72 - 6.77	$0.23 \pm 0.06$
6.80	6.77 - 6.83	$0.38 \pm 0.07$
6.85	6.83 - 6.88	$0.34 \pm 0.07$
6.90	6.88 - 6.93	$0.51 \pm 0.09$
6.95	6.93 - 6.98	$0.50 \pm 0.09$
7.01	6.98 - 7.03	$0.94 \pm 0.09$
7.06	7.03 - 7.09	$5.45 \pm 0.22$
7.12	7.09 - 7.14	$9.25 \pm 0.27$
7.17	7.14 - 7.20	$13.13 \pm 0.31$
7.24	7.20 - 7.27	$18.54 \pm 0.39$
7.30	7.27 - 7.33	$21.54 \pm 0.43$
7.37	7.33 - 7.40	$25.00 \pm 0.45$
7.44	7.40 - 7.47	$28.38 \pm 0.49$
7.51	7.47 - 7.55	$29.09 \pm 0.47$
7.58	7.55 - 7.62	$29.22 \pm 0.51$
7.66	7.62 - 7.69	$26.60 \pm 0.47$
7.73	7.69 - 7.76	$25.13 \pm 0.48$
7.79	7.76 - 7.83	$21.96 \pm 0.44$
7.86	7.83 - 7.89	$19.57 \pm 0.43$
7.92	7.89 - 7.95	$17.34 \pm 0.39$
7.98	7.95 - 8.01	$15.26 \pm 0.37$
8.04	8.01 - 8.07	$13.95 \pm 0.36$

### A.3 Signal shape study: toy MC results

Results from the toy MC validation study, performed on the simulated signals for different mass hypotheses of the standard  $Z'$  boson, are reported below.

**Table A.3:** The distributions of *pullMean* and *pullSigma* values of  $\sigma_{\text{CB}}$  for every generated  $Z'$  mass point are listed below.

$M_{Z'}$ [GeV/c <sup>2</sup> ]	<i>pullMean</i>	<i>pullSigma</i>
0.5	$-0.0069 \pm 0.032$	$1.009 \pm 0.023$
1.0	$-0.0321 \pm 0.031$	$0.972 \pm 0.022$
1.5	$-0.0369 \pm 0.032$	$1.010 \pm 0.023$
2.0	$-0.0043 \pm 0.032$	$1.005 \pm 0.022$
2.5	$-0.0633 \pm 0.030$	$0.957 \pm 0.021$
3.0	$-0.066 \pm 0.034$	$1.077 \pm 0.024$
3.5	$-0.0272 \pm 0.033$	$1.056 \pm 0.024$
4.0	$-0.0928 \pm 0.031$	$0.991 \pm 0.022$
4.5	$-0.0583 \pm 0.032$	$0.997 \pm 0.022$
5.0	$-0.0435 \pm 0.032$	$1.008 \pm 0.023$
5.5	$-0.0690 \pm 0.032$	$1.004 \pm 0.022$
6.0	$-0.0629 \pm 0.032$	$1.005 \pm 0.022$
6.5	$-0.0433 \pm 0.032$	$1.015 \pm 0.023$
7.0	$-0.0334 \pm 0.033$	$1.033 \pm 0.023$
7.5	$0.004 \pm 0.031$	$0.969 \pm 0.022$
8.0	$0.039 \pm 0.031$	$0.978 \pm 0.022$

**Table A.4:** The distributions of *pullMean* and *pullSigma* values of  $\sigma_{\text{Gauss}}$  for every generated  $Z'$  mass point are reported.

$M_{Z'}$ [GeV/c <sup>2</sup> ]	<i>pullMean</i>	<i>pullSigma</i>
0.5	$0.037 \pm 0.031$	$0.983 \pm 0.022$
1.0	$-0.0386 \pm 0.031$	$0.967 \pm 0.022$
1.5	$-0.0381 \pm 0.032$	$1.015 \pm 0.023$
2.0	$-0.0792 \pm 0.032$	$1.002 \pm 0.022$
2.5	$0.026 \pm 0.032$	$1.000 \pm 0.022$
3.0	$-0.0744 \pm 0.034$	$1.081 \pm 0.024$
3.5	$-0.0338 \pm 0.033$	$1.035 \pm 0.023$
4.0	$-0.3522 \pm 0.040$	$1.251 \pm 0.028$
4.5	$-0.1007 \pm 0.032$	$1.026 \pm 0.023$
5.0	$0.038 \pm 0.033$	$1.031 \pm 0.023$
5.5	$0.024 \pm 0.031$	$0.976 \pm 0.022$
6.0	$-0.0938 \pm 0.033$	$1.032 \pm 0.023$
6.5	$-0.1174 \pm 0.033$	$1.032 \pm 0.023$
7.0	$-0.0511 \pm 0.031$	$0.991 \pm 0.022$
7.5	$-0.0280 \pm 0.033$	$1.034 \pm 0.023$
8.0	$-0.0281 \pm 0.032$	$1.025 \pm 0.023$

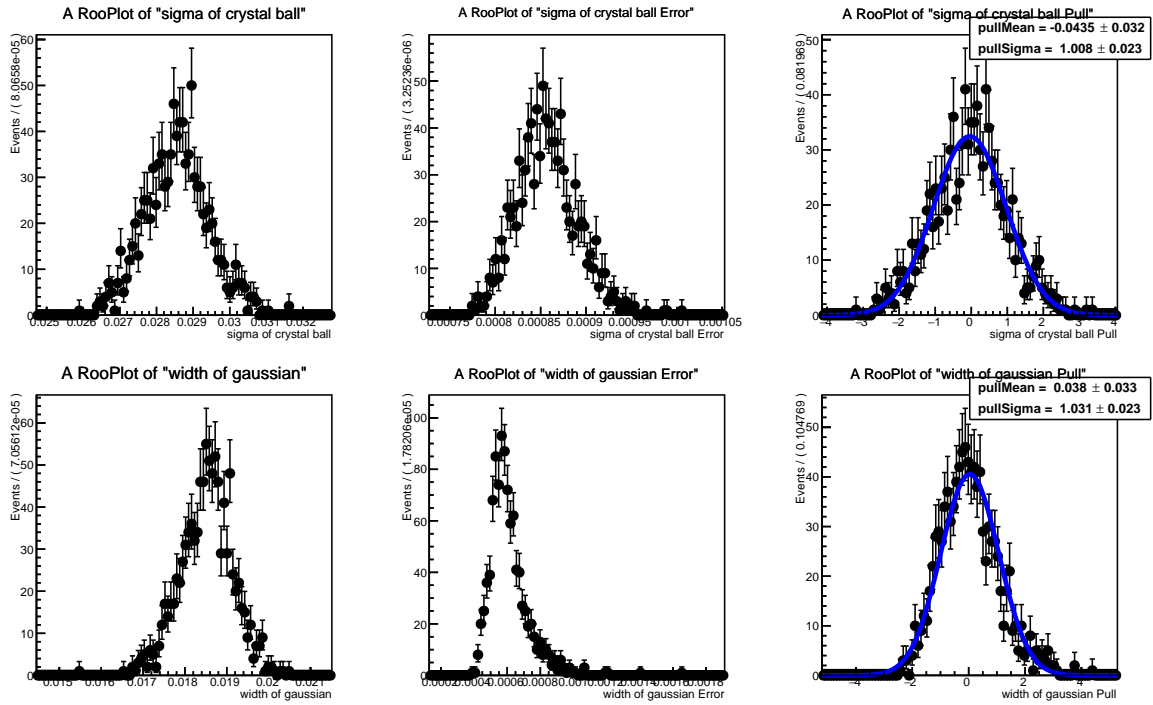


**Figure A.1:** Validation plots of  $\sigma_{\text{CB}}$  and  $\sigma_{\text{Gauss}}$  for  $M_{Z'} = 5$  GeV. The pull distribution for every parameter is fitted with a Gaussian (blue line). The fit results are shown in the top right corner of the graph and are consistent with a normalized distribution of null mean and unitary width, which assesses the signal fit procedure is reliable and unbiased.

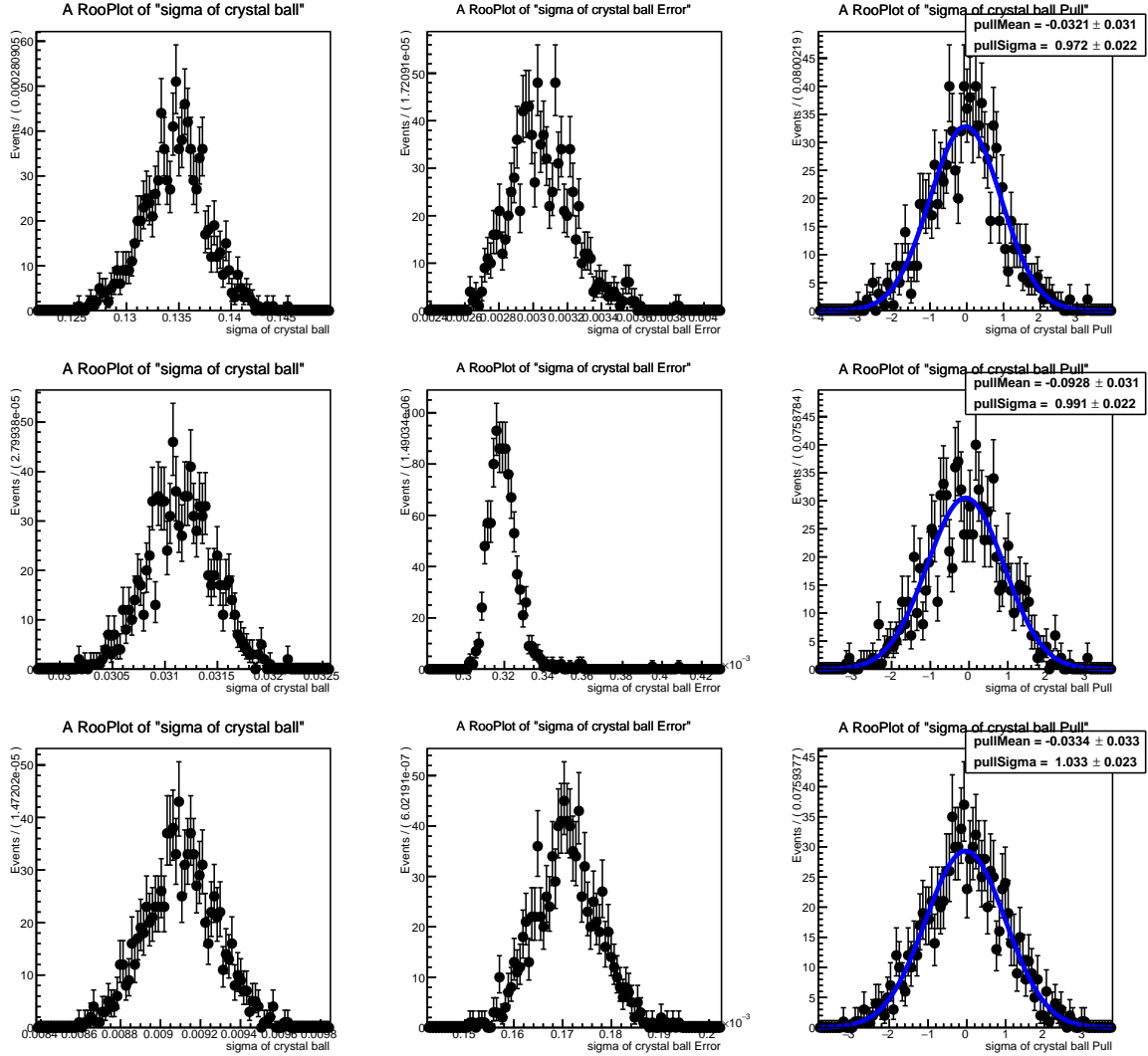


**Figure A.2:** Validation plots of  $\sigma_{CB}$  for  $M_{Z'} = 1, 4$  and  $7$  GeV. The pull distribution for every parameter is fitted with a Gaussian (blue line). The fit results are shown in the top right corner of the graph and are consistent with a normalized distribution of null mean and unitary width, which assesses the signal fit procedure is reliable and unbiased.

# Appendix B

## Performance studies on Phase 2 data

### B.1 The trigger efficiency study

The complete study is reported in [88], which is an internal Belle II note, therefore for the readers who cannot access the document it is also summarized hereby.

In Phase 2, two-track events could pass the hardware trigger system by firing the CDC-based trigger `ffo`, bit 7 of the global decision logic, hereafter defined as `bitCDC` to adopt the same convention as in Chapter 7. For an event to comply with `bitCDC` conditions, it should have more than one 2D-CDC track with the opening angle more than  $90^\circ$  in the transverse plane and not trigger the Bhabha veto. Due to the problems with the readout electronics and changes of the configuration during the data taking, the real conditions of the `bitCDC` fluctuated run by run, thus being a performance study necessary for physics analyses relying on the CDC trigger.

The CDC trigger performance has been evaluated on events that passed the trigger system due to the orthogonal ECL trigger `hie` (trigger bit 8, hereafter referred to as `bitECL`). Since the CDC and ECL trigger decisions are independent, efficiency of the CDC trigger selection measured for ECL-selected events is assumed to be identical to that for the events that do not fire ECL trigger. Moreover the selected sample on Phase 2 data has to fulfill the following requirements:

- exactly two *good* tracks must originate from the vertex with  $|d_z| < 2.0$  and  $|d_r| < 0.5$  and being identified as electrons, with the ratio of energy deposited in ECL to the track momentum measured in the laboratory frame higher than 0.8;
- the events are required to fire trigger `bitECL`, which implies the energy deposit in the ECL to be higher than 1.5 GeV and not to be rejected by the Bhabha veto;
- both tracks should be associated with an ECL cluster detected in the barrel region and have transverse momentum more than 1 GeV/c.

After these selections, 656103 events were left for the study.

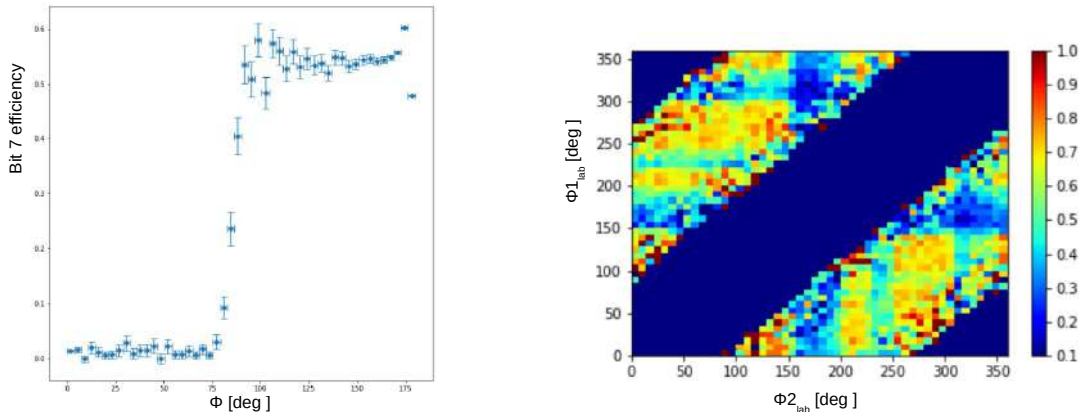


**Figure B.1:** The trigger  $\text{bit}_{\text{CDC}}$  efficiency as a function of the opening 2D  $\phi$  angle (left) and the  $\text{bit}_{\text{CDC}}$  efficiency map in bins of the azimuthal angles of the two lepton tracks (right) are reported.

### B.1.1 Plateau efficiency

The activation curve of the  $\text{bit}_{\text{CDC}}$  is expected to be a sigmoid as a function of the 2D opening angle  $\phi$ , which is defined as the angle between the projections of the two tracks on the transverse plane perpendicular to the beam pipe. With a finer binning in  $\phi$ , the efficiency drop for the back-to-back events corresponding to the high  $\phi$  values can be observed, as shown in the Figure B.1. The low plateau efficiency and the drop of efficiency in back-to-back events can be understood from the analysis of the  $\text{bit}_{\text{CDC}}$  efficiency map calculated in bins of the azimuthal angles of the two tracks (Figure B.1, right plot). The main features of this plot have been investigated:

- diagonal lines with 0 efficiency corresponds to the requirement of the two tracks to have  $90^\circ$  opening angle;
- vertical and horizontal lines of the low efficiency correspond to the  $\phi$  regions covered with malfunctioning modules of the CDC trigger system. Three inefficiency regions can be spotted in  $\phi$  with approximate borders at  $[150^\circ, 200^\circ]$ ,  $[220^\circ, 250^\circ]$  and  $[300^\circ, 340^\circ]$ ;
- overlap of horizontal and vertical inefficiency regions can be understood as the two inefficiency region located at the two diametrically opposite regions of the CDC. Such overlaps are responsible for the structure in plateau efficiency observed for the back-to-back events.

For the rest of the study the high- $\phi$  regions showing large inefficiencies are not considered when computing the flat plateau efficiency distribution, which is defined as the efficiency of the selection of two-track events with opening angle higher than  $90^\circ$  and smaller than  $172^\circ$ , and it is also shown in Figure B.2 as a function of the run number. The total trigger  $\text{bit}_{\text{CDC}}$  efficiency is therefore computed as the average run plateau efficiency, weighted with the corresponding run luminosity, for all those run  $i$  with non-zero CDC trigger efficiency:

$$\epsilon_{\text{CDC}} = \frac{\sum_i \epsilon_i^{\text{bit}_{\text{CDC}}} \times \mathcal{L}_i}{\sum_i \mathcal{L}_i}. \quad (\text{B.1})$$

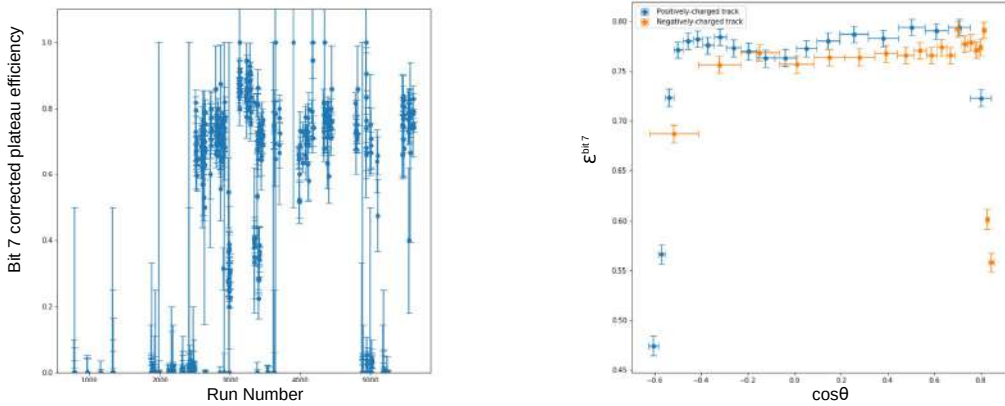


**Figure B.2:** The plateau efficiency as defined after the selections on the opening angle is shown as a function of the run number (left) and of the  $\cos\theta$  of the selected tracks (right).

**Table B.1:** Results of the  $\text{bit}_{\text{CDC}}$  trigger efficiency study on the runs selected as previously described, with the list of the corresponding relative systematic uncertainties due to kinematic dependencies. The total relative systematic error is the sum in quadrature of all the contributions.

Efficiency ( $\epsilon_{\text{CDC}}$ )	Luminosity [ $\text{fb}^{-1}$ ]	$\sigma^{n\text{CDCHits}}$ , %	$\sigma^{pT}$ , %	$\sigma^{l1 \cos\theta}$ , %	$\sigma^{l2 \cos\theta}$ , %	$\sigma^\phi$ , %
0.79	276	4	1	1	2	3

### B.1.2 Systematic uncertainty evaluation

The systematic uncertainty of the method has been estimated by studying the dependence of the plateau efficiency on the kinematic and track-quality variables of the selected candidates and using its variation in bins of these variables as the systematic uncertainty.

This study shows that the plateau efficiency depends on  $\theta$  angle of the tracks as shown in the Figure B.2 (right) and that it drops on the edges of the CDC acceptance, while a flat distribution is shown for tracks with  $\cos(\theta) \in (-0.5, 0.8)$ , this region being referred to as reduced CDC acceptance. The dependencies on the minimum number of CDC hits ( $n\text{CDCHits}$ ) and on the minimum transverse momentum of the two reconstructed tracks ( $pT_{\text{min}}$ ) have also been studied, and the final results has found to be stable in a reduced CDC acceptance, for the selected events as described above, with back-to-back events excluded from the computation.

The systematic uncertainties in the measurement of  $\epsilon_{\text{CDC}}$  are reported in Table B.1 for each of the studied kinematic variable and they are calculated as half of the variance in plateau efficiency among different bins of the selected variable divided by the total efficiency. The final result of this study assesses a CDC trigger efficiency for events satisfying the above described selections which correponds to  $(79 \pm 6_{\text{sys}})\%$ , where the statistical uncertainty has found to be negligible and the total systematic uncertainty is the sum in quadrature of the measured contributions reported in Table B.1.

**Table B.2:** Selection requirements used in the lepton ID performance study and tag requirement to identify the tagged muon track, by exploiting the muon ID probability as computed from KLM information only.

Exactly two tracks from the IP	$ d_z  < 2 \text{ cm AND }  d_r  < 0.5 \text{ cm}$
At least one high-momentum track	$p_1^{LAB} > 0.5 \text{ GeV}/c$ OR $p_2^{LAB} > 0.5 \text{ GeV}/c$
Minimum transverse momentum required	$pT_1^{LAB} > 0.25 \text{ GeV}/c$ AND $pT_2^{LAB} > 0.25 \text{ GeV}/c$
Maximum value for the sum of the absolute values of the momenta	$ p_1^{LAB}  +  p_2^{LAB}  > 4 \text{ GeV}/c$
Maximum value for total transverse momentum	$ pT_1^{LAB} + pT_2^{LAB}  < 1.5 \text{ GeV}/c$
Muon tag	$P(\text{muonID})_{\text{KLM}} > 0.1$

## B.2 The lepton identification study

One of simplest discriminations between electron and muon tracks can be done through the energy deposition in the electromagnetic calorimeter relative to the momentum of the particles in the laboratory frame, later on referred to as the  $E/p$  variable. Electron tracks are expected to be absorbed by the material in the ECL and therefore the ratio  $E/p$  should peak at 1, while muons (and generally hadrons) are expected to pass through the ECL, leaving  $\sim 10 - 30\%$  of the energy there. The goal of the study is to evaluate the probability for a track to be correctly identified as a muon, if  $E/p < 0.4$  and the energy deposited in ECL is within  $[0.15, 0.4]$  GeV window. An overview of the analysis strategy and the main findings, which are described with more details in the dedicated internal note [98], are reported hereafter.

### Data sets and event selection

Data collected during Phase 2 and reprocessed during the sixth production campaign (prod6) are exploited, while for what concerns the simulation MC samples from the 11<sup>th</sup> campaign MC11 have been studied, corresponding to a luminosity of  $10 \times 10^6$  generated events of Bhabha scattering,  $e^+e^- \rightarrow e^+e^-e^+e^-$ ,  $e^+e^- \rightarrow e^+e^-\mu^+\mu^-$  and  $e^+e^- \rightarrow \mu^+\mu^-$  processes. Also  $368 \times 10^6$  events of the process  $e^+e^- \rightarrow \tau^+\tau^-$  have been generated.

Events have been selected requiring exactly two charged tracks coming from the IP and the reconstructed two-track candidate to satisfy the requirements listed in Table B.2. The purpose is to perform a self-tagging analysis on  $e^+e^-\mu^+\mu^-$  events where electrons escape the detection along the beam pipe and one of the reconstructed tracks has been correctly tagged as muon by exploiting KLM information. The retention rate (fraction of selected events) for each generated sample is reported in Table B.3.

During Phase 2, KLM performances were not constant over different runs and hardly predictable, making impossible to use the KLM information as a reliable and stable selection in the analysis, without a precise measurement of its run by run efficiency. However, it can be exploited for self-tagging performance study to test the ECL-based selection efficiency on tracks detected by the KLM. Asking a muon identity probability measured with the KLM only

to be  $> 0.1$  acts as self-tag on the selected track, which is then assumed to be a true muon. The fraction of these tracks passing the ECL-based selection is the estimation of the muon selection efficiency expected in this analysis. The study is performed in bins of transverse

**Table B.3:** Expected contribution of the different simulated processes to the final selected sample.

Sample	$\mu^+$ -tag	$\mu^-$ -tag
Bhabha	$< 0.05\%$	$< 0.05\%$
$e^+e^- \rightarrow e^+e^-e^+e^-$	0.2%	0.1%
$e^+e^- \rightarrow e^+e^-\mu^+\mu^-$	99.1%	99.1%
$e^+e^- \rightarrow \mu^+\mu^-$	0.2%	0.2%
$e^+e^- \rightarrow \tau^+\tau^-$	0.5%	0.5%

momentum of  $(p_T; \cos(\theta))$ , where borders of momentum bins are 0.3, 0.5, 1, 7 GeV/c, and borders of  $\theta$  bins correspond to ECL main regions. The efficiency of the muon selection on Phase 2 data using ECL variables is computed as the ratio of the  $\mu$ -tagged tracks before and after ECL-based selection in each phase space bin. Correction scale factors due to data-MC differences have been computed as the ratio of the efficiencies measured in  $e^+e^-\mu^+\mu^-$  events on data and on simulation. The associated statistical uncertainty is dominated by the size of the final selected muon sample and the systematic uncertainty of the method has been evaluated as the fraction of fake muon tracks passing the selection as measured from the simulations, which is found to be negligible ( $< 0.5\%$ ) compared to the uncertainty coming from the data-MC comparison.

The deviation of the measured correction factors from unit, in bins of  $(p_T, \cos\theta)$ , gives the estimation of the systematic uncertainty in the muon selection efficiency for the  $Z'$  search study. From the results of the self-tagging analysis on the four-lepton final state events, considering the fiducial region which corresponds to the barrel ECL ( $-0.5 < \cos\theta < 0.8$ ) and after subtracting the contribution of the statistical uncertainty, the residual data-MC discrepancy is found to be 2% per track.

### B.3 The track reconstruction efficiency study

The results of the data/MC comparison referred to in Section 7.4 are hereby reported, for the electron and muon channels respectively. All of the requirements described for track selections and background suppression in Section 7.4 are applied. Additionally, the MC yields are normalized to the effective luminosity of the sample ( $\frac{N_{gen}}{\sigma[pb]}$ , see Table 7.2), scaled to 381 pb<sup>-1</sup> and corrected in a bin-by-bin manner by the measured trigger efficiency in data (see Equation 7.5).

#### Electron channel

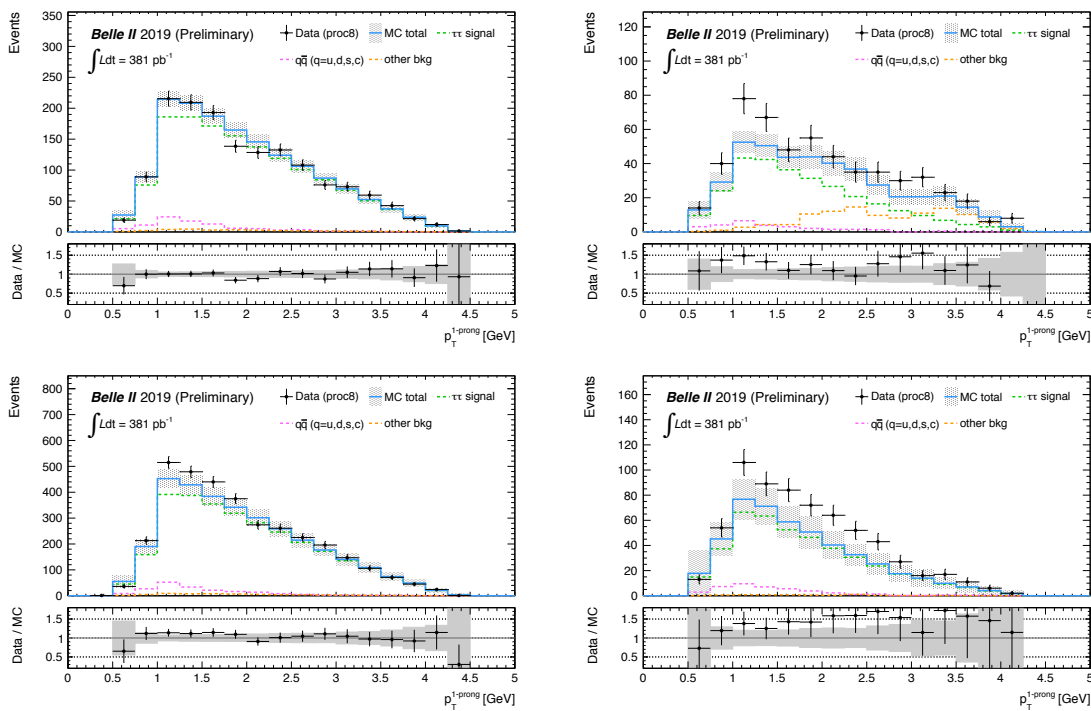


**Figure B.3:** Distribution of the 1-prong track  $p_T$  in the electron  $\tau$ -decay channel for the analyzed samples: OS charged events in the 4-track sample (top-left), OS charged events in the 3-track sample (top-right), SS charged events in the 4-track sample (bottom-left) and SS charged events in the 3-track sample (bottom-right).

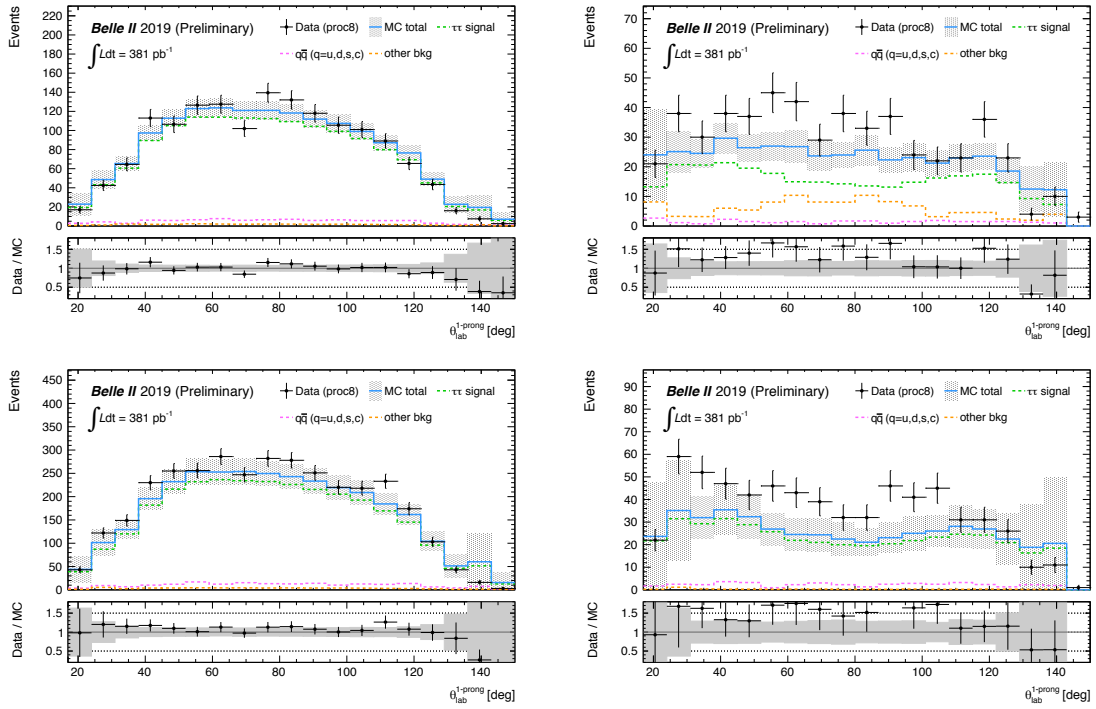


**Figure B.4:** Distribution of the 1-prong track  $\theta$  in the electron  $\tau$ -decay channel for the analyzed samples: OS charged events in the 4-track sample (top-left), OS charged events in the 3-track sample (top-right), SS charged events in the 4-track sample (bottom-left) and SS charged events in the 3-track sample (bottom-right).

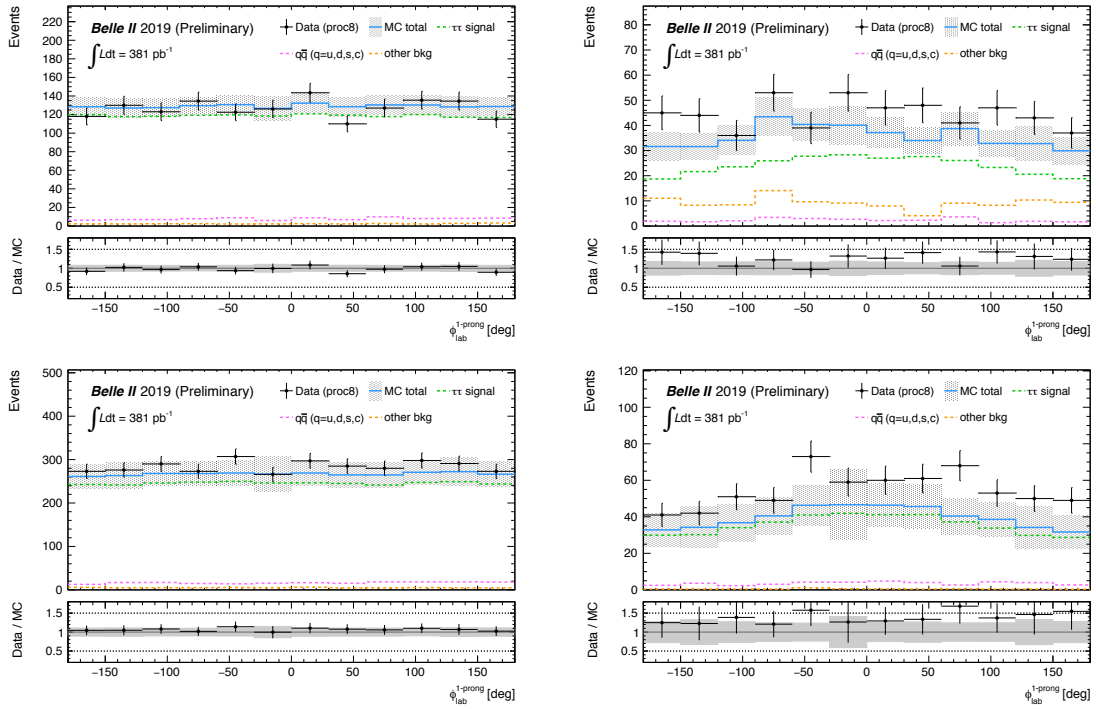


**Figure B.5:** Distribution of the 1-prong track  $\phi$  in the electron  $\tau$ -decay channel for the analyzed samples: OS charged events in the 4-track sample (top-left), OS charged events in the 3-track sample (top-right), SS charged events in the 4-track sample (bottom-left) and SS charged events in the 3-track sample (bottom-right).

## Muon channel

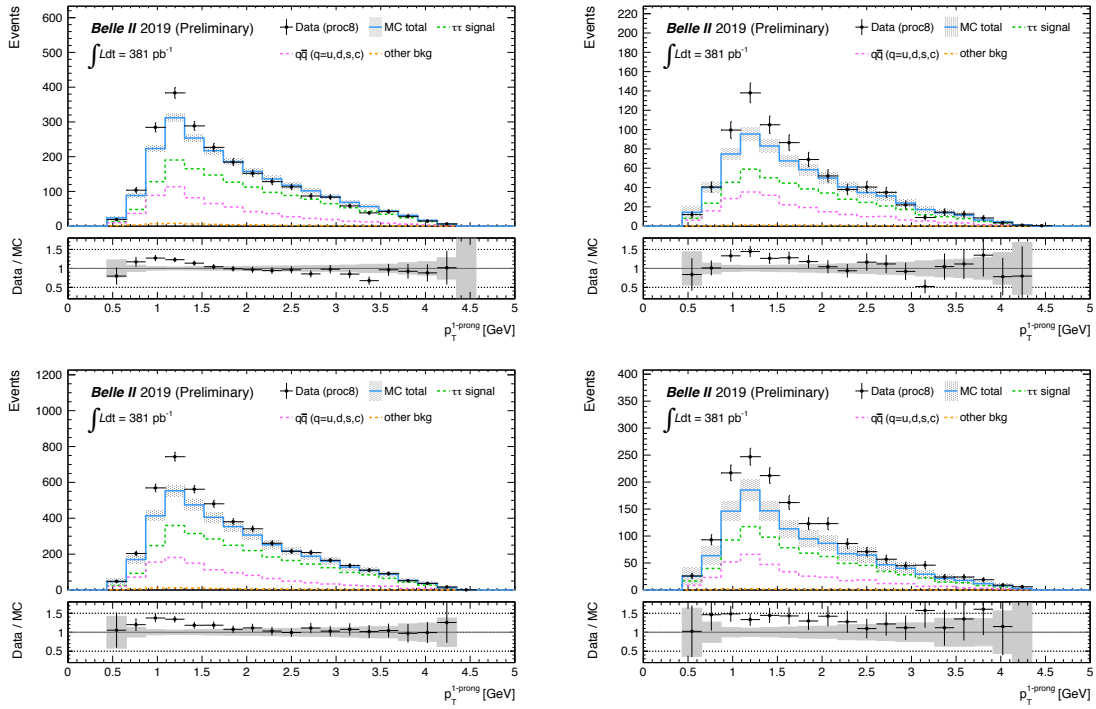


**Figure B.6:** Distribution of the 1-prong track  $p_T$  in the muon  $\tau$ -decay channel for the analyzed samples: OS charged events in the 4-track sample (top-left), OS charged events in the 3-track sample (top-right), SS charged events in the 4-track sample (bottom-left) and SS charged events in the 3-track sample (bottom-right).

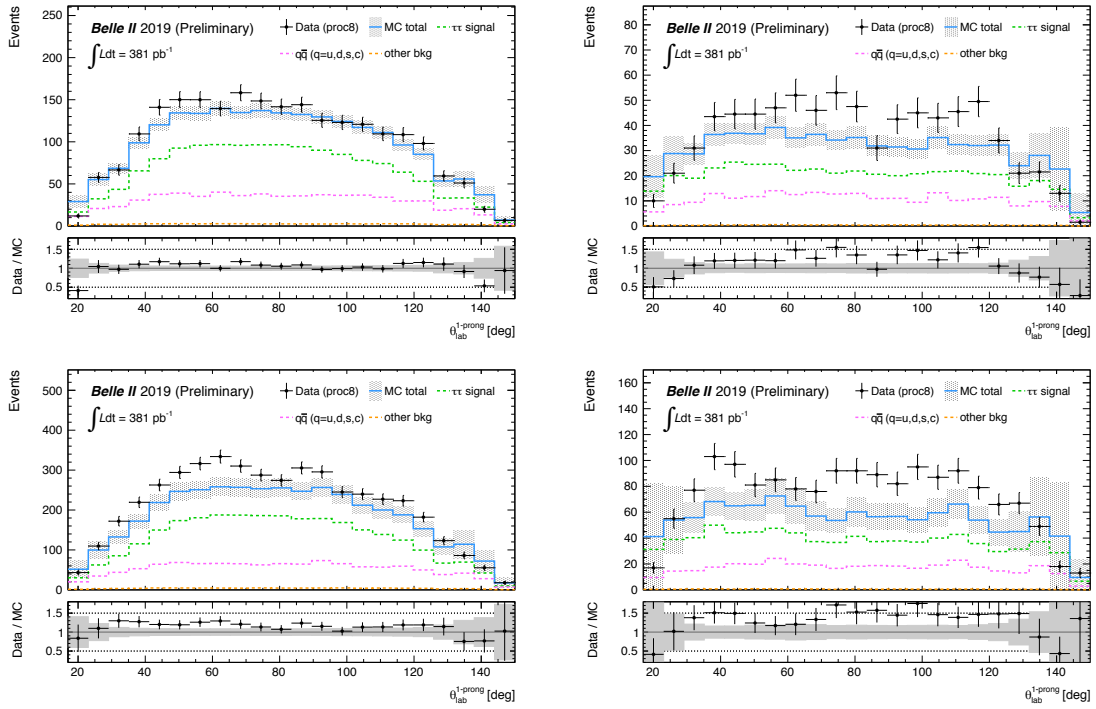


**Figure B.7:** Distribution of the 1-prong track  $\theta$  in the muon  $\tau$ -decay channel for the analyzed samples: OS charged events in the 4-track sample (top-left), OS charged events in the 3-track sample (top-right), SS charged events in the 4-track sample (bottom-left) and SS charged events in the 3-track sample (bottom-right).

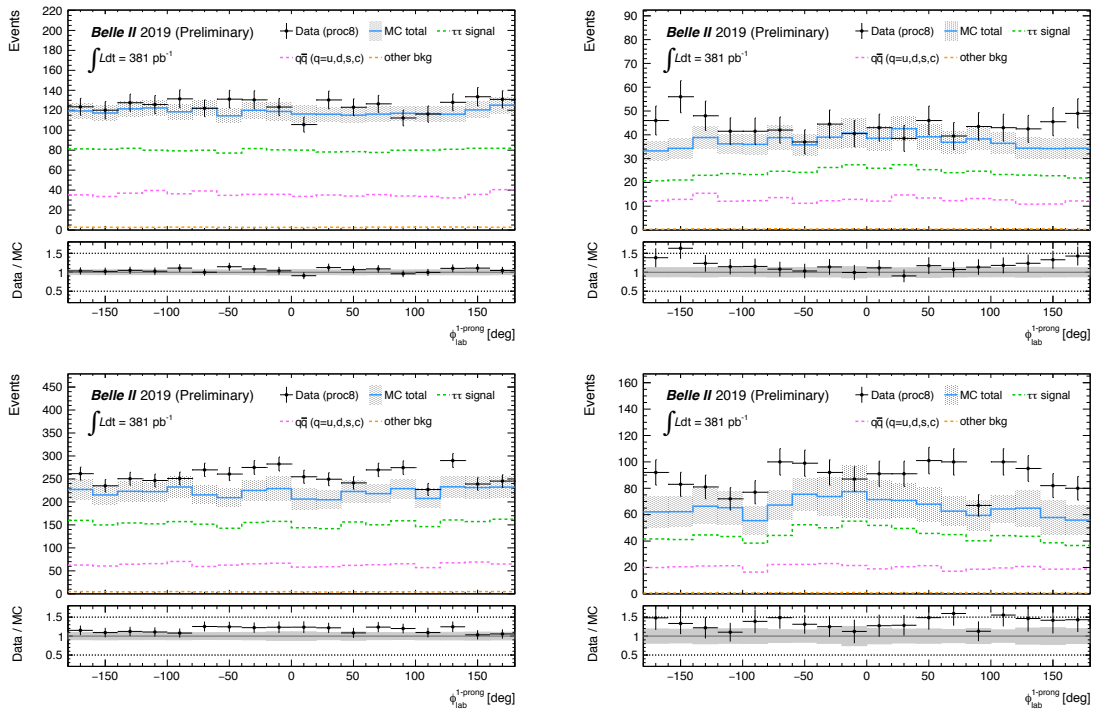


**Figure B.8:** Distribution of the 1-prong track  $\phi$  in the muon  $\tau$ -decay channel for the analyzed samples: OS charged events in the 4-track sample (top-left), OS charged events in the 3-track sample (top-right), SS charged events in the 4-track sample (bottom-left) and SS charged events in the 3-track sample (bottom-right).

### B.3.1 Calibration procedure

The distributions for the efficiency estimator computed on the default and modified MC samples for OS and SS charge, for the electron and muon channel events have been studied, for different values of  $\delta_{MC}$ . The plots showing results as a function of the 1-prong  $\phi^{CM}, \theta_{lab}$  are reported in FigureB.9, FigureB.10 for the electron decay and in FigureB.11, FigureB.12 for the muon decay, divided by charged and channel.

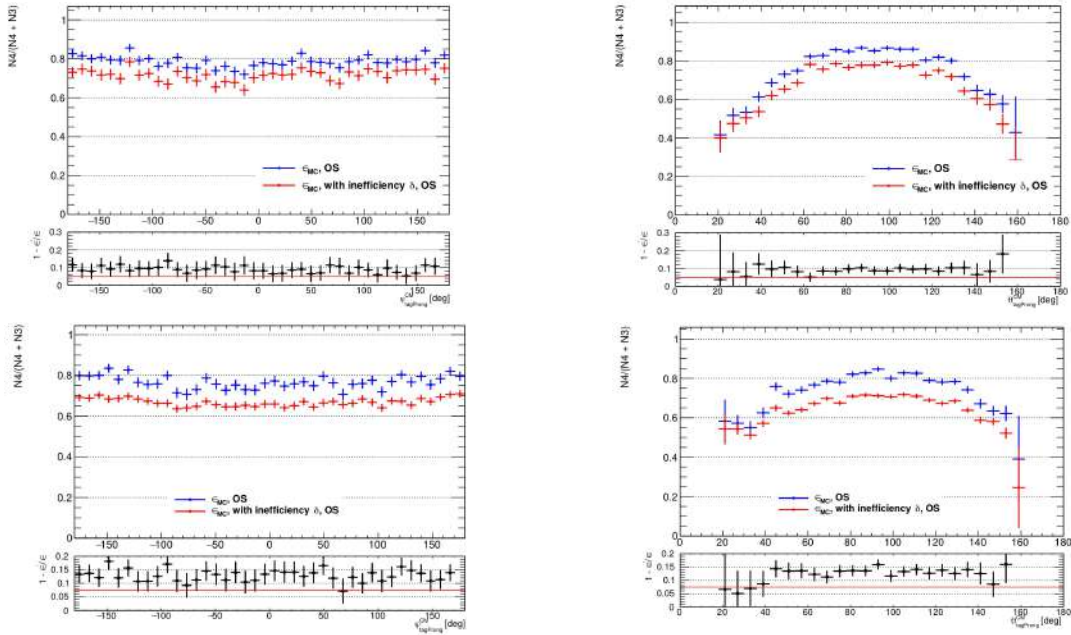


**Figure B.9:** Efficiency estimator distributions for default (blue crosses) and modified (red crosses) MC as a function of the 1-prong azimuthal (left) and polar (right) angles, for OS charge, electron channel. The measured discrepancy (black dots) is shown in inset plots compared to the generated inefficiency  $\delta_{MC}$  (red line). The first row of each block corresponds to a generated  $\delta_{MC} = 0.05$ , the second shows results for  $\delta_{MC} = 0.075$ .

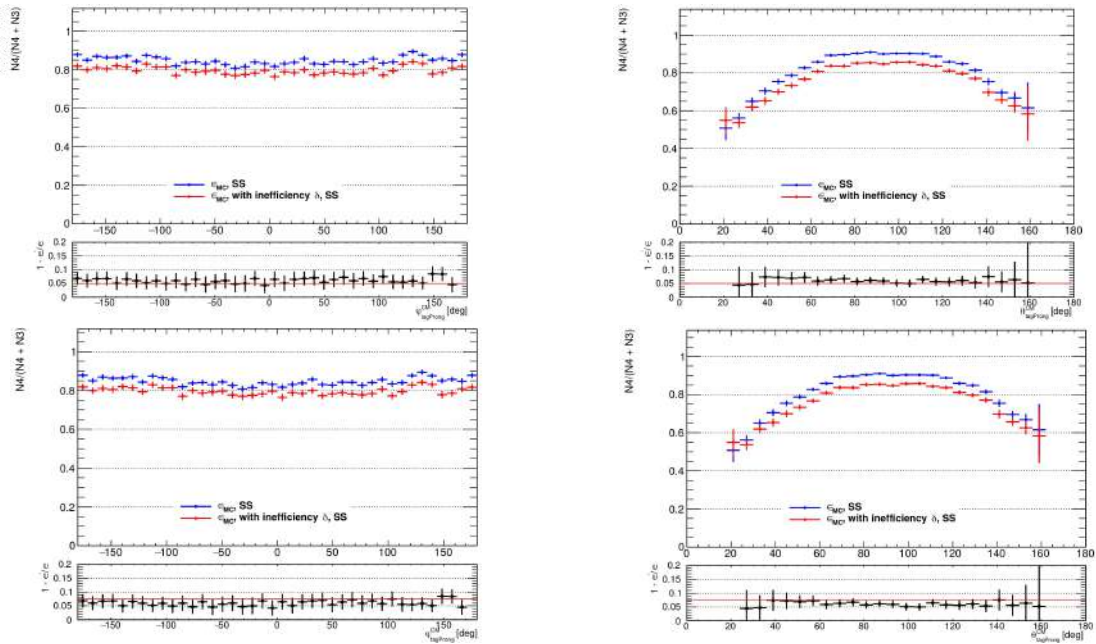


**Figure B.10:** Efficiency estimator distributions for default (blue crosses) and modified (red crosses) MC as a function of the 1-prong azimuthal (left) and polar (right) angles, for SS charge, electron channel. The measured discrepancy (black dots) is shown in inset plots compared to the generated inefficiency  $\delta_{MC}$  (red line). The first row of each block corresponds to a generated  $\delta_{MC} = 0.05$ , the second shows results for  $\delta_{MC} = 0.075$ .

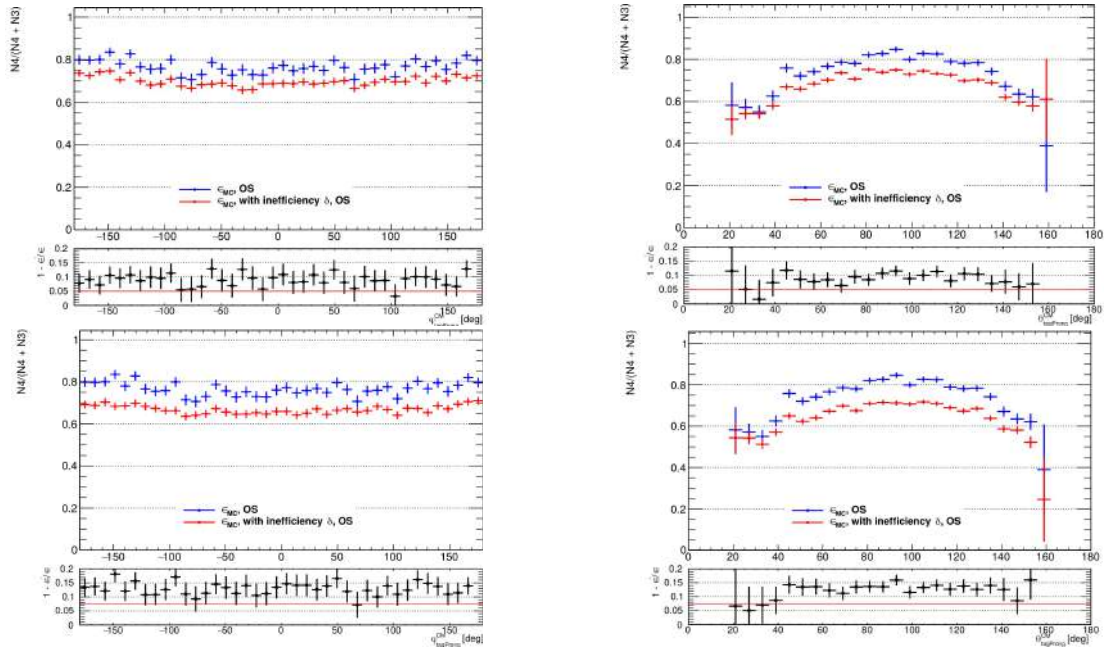


**Figure B.11:** Muon channel, efficiency estimator distributions for default (blue crosses) and modified (red crosses) MC as a function of the 1-prong azimuthal (left) and polar (right) angles, for OS charge. The measured discrepancy (black dots) is shown in inset plots compared to the generated inefficiency  $\delta_{MC}$  (red line). The first row of each block corresponds to a generated  $\delta_{MC} = 0.05$ , the second shows results for  $\delta_{MC} = 0.075$ .

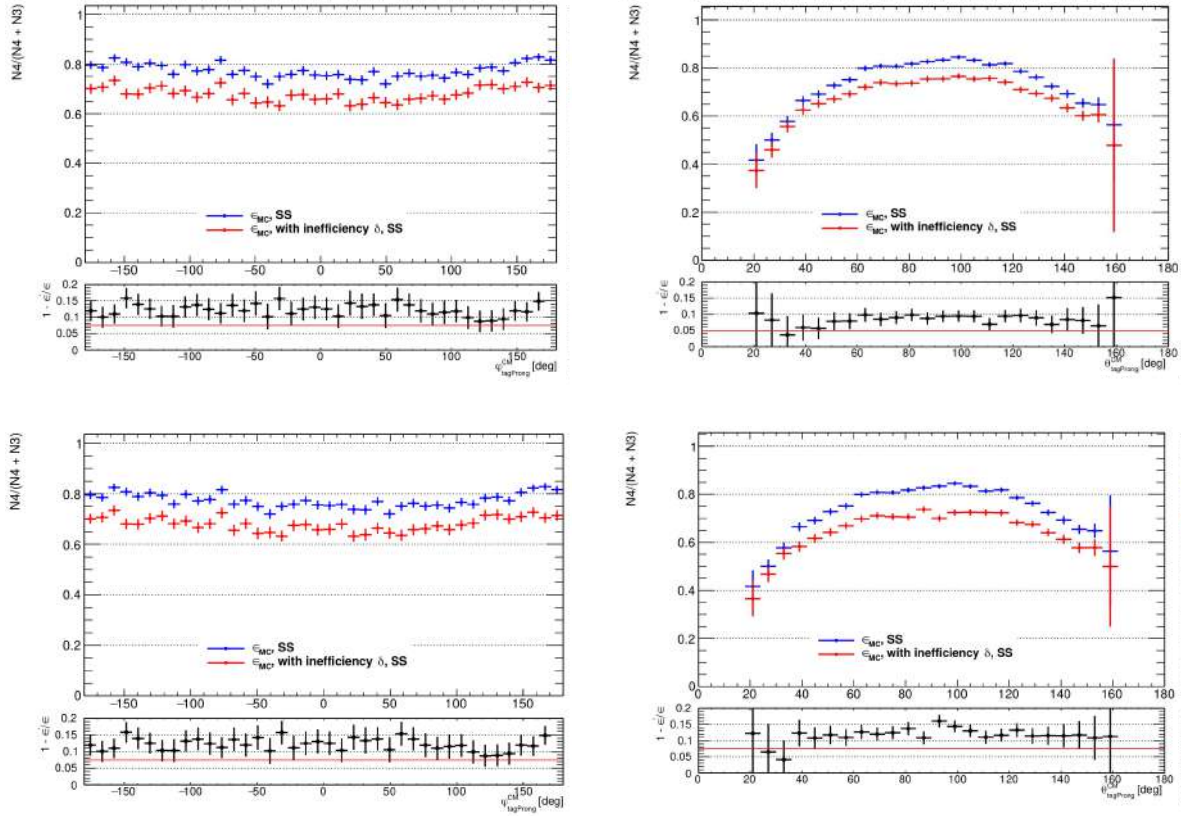


**Figure B.12:** Muon channel, efficiency estimator distributions for default (blue crosses) and modified (red crosses) MC as a function of the 1-prong azimuthal (left) and polar (right) angles, for SS charge. The measured discrepancy (black dots) is shown in inset plots compared to the generated inefficiency  $\delta_{MC}$  (red line). The first row of each block corresponds to a generated  $\delta_{MC} = 0.05$ , the second shows results for  $\delta_{MC} = 0.075$ .

### B.3.2 Systematic uncertainty evaluation

The results from the evaluation of the various contributions to the systematic uncertainty in the tracking efficiency measurement as discussed in Section 7.4 are reported below.

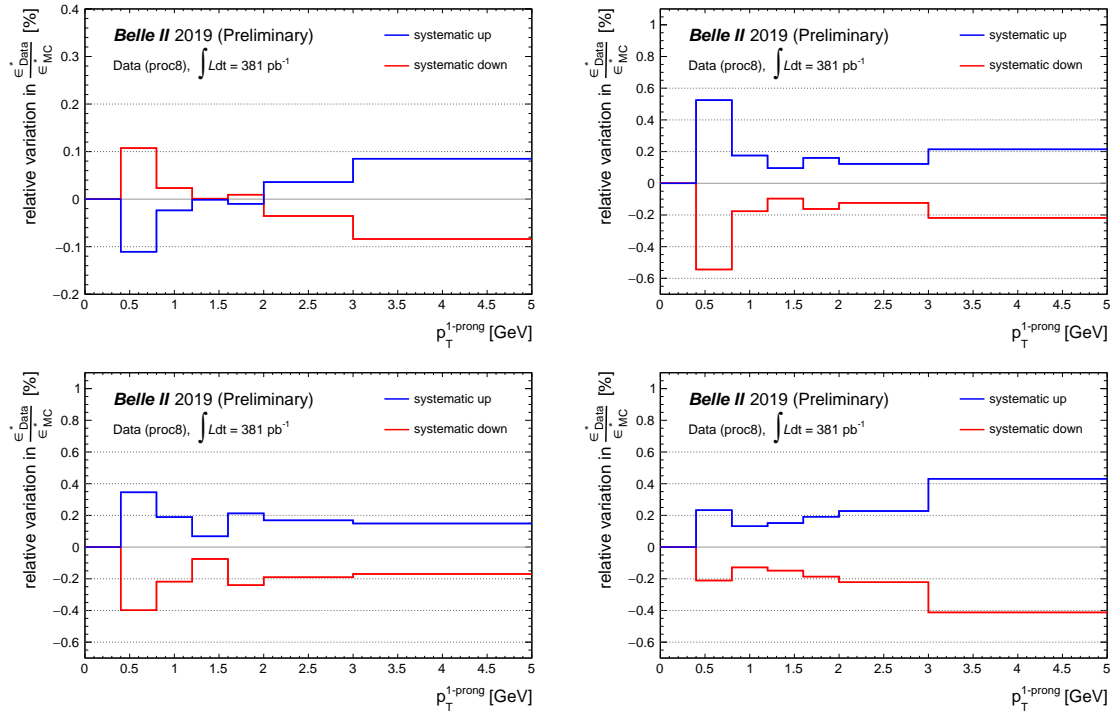


**Figure B.13:** Relative variations in the calibrated  $\epsilon_{Data}/\epsilon_{MC}$  as a function of the 1-prong track  $p_T$  after varying up/down one sigma: the luminosity (top-left), the trigger efficiency (top-right), the calibration  $k$ -factors (bottom-left) and the background subtraction uncertainty (bottom-right).

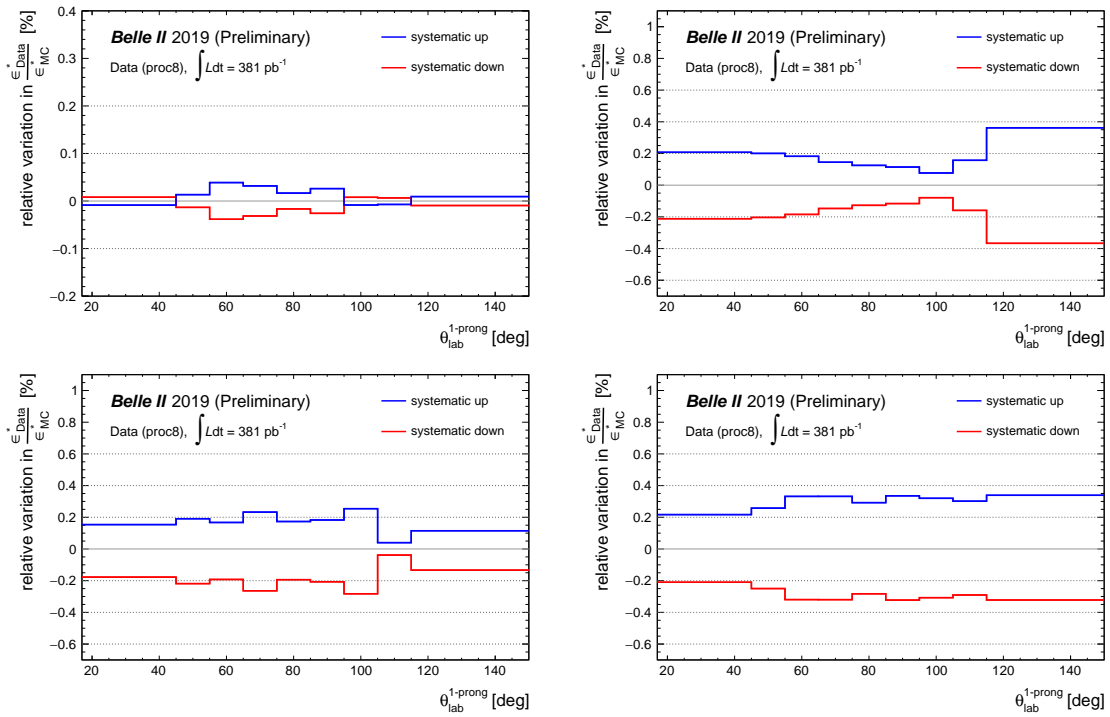


**Figure B.14:** Relative variations in the calibrated  $\epsilon_{Data}/\epsilon_{MC}$  as a function of the 1-prong track  $\theta$  after varying up/down one sigma: the luminosity (top-left), the trigger efficiency (top-right), the calibration  $k$ -factors (bottom-left) and the background subtraction uncertainty (bottom-right).

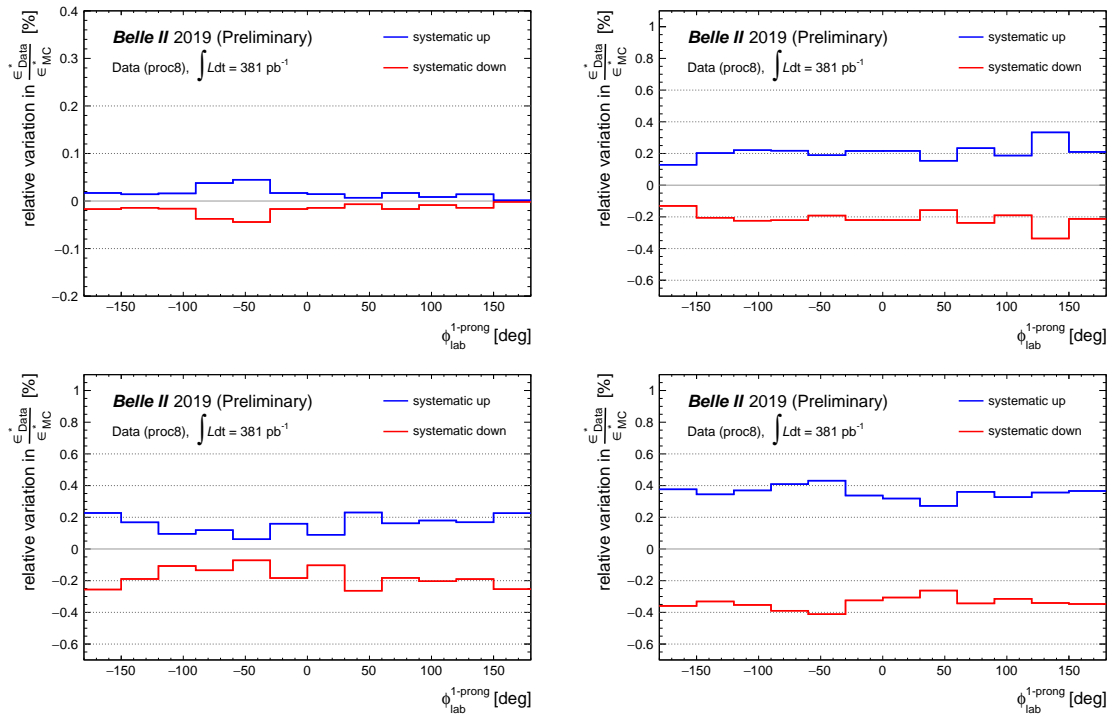


**Figure B.15:** Relative variations in the calibrated  $\epsilon_{Data}/\epsilon_{MC}$  as a function of the 1-prong track  $\phi$  after varying up/down one sigma: the luminosity (top-left), the trigger efficiency (top-right), the calibration  $k$ -factors (bottom-left) and the background subtraction uncertainty (bottom-right).

# Appendix C

## Upper limit calculation

### C.1 Bayesian approach procedure and results

The 90% Confidence Level (CL) upper limit to the measured  $Z'$  signal cross section has been computed within the Bayesian Analysis Toolkit (BAT) framework [95], in which all the relevant prior distributions have been defined, according to the following assumptions:

- the likelihood of the observed number of events is assumed to be Poissonian;
- the prior distribution for the  $Z'$  cross section is assumed to be flat between 0 and  $10^5$  fb;
- all the distributions related to systematic uncertainties (trigger efficiency, tracking efficiency, particle ID selection, luminosity determination,  $\tau$  suppression effect on background, effects on signal efficiency and background level from discrepancies) are modeled with Gaussian functions, with a width equal to the estimated size of the effect (Table 7.1);
- the expected background number of events (estimated from Monte Carlo and eventually corrected according to the results of the validation procedure) is assumed to be Poissonian.

In the standard  $Z'$  case, the following equation holds:

$$N_{\text{obs}} = \sigma_{Z'} \times L \times \epsilon_{\text{sig}} + B_{\text{exp}} \quad (\text{C.1})$$

where  $N_{\text{obs}}$  is the observed number of events,  $\epsilon_{\text{sig}}$  is the -35% rescaled signal efficiency (see Table A.1),  $B_{\text{exp}}$  is the -35% rescaled expected background (see Table A.1). With the previous assumptions on likelihood and distributions, taking the number in Table A.1 as inputs and taking into account the previous considerations about background and efficiency rescaling, the BAT toolkit can be used to estimate a 90% CL upper limit on  $\sigma_{Z'}$  by means of Equation C.1. With a still blinded data sample, only the expected sensitivity on  $\sigma_{Z'}$  can be computed, defined as the average upper limit obtained by an ensemble of pseudo-experiments with the expected background  $B_{\text{exp}}$  and no signal. The calculation has been worked out by using for  $N_{\text{obs}}$  a Poissonian distribution convoluted with a Gaussian that summarizes the effects of all the systematic uncertainties. Results for the sensitivity expected in each mass bin for the cross section of a standard  $Z'$  are shown in Table C.1, where efficiency and background numbers are rescaled with respect to the ones in Table A.1.

**Table C.1:** The results of the Bayesian statistical analysis for the standard  $Z'$  case are shown, where the last column gives the 90% CL upper limit in terms of the cross section measurement. The uncertainties quoted here are MC statistical only.

$M_{Z'}$ [GeV/ $c^2$ ]	Efficiency	Background events	$\sigma$ [fb]
0.500	0.0282 $\pm$ 0.0008	0.438 $\pm$ 0.034	387.285
1.391	0.0494 $\pm$ 0.0011	0.213 $\pm$ 0.023	208.723
1.807	0.0515 $\pm$ 0.0011	0.167 $\pm$ 0.021	200.289
2.134	0.0521 $\pm$ 0.0011	0.145 $\pm$ 0.020	196.097
2.424	0.0524 $\pm$ 0.0011	0.121 $\pm$ 0.019	190.918
2.683	0.0522 $\pm$ 0.0011	0.092 $\pm$ 0.017	190.399
2.911	0.0519 $\pm$ 0.0011	0.078 $\pm$ 0.016	188.887
3.112	0.0506 $\pm$ 0.0011	0.073 $\pm$ 0.015	192.754
3.294	0.0488 $\pm$ 0.0011	0.114 $\pm$ 0.019	197.874
3.461	0.0472 $\pm$ 0.0010	0.104 $\pm$ 0.018	203.425
3.618	0.0472 $\pm$ 0.0010	0.102 $\pm$ 0.019	203.255
3.767	0.0477 $\pm$ 0.0011	0.136 $\pm$ 0.021	204.210
3.909	0.0482 $\pm$ 0.0011	0.169 $\pm$ 0.029	207.774
4.044	0.0481 $\pm$ 0.0011	0.151 $\pm$ 0.029	206.742
4.173	0.0469 $\pm$ 0.0010	0.153 $\pm$ 0.023	210.691
4.295	0.0457 $\pm$ 0.0010	0.160 $\pm$ 0.029	216.419
4.412	0.0446 $\pm$ 0.0010	0.171 $\pm$ 0.024	219.785
4.524	0.0437 $\pm$ 0.0010	0.182 $\pm$ 0.030	229.653
4.633	0.0432 $\pm$ 0.0010	0.143 $\pm$ 0.022	225.077
4.740	0.0427 $\pm$ 0.0010	0.186 $\pm$ 0.025	232.104
4.845	0.0422 $\pm$ 0.0010	0.180 $\pm$ 0.035	236.445
4.947	0.0417 $\pm$ 0.0010	0.206 $\pm$ 0.040	237.243
5.045	0.0411 $\pm$ 0.0010	0.166 $\pm$ 0.024	242.966
5.138	0.0403 $\pm$ 0.0010	0.264 $\pm$ 0.049	261.701
5.226	0.0395 $\pm$ 0.0010	0.152 $\pm$ 0.029	253.465
5.307	0.0388 $\pm$ 0.0010	0.175 $\pm$ 0.025	257.960
5.384	0.0381 $\pm$ 0.0010	0.233 $\pm$ 0.041	274.400
5.457	0.0375 $\pm$ 0.0009	0.200 $\pm$ 0.040	270.777
5.527	0.0368 $\pm$ 0.0009	0.211 $\pm$ 0.040	279.722
5.595	0.0362 $\pm$ 0.0009	0.190 $\pm$ 0.035	280.372
5.663	0.0355 $\pm$ 0.0009	0.221 $\pm$ 0.037	289.249
5.731	0.0349 $\pm$ 0.0009	0.291 $\pm$ 0.050	304.278
5.799	0.0343 $\pm$ 0.0009	0.228 $\pm$ 0.037	304.053
5.868	0.0336 $\pm$ 0.0009	0.252 $\pm$ 0.042	307.512
5.937	0.0329 $\pm$ 0.0009	0.202 $\pm$ 0.040	306.752
6.007	0.0323 $\pm$ 0.0009	0.196 $\pm$ 0.036	311.278
6.077	0.0314 $\pm$ 0.0009	0.374 $\pm$ 0.065	342.051
6.146	0.0305 $\pm$ 0.0009	0.194 $\pm$ 0.043	328.822
6.214	0.0296 $\pm$ 0.0008	0.268 $\pm$ 0.049	343.790
6.280	0.0288 $\pm$ 0.0008	0.237 $\pm$ 0.048	351.132

Continued on next page

Table C.1 – *Continued from previous page*

$M_{Z'}$ [GeV/ $c^2$ ]	Efficiency	Background events	$\sigma$ [fb]
6.345	$0.0279 \pm 0.0008$	$0.342 \pm 0.065$	383.643
6.407	$0.0271 \pm 0.0008$	$0.248 \pm 0.057$	378.579
6.468	$0.0264 \pm 0.0008$	$0.225 \pm 0.054$	381.158
6.527	$0.0263 \pm 0.0008$	$0.186 \pm 0.043$	379.797
6.584	$0.0270 \pm 0.0008$	$0.354 \pm 0.067$	403.602
6.640	$0.0277 \pm 0.0008$	$0.367 \pm 0.068$	392.536
6.694	$0.0284 \pm 0.0008$	$0.537 \pm 0.087$	404.324
6.747	$0.0291 \pm 0.0008$	$0.860 \pm 0.115$	435.423
6.799	$0.0297 \pm 0.0008$	$0.766 \pm 0.099$	409.427
6.850	$0.0304 \pm 0.0009$	$0.959 \pm 0.117$	433.142
6.901	$0.0310 \pm 0.0009$	$1.176 \pm 0.131$	439.777
6.953	$0.0317 \pm 0.0009$	$1.203 \pm 0.128$	432.049
7.005	$0.0329 \pm 0.0009$	$2.004 \pm 0.158$	483.396
7.059	$0.0385 \pm 0.0009$	$6.069 \pm 0.242$	661.692
7.115	$0.0443 \pm 0.0010$	$11.357 \pm 0.328$	769.345
7.174	$0.0504 \pm 0.0010$	$15.229 \pm 0.372$	815.382
7.235	$0.0568 \pm 0.0011$	$21.406 \pm 0.460$	900.544
7.300	$0.0635 \pm 0.0012$	$26.799 \pm 0.524$	940.199
7.368	$0.0706 \pm 0.0012$	$32.765 \pm 0.593$	980.323
7.511	$0.0840 \pm 0.0013$	$45.060 \pm 0.736$	1069.089
7.583	$0.0823 \pm 0.0013$	$47.553 \pm 0.772$	1137.010
7.655	$0.0806 \pm 0.0013$	$49.545 \pm 0.804$	1200.519
7.725	$0.0790 \pm 0.0013$	$49.448 \pm 0.810$	1224.530
7.793	$0.0774 \pm 0.0013$	$51.369 \pm 0.843$	1287.554
7.859	$0.0759 \pm 0.0013$	$52.360 \pm 0.865$	1339.809
7.922	$0.0744 \pm 0.0013$	$50.480 \pm 0.855$	1320.182
7.983	$0.0729 \pm 0.0013$	$52.640 \pm 0.884$	1394.299
8.042	$0.0713 \pm 0.0013$	$54.018 \pm 0.907$	1459.685

### C.1.1 LFV $Z'$ expected sensitivity results

In the LFV  $Z'$  case, being at present impossible to estimate a signal efficiency in absence of a robust model, a slightly modified version of Equation C.1 has been used, where  $(\sigma_{Z'} \times \epsilon_{\text{sig}})$  must be considered as a single parameter. The same procedures and similar considerations as in the standard  $Z'$  are applied, after rescaling down by 10% the expected number of background events. The treatment of the systematic uncertainties is similar to the  $Z'$  case and Gaussian functions are used to model the error contributions and integrate them out in the upper limit calculation. Results for the sensitivity expected in each mass bin for the efficiency  $\times$  cross section of a LFV  $Z'$  are shown in Table C.2 ( the number of background events is rescaled with respect to Table A.2).

**Table C.2:** The results of the Bayesian statistical analysis for the LFV  $Z'$  case are reported, where the last column shows the 90% CL upper limit in terms of the signal efficiency  $\times$  cross section measurement. The uncertainties quoted here are MC statistical only.

$M_{Z'}$ [GeV/ $c^2$ ]	Background events	$\epsilon_{\text{sig}} \times \sigma$ [fb]
0.500	0.000 $\pm$ 0.000	9.630
1.391	0.018 $\pm$ 0.010	9.616
1.807	0.030 $\pm$ 0.013	9.630
2.134	0.036 $\pm$ 0.015	9.649
2.424	0.006 $\pm$ 0.006	9.647
2.683	0.048 $\pm$ 0.017	9.939
2.911	0.030 $\pm$ 0.013	9.643
3.112	0.065 $\pm$ 0.020	10.049
3.294	0.068 $\pm$ 0.020	10.086
3.461	0.153 $\pm$ 0.030	10.586
3.618	0.096 $\pm$ 0.023	10.214
3.767	0.078 $\pm$ 0.021	10.133
3.909	0.117 $\pm$ 0.026	10.307
4.044	0.163 $\pm$ 0.031	10.624
4.173	0.077 $\pm$ 0.021	10.138
4.295	0.145 $\pm$ 0.029	10.563
4.412	0.115 $\pm$ 0.026	10.300
4.524	0.172 $\pm$ 0.032	10.705
4.633	0.083 $\pm$ 0.022	10.144
4.740	0.139 $\pm$ 0.041	10.519
4.845	0.107 $\pm$ 0.025	10.299
4.947	0.131 $\pm$ 0.028	10.414
5.045	0.065 $\pm$ 0.020	10.052
5.138	0.151 $\pm$ 0.042	10.569
5.226	0.143 $\pm$ 0.029	10.530
5.307	0.178 $\pm$ 0.033	10.713
5.384	0.131 $\pm$ 0.028	10.408
5.457	0.172 $\pm$ 0.032	10.729
5.527	0.143 $\pm$ 0.029	10.507
5.595	0.187 $\pm$ 0.044	10.779
5.663	0.167 $\pm$ 0.043	10.682
5.731	0.177 $\pm$ 0.052	10.702
5.799	0.101 $\pm$ 0.025	10.262
5.868	0.151 $\pm$ 0.042	10.581
5.937	0.243 $\pm$ 0.063	11.040
6.007	0.127 $\pm$ 0.040	10.362
6.077	0.133 $\pm$ 0.040	10.399
6.146	0.113 $\pm$ 0.026	10.343
6.214	0.151 $\pm$ 0.042	10.568
6.280	0.098 $\pm$ 0.038	10.251

Continued on next page

Table C.2 – *Continued from previous page*

$M_{Z'}$ [GeV/ $c^2$ ]	Background events	$\epsilon_{\text{sig}} \times \sigma$ [fb]
6.345	$0.149 \pm 0.030$	10.557
6.407	$0.053 \pm 0.018$	9.985
6.468	$0.080 \pm 0.036$	10.135
6.527	$0.098 \pm 0.038$	10.258
6.584	$0.109 \pm 0.039$	10.285
6.640	$0.151 \pm 0.042$	10.597
6.694	$0.172 \pm 0.032$	10.715
6.747	$0.207 \pm 0.054$	10.897
6.799	$0.338 \pm 0.067$	11.538
6.850	$0.310 \pm 0.066$	11.413
6.901	$0.461 \pm 0.078$	12.070
6.953	$0.450 \pm 0.078$	11.973
7.005	$0.849 \pm 0.082$	13.509
7.059	$4.905 \pm 0.194$	22.420
7.115	$8.327 \pm 0.244$	28.415
7.174	$11.817 \pm 0.283$	34.133
7.235	$16.685 \pm 0.352$	41.767
7.300	$19.384 \pm 0.385$	46.206
7.368	$22.504 \pm 0.403$	50.908
7.438	$25.539 \pm 0.437$	55.710
7.511	$26.179 \pm 0.427$	56.504
7.583	$26.301 \pm 0.456$	56.791
7.655	$23.941 \pm 0.427$	53.188
7.725	$22.620 \pm 0.428$	51.059
7.793	$19.767 \pm 0.400$	46.376
7.859	$17.611 \pm 0.387$	43.394
7.922	$15.609 \pm 0.354$	40.203
7.983	$13.736 \pm 0.336$	37.160
8.042	$12.557 \pm 0.325$	35.238

## C.2 Frequentist approach procedure and results

The expected sensitivity has been computed also with a frequentist approach and compared to the results obtained from the Bayesian procedure, as cross-check of the robustness of the calculation, and results have found to be consistent between the two methods, as reported in Section 8.1. Below the description of the frequentist method implemented for this study is provided.

In their work [96], G.J.Feldman and R.D.Cousins proposed an approach for setting confidence intervals that works both for two-sided and upper limit cases. Following Neyman's construction, the first step is to build a confidence belt in the (observable  $x$ ; parameter  $\theta$ ) space, which consists of horizontal lines calculated for each value of  $\theta$ . For Poissonian case, Feldman and Cousins suggest the following algorithm of building such horizontal acceptance interval for a given value  $\theta$ :

- define  $\theta_{best}$  that provides the highest  $P_{best}(x) \equiv P(x|\theta_{best})$ , for each integer value of  $x$ .
- compute the ranking variable  $R = P(x|\theta)/P_{best}(x)$ , for each integer value of the observable  $x$ .
- add to the interval values of  $x_i$  with highest  $R$  until

$$\sum_i P(x_i|\theta) \geq CL$$

Once the confidence belt is built, the confidence interval for an observed value  $x_0$  is obtained as an intersection of the confidence interval with the vertical line at  $x_0$ . This procedure is illustrated in Figure C.1. In this analysis, the observable  $x$  corresponds to the number of observed events in the given bin and the parameter  $\theta$  can be either the number of signal events or the cross section of the signal process. The first approach is used for the LFV  $Z'$  analysis and the second for the standard  $Z'$  case.

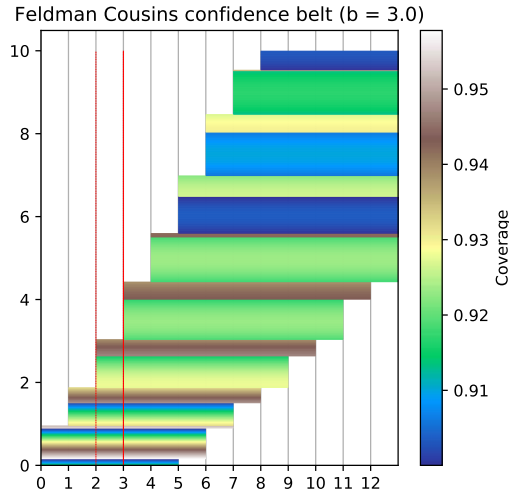


**Figure C.1:** Feldman Cousins confidence belt constructed under the assumption of 3 background events. The red line intercepting with the horizontal acceptance regions shows the upper limit in case of 3 observed events.

### Error propagation

The probability density function  $P(x|\theta)$  may contain hidden parameters

$$P(x|\theta) \rightarrow P(x|\theta, b) \tag{C.2}$$

with values distributed according to some probability density function (PDF)  $P(b)$ . The hidden parameter can be integrated out as follows:

$$P(x|\theta) = \int P(x|\theta, \hat{b})P(\hat{b})d\hat{b} \tag{C.3}$$

For this study, the hidden parameter is the expected number of background events, that has two uncertainties: one comes from the limited size of the simulation samples and is of statistical nature; the second comes from the data-MC discrepancy. As far as the former is concerned, the probability can be modified as:

$$P(x|\theta) = \int_{\hat{N}_1^{sel}=0}^{\infty} \cdots \int_{\hat{N}_i^{sel}=0}^{\infty} P(x|\theta, \hat{N}_1^{sel} \dots \hat{N}_i^{sel}) \prod_i P(\hat{N}_i^{sel} | N_i^{sel}) d\hat{N}_1^{sel} \dots d\hat{N}_i^{sel} \quad (C.4)$$

This is nothing more but averaging of the  $P(x|\theta)$  over the possible background yields. Within this assumption, the numerical computation of the following equation is implemented:

$$P(x|\theta) \approx \frac{1}{M} \sum_j P(x|\theta, \tilde{N}_1^{sel} \dots \tilde{N}_i^{sel}) \equiv \frac{1}{M} \sum_j P(x|\theta, \sum_i \tilde{N}_i^{sel}) \quad (C.5)$$

where the sum runs over set of  $(\tilde{N}_1^{sel} \dots \tilde{N}_i^{sel})$  random vectors of size  $M$ , simulated with Poissonian PDF. As for the latter, to account for systematic effects, it is possible to use a mixed-Bayesian approach described in [99] that implies modification of  $P(x|\theta, \sum_i \tilde{N}_i^{sel})$  to include the systematic uncertainty. This will lead to

$$P(x|\theta) \approx \frac{1}{M} \sum_j P(x|\theta, \tilde{r}_i \times \sum_i \tilde{N}_i^{sel}) \quad (C.6)$$

where random vectors  $(\tilde{r}_i, \tilde{N}_1^{sel} \dots \tilde{N}_i^{sel})$  also include a correction factor  $\tilde{r}_i$  generated according to normal distribution with mean ( $r$ ) and width ( $\delta r$ ) defined from systematics studies.

In the standard  $Z'$  scenario, the goal is to find the confidence interval for the cross section of the signal process. The correlations in the uncertainties of signal and background efficiencies have to be accounted for when computing the Neyman structure. Thus,  $\theta$  is considered to be the studied cross section, and, assuming  $\mathcal{L}$  to be luminosity and  $\epsilon$  to be signal efficiency, Equation C.6 can be written as:

$$P(x|\theta) \approx \frac{1}{M} \sum_j P(x|\theta \times \mathcal{L} \times \tilde{\epsilon}, \tilde{r}_i \times \sum_i \tilde{N}_i^{sel}) \quad (C.7)$$

where  $\tilde{\epsilon}$  is a random value of efficiency generated according to its PDF simultaneously with  $\tilde{r}_i$ . The Neyman construction obtained for this definition of  $P(x|\theta)$  will show the number of observed events on  $X$  axis and cross section values of  $ee \rightarrow \mu\mu Z'$  ( $Z' \rightarrow$  invisible) process on  $Y$ . These values are reported for the standard  $Z'$  analysis (see Table C.3).

## Sensitivity

Following the original suggestion from the paper of Feldman and Cousins [96], the sensitivities of the analysis in each recoil mass bin are provided. The sensitivity, which is a characteristic of the method, is an average upper limit obtained by an ensemble of pseudo-experiments with the expected background and no true signal. In each pseudo-experiment, an upper limit is taken as a numerical solution of the equation

$$CL = \frac{\int_0^{u.l.} P(N, x+b) dx}{\int_0^{\infty} P(N, x+b) dx} \quad (C.8)$$

where  $CL$  is a chosen confidence level (90%), and  $P$  is probability to find  $N$  events. Following arguments of section C.2, the sensitivity is calculated as

$$CL = \frac{1}{M} \sum_j \left( \frac{\int_0^{u.l.} P(N, x + \tilde{b}_i) dx}{\int_0^{\infty} P(N, x + \tilde{b}_i) dx} = 0.9 \right) \quad (C.9)$$

where

$$\tilde{b}_i = \tilde{r}_i \times \sum_i \tilde{N}_i^{sel}. \quad (C.10)$$

### Sensitivity to the cross section

Since some of the systematic uncertainties are the same for the signal and background, the upper limit on cross section is computed as:

$$CL = \frac{1}{M} \sum_j \frac{\left( \frac{\int_0^{u.l.} P(N, x + \tilde{b}_j) dx}{\int_0^{\infty} P(N, x + \tilde{b}_j) dx} = 0.9 \right)}{\tilde{\epsilon}_j \times \mathcal{L}}. \quad (C.11)$$

Here the nominator is identical to that in Equation C.9 and  $\tilde{\epsilon}$  is signal efficiency value generated according to its PDF. Let  $\tilde{r}^c$  and  $\delta\tilde{r}^c$  as data-MC correction and its uncertainty common for signal and background, and  $\tilde{r}^{s(b)}$  and  $\delta\tilde{r}^{s(b)}$  as a signal (background) only corrections and uncertainties, we obtain:

$$\begin{aligned} \tilde{b}_j &= \tilde{r}_j^c \times \tilde{r}_j^b \times \sum_i \tilde{N}_{i,j}^{sel}; \\ \tilde{\epsilon}_j &= \tilde{r}_j^c \times \tilde{r}_j^s \times \tilde{\epsilon}_j^{MC}, \end{aligned} \quad (C.12)$$

where  $\tilde{r}_j^{c,s,b}$  are correction values generated as described in section C.2,  $\tilde{\epsilon}_j^{MC}$  is a random value generated with binomial distribution with mean equal the signal efficiency and square root of variance centered at the statistical uncertainty of the signal efficiency, and  $(\tilde{N}_{1,j}^{sel} \dots \tilde{N}_{i,j}^{sel})$  is vector of random Poisson values. All variables with the same  $j$  index are computed simultaneously  $M$  times and sensitivity for the cross section is defined as the average of  $M$  upper limits.

## Results

In Table C.3 and Table C.4 the cross section (cross section  $\times$  selection efficiency for the LFV scenario) under the assumption of background only hypothesis are reported. Both statistical and systematic uncertainties are taken into account. A graphic visualization of the expected sensitivities reported in the Table below is given in Section 8.1 where results from the sensitivity studies are plotted in Figure 8.1, 8.2.

**Table C.3:** Upper and lower limits of 90% CL Feldman Cousins interval (semi-Bayesian approach, interval corresponds to number of observed events equal to rounded background expectation), sensitivity to cross section in  $Z'$  mass bins for standard  $Z'$ . Inputs from Table A.1.

$M_{Z'}$ [GeV/ $c^2$ ]	Exp. bkg	90% CL interval [fb]	$\sigma$ [fb]	
0.500000	0.438018	0.0	257.3	376.0
1.391160	0.212978	0.0	176.4	194.0
1.807331	0.167320	0.0	169.1	181.0
2.134437	0.145263	0.0	167.3	179.0
2.424160	0.120882	0.0	166.3	175.0
2.683574	0.091934	0.0	166.9	173.0
2.911720	0.078408	0.0	167.9	174.0
3.112817	0.072981	0.0	172.0	177.0
3.294203	0.113736	0.0	178.4	188.0
3.461637	0.104172	0.0	184.6	193.0
3.618703	0.102278	0.0	184.5	191.0
3.767561	0.135967	0.0	167.4	191.0
3.909355	0.169201	0.0	180.8	194.0
4.044485	0.150677	0.0	181.2	195.0
4.173020	0.153202	0.0	185.8	198.0
4.295278	0.159811	0.0	190.5	206.0
4.412056	0.171296	0.0	195.1	212.0
4.524494	0.182473	0.0	182.7	216.0
4.633830	0.143208	0.0	201.7	215.0
4.740874	0.186462	0.0	204.1	225.0
4.845698	0.179773	0.0	189.3	227.0
4.947710	0.206115	0.0	191.4	235.0
5.045792	0.166299	0.0	212.1	229.0
5.138775	0.264052	0.0	198.4	247.0
5.226076	0.151711	0.0	220.6	240.0
5.307839	0.175003	0.0	224.7	244.0
5.384696	0.232739	0.0	209.6	255.0
5.457585	0.200084	0.0	213.1	256.0
5.527632	0.210682	0.0	216.8	260.0
5.595998	0.189942	0.0	240.7	264.0
5.663653	0.221307	0.0	224.7	270.0
5.731300	0.291281	0.0	228.8	286.0
5.799396	0.228373	0.0	233.1	284.0
5.868171	0.251541	0.0	237.6	293.0
5.937605	0.201548	0.0	242.4	297.0
6.007421	0.195543	0.0	270.1	298.0
6.077127	0.373949	0.0	254.6	334.0
6.146163	0.193851	0.0	262.0	320.0
6.214061	0.268015	0.0	269.7	343.0
6.280470	0.237254	0.0	277.6	344.0

Continued on next page

Table C.3 – *Continued from previous page*

$M_{Z'}$ [GeV/ $c^2$ ]	Exp. bkg	90% CL interval [fb]	$\sigma$ [fb]
6.345147	0.342328	0.0	259.9
6.407952	0.247598	0.0	294.3
6.468829	0.224963	0.0	303.0
6.527794	0.185855	0.0	268.6
6.640409	0.367461	0.0	288.0
6.694420	0.536907	0.0	383.4
6.747235	0.860229	0.0	324.7
6.799163	0.766490	0.0	317.5
6.850560	0.958621	0.0	310.8
6.901827	1.176362	0.0	351.1
6.953420	1.202914	0.0	343.9
7.005871	2.004179	0.0	375.6
7.059783	6.068703	0.0	543.5
7.115758	11.356861	0.0	603.2
7.174316	15.229113	0.0	657.1
7.235851	21.406057	0.0	703.2
7.300555	26.799011	0.0	742.9
7.368350	32.765375	0.0	777.7
7.438796	40.935873	0.0	805.2
7.511010	45.060460	0.0	798.5
7.583725	47.552798	0.0	899.7
7.655670	49.544840	0.0	979.7
7.725912	49.447739	0.0	900.8
7.793887	51.369198	0.0	985.0
7.859391	52.360280	0.0	1033.7
7.922501	50.480429	0.0	990.8
7.983504	52.640400	0.0	1110.7
8.042857	54.018064	0.0	1172.6

**Table C.4:** Upper and lower limits of 90% CL Feldman Cousins interval (semi-Bayesian approach, interval corresponds to number of observed events equal to rounded background expectation), sensitivity to cross section $\times$ efficiency in  $Z'$  mass bins for LFV  $Z'$ . Inputs from Table A.2.

$M_{Z'}$ [GeV/ $c^2$ ]	Exp. bkg	90% CL interval [fb]	$\sigma \times \epsilon$ [fb]
0.500000	0.000000	0.0	8.711592
1.391160	0.017833	0.0	8.711592
1.807331	0.029721	0.0	8.711592
2.134437	0.035666	0.0	8.711592
2.424160	0.005944	0.0	8.711592
2.683574	0.047554	0.0	7.985626
2.911720	0.029721	0.0	8.711592
3.112817	0.065387	0.0	7.985626

Continued on next page

Table C.4 – *Continued from previous page*

$M_{Z'}$ [GeV/ $c^2$ ]	Exp. bkg	90% CL interval [fb]	$\sigma \times \epsilon$ [fb]
3.294203	0.067850	0.0	7.985626
3.461637	0.152810	0.0	7.985626
3.618703	0.095831	0.0	7.985626
3.767561	0.077999	0.0	7.985626
3.909355	0.117145	0.0	7.985626
4.044485	0.162959	0.0	7.985626
4.173020	0.077275	0.0	7.985626
4.295278	0.145126	0.0	7.985626
4.412056	0.115405	0.0	7.985626
4.524494	0.172384	0.0	7.985626
4.633830	0.083220	0.0	7.985626
4.740874	0.139137	0.0	7.985626
4.845698	0.106997	0.0	7.985626
4.947710	0.130774	0.0	7.985626
5.045792	0.065387	0.0	7.985626
5.138775	0.151026	0.0	7.985626
5.226076	0.142662	0.0	7.985626
5.307839	0.178328	0.0	7.985626
5.384696	0.130774	0.0	7.985626
5.457585	0.172384	0.0	7.985626
5.527632	0.142662	0.0	7.985626
5.595998	0.186691	0.0	7.985626
5.663653	0.167118	0.0	7.985626
5.731300	0.177222	0.0	7.985626
5.799396	0.101052	0.0	7.985626
5.868171	0.151026	0.0	7.985626
5.937605	0.243287	0.0	7.985626
6.007421	0.127249	0.0	7.985626
6.077127	0.133193	0.0	7.985626
6.146163	0.112941	0.0	7.985626
6.214061	0.151026	0.0	7.985626
6.280470	0.097527	0.0	7.985626
6.345147	0.148607	0.0	7.985626
6.407952	0.053498	0.0	7.985626
6.468829	0.079695	0.0	7.985626
6.527794	0.097527	0.0	7.985626
6.584937	0.109416	0.0	7.985626
6.640409	0.151026	0.0	7.985626
6.694420	0.172384	0.0	7.985626
6.747235	0.206943	0.0	7.985626
6.799163	0.338396	0.0	7.259660
6.850560	0.310415	0.0	7.259660
6.901827	0.461440	0.0	6.533694

Continued on next page

Table C.4 – *Continued from previous page*

$M_{Z'}$ [GeV/ $c^2$ ]	Exp. bkg	90% CL interval [fb]	$\sigma \times \epsilon$ [fb]
6.953420	0.449552	0.0	6.533694
7.005871	0.848923	0.0	9.437558
7.059783	4.904603	0.0	18.366940
7.115758	8.327218	0.0	23.376105
7.174316	11.816673	0.0	30.853555
7.235851	16.684712	0.0	37.750231
7.300555	19.383820	0.0	38.331004
7.368350	22.504177	0.0	46.752210
7.438796	25.539436	0.0	52.632534
7.511010	26.179010	0.0	49.002704
7.583725	26.300923	0.0	47.187789
7.655670	23.940717	0.0	47.042596
7.725912	22.619869	0.0	46.752210
7.793887	19.767324	0.0	41.525255
7.859391	17.610801	0.0	39.637743
7.922501	15.609016	0.0	37.242055
7.983504	13.736242	0.0	32.668469
8.042857	12.556923	0.0	32.087697

### C.3 Null hypothesis testing

To perform a model-independent test for non-SM signal, the probability of the null hypothesis, assuming SM yields only, is computed for each recoil mass bin in Table A.1 and Table A.2. Given the number  $N$  of observed and number  $B$  of background events, the  $p$ -value is defined as

$$p = \sum_{x=N}^{x=\infty} P(x|B) \quad (\text{C.13})$$

where  $P$  is the Poissonian probability. In this analysis, the number of expected background events is defined with an uncertainty  $\Delta B$  and thus Equation C.13 is modified as follows:

$$p = \sum_{x=N}^{x=\infty} \int_{b=0}^{b=\infty} P(x|B) P(B|b, \Delta B) db, \quad (\text{C.14})$$

where  $P(B|b, \Delta B)$  is the PDF for the expected number of background events. The latter can be written as

$$B = L \times \sum_i (\sigma_i \times \epsilon_i), \quad (\text{C.15})$$

where  $L$  is the total luminosity and the sum is done over the different background components with their own cross section  $\sigma_i$  and selection efficiencies  $\epsilon_i$ . As the selection efficiencies measured from the simulation might differ from the real ones due to detector effects, Equation C.15 becomes:

$$B = L \times \sum_i \left( \sigma_i \times \frac{N_i^{sel}}{N_i^{gen}} \times r_i \right), \quad (\text{C.16})$$

where  $N_i^{sel}$ ,  $N_i^{gen}$  is the number of selected and generated events of a given background type and  $r_i$  is the efficiency correction factor derived from validation on data. Uncertainties on the components in Equation C.16 end up in the total uncertainty  $\Delta B$  and the individual PDFs for each background component generate  $P(B|b, \Delta B)$ . While for the statistical errors the PDF is known to be Poissonian, for the systematic uncertainties determining its nature is less straightforward. Hereby, choosing the proper PDF is the key step to calculate  $p$ -values:

- for  $N_i^{sel}$  a Poissonian distribution with mean fixed to the result from MC studies is assumed;
- for  $r$  the PDF is unknown; this term characterizes the degree of the understanding of the detector and it is parameterized as a normal distribution with center at  $r$  and width of  $\delta(r)$  where  $\delta(r)$  is the uncertainty coming from corrections measured on data validation studies.

In order to ease the calculations, the  $p$ -value is defined as:

$$p = 1 - \sum_{x=0}^{N-1} \int_{\hat{r}=0}^{\infty} \int_{\hat{N}_1^{sel}=0}^{\infty} \cdots \int_{\hat{N}_i^{sel}=0}^{\infty} P(x|\hat{N}_1^{sel} \dots \hat{N}_i^{sel}, \hat{r}_1 \dots \hat{r}_i) \times \\ \times P(\hat{r}|r) d\hat{r} \times \prod_i P(\hat{N}_i^{sel}|N_i^{sel}) d\hat{N}_1^{sel} \dots d\hat{N}_i^{sel}. \quad (\text{C.17})$$

To further facilitate numerical computations, it can be noticed that the integral in Equation C.17 is nothing but the averaging of the probability over different values of the background and data-MC correction, and hence we can write

$$p = 1 - \frac{1}{M} \sum_{x=0}^{N-1} \sum_{j=1}^M P(x|(\tilde{N}_1^{sel} \dots \tilde{N}_i^{sel})_j, \tilde{r}_j) \quad (\text{C.18})$$

where the sum runs over a set of  $(\tilde{r}_j, \tilde{N}_1^{sel} \dots \tilde{N}_i^{sel})_j$  random vectors of size  $M$  simulated with corresponding PDFs. This exercise has been useful to set up the machinery for the null hypothesis testing, though the  $p$ -values are almost meaningless in absence of data and can be only a sanity check for the calculation strategy. The null hypothesis test has been calculated only after data unblinding with the yields measured from the recoil mass distribution on Phase 2 Data. Results are reported in Figure C.2 for the standard  $Z'$ , in Figure C.3 for the LFV  $Z'$ . No significant deviation above the  $3\sigma$  evidence has been found in neither cases.

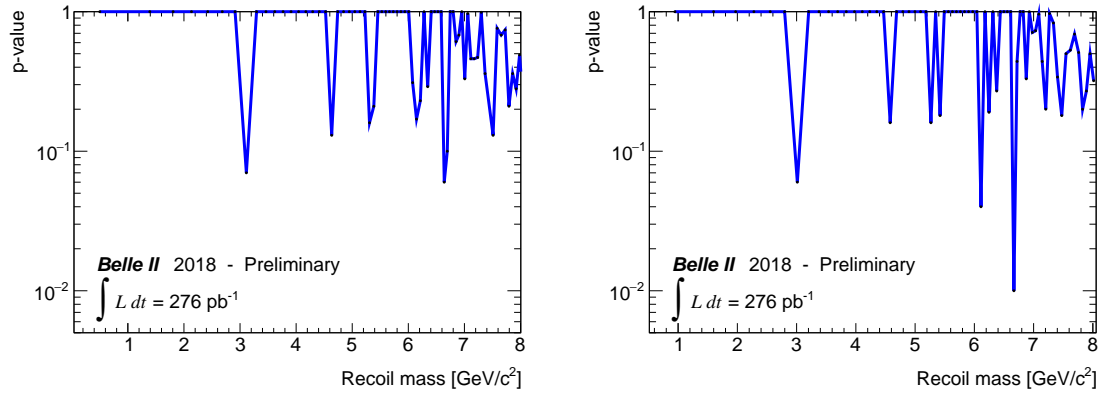


**Figure C.2:** The  $p$ -values computed on the unblinded  $e^+e^- \rightarrow \mu^+\mu^-Z'$  Phase 2 data as a function of the recoil are displayed, for the normal binning scheme (left) and the half bin shifted option (right).

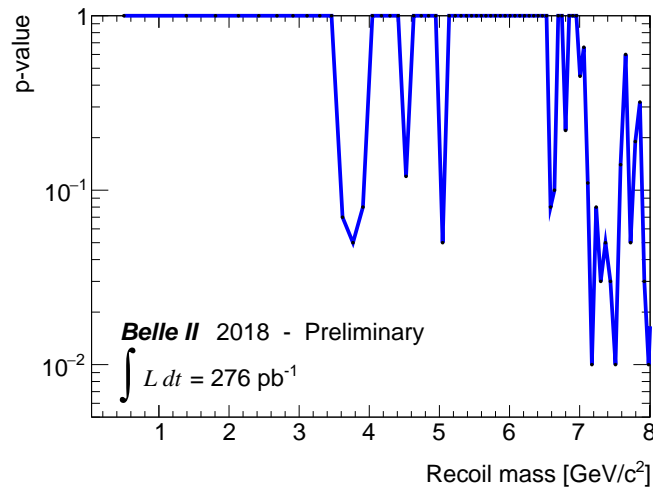


**Figure C.3:** The  $p$ -values computed on the unblinded  $e^+e^- \rightarrow e^\pm\mu^\mp Z'$  Phase 2 data as a function of the recoil are displayed.

## Appendix D

# Phase 3 improvement and prospects: supplementary plots

Results from preliminary lepton ID studies on Phase 3 data are reported here. The improvement in background rejection when applying a tight muon ID selection to the reconstruction of the decay  $J/\psi \rightarrow \mu^+\mu^-$  is shown in Figure D.1.

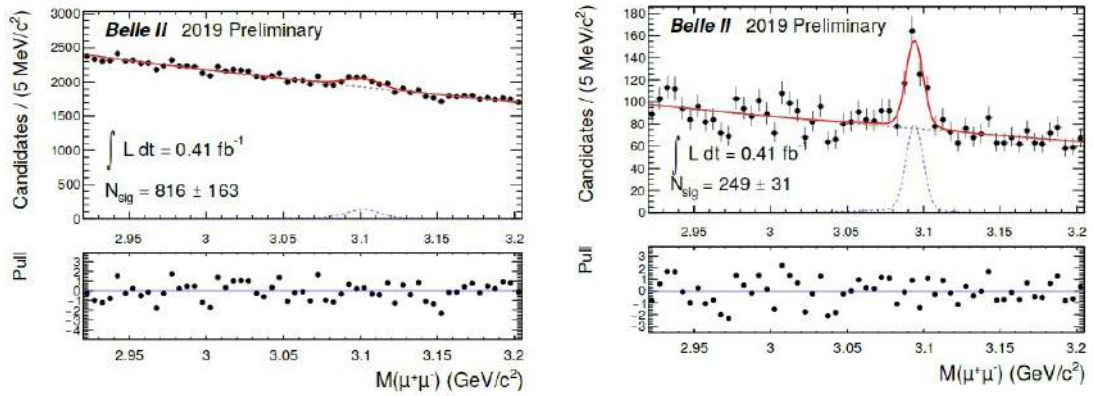


**Figure D.1:** The dimuon invariant mass for the reconstructed  $J/\psi \rightarrow \mu^+\mu^-$  events on  $0.41 \text{ fb}^{-1}$  of Belle II 2019 data is here reported. On the left, only loose track quality selections are applied and no selection on the muon ID probability is required, while on the right the muon ID probability is asked to be larger than 0.95. The number of fitted background events reduces of from  $23457 \pm 55$  to  $917 \pm 11$ .

Results of the signal shape study performed on signal MC samples simulated with early Phase 3 geometry and beam background conditions. The fits to the different  $Z'$  mass simulations and the corresponding values of the shape parameters, particularly the Gaussian and CB function widths, are reported in Figure D.2 in Appendix D.

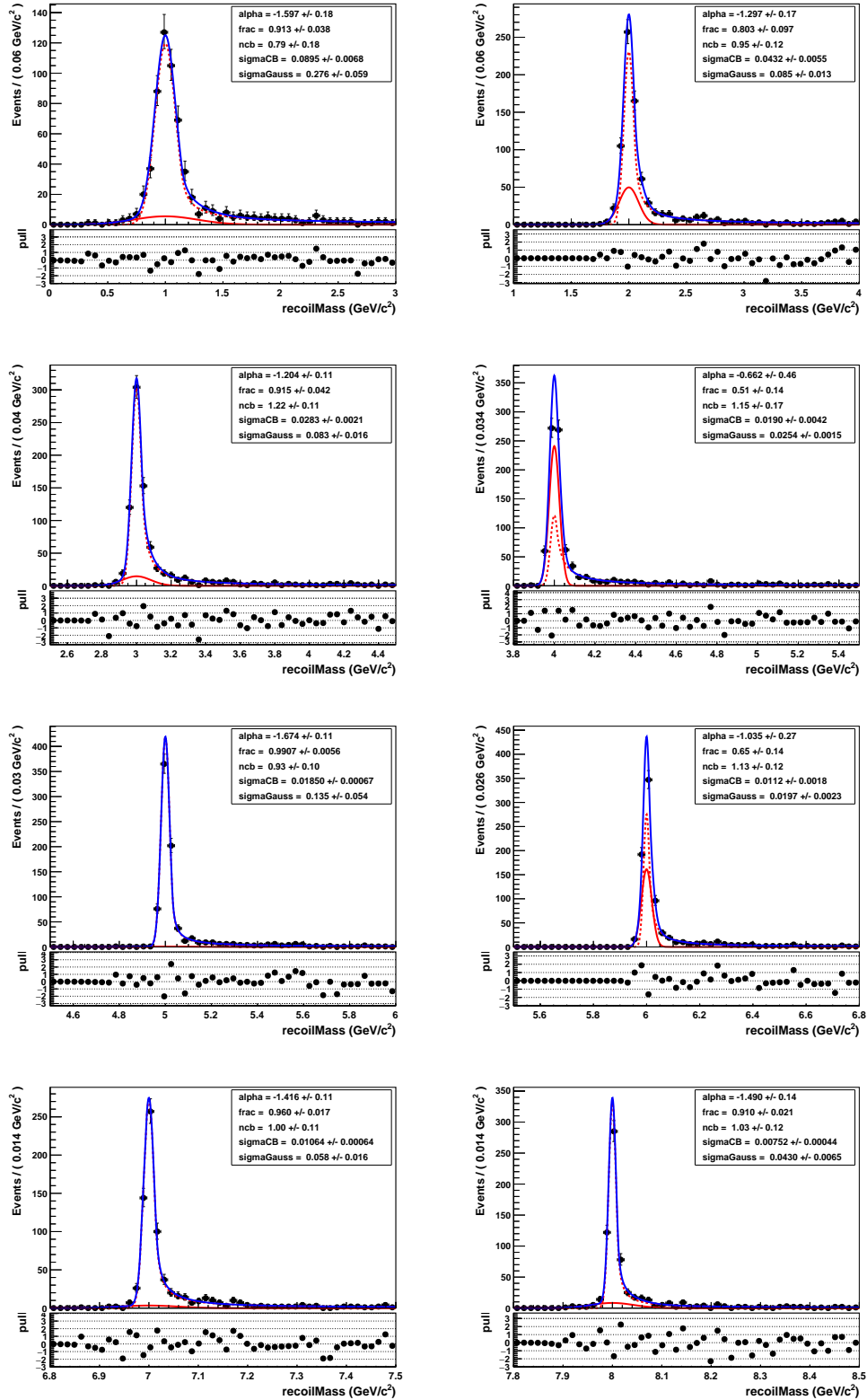


**Figure D.2:** Example of recoil mass distributions of the simulated Phase 3 signal samples, with the fitted PDF model superimposed (blue line), showing both the Gaussian (red filled line) and the CB function (red dashed line) components. Fit results are plotted in the upper right box of each graph and the inset plots show the pull distributions.

# Acknowledgment

For being arrived at the end of this journey, I have to thank many people and their precious guidance. I wish to acknowledge them not just because I managed to arrive here, but also for *how* I have arrived, for the experience I have lived and shared with them and for everything I have learned along the way. The first person is of course my professor, supervisor, advisor, mentor Francesco. He has taught me almost everything, but most important it is the way he did this, by giving the example in person. From him I learned the importance to be present, always focused, always motivated, always determined, eager to stand any efforts when it's about to achieve the planned results and, most important, to distinguish what it is meaningful to be pursued and what it's not worth to spend energies and time for, instead. He taught me that impossible is (almost) nothing, with the right motivation, aware-thinking, dedication and patience. And if things do not go as expected, no defeat exists until one can learn something and how to better behave at the next challenge. I just wish to be able to always follow his model, even if I won't have his office just two doors away from mine anymore. I just wish to continue making him proud of my work and to repay him back for these priceless years of learning and guidance with always better and better achievements. And this applies to all my exceptional colleagues of the Pisa Group: to the tireless Giuliana; to the spectacular Giulia; to the irreplaceable Antonio El Paladin; to Stefano il Super Betta; to the all-knowing Eugenio; to the patient Luigi. Of course, I have to include also my colleagues that moved from Pisa, the *Z' gangers* who shared the good and bad time of the never-ending analysis effort and all the people from the Belle II collaboration I have been lucky to work and spend time with in these years. I know that I owe everything to them, all the achievements, all the fun, all the personal and professional discoveries. No way to survive 24h shift in B3, or to discover Shibuya party life, or again to eat 16 plates in a row at Genki sushi, if I couldn't have shared all this with them.

A special thanks goes to my friends, to the ones in Pisa, from University, the ones who moved away, the ones at home, the ones I have lived with, since they have been always eager to know my next destination and to support my upcoming adventures, to share worries and laughter. Also, they managed not to get crazy when I used to be in four different countries in less than three weeks and they were just trying to understand in which city we could meet for an aperitivo.

And last, but absolutely not least, thanks to my family, who always took so seriously my student and researcher duties, who learned to enjoy with me cold soba and matcha, who always supported me. I am aware that you are the reason why I could leave, study and become independent, and most of all the reason why it's worth to always come back to tell you the things I have seen and the places I have lived. Was I in Japan, Pisa or Marseille, you are always with me.

Finally, thanks to my dear friend, Japan, that in these last two years brought me to a new life. It really changed everything drastically and beautifully in the same way as the *sakura* changes the cold face of winter into a reborn spring. *Arigatou gozaimasu.*

What I have learned and I would like to thank for at the end of my PhD is that I have been so lucky and I received so much in my life, that I just have to keep on trying my best, pursuing my passions, dedicating to my work, studying and sharing my achievements, my knowledge, my joy with the people I'll meet along the journey. It could sound obvious, but this is the most important thing to me: happiness is real only when shared. Learning, teaching and publishing good scientific results is the way I know to do all this. I am deeply grateful.

Vielen dank.

Grazie.

*But it's been no bed of roses, no pleasure cruise,  
I consider it a challenge before the whole  
human race and I ain't gonna loose.  
We are the champions, my friends.  
We'll keep on fighting till the end.*

# Bibliography

- [1] J. Bernstein, *Spontaneous symmetry breaking, gauge theories, the Higgs mechanism and all that*, Rev. Mod. Phys. **46** (Jan, 1974) 7–48.  
<http://link.aps.org/doi/10.1103/RevModPhys.46.7>.
- [2] N. Cabibbo, *Unitary Symmetry and Leptonic Decays*, Phys. Rev. Lett. **10** (Jun, 1963) 531–533. <http://link.aps.org/doi/10.1103/PhysRevLett.10.531>.
- [3] M. Kobayashi and T. Maskawa, *CP Violation in the Renormalizable Theory of Weak Interaction*, Prog. Theor. Phys. **49** (1973) 652–657.
- [4] T. S. V. Albada, R. Sancisi, M. Petrou, and R. J. Tayler, *Dark Matter in Spiral Galaxies [and Discussion]*, Phil. Trans. Roy. Soc. Lond. **A320** (1986) no. 1556, 447–464.
- [5] G. Bertone, D. Hooper, and J. Silk, *Particle dark matter: Evidence, candidates and constraints*, Phys. Rept. **405** (2005) 279–390, [arXiv:hep-ph/0404175](https://arxiv.org/abs/hep-ph/0404175) [hep-ph].
- [6] C. Alcock et al., MACHO, *The MACHO project: Microlensing results from 5.7 years of LMC observations*, Astrophys. J. **542** (2000) 281–307, [arXiv:astro-ph/0001272](https://arxiv.org/abs/astro-ph/0001272) [astro-ph].
- [7] M. Signore and D. Puy, *Cosmic microwave background and first molecules in the early universe*, Eur. Phys. J. **C59** (2009) 117–172.
- [8] P. Montero-Camacho, X. Fang, G. Vasquez, M. Silva, and C. M. Hirata, *Revisiting constraints on asteroid-mass primordial black holes as dark matter candidates*, JCAP **1908** (2019) 031, [arXiv:1906.05950](https://arxiv.org/abs/1906.05950) [astro-ph.CO].
- [9] I. I. Y. Bigi, *CP violation: An Essential mystery in nature’s grand design*, Surveys High Energ. Phys. **12** (1998) 269–336, [arXiv:hep-ph/9712475](https://arxiv.org/abs/hep-ph/9712475) [hep-ph]. [Proc. Int. Sch. Phys. Fermi137,451(1998)].
- [10] R. D. Peccei and H. R. Quinn, *Constraints imposed by CP conservation in the presence of pseudoparticles*, Phys. Rev. D **16** (Sep, 1977) 1791–1797.  
<https://link.aps.org/doi/10.1103/PhysRevD.16.1791>.
- [11] G. Bertone, D. Hooper, and J. Silk, *Particle dark matter: Evidence, candidates and constraints*, Phys. Rept. **405** (2005) 279–390, [arXiv:hep-ph/0404175](https://arxiv.org/abs/hep-ph/0404175) [hep-ph].
- [12] R. Barbieri, C. Braggio, G. Carugno, C. S. Gallo, A. Lombardi, A. Ortolan, R. Pengo, G. Ruoso, and C. C. Speake, *Searching for galactic axions through magnetized media:*

- the QUAX proposal*, Phys. Dark Univ. **15** (2017) 135–141, arXiv:1606.02201 [hep-ph].
- [13] J. Ferretti, *STAX. An Axion-like Particle Search with Microwave Photons*, in *Proceedings, 12th Patras Workshop on Axions, WIMPs and WISPs (PATRAS 2016): Jeju Island, South Korea, June 20-24, 2016*, pp. 35–38. 2017. arXiv:1609.05105 [hep-ph].
- [14] I. Stern, *ADMX Status*, PoS **ICHEP2016** (2016) 198, arXiv:1612.08296 [physics.ins-det].
- [15] P. S. Bhupal Dev, A. Mazumdar, and S. Qutub, *Constraining Non-thermal and Thermal properties of Dark Matter*, Front.in Phys. **2** (2014) 26, arXiv:1311.5297 [hep-ph].
- [16] T. Marrodán Undagoitia and L. Rauch, *Dark matter direct-detection experiments*, J. Phys. **G43** (2016) no. 1, 013001, arXiv:1509.08767 [physics.ins-det].
- [17] J. McDonald, *Generation of WIMP Miracle-like Densities of Baryons and Dark Matter*, arXiv:1201.3124 [hep-ph].
- [18] C. Boehm and P. Fayet, *Scalar dark matter candidates*, Nucl. Phys. **B683** (2004) 219–263, arXiv:hep-ph/0305261 [hep-ph].
- [19] S. Tulin, H.-B. Yu, and K. M. Zurek, *Beyond Collisionless Dark Matter: Particle Physics Dynamics for Dark Matter Halo Structure*, Phys. Rev. **D87** (2013) no. 11, 115007, arXiv:1302.3898 [hep-ph].
- [20] M. Vogelsberger, J. Zavala, and A. Loeb, *Subhaloes in Self-Interacting Galactic Dark Matter Haloes*, Mon. Not. Roy. Astron. Soc. **423** (2012) 3740, arXiv:1201.5892 [astro-ph.CO].
- [21] D. E. Kaplan, M. A. Luty, and K. M. Zurek, *Asymmetric Dark Matter*, Phys. Rev. **D79** (2009) 115016, arXiv:0901.4117 [hep-ph].
- [22] Y. Hochberg, E. Kuflik, T. Volansky, and J. G. Wacker, *Mechanism for Thermal Relic Dark Matter of Strongly Interacting Massive Particles*, Phys. Rev. Lett. **113** (2014) 171301, arXiv:1402.5143 [hep-ph].
- [23] F. F. Deppisch, P. S. Bhupal Dev, and A. Pilaftsis, *Neutrinos and Collider Physics*, New J. Phys. **17** (2015) no. 7, 075019, arXiv:1502.06541 [hep-ph].
- [24] G. Krnjaic, *Probing Light Thermal Dark-Matter With a Higgs Portal Mediator*, Phys. Rev. **D94** (2016) no. 7, 073009, arXiv:1512.04119 [hep-ph].
- [25] R. Essig et al., *Working Group Report: New Light Weakly Coupled Particles*, in *Proceedings, 2013 Community Summer Study on the Future of U.S. Particle Physics: Snowmass on the Mississippi (CSS2013): Minneapolis, MN, USA, July 29-August 6, 2013*. 2013. arXiv:1311.0029 [hep-ph]. <http://www.slac.stanford.edu/econf/C1307292/docs/IntensityFrontier/NewLight-17.pdf>.

- [26] M. Pospelov, A. Ritz, and M. B. Voloshin, *Secluded WIMP Dark Matter*, Phys. Lett. **B662** (2008) 53–61, [arXiv:0711.4866 \[hep-ph\]](#).
- [27] N. Arkani-Hamed, D. P. Finkbeiner, T. R. Slatyer, and N. Weiner, *A theory of dark matter*, Phys. Rev. D **79** (Jan, 2009) 015014.  
<https://link.aps.org/doi/10.1103/PhysRevD.79.015014>.
- [28] B. Holdom, *Two  $U(1)$ 's and Epsilon Charge Shifts*, Phys. Lett. **166B** (1986) 196–198.
- [29] A. K. Drukier, K. Freese, and D. N. Spergel, *Detecting cold dark-matter candidates*, Phys. Rev. D **33** (Jun, 1986) 3495–3508.  
<https://link.aps.org/doi/10.1103/PhysRevD.33.3495>.
- [30] M. Ackermann et al., Fermi-LAT, *Measurement of separate cosmic-ray electron and positron spectra with the Fermi Large Area Telescope*, Phys. Rev. Lett. **108** (2012) 011103, [arXiv:1109.0521 \[astro-ph.HE\]](#).
- [31] O. Adriani et al., PAMELA, *An anomalous positron abundance in cosmic rays with energies 1.5–100 GeV*, Nature **458** (2009) 607–609, [arXiv:0810.4995 \[astro-ph\]](#).
- [32] M. Aguilar et al., AMS, *First Result from the Alpha Magnetic Spectrometer on the International Space Station: Precision Measurement of the Positron Fraction in Primary Cosmic Rays of 0.5–350 GeV*, Phys. Rev. Lett. **110** (2013) 141102.
- [33] *Fundamental Physics at the Intensity Frontier*. 2012. [arXiv:1205.2671 \[hep-ex\]](#).  
<http://lss.fnal.gov/archive/preprint/fermilab-conf-12-879-ppd.shtml>.
- [34] A. Hook, Y. Kahn, B. R. Safdi, and Z. Sun, *Radio Signals from Axion Dark Matter Conversion in Neutron Star Magnetospheres*, Phys. Rev. Lett. **121** (2018) no. 24, 241102, [arXiv:1804.03145 \[hep-ph\]](#).
- [35] B. Batell, R. Essig, and Z. Surujon, *Strong Constraints on Sub-GeV Dark Sectors from SLAC Beam Dump E137*, Phys. Rev. Lett. **113** (2014) no. 17, 171802, [arXiv:1406.2698 \[hep-ph\]](#).
- [36] S. Schael et al., ALEPH, DELPHI, L3, OPAL, SLD, LEP Electroweak Working Group, SLD Electroweak Group, SLD Heavy Flavour Group, *Precision electroweak measurements on the Z resonance*, Phys. Rept. **427** (2006) 257–454, [arXiv:hep-ex/0509008 \[hep-ex\]](#).
- [37] N. Borodatchenkova, D. Choudhury, and M. Drees, *Probing MeV dark matter at low-energy  $e+e-$  colliders*, Phys. Rev. Lett. **96** (2006) 141802, [arXiv:hep-ph/0510147 \[hep-ph\]](#).
- [38] G. Aad et al., ATLAS, *Search for Higgs bosons decaying to  $aa$  in the  $\mu\mu\tau\tau$  final state in  $pp$  collisions at  $\sqrt{s} = 8$  TeV with the ATLAS experiment*, Phys. Rev. **D92** (2015) no. 5, 052002, [arXiv:1505.01609 \[hep-ex\]](#).
- [39] V. Khachatryan et al., CMS, *Search for a very light NMSSM Higgs boson produced in decays of the 125 GeV scalar boson and decaying into  $\tau$  leptons in  $pp$  collisions at  $\sqrt{s} = 8$  TeV*, JHEP **01** (2016) 079, [arXiv:1510.06534 \[hep-ex\]](#).

- [40] R. Aaij et al., LHCb, *Search for hidden-sector bosons in  $B^0 \rightarrow K^{*0} \mu^+ \mu^-$  decays*, Phys. Rev. Lett. **115** (2015) no. 16, 161802, arXiv:1508.04094 [hep-ex].
- [41] R. Aaij et al., LHCb, *Search for long-lived particles decaying to jet pairs*, Eur. Phys. J. **C75** (2015) no. 4, 152, arXiv:1412.3021 [hep-ex].
- [42] J. Alexander et al., *Dark Sectors 2016 Workshop: Community Report*, 2016. arXiv:1608.08632 [hep-ph].  
<http://lss.fnal.gov/archive/2016/conf/fermilab-conf-16-421.pdf>.
- [43] W. Altmannshofer et al., Belle-II, *The Belle II Physics Book*, arXiv:1808.10567 [hep-ex].
- [44] H. Davoudiasl, H.-S. Lee, and W. J. Marciano, *Muon  $g - 2$ , rare kaon decays, and parity violation from dark bosons*, Phys. Rev. **D89** (2014) no. 9, 095006, arXiv:1402.3620 [hep-ph].
- [45] P. del Amo Sanchez et al., BaBar, *Search for Production of Invisible Final States in Single-Photon Decays of  $\Upsilon(1S)$* , Phys. Rev. Lett. **107** (2011) 021804, arXiv:1007.4646 [hep-ex].
- [46] J. P. Lees et al., BaBar, *Search for a Dark Photon in  $e^+e^-$  Collisions at BaBar*, Phys. Rev. Lett. **113** (2014) no. 20, 201801, arXiv:1406.2980 [hep-ex].
- [47] J. P. Lees et al., BaBar, *Search for Invisible Decays of a Dark Photon Produced in  $e^+e^-$  Collisions at BaBar*, Phys. Rev. Lett. **119** (2017) no. 13, 131804, arXiv:1702.03327 [hep-ex].
- [48] B. Batell, M. Pospelov, and A. Ritz, *Probing a Secluded  $U(1)$  at  $B$ -factories*, Phys. Rev. **D79** (2009) 115008, arXiv:0903.0363 [hep-ph].
- [49] R. Essig, J. Mardon, M. Papucci, T. Volansky, and Y.-M. Zhong, *Constraining Light Dark Matter with Low-Energy  $e^+e^-$  Colliders*, JHEP **11** (2013) 167, arXiv:1309.5084 [hep-ph].
- [50] X.-G. He, G. C. Joshi, H. Lew, and R. R. Volkas, *Simplest  $Z$ -prime model*, Phys. Rev. **D44** (1991) 2118–2132.
- [51] J. P. Lees et al., BaBar, *Search for a muonic dark force at BABAR*, Phys. Rev. **D94** (2016) no. 1, 011102, arXiv:1606.03501 [hep-ex].
- [52] W. Altmannshofer, S. Gori, M. Pospelov, and I. Yavin, *Neutrino Trident Production: A Powerful Probe of New Physics with Neutrino Beams*, Phys. Rev. Lett. **113** (2014) 091801, arXiv:1406.2332 [hep-ph].
- [53] W. Altmannshofer, S. Gori, M. Pospelov, and I. Yavin, *Quark flavor transitions in  $L_\mu - L_\tau$  models*, Phys. Rev. **D89** (2014) 095033, arXiv:1403.1269 [hep-ph].
- [54] T. Araki, S. Hoshino, T. Ota, J. Sato, and T. Shimomura, *Detecting the  $L_\mu - L_\tau$  gauge boson at Belle II*, Phys. Rev. **D95** (2017) no. 5, 055006, arXiv:1702.01497 [hep-ph].

- [55] M. G. Aartsen, M. Ackermann, et al., IceCube Collaboration, *Observation of High-Energy Astrophysical Neutrinos in Three Years of IceCube Data*, Phys. Rev. Lett. **113** (Sep, 2014) 101101. <https://link.aps.org/doi/10.1103/PhysRevLett.113.101101>.
- [56] B. Shuve and I. Yavin, *Dark matter progenitor: Light vector boson decay into sterile neutrinos*, Phys. Rev. **D89** (2014) no. 11, 113004, [arXiv:1403.2727](https://arxiv.org/abs/1403.2727) [hep-ph].
- [57] W. Altmannshofer, S. Gori, S. Profumo, and F. S. Queiroz, *Explaining dark matter and  $B$  decay anomalies with an  $L_\mu - L_\tau$  model*, JHEP **12** (2016) 106, [arXiv:1609.04026](https://arxiv.org/abs/1609.04026) [hep-ph].
- [58] R. Aaij et al., LHCb, *Measurement of Form-Factor-Independent Observables in the Decay  $B^0 \rightarrow K^{*0} \mu^+ \mu^-$* , Phys. Rev. Lett. **111** (2013) 191801, [arXiv:1308.1707](https://arxiv.org/abs/1308.1707) [hep-ex].
- [59] A. M. Sirunyan et al., CMS, *Search for an  $L_\mu - L_\tau$  gauge boson using  $Z \rightarrow 4\mu$  events in proton-proton collisions at  $\sqrt{s} = 13$  TeV*, Phys. Lett. **B792** (2019) 345–368, [arXiv:1808.03684](https://arxiv.org/abs/1808.03684) [hep-ex].
- [60] S. R. Mishra, S. A. Rabinowitz, C. Arroyo, K. T. Bachmann, R. E. Blair, C. Foudas, B. J. King, W. C. Lefmann, W. C. Leung, E. Oltman, P. Z. Quintas, F. J. Sciulli, B. G. Seligman, M. H. Shaevitz, F. S. Merritt, M. J. Oreglia, B. A. Schumm, R. H. Bernstein, F. Borchering, H. E. Fisk, M. J. Lamm, W. Marsh, K. W. B. Merritt, H. Schellman, D. D. Yovanovitch, A. Bodek, H. S. Budd, P. de Barbaro, W. K. Sakumoto, P. H. Sandler, and W. H. Smith, *Neutrino tridents and  $W$ - $Z$  interference*, Phys. Rev. Lett. **66** (Jun, 1991) 3117–3120. <https://link.aps.org/doi/10.1103/PhysRevLett.66.3117>.
- [61] D. Curtin, R. Essig, S. Gori, and J. Shelton, *Illuminating Dark Photons with High-Energy Colliders*, JHEP **02** (2015) 157, [arXiv:1412.0018](https://arxiv.org/abs/1412.0018) [hep-ph].
- [62] I. Galon, A. Kwa, and P. Tanedo, *Lepton-Flavor Violating Mediators*, JHEP **03** (2017) 064, [arXiv:1610.08060](https://arxiv.org/abs/1610.08060) [hep-ph].
- [63] I. Galon and J. Zupan, *Dark sectors and enhanced  $h \rightarrow \tau\mu$  transitions*, JHEP **05** (2017) 083, [arXiv:1701.08767](https://arxiv.org/abs/1701.08767) [hep-ph].
- [64] L. Goodenough and D. Hooper, *Possible Evidence For Dark Matter Annihilation In The Inner Milky Way From The Fermi Gamma Ray Space Telescope*, [arXiv:0910.2998](https://arxiv.org/abs/0910.2998) [hep-ph].
- [65] A. J. Bevan et al., *The Physics of the  $B$  Factories*, The European Physical Journal C **74** (2014) no. 11, 84–87. <http://dx.doi.org/10.1140/epjc/s10052-014-3026-9>.
- [66] K. A. Olive et al., Particle Data Group, *Review of Particle Physics*, Chin. Phys. **C38** (2014) 090001.
- [67] P. ODDONE, *An Asymmetric  $B$ -Factory Based on PEPa*, Annals of the New York Academy of Sciences **578** (1989) no. 1, 237–247. <http://dx.doi.org/10.1111/j.1749-6632.1989.tb50614.x>.

- [68] T. Abe et al., Belle-II, *Belle II Technical Design Report*, arXiv:1011.0352 [physics.ins-det].
- [69] B. Aubert et al., BaBar, *Measurement of CP violating asymmetries in  $B^0$  decays to CP eigenstates*, Phys. Rev. Lett. **86** (2001) 2515–2522, arXiv:hep-ex/0102030 [hep-ex].
- [70] K. Abe et al., Belle, *Observation of large CP violation in the neutral B meson system*, Phys. Rev. Lett. **87** (2001) 091802, arXiv:hep-ex/0107061 [hep-ex].
- [71] M. e. a. Staric, Belle Collaboration, *Evidence for  $D^0-\bar{D}^0$  Mixing*, Phys. Rev. Lett. **98** (May, 2007) 211803. <https://link.aps.org/doi/10.1103/PhysRevLett.98.211803>.
- [72] S.-K. e. a. Choi, Belle Collaboration, *Observation of a Narrow Charmoniumlike State in Exclusive  $B^\pm \rightarrow K^\pm \pi^+ \pi^- J/\psi$  Decays*, Phys. Rev. Lett. **91** (Dec, 2003) 262001. <https://link.aps.org/doi/10.1103/PhysRevLett.91.262001>.
- [73] S.-K. e. a. Choi, Belle Collaboration, *Observation of a Resonancelike Structure in the  $\pi^{+-} \psi'$  Mass Distribution in Exclusive  $B \rightarrow K \pi^{+-} \psi'$  Decays*, Phys. Rev. Lett. **100** (Apr, 2008) 142001. <https://link.aps.org/doi/10.1103/PhysRevLett.100.142001>.
- [74] P. M. Lewis et al., *First Measurements of Beam Backgrounds at SuperKEKB*, Nucl. Instrum. Meth. **A914** (2019) 69–144, arXiv:1802.01366 [physics.ins-det].
- [75] T. Kuhr, C. Pulvermacher, M. Ritter, T. Hauth, and N. Braun, Belle-II Framework Software Group, *The Belle II Core Software*, Comput. Softw. Big Sci. **3** (2019) no. 1, 1, arXiv:1809.04299 [physics.comp-ph].
- [76] W. Altmannshofer et al., Belle-II, *The Belle II Physics Book*, arXiv:1808.10567 [hep-ex]. Section 5, Reconstruction Software.
- [77] R. Frühwirth, *Application of Kalman filtering to track and vertex fitting*, Nuclear Instruments and Methods in Physics Research Section A: Accelerators, Spectrometers, Detectors and Associated Equipment **262** (1987) no. 2, 444 – 450. <http://www.sciencedirect.com/science/article/pii/0168900287908874>.
- [78] S. Agostinelli et al., GEANT4, *GEANT4: A Simulation toolkit*, Nucl.Instrum.Meth. **A506** (2003) 250–303.
- [79] M. Ritter et al., *Belle II Conditions Database*, J. Phys. Conf. Ser. **1085** (2018) no. 3, 032032.
- [80] S. Jadach, B. F. L. Ward, and Z. Was, *The Precision Monte Carlo event generator K K for two fermion final states in  $e^+ e^-$  collisions*, Comput. Phys. Commun. **130** (2000) 260–325, arXiv:hep-ph/9912214 [hep-ph].
- [81] N. Davidson, G. Nanava, T. Przedzinski, E. Richter-Was, and Z. Was, *Universal Interface of TAUOLA Technical and Physics Documentation*, Comput. Phys. Commun. **183** (2012) 821–843, arXiv:1002.0543 [hep-ph].

- [82] G. Balossini, C. Bignamini, C. M. C. Calame, G. Montagna, O. Nicosini, and F. Piccinini, *Photon pair production at flavour factories with per mille accuracy*, Phys. Lett. **B663** (2008) 209–213, [arXiv:0801.3360 \[hep-ph\]](#).
- [83] F. A. Berends, P. H. Daverveldt, and R. Kleiss, *Complete Lowest Order Calculations for Four Lepton Final States in electron-Positron Collisions*, Nucl. Phys. **B253** (1985) 441–463.
- [84] H. Czyż, M. Gunia, and J. H. Kühn, *Simulation of electron-positron annihilation into hadrons with the event generator PHOKHARA*, JHEP **08** (2013) 110, [arXiv:1306.1985 \[hep-ph\]](#).
- [85] J. Alwall, R. Frederix, S. Frixione, V. Hirschi, F. Maltoni, O. Mattelaer, H. S. Shao, T. Stelzer, P. Torrielli, and M. Zaro, *The automated computation of tree-level and next-to-leading order differential cross sections, and their matching to parton shower simulations*, JHEP **07** (2014) 079, [arXiv:1405.0301 \[hep-ph\]](#).
- [86] F. Abudinén et al., Belle-II, *Measurement of the integrated luminosity of the Phase 2 data of the Belle II experiment*, [arXiv:1910.05365 \[hep-ex\]](#).
- [87] K. Hanagaki, H. Kakuno, H. Ikeda, T. Iijima, and T. Tsukamoto, *Electron identification in Belle*, Nucl. Instrum. Meth. **A485** (2002) 490–503, [arXiv:hep-ex/0108044 \[hep-ex\]](#).
- [88] I. Komarov and G. Inguglia, *Performance of the CDC trigger for very low multiplicity studies in Phase 2 data*, BELLE2-NOTE-TE-2018-017 (Internal), 2018.
- [89] G. Punzi, *Sensitivity of searches for new signals and its optimization*, eConf **C030908** (2003) MODT002, [arXiv:physics/0308063 \[physics\]](#). [,79(2003)].
- [90] F. Pedregosa, G. Varoquaux, A. Gramfort, V. Michel, B. Thirion, O. Grisel, M. Blondel, P. Prettenhofer, R. Weiss, V. Dubourg, J. Vanderplas, A. Passos, D. Cournapeau, M. Brucher, M. Perrot, and E. Duchesnay, *Scikit-learn: Machine Learning in Python*, J. Mach. Learn. Res. **12** (Nov., 2011) 2825–2830. <http://dl.acm.org/citation.cfm?id=1953048.2078195>.
- [91] R. Brun and F. Rademakers, *ROOT - An Object Oriented Data Analysis Framework, version 6.08/7*, in *AIHENP'96 Workshop, Lausanne*, vol. 389, pp. 81–86. 1997.
- [92] W. Verkerke and D. P. Kirkby, *The RooFit toolkit for data modeling*, eConf **C0303241** (2003) MOLT007.
- [93] T. Skwarnicki, *A study of the radiative cascade transitions between the Upsilon-prime and Upsilon resonances*, DESY-F31-86-02, Appendix E, 1986.
- [94] T. Allmendinger et al., *Track Finding Efficiency in BaBar*, Nucl. Instrum. Meth. **A704** (2013) 44–59, [arXiv:1207.2849 \[hep-ex\]](#).
- [95] A. Caldwell, D. Kollár, and K. Kröninger, *BAT - The Bayesian analysis toolkit*, Computer Physics Communications **180** (2009) no. 11, 2197 – 2209.

- 
- [96] G. J. Feldman and R. D. Cousins, *A Unified approach to the classical statistical analysis of small signals*, Phys. Rev. **D57** (1998) 3873–3889, [arXiv:physics/9711021](#) [[physics.data-an](#)].
- [97] I. Adachi et al., Belle-II, *Search for an invisibly decaying  $Z'$  boson at Belle II in  $e^+e^- \rightarrow \mu^+\mu^-(e^\pm\mu^\mp)$  plus missing energy final states*, [arXiv:1912.11276](#) [[hep-ex](#)].
- [98] I. Komarov, A. Martini, and G. De Pietro, *Study of muon identification performance in Phase 2 using ECL variables*, BELLE2-NOTE-TE-2018-019 (Internal), 2018.
- [99] J. Conrad, O. Botner, A. Hallgren, and C. Perez de los Heros, *Including systematic uncertainties in confidence interval construction for Poisson statistics*, Phys. Rev. **D67** (2003) 012002, [arXiv:hep-ex/0202013](#) [[hep-ex](#)].